Aeroelastic Phenomena and Pedestrian-Structure Dynamic Interaction on Non-Conventional Bridges and Footbridges

a cura di

CLAUDIO BORRI
CLAUDIO MANNINI

Firenze University Press

STRUMENTI
PER LA DIDATTICA E LA RICERCA

– 107 –

Aeroelastic Phenomena and Pedestrian-Structure Dynamic Interaction on Non-Conventional Bridges and Footbridges

Edited by
Claudio Borri & Claudio Mannini

Firenze University Press
2010

AER-BRIDGE is the acronym of a Research Project in Wind Engineering and Bridge Dynamics co-financed by the Italian Ministry for Education, University and Research (MIUR), carried out by five Italian Universities for two years (February 2007- February 2009).
This book presents in an extensive form a selection of the results obtained in the project, the main target of which was the investigation of flow-structure and pedestrian-structure interaction phenomena on bridges and footbridges in order to improve their performances.

Project Co-ordinating Institution:

CRIACIV

Centro di Ricerca Interuniversitario di
Aerodinamica delle Costruzioni ed Ingegneria del Vento

Università di Firenze, Università di Roma "La Sapienza", Università di Perugia,
Università di Trieste, Università IUAV di Venezia, Università di Chieti-Pescara

Cover photo and image:
Render of "Ponte della Musica", Roma, Italy (final design: Buro Happold – Kit Powel-Williams – Lotti & Ass.; executive design and workshop drawings: Mario Petrangeli & Ass. – SBG & Partners); by courtesy of Mattioli S.p.A. *(no reproduction can be made without the written permission of the authors)*

Aeroelastic Phenomena and Pedestrian-Structure Dynamic Interaction
on Non-Conventional Bridges and Footbridges

INDEX

FOREWORD

Within the series of the PRIN projects (Progetti di Ricerca di Interesse Nazionale of the Italian Ministry of Education, University and Research) a wide part of the Italian "wind engineering" community has joined the latest proposal (2006) with the title "**Aeroelastic phenomena and other dynamic interactions on non-conventional bridges and footbridges (AER-BRIDGE)**" which has been selected, co-financed and activated in December 2006. The main target has consisted in developing new operative tools "... to avoid more serious disasters (those due to the lacked serviceability or even to the collapse) which can occur on main structures…", i.e., those systems which offer an increasing sensitivity to wind hazard due to their lightness, slenderness and challenging performances.

The project has been developed thanks to the cooperation amongst five research Units based at the University of Florence, Chieti-Pescara, Venice, Turin and Reggio Calabria, which have dealt with the most critical emerging topics in specific areas, as diffusely described in the Introduction.

This volume presents the main results and detailed scientific outcomes to a wide audience of users amongst professionals, doctoral students and researchers, aiming to increase their consciousness and basic know-how in the field. The international dimension and relevance of the achieved results is also evidenced by means of those cooperation activities carried out with primary laboratories and research groups worldwide. This confirms the well recognised scientific qualification of the Italian wind engineering community within the international context and competition.

About 45 researchers have been contributing and taking part in the activity along the two-year duration of the project, producing more than 40 scientific publications in refereed journals, and presenting their work within all major conferences of the sector concerned. AER-BRIDGE has therefore widely reached the proposed objectives and can be considered as one more example of good-practice of scientific cooperation in the field of wind engineering in Italy.

ACKNOWLEDGMENTS

Claudio Borri & Claudio Mannini

Firenze, November 2010

Introduction

Claudio Borri
National Scientific Coordinator of *AER-BRIDGE*
Head of CRIACIV (c/o Dip. di Ingegneria Civile e Ambientale)
Università degli Studi di Firenze

OBJECTIVES

The project "*Aeroelastic Phenomena and Other Dynamic Interactions on Non-Conventional Bridges and Footbridges*" (in the following referred to as *AER-BRIDGE*, approved and granted within the Research Projects of National Interest (PRIN) of MIUR, the Italian Ministry of Education and Research in 2007-09) has been launched and carried out as a natural follow-up of previous projects in the same line, namely: "*Life-cycle Performance, Innovation and Design Criteria for Structures and Infrastructures Facing Eolian and Other Natural Hazards*" (*PERBACCO*, 2003-05), "*Wind and Infrastructures Dominating Eolian Risk for Utilities and Lifelines*" (*WINDERFUL*, 2001-03) and "*Analysis, Control and Mitigation of Aeolian Risk on Constructions and Urban Environment*" (*ACME CUE*, 1999-01). These "predecessors", to some extent run by the same research teams as in *AER-BRIDGE*, left many open questions in terms of risk and performances of bridges and footbridges facing the storm hazard. This is why the fourth project in the series has focused on such specific category of structures.

It is important to underline that the research group under the leadership of CRIACIV has reached, in recent years, a primary position in Italy mainly due to the common large scale research facility (i.e., the large Wind Engineering laboratory), this last being managed by six Italian Universities (CRIACIV is the Italian acronym for "Interuniversity Research Centre for Building Aerodynamics and Wind Engineering"). About 45 researchers are working together from different Universities/Institutions on common projects, including the series of PRINs (all financed in the last 20 years), with the main aim of promoting wind engineering and building/environmental aerodynamics in the country and internationally (important international/European cooperation has also been developed in the last years).

The present volume, which collects the main outcome of the *AER-BRIDGE* project, has a double aim: first, to make the achieved results available and sustainable for a wider scientific community and for professional users; second, to offer a more extensive version of the results, which have been more deeply evaluated during the time elapsed after the project conclusion (February 2009). In fact, the closure of such a wide two-year project requires a big effort (included the ad-

ministrative one) and the scientific results normally suffer for being constrained within a limited format (also due to the on-line tool available: the MIUR/Cineca web-site).

Furthermore, this book is far from pretending to cover the wide range of activities carried out and results obtained, while it presents a selection of them in extended form. In the five Chapters (Chapt. 1: Aerodynamic and aeroelastic behaviour of bridge decks: CFD investigation and simplified approach to flutter; Chapt. 2: Innovative deck configurations and suspension systems for long-span bridges; Chapt. 3: Structural design assisted by wind tunnel testing; Chapt. 4: Computational simulation of crowd and wind flow over bridge structures; Chapt. 5: Synchronisation phenomena and their implications in the design of footbridges) the contributions of the respective research Units will be presented and widely discussed, under the coordination of the Chapter Authors.

The declared overall aim of the *AER-BRIDGE* project was to avoid that severe damages (those limiting serviceability or even leading to collapse) can occur to main infrastructures, which are more sensitive to dynamic problems of self-excitation under wind action, i.e., very long span bridges and non-conventional footbridges. In order to focus the general aim, this may be summarized as "to ensure a high performance level for the serviceability of bridges and non-conventional footbridges during and after an intense wind storm". In addition to that, the crowd load on footbridges and the interaction phenomena have been widely addressed.

AER-BRIDGE has developed following some main research lines:

1. problems of "pure" aeroelastic interaction, concerning the systems that are more sensitive to self-excited forces (bridge decks, slender structures, cables, etc.); the theoretical-experimental approach was focused to the definition and the development of models, with special regard to the time-domain ones. Among the types of structures under investigation, special attention was given to long- and very-long-span bridges (up to and over 3000 m) and to non-conventional footbridges. The aspects of innovation were ranging from the use of light structural materials to the optimization of bridge deck section (including single- and multi-box decks as well as the Reynolds number effects on the aerodynamic behaviour);

2. self-excited dynamic effects in cable-stayed systems, through a further development of the available models (extended to the time domain) to the large suspended or cable-stayed structures, for which aeroelastic phenomena may induce large and potentially catastrophic effects of amplification of the oscillations;

3. development of computational procedures for the simulation of wind-structure and pedestrians-structure interactions, both through analytical models and CFD. The investigation has included simulation of the dynamic synchronization phenomena and of the vortex-shedding that affects the structures of bridges and footbridges. The specific aim was here to compare and to validate the models available in the scientific literature.

OUTCOMES

While closing the *AER-BRIDGE* project, the Coordinator wishes to underline the synergy, passion and competence shown by all research teams involved. The research Units have also committed own human resources and equipments in order to fulfil the proposed aims. As already mentioned before, the wind engineering laboratory of CRIACIV has served again as the common main research facility from the experimental point of view (one asset of absolute importance in such large research projects). Clear examples of that is the support to the experimental activities of the Units of Torino (validation of CFD results), of Chieti-Pescara (multi-box bridge decks) and Reggio Calabria (pedestrian loads on footbridges).

In details, the activities carried out by the five research Units may be summarised as in the following.

The widest and heaviest part of the activity at the Research Unit FI-CRIACIV was devoted to experimental activity in the wind tunnel laboratory (also on behalf of other research Units) and specific analyses on long-span bridges. During the two years of the project, an intense experimental research regarding the aerodynamic and aeroelastic behaviour of long span bridges has been carried out. First, a forced-vibration system to measure self-excited forces, which characterize a bridge deck or a generic prismatic structure at several reduced wind speed, was conceived and designed. The system is activated by four brushless engines, i.e., three-phase synchronous engines with permanent magnets. They guarantee high-precision positioning and high performance operation. The kinematic solution which was chosen is a modification of the traditional system: a disk connected to the driven shaft transmits the motion, by means of a linear guide, to a connecting rod. The latter can only slide along the vertical direction. In this way, the motion of the extremes of the rocker arm activated by the connecting rod is perfectly harmonic.

The experimental and numerical activities on multi-box decks, whose geometry is similar to the Messina bridge, were performed in a close cooperation with the Research Unit of Chieti-Pescara. In view of an optimization of the cross-section, it was studied the effect of a reduction of space between the lateral boxes and the central one on the aerodynamic behaviour and aeroelastic stability of the deck. The measure of the flutter derivates, as well as several tests in "ambient vibrations" in the wind tunnel, showed that a limited reduction of the distance between the boxes is possible without any reduction of the critical flutter velocity.

By the use of the experimental free-vibration set-up, the aeroelastic derivatives of a bridge deck having a trapezoidal cross-section were measured for different values of the angle of attack.

Thanks to the collaboration with the Institute of Aeroelasticity of the German Aerospace Centre (DLR) in Göttingen, an extensive campaign of numerical simulations (CFD) was also performed. The non-commercial finite-volume code TAU - developed at DLR - was used. The main purpose of the research was to explain some discrepancies between the experimental results obtained at the CRIACIV wind tunnel and at the Western Ontario Laboratory in Canada on the section model of the Sunshine Skyway Bridge. The numerical approach was based on the Unsteady Reynolds-Averaged Navier-Stokes equations (URANS), numerically integrated on two-dimensional grids of hybrid type. The numerical simulations confirmed the initial suspicion that the cause of the discrepancies was the different degree of sharpness of the lower edges in the two models.

Another field of research regarded the experimental and numerical study of the aerodynamic properties of a two-dimensional prism having rectangular cross section and ratio $B/D = 0.5$ (being B the width and D the height of the rectangle). Such a geometry is a reference for studies on the aerodynamic and aeroelastic behaviour of bridge decks, and an international benchmark has recently been launched (http://www.aniv-iawe.org/barc).

Furthermore, the activity of CRIACIV continued with the study of the effects of accessory structures and non-structural elements on the aerodynamic and aeroelastic behaviour of bridge decks, focusing on the problem of the correct reproduction of such details at small scales in the wind tunnel. In some cases such details are so small that they can only be reproduced by equivalent configurations. Moreover, even when the dimensions do not represent a problem, it is well known that the reduced scale may have significant effects on the flow field, and consequently on the forces acting on the structure.

With regard to the theoretical and numerical analyses (innovative numerical simulations based on semi-empirical models), wind load models were developed further, with particular focus on the extension of the model of indicial functions to the turbulent flow and modelling of the buffeting forces. Through the indicial functions, admittance functions have been obtained, so that the modelling was extended in the time domain using more realistic functions than the Sears one (which is only valid for an extremely thin airfoil). Moreover, the three-dimensional code for aeroelastic and aerodynamic simulations of flexible bridges was developed further. New modules for the parametric generation of suspension and cable-stayed bridges were added and new simulation techniques in the frequency and time domain were implemented, with original contributions both in the multi-modal analysis in the frequency domain and in the time domain simulations. The numerical tool was used to validate load models which were already developed, by means of comparison between experimental and simulation results.

RESEARCH UNIT AT THE UNIV. "G. D'ANNUNZIO" OF CHIETI-PESCARA

At the Research Unit at the Univ. G. D'Annunzio of Chieti (Pescara Campus), the activity was focused on very long span road and railway suspension bridges, with steel multi-box decks. The starting point of the research was the study of the classical multi-box deck (such as the Messina bridge, 1992) with the objective of finding a compromise between a creative structural design and economy of construction, in order to guarantee, at the same time, adequate performances in terms of aeroelastic stability.

In order to define the ranges of optimum design of the deck and the suspension system, new configurations of long span bridges were investigated, following three different approaches: analysis of the aeroelastic response of the multi-box deck for different values of the distance between the boxes (A); introduction of simple structural devices on the system of suspension and study of their effect on the stability with regard to classical flutter (B); investigation on the configuration of very long span bridges with multi-box deck for which there is the inversion of the critical frequencies of the modes involved in the classical flutter instability (C). For all the investigated configurations, some characteristics of the original project of the Messina bridge (1992) were kept unchanged.

As regards the approach "A", four new solutions for the design of the deck were investigated, characterized by a progressive and systematic reduction of the distance between the longitudinal boxes (8 m, 6 m, 4 m, 2 m). After evaluating the reduction in weight of these structures, the structural behaviour under wind loading was analyzed, by means of both numerical analyses (with the software TENSO) and experimental ones (in the CRIACIV wind tunnel). Both the experimental and the numerical results were encouraging: the modal analyses showed that, as the empty space between the caissons decreases, the separation of the modes involved into the flutter phenomenon increases; the experimental analyses highlighted that, within some limits, there is small sensitivity of the flutter critical wind speed to the reduction of the distance between the boxes, while the sensitivity to the configurations of accessory structures is high. The numerical analyses in time history (according to the quasi-steady theory) confirmed that, if the aerodynamic properties are the same, there is a small variation of the flutter critical velocities as the distance between the boxes decreases.

As regards the approach "B" (for the bridges analyzed according to the approach "A") the structural response was studied with regard to the classical flutter, after having introduced four couples of crossed hangers at a distance of 360 m, 390 m, 1050 m and 1080 m from each tower. The analyses in time history showed that the introduction of suspensions has a positive effect on

the separation of frequencies of the modes involved in the classical flutter and, consequently, on the critical flutter velocity.

Concerning the approach "C", two configurations of multi-box deck were investigated: in one of them there was a third cable in the middle of the deck, in the other one there were only two boxes, since the central box was eliminated and the suspension cables were translated internally with respect to the boxes. After having evaluated the weight reduction of the structures, the results of the numerical analyses in the first case (characterized by the introduction of the third suspension cable) showed an unsatisfactory reduction of the ratio of the periods of the critical modes; instead, in both the numerical and the experimental analyses of the deck with two boxes the classical flutter instability did not arise (at least up to a reasonably high wind speed).

Concluding, the study of the decks achieved the objectives which had been planned. As regards numerical and analytical modelling of the load due to vortex shedding, theoretical-numerical studies are underway, as well as the setting of the updated version of the code of calculation TENSO.

RESEARCH UNIT AT THE UNIV. IUAV OF VENICE

Two main issues were investigated at IUAV Research Unit in Venice, the wind-structure interaction and the pedestrian-structure interaction.

As for the first problem, 1) the influence of the effective angle of attack, 2) the influence of the frequency of the structural motion on the forces and 3) overall geometrical non-linearity were investigated. The analysis of the response of a bridge was set according to the following strategy:

- from the theoretical point of view: by the use of a synthetic formulation in the time domain. Such a formulation, based on the classical expressions that describe the aeroelasticity and the aerodynamics of bridges, allows the evaluation of the sensitivity of the structure and a parametric investigation of the response. Although the synthetic formulation represents a simplification of the complex phenomena characterizing the wind flow on a bridge, it makes a synthetic evaluation of the dynamic phenomenon which will establish;

- from the numerical point of view: by the use of models to investigate the fluid-structure interaction on bridges. Through the use of CFD tools, wind tunnel tests were retraced in order to evaluate the aerodynamic and aeroelastic parameters by the investigation of the angle of attack. CFD tools were also used to evaluate the non-linear behaviour, function of the angle of attack, in rigorous and exhaustive terms.

Two main issues were developed in the research, concerning the fluid-structure interaction on cable-stayed bridges. It was referred to a project supervised by the Responsible of the Research Unit of a bridge on the Adige river, concerning the study of the excitation of the bridge deck and the mitigation of the vibrations of the cables. As regards the first issue, the focus was on the flutter instability and on the excitation induced by the vortex shedding. The problem was also approached through wind tunnel tests at Politecnico di Milano for the evaluation of the aeroelastic parameters. As regards the second topic, it is well known that one of the main problems of bridges is the excitations of cables due to wind, to the interaction with traffic and to the motion of the deck and of the towers. During the research, having the Adige bridge as reference, a viscous-elastic damping system was investigated. In particular, the focus was on the criteria to detect the optimum damping and the power dissipated. For such studies, analytical tools were developed, the use of which can also be extended to other fields of the dynamics of structures and mitigation of vibrations.

As for the pedestrians-structure interaction, relying on experimental tests on the movement of a single pedestrian, an experimental methodology for the elaboration of accelerometric measure-

ments was developed. In addition, a theoretical model was set, based on the force generated by the single pedestrian. Using the model, the synchronization of the pedestrians with the structure can be described following a unitary approach. Last, but not least, tests on a cable-stayed footbridge – designed by the Responsible of the Research Unit – were performed and aimed to a dynamic characterization of the structure (in terms of frequencies and damping) and to the evaluation of the vibrations induced by the pedestrians in several dynamic load configurations.

RESEARCH UNIT AT POLITECNICO DI TORINO

In the Research Unit at Politecnico di Torino, the applications regarding the pedestrians-structure and the wind-structure interaction were developed in the following steps:
1. set-up of the physical-mathematical models;
2. direct simulation of the interaction phenomena;
3. identification of the linear transfer functions in the frequency domain;
4. identification of the non-linear transfer functions in the time domain.

The study of the pedestrians-structure interaction mainly aimed to develop the points 1 and 2: the initial objective has been fully achieved.

The study of the wind-structure interaction aimed to be articulated in all the four phases. But during the research new interesting fields emerged concerning the second and the third phases. It was then decided to deeply develop them, in view of a "curiosity driven" research. Without them the development of new procedures of identification (phase 4) would have been lacking of the necessary phenomenological aerodynamic bases.

-       Pedestrian-structure interaction: the Unit gave a significant contribution to the study of lateral synchronized excitation, proposing and developing a new approach for modeling the crowd-structure interaction. The mathematical model was then implemented into a multi-physical code of calculation developed ad-hoc. The model has been tested both on ideal tests and on a real event registered on a footbridge. The comparison between simulations and experimental measurements confirmed the validity and the accuracy of the proposed model, referring to the dynamics of the crowd and of the structure.

-       Wind-structure interaction: the modeling of the turbulent wind flow in the vicinity of bridge decks was integrated with the estimation of the accuracy of two models on the aerodynamics of bluff-bodies. The models have been applied to three study cases: a thin plate, the deck of the Sunshine Skyway bridge, a cylinder of rectangular cross-section with ratio base/height equals to 5 and sharp edges (bluff-body). The analysis of the second test case was carried out in cooperation with the Research Unit in Florence, and it was aimed to the evaluation of the sensitivity of the aerodynamic behavior of the bridge deck with regard to small variations of some geometrical parameters, such as the rounding of the edges of the trapezoidal cross-section. The study of the third test case was undertaken in a wider initiative aiming to promote – at an international level – a benchmark of bluff-bodies aerodynamics. The benchmark, namely "Benchmark on the Aerodynamics of a Rectangular 5:1 Cylinder" (BARC, http://www.aniv-iawe.org/barc) was also promoted, among the others, by some members of the Unities of Research of Florence and Reggio Calabria, in addition to the one of Torino and with the patronage of the Italian Association of Wind Engineering (ANIV), the International Association for Wind Engineering (IAWE), in cooperation with the European Research Community On Flow, Turbulence And Combustion (ERCOFTAC). The study of the first test case allowed the evaluation of the sensitivity to the variation of parameters which were previously regarded as deterministic and then characterized as stochastic variables. In particular, the Reynolds number, i.e., the velocity of the incident flow, was chosen as the main parameter. The aeroelastic behaviour was evaluated referring to the semi-

empirical model by Scanlan, where the aeroelastic force is expressed as a function of the so-called flutter derivatives. In the project, techniques of identification of the flutter derivatives were developed (modified indicial approach) relying on the input data (motion of the structure) and output data (aeroelastic forces) given by the computational simulation. The results highlighted the pronounced sensitivity of the flutter derivatives to the Reynolds number and allowed to characterize them statistically, by computing the stochastic Navier-Stokes equations (stochastic flutter derivatives).

RESEARCH UNIT AT UNIV. "MEDITERRANEA" OF REGGIO CALABRIA

The Research Unit at Univ. of Reggio Calabria aimed at investigating the dynamic interaction phenomena characterizing footbridges, in order to compare, validate and criticize the current models available in literature and propose new design criteria.

The activities are described in the following, some of them are currently on-going.

1. Analysis of the undisturbed walking: measurements on 124 people were performed. They were asked to walk for a distance of 72 m. For each person, the time and number of steps were registered for the estimation of statistics.

2. Development of a model of vertical response: the vertical load produced by the crowd was generated by a Monte Carlo simulation. The response of the footbridge was computed by the numerical solution in the time domain of the equation of motion. Relying on these results, a response spectrum was defined, so that the designer is able to determine the peak acceleration on footbridges depending on the return period.

3. Definition of a response model for the single crossing: to do that, the approximated equations of the response of a beam under a harmonic load travelling with constant velocity were written. The formulation was particularly accurate in the evaluation of the maximum displacement and the maximum acceleration.

4. Experimental investigation on a bridge model: in order to study the effects produced by the oscillations of footbridges on the parameters of walking, experimental tests on a 12 m-footbridge, vibrating in the vertical direction, were performed at the Technical University of Denmark. These tests also allowed to estimate the limits of application of the analytical results.

5. Development of a device for the experimental analysis of the dynamics of the crowds: in order to evaluate the dynamic behaviour of a group of people and more or less dense crowds, a pedometer was set and attached to a shoe of each pedestrian.

6. Experiments on the dynamics of crowds: by now, only preliminary tests on groups of 2, 5 and 10 people have been performed. The research will be carried out in the following months, depending on the availability of resources.

7. Validation of the models proposed in the past: the researchers involved in the project had proposed a load model to evaluate the response of footbridges under scarcely dense crowd and so unable to generate synchronization phenomena. In order to validate this model, a numerical investigation on footbridges with different geometrical and mechanical parameters was performed.

8. Laboratory experiments on the pedestrians-footbridge interaction: in order to appreciate the governing mechanism of such interaction, an experimental campaign was initiated, with the use of the treadmill temporarily installed at the CRIACIV wind tunnel.

SOME CONCLUDING REMARKS

The previous overview shows very clearly the outstanding vitality of the research group and its capability to work with very high synergy. Although this might be a natural, long lasting pheno-

menon due to the numerous previous projects that the group has performed in previous years, the research outcomes may be considered unique in the entire national scientific scenery. For sure, the group working in *AER-BRIDGE* has represented the most accredited and entitled research pole in Wind Engineering in Italy for a long period, thanks to a successful and efficient cooperation strategy which has become, nowadays, well consolidated.

The Author of this Introductory Chapter, being at the same time the national Scientific Coordinator of the project, is given the chance to acknowledge sincerely everybody's contribution to the project in the past three years. It would be too long here to mention all the participants (Ph.D. students, technicians and administrative staff, research engineers and associate Professors) who have contributed actively at different levels. Nevertheless, I cannot omit here a grateful *Thank you*: this goes to the Co-Editor of this volume, Dr. C. Mannini (Florence).

To Firenze University Press, Dr. Guatelli, our acknowledgment for the patience and supportive commitment of the Publisher.

1 Aerodynamic and aeroelastic behaviour of bridge decks: CFD investigation and simplified approach to flutter

Claudio Mannini, Gianni Bartoli, Claudio Borri
Università degli Studi di Firenze

The research Unit of the University of Florence has dealt with the investigation of the aerodynamic and aeroelastic behaviour of bridges and footbridges. The main results obtained are summarized in this chapter and divided into two contributions. The first one (part I) reports the numerical simulation of the three-dimensional unsteady flow past an infinitely long 5:1 rectangular cylinder, which is considered as a benchmark geometry for studies dealing with bridge aerodynamics and aeroelasticity. This activity has been coordinated with the research Unit of Politecnico di Torino, whose results are presented in Chapter 4. The second contribution (part II) focuses on a simplified method of flutter assessment for flexible bridge structures and highlights some important aspects of the aeroelastic instability mechanism.

PART I
Numerical simulation of flow around a benchmark section

1.1 INTRODUCTION

The numerical simulation of flow around bridge decks and bluff bodies in general is still a challenge due to complex physical phenomena such as massive separation and reattachment, laminar-to-turbulent transition and alternating detachment of large eddies. In addition, these types of flow are three-dimensional even for simple two-dimensional geometries, thus posing significant problems with respect to the computational cost. In particular, the unsteady flow around a stationary two-dimensional rectangular cylinder with chord-to-thickness ratio $B/D = 5.0$, at low Mach number ($M_\infty = 0.1$), relatively high Reynolds number ($Re = 26,400$ based on the body thickness D) and zero flow incidence ($\alpha = 0°$), has been numerically simulated. This geometry is often assumed as a reference test case for studies dealing with bridge aerodynamics and aeroelasticity and a benchmark study (BARC, which stands for Benchmark on the Aerodynamics of a Rectangular 5:1 Cylinder) was launched in July 2008 [a].

As previously mentioned, the simulations discussed here refer to a configuration with a zero-degree angle of attack, which is the basic test case of the BARC. Nevertheless, the experiments

conducted by Schewe [b] in the high-pressure wind tunnel in Göttingen, Germany, highlighted the interesting case of configurations with small flow incidence, where significant Reynolds number effects can be observed. For instance, for $\alpha = 2°$ the lift coefficient increases of nearly 100 % passing from a Reynolds number of 4,000 to 120,000. Similarly, for $\alpha = 4°$ the increase is of about 70 % with a double-bent pattern if the Reynolds number ranges from 5,200 to 370,000. This last configuration was also numerically studied [1] solving the 2-D unsteady Reynolds-averaged Navier-Stokes (URANS) equations in combination with an explicit algebraic Reynolds stress model (EARSM). The results suggested that the progressive upstream migration of the time-averaged shear-layer reattachment location on one side of the rectangular cylinder is responsible for the strong Reynolds number effects previously mentioned. Different mechanisms of vortex shedding at low and high Reynolds numbers were highlighted too.

Along with one of the authors' research activity [1-8] (in particular, in [3] the case of an harmonically oscillating cylinder is also considered), other numerical simulations on the same geometry were performed by Shimada and Ishihara [c], who investigated rectangular cylinders with various chord-to-thickness ratios with a 2-D two-layer k-ε turbulence model. In the framework of the BARC, Bruno et al. [d] performed a 3-D Large Eddy Simulation (LES) with a dynamic sub-grid scale model and studied the mechanism of vortex shedding with the help of proper orthogonal decomposition techniques (see also Chapter 4).

Three-dimensional Detached-Eddy Simulation (DES) is employed in this work as strategy of turbulence modeling. This hybrid method combines the Reynolds-averaged Navier-Stokes approach near solid walls and Large-Eddy Simulation away from walls, where significant amounts of turbulent kinetic energy can be economically resolved.

The numerical results obtained with DES are compared with experimental data, as well as with the results of 3-D unsteady RANS computations. Moreover, the role played by the spanwise period of the computational domain is investigated. Results obtained with spanwise extensions of one and two chord lengths are compared in terms of integral quantities and correlation of fluctuating pressures.

1.2   EXPERIMENTAL RESULTS

For the geometry considered there are not many sets of experimental data available in the literature. In particular, the authors are not aware of any data concerning measurements of the local flow field. Besides general studies on rectangular cylinders with various chord-to-thickness ratios (e.g. [e-g]), the main experimental data considered for comparison and validation in the current work are those measured by Schewe [b] in a high-pressure wind tunnel. In this low-turbulence closed-circuit facility the force coefficients, the Strouhal number and the mean base pressure were measured for a wide range of Reynolds numbers and for several angles of attack, on a fixed model. The measured drag ($C_D \approx 1.0$, normalized with respect to the body thickness D) is in good agreement with other wind-tunnel results available in the literature [g-i]. For the Strouhal number ($St = f_s D/U_\infty$, where f_s is the dominant frequency of vortex shedding observed in the lift spectrum and U_∞ the free-stream velocity) the experimental data are more scattered: Nakamura and Yoshimura [j] and Nakamura and Nakashima [k] obtained $St = 0.115$, Okajima [e] as well as Parker and Welsh [l] $St = 0.106$, whilst Matsumoto et al. [m] found a slightly larger value, i.e., $St = 0.132$. Finally, Stokes and Welsh [n] measured $St = 0.118$ and $St = 0.109$ respectively for plates with chord-to-thickness ratios of 4.9 and 5.2.

The pressure coefficient distribution at zero-degree angle of attack for two different Reynolds numbers was measured by Matsumoto [i] in the Kyoto University wind tunnel, Japan (see [m] for

details concerning the experimental set-up). Finally, the pressure measurements performed in the CRIACIV wind tunnel in Prato, Italy [o,p] are also referred to.

Given the lack of local flow field measurements for this geometry, a qualitative reference are the results obtained by Mizota and Okajima [c] for a slightly bluffer 4:1 rectangular cylinder, whose flow field is supposed to be similar to that for the profile considered.

1.3   NUMERICAL METHODS

The numerical simulations were performed using the finite-volume unstructured solver DLR-Tau code [q], developed by the German Aerospace Center (DLR). The code solves the compressible Navier-Stokes equations using vertex-centered metrics with second-order spatial and temporal accuracy. Viscous terms are treated using a conventional second-order central differencing scheme. In the current work the inviscid fluxes are approximated using a central difference scheme stabilized with artificial dissipation. The convective term in the additional turbulent equation is also discretized with second-order central differencing.

The advancing in time is performed through the dual time-stepping approach. The time derivatives are first discretized with a second-order backward difference formula and the resulting sequence of nonlinear steady-state problems is solved in pseudo-physical time by an explicit three-stage Runge-Kutta scheme, until a steady state in pseudo-time is reached. The local convergence within each physical time increment is accelerated by means of the local time-step technique, where the largest time step compatible with the Courant-Friedrichs-Lewy (CFL) criterion is chosen cell by cell for each inner iteration. Explicit smoothing of the residuals and a 3V multigrid algorithm based on the agglomeration of the dual-grid volumes are adopted as additional techniques of acceleration of the convergence of the solution within each time step.

An economical strategy to approach turbulent flows is to solve the unsteady RANS equations in combination with additional equations for turbulence modeling. Nevertheless, in spite of their simplicity and computational efficiency, turbulence models, especially if based on the linear Boussinesq eddy-viscosity hypothesis, are unable to capture complex interaction mechanisms between Reynolds stresses and mean velocity field. As a consequence, these models often fail for strong streamline curvature, which characterizes the flow past bluff bodies [r,s]. The 2-D URANS approach was recently explored by one of the writers for the 5:1 rectangular cylinder [1] and for a bridge section [2] and some interesting results were obtained in combination with an explicit algebraic Reynolds stress model. Nevertheless, limited accuracy for these complex flows was apparent.

A better alternative to the unsteady RANS approach for the simulation of problems with massively separated flow is to use the Large Eddy Simulation (LES) approach. However, LES requires three-dimensional grids and wall-resolved LES (WRLES) becomes unaffordable when high-Reynolds-number thin turbulent boundary layers have to be resolved due to the necessary grid refinement, as the costs are of the order of a poorly resolved Direct Numerical Simulation [t]. Wall-modeled LES (WMLES) reduces the computational requirements at high Reynolds numbers, but the decision about the location of the interface between LES and modeled flow regions is highly critical for the success of a zonal WMLES.

In order to overcome these difficulties the non-zonal Detached-Eddy Simulation (DES) method was introduced by Spalart et al. [t] and Shur et al. [r]. DES is a non-zonal hybrid RANS-LES method and the switching between the RANS and LES modes is controlled by the turbulent length scale, which for the Spalart-Allmaras variant (SA-DES) used in this work is related to the wall distance. In practice, this approach combines RANS model near solid walls, where a wall-resolved LES is unaffordable or too expensive, and LES away from walls, where massive separa-

tion occurs, a RANS formulation is not consistent with the flow physics and turbulent kinetic energy can be economically resolved. 3-D meshes are still needed and, while the number of grid points required for a properly designed DES mesh is not much higher than that for a URANS mesh, the requirement to adopt smaller time steps and the need to obtain the statistical convergence of the solution have limited the use of DES within industry. For the present geometry, due to the presence of sharp edges and the absence of thin turbulent boundary layers, a pure LES method might give fair results with the same level of refinement of the spatial discretization. A few doubts are posed by the short regions of unsteady shear-layer reattachments and it would be extremely interesting to compare the DES results with those obtained by extending up to the walls the sub-grid scale model while keeping unchanged the computational mesh and the discretization algorithms.

The switch between RANS and LES modes is based on a modified definition of the characteristic length scale d^* in the Spalart-Allmaras turbulence model [u], depending on the distance from the wall d and the largest edge length Δ of the local grid cell:

$$d^* = \min\{d, C_{DES}\Delta\} \qquad \Delta = \max\{\Delta_x, \Delta_y, \Delta_z\} \tag{1.1}$$

Near the wall $d^* = d$ as $d < C_{DES}\,\Delta$, and therefore the RANS mode of the DES model is active, i.e., the additional equation works as an eddy-viscosity model. In regions where $C_{DES}\,\Delta < d$, $d^* = C_{DES}\,\Delta$ and, under an equilibrium assumption, the turbulence model reduces to a Smagorinsky sub-grid scale model. The additional parameter with respect to pure URANS simulations is the constant C_{DES}. Shur et al. [r] calibrated this parameter against decaying homogeneous isotropic turbulence (DHIT) to ensure that the LES mode returns a proper turbulent kinetic energy cascade (i.e., the Kolmogorov 5/3's law is resolved). $C_{DES} = 0.65$ is the recommended value, obtained by adopting a centered fourth-order accurate differencing scheme. A smaller value of the DES constant can be used for more dissipative codes [v,w]. However, the optimal choice of C_{DES} is closely tied into the numerical properties of the numerical scheme adopted. Spalart [v] claims that DES is not very sensitive to this parameter. In the present work $C_{DES} = 0.45$ is assumed according to the numerical diffusion of the central-difference scheme employed, on the basis of the calibration using DHIT in the case of second-order accurate spatial discretization of the fluxes, as reported in [x].

1.4   SPATIAL AND TEMPORAL DISCRETIZATION

In this work hybrid meshes are employed, characterized by structured quadrilateral cells around the body profile, in order to better capture the large viscous effects, and unstructured triangular cells in the remaining part of the domain. The use of hybrid grids presents several drawbacks: the discretization of the flow fluxes in the unstructured domain is more diffusive than in the structured domain, and usually a finer spatial discretization is necessary to obtain grid-independent results. In addition, it is complicated to obtain stable algorithms with order of accuracy higher than second for the unstructured discretization of gradients. Another disadvantage of hybrid grids is the fact that standard methods of grid-convergence study, such as Richardson extrapolation, are very difficult to employ rigorously. Nevertheless, unstructured grids allow much easier and faster meshing of complex geometries, as well as convenient and economic mesh refinements just where it is needed. For these reasons their use has become increasingly popular both in research and industrial applications. Despite the fact that, due to the simplicity of the geometry, structured or even Cartesian grids would have been more appropriate for the present

test case, the use of hybrid meshes was preferred for ease of wake refinement and as an exploring study for more complex bluff-body geometries.

Fig. 1.1 shows the 3-D grid (1,703,585 nodes and 2,957,440 cells) obtained by extruding a 2-D grid for one-chord length in the spanwise z-direction ($L/B = 1.0$), using 65 nodes to discretize the resulting edges ($\Delta z/B = 1/64$). Therefore the mesh is perfectly structured in the spanwise direction. The second grid used is identical to the first one but presents a double spanwise period ($L/B = 2.0$) and the same z-spacing (3,380,961 nodes and 5,914,880 cells).

The height of the first structured layer is chosen in order to have maximum wall-unit values in the normal direction $y^+ \approx 1$ ($\Delta y_1/B = 5.0 \times 10^{-5}$). The mesh consists of 28 prismatic layers with a stretching factor in the wall normal direction $\Delta y_{j+1}/\Delta y_j = 1.23$, for a total height of $0.353 \cdot D$. It is worth noting that Spalart [v] observed that in DES applications very little is typically gained by going below $y^+ = 1$ and $\Delta y_{j+1}/\Delta y_j = 1.2$. In the streamwise and spanwise directions the spacing is such that $x^+ \approx z^+ \approx 300$, with significant refinement in the neighborhood of the sharp edges.
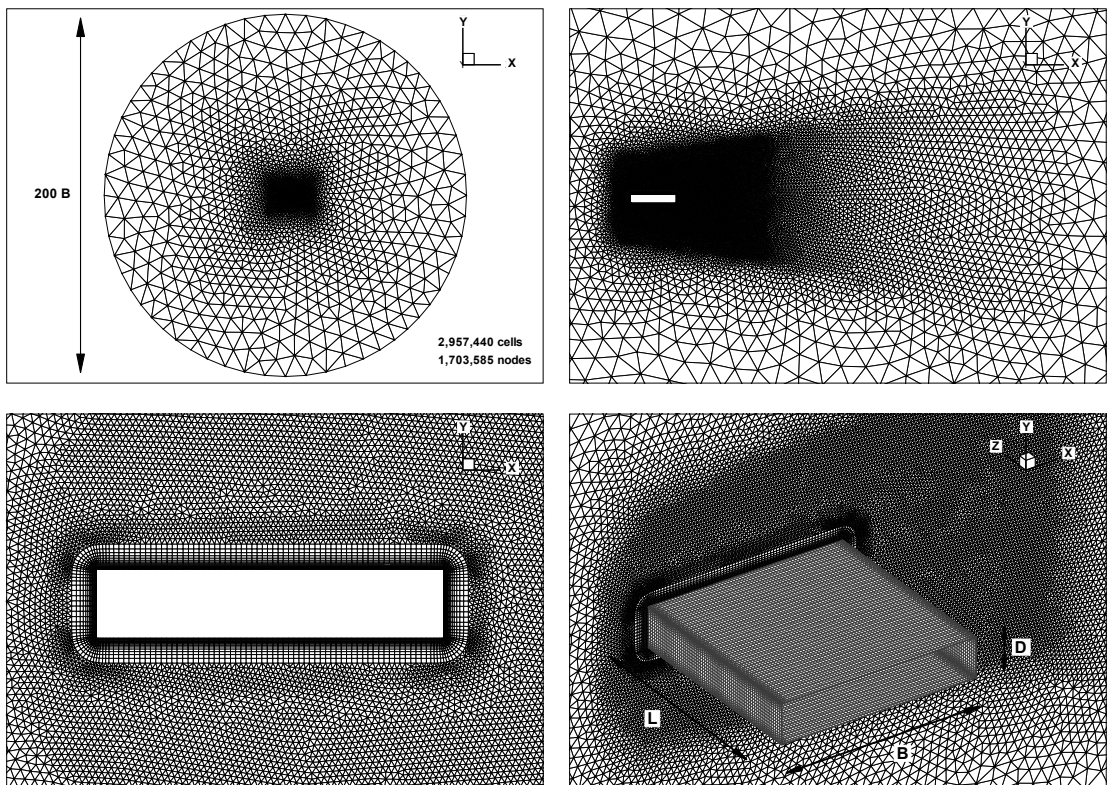
Figure 1.1   Three-dimensional mesh used in the computations ($L/B = 1.0$)

Isotropic cells with dimension equal to $B/64$ are designed in the so-called "focus region", where the largest geometry-dependent turbulence structures are generated, which represents the optimal conformation for the LES mode of DES. In fact, the premise of a well resolved LES is to filter out only eddies that are small enough to be products of the energy cascade, and therefore statistically isotropic [v]. Consequently, in this physically correct condition for LES, refinement in just one or two directions is a waste of resources. The extension of the assumed focus region is

shown in the top-right frame of Fig. 1.1 (one chord downstream the rectangular cylinder). The grid spacing is smoothly enlarged when going into the supposed "departure region" and becomes very coarse in the "Euler region" (according once again to the terminology followed in [v]). With the designed grid and the chosen value of the DES constant, the LES mode was active in the 86 % of the computational volumes.

The nondimensional time-step size is $\Delta t^* = 0.017$, where $t^* = tU_\infty/D$ is the number of travelled lengths D by a fluid particle in a time unit ($U_\infty = 34.0$ m/s is the free-stream velocity), in order to discretize the expected period of vortex shedding with more than 500 time steps. This temporal discretization is finer than the one suggested in [v] on the basis of the cell size in the focus region.

The choice of the resolution of the spatial and temporal discretization relies on literature results but it is also based on the indications offered by the URANS grid-convergence study presented in [1] and by the preliminary DES computations discussed in [3,4]. It is also worth noting that grid-convergence studies for DES simulations are not only burdensome but also particularly problematic [x] and they were not attempted in this work.

The governing equations are solved on a cylindrical computational domain with a radius equal to $100 \cdot B$ (top-left frame of Fig. 1.1). The farfield boundary condition is placed at the external contour of the domain, i.e., free-stream values of the flow variables are assigned as external values and values at the boundary are calculated employing the theory in [y]. The calculation of the fluxes crossing the boundary faces is done using the AUSM Riemann solver. The no-slip and periodic boundary conditions are imposed respectively at the body surface and at the lateral planes of the computational domain. The turbulence model is activated everywhere by prescribing at the farfield boundary small values of the turbulent viscosity (10 % of the laminar viscosity). Nevertheless, no resolved turbulence is generated upstream the rectangular cylinder (smooth flow). As initial condition, free-stream values of the flow variables are imposed at all grid nodes.

1.5   DISCUSSION OF THE RESULTS

The first DES simulation considered was performed on the grid with a spanwise period equal to the chord length of the cylinder ($L/B = 1.0$). In [1,5] the results of this 3-D simulation were compared to those of 2-D URANS computations obtained with the eddy-viscosity one-equation turbulence model of Spalart and Allmaras [u] and an EARSM model, namely the Linearized Explicit Algebraic (LEA) model [z], closed with the k-ω equations of Wilcox [aa]. It was remarked that, despite the fact that the Spalart-Allmaras model represents the additional equation for the DES approach followed here, the URANS solution with this eddy-viscosity model was steady and inaccurate. A significant improvement of the result is given by the 2-D URANS-LEA solution. In contrast, no large difference can be observed between the 2-D and 3-D solutions as the flow field resolved by the URANS equations presents limited three-dimensional features [1]. This result is not surprising as it was noted in [bb] that 3-D URANS simulations must be conducted using significantly larger spanwise periods than those necessary to develop three-dimensionality in DES or LES. Also, the result seems to be very sensitive to the period and turbulence model chosen, so that Shur et al. claim that 3-D URANS computations can be effective in order to better predict the mean drag coefficient but are often not very beneficial where transient flow characteristics are concerned. In addition, in many cases three-dimensionality has to be triggered by introducing a random perturbation in the initial condition. In one instance discussed in [bb] 3-D structures could be sustained only by restarting from a DES flow field.

In Tab. 1.1 the mean and standard-deviation values of the force coefficients and the Strouhal number are compared with the experimental results of Schewe [b]. All the quantities are normalized with respect to the body thickness D. It is worth noting that it is difficult to assess a precise

reference experimental value for the standard deviation of the force coefficients since several phenomena can strongly influence it. Sub- or super-harmonic resonances with the vortex shedding can increase the mean-fluctuation values, especially when the natural frequency of the model is low. As standard deviation of the lift coefficient, $C_L' = 0.4$ seemed to be a reasonable reference value [b]. It can be remarked that the URANS-LEA simulation slightly underestimates the Strouhal number, whilst C_L' is significantly overpredicted. Non-negligible improvement can be obtained by applying DES, especially in terms of mean-fluctuating value of the lift coefficient, which is reduced by almost 50 %. Nevertheless Strouhal number seems to be still underestimated by about 7 %. It is worth adding that the result of the URANS-LEA simulation is nearly periodic, whereas significant chaotic behaviour characterizes the DES solution.

	St	C_L	C_D	C_L'	C_D'	t^*_{INT}
3-D URANS-LEA ($L/B = 1.0$)	0.095	0.013	1.071	1.035	0.029	84.5
3-D SA-DES ($L/B = 1.0$)	0.103	0.047	1.016	0.553	0.055	464.5
3-D SA-DES ($L/B = 2.0$)	0.102	0.005	1.029	0.421	0.043	715.0
Experiments [b]	0.111	0.0	1.029	~0.4		

Tab. 1.1 Comparison with experiments of Strouhal number and mean (C_D, C_L) and standard-deviation (C_D', C_L') values of drag and lift coefficients. t^*_{INT} denotes the nondimensional time units considered for the calculation of the statistics
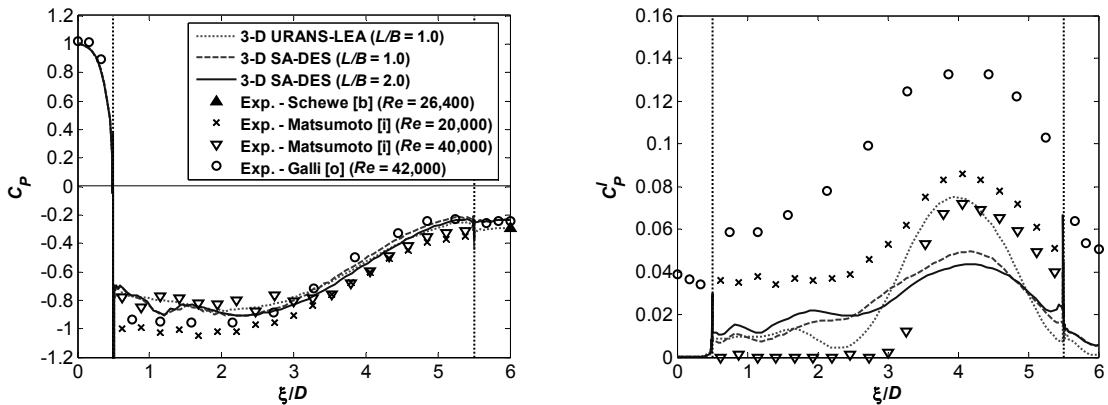

Figure 1.2 Comparison with experiments of the mean (left) and standard-deviation values (right) of the computed pressure coefficient distribution. $\xi/D = 0$ and $\xi/D = 6$ denote respectively the stagnation and the base body contour points
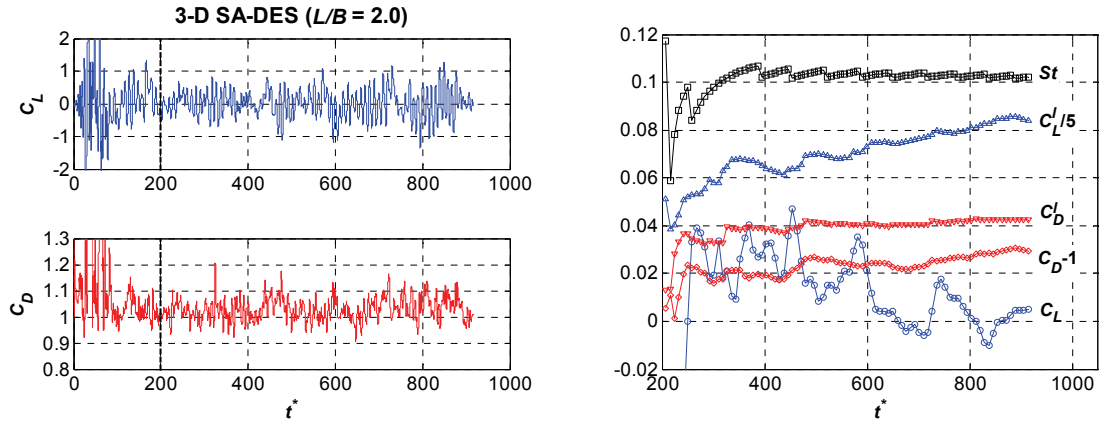
Fig. 1.2 shows the mean and standard-deviation values of the pressure coefficient on the body surface. A few wind-tunnel test results are reported for comparison. The mean pressure coefficients of both URANS-LEA and SA-DES computations, that are also spanwise-averaged, are in good agreement with experiments, which are characterized by limited scatter. Slightly lower values of the mean base pressure are predicted by the DES computation with respect to the URANS one. In contrast, wind-tunnel data for the standard deviation of the pressure coefficients present a significant dispersion. All the simulations predict the same position of the peak of the mean fluctuations, at a streamwise position $x/D \approx 3.6$ ($\xi/D \approx 4.1$ in the figure), in agreement with experiments. Nevertheless, with respect to wind-tunnel data (and also to URANS-LEA results) the SA-DES computation underestimates the magnitude of the peak. In addition, the URANS-LEA and SA-DES computations predict the same values of C_P' immediately after the leading edge for a distance of about D, then, for a length of about $1.5D$ the fluctuating pressures computed with DES are larger than those obtained with the URANS equations. The opposite condition is observed around the aforementioned peak of C_P', where the URANS-LEA results are in better agreement with the experiments of Matsumoto [i]. Finally, near the trailing edge and in the base region, the DES fluctuations are again larger. However, despite the considerable length of the computation, it is worth noting that a perfect convergence of the second statistical moment of the pressure fluctuations has not been reached yet. The experimental results of Galli [o] for C_P' are surprisingly large, also in the stagnation face, and that might be due partly to residual wind-tunnel turbulence.

In Fig. 1.3 the DES time-averaged flow field is depicted showing that the shear-layer mean reattachment occurs near the downstream vertices of the rectangular section, at $x/D = 2.25$ ($x = 0$ denotes the center of the rectangular cylinder), in agreement with the computational results of Bruno et al. [d], who found $x/D = 2.165$ (see also Chapter 4). The length of the recirculation region behind the body is slightly larger with respect to the LES result in [d], the time-averaged saddle point being located at $x/D = 3.47$. A nearly-steady counter-rotating secondary vortex embedded in the main unsteady bubble is resolved close to the leading edge (Fig. 1.3). The secondary vortex is also evident in the LES simulation in [d] but in that case it looks longer and thinner. In the URANS-LEA results described in [1] this counter-rotating vortex is present too but much smaller. In addition, the center of the time-averaged main bubbles was found significantly downstream with respect to the present position.
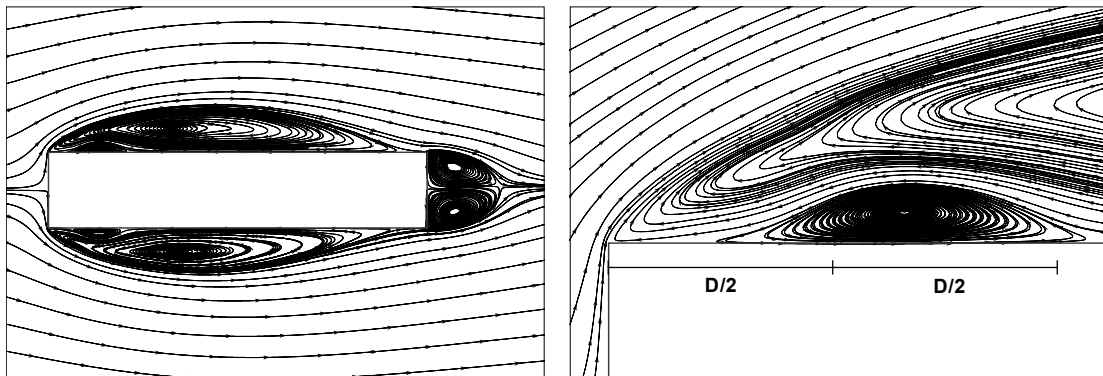

Figure 1.3   Streamlines of the time-averaged flow field. A close-up view near the upstream top edge is reported in the right frame

A computation with the same parameters discussed in the previous section was repeated on the grid with double spanwise period ($L/B = 2.0$). The computed force coefficients are shown in Fig. 1.4 (left frame). Low-frequency modulations in the lift coefficient time history are apparent. The Strouhal number as well as the mean and standard-deviation values of lift and drag coefficients are reported in Tab. 1.1 and their statistical convergence with respect to the length of the computation is highlighted in the right frame of Fig. 1.4. It can be remarked that more than 900 nondimensional time units are necessary to obtain stable values of the second-order statistical moments and a mean value of the lift coefficient satisfactorily close to zero. Even longer signals are needed to obtain stable higher-order moments, which makes these computations extremely expensive (see also [s]). By doubling the spanwise extension of the computational domain no significant changes are observed for the Strouhal number and mean drag, while the mean fluctuations of the force coefficients, as expected, significantly decrease. In contrast, the mean and standard-deviation values of the pressure distribution do not change appreciably (Fig. 1.2).

Figure 1.4   Lift and drag coefficient time histories for the computation with two-chord spanwise period (left) and pattern of convergence of Strouhal number and mean and standard-deviation values of the force coefficients (right). The dashed vertical line on the left indicates the nondimensional time instant after which the signals are considered to calculate the results reported in Tab. 1.1
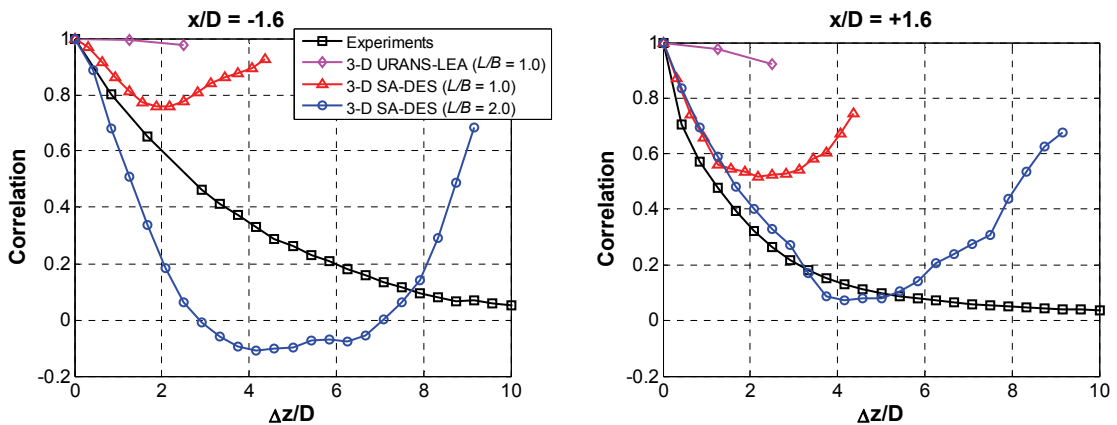
Figure 1.5   Spanwise correlation of the pressure coefficients corresponding to an upstream (x/D = -1.6) and a downstream location (x/D = 1.6). Experimental data [p] refer to a Reynolds number of 63,600

In order to better investigate the effect of the spanwise period considered, the correlation coefficient of the pressure fluctuations at different spanwise positions is shown in Fig. 1.5. The results suggest that the common choice of a distance between the periodic boundary planes equal to the chord of the cylinder is not enough in this case to allow the natural loss of correlation of pressures and the free development of large-scale turbulent structures. As a matter of fact, correlation first decreases with spanwise separation, reaches a minimum and then starts to increase again, due to the effect of periodic boundary conditions. As a consequence, the standard deviation of integral force coefficients might be overestimated. If a two-chord spanwise length of the cylinder is adopted, one observes a remarkable faster decrease of the pressure correlation, which corresponds to a reduction of lift and drag mean fluctuations of more than 20 %. Nevertheless, the effect of periodic boundary conditions imposed at the lateral planes is still non-negligible and an even larger spanwise period may be convenient to allow the free development of the three-dimensional wake of the cylinder. In particular, Fig. 1.5 shows that, considering an array of pressures in the downstream half portion of the cylinder ($x/D = 1.6$), the correlation coefficient for the case $L/B = 2.0$ is close to that obtained from measurements. For spanwise separations $\Delta z/D$ less than 1.5 correlations for one-chord and two-chord spanwise periods are identical. Conversely, the results for the upstream array ($x/D = -1.6$) clearly overestimate or underestimate the experimental data respectively for $L/B = 1.0$ and $L/B = 2.0$. It is also worth noting that in the last case negative correlation is obtained for about $3 < \Delta z/D < 7$ and that the results of the two simulations are different also for very small spanwise separations. Results for the 3-D URANS-LEA simulation are also reported. The large values of the correlation coefficient well agree with the fact that the computed flow field is characterized by limited three-dimensional features.

1.6   CONCLUDING REMARKS

It was shown that with the DES approach and a carefully designed three-dimensional grid fairly accurate results can be obtained for the benchmark test case of the 5:1 rectangular cylinder. In particular, the quality of the simulation is improved with respect to 2-D and 3-D URANS methods. Nevertheless, requirements of fine three-dimensional meshes, small time steps and statistical convergence of the computed flow field make this approach very expensive for bluff-body flows.

The cost of the computation is tightly related also to the choice of the spanwise period of the computational domain and in the present work it was shown that one-chord length might be not enough to allow the free development of three-dimensional large-scale flow structures. A clear improvement was obtained by doubling the spanwise period but this is probably still not sufficient to make negligible the effect of periodic boundary conditions imposed at the lateral planes of the computational domain.

Finally, the good results obtained with DES for the BARC case study, employing hybrid meshes and an unstructured solver, are promising in view of the challenge offered by detailed engineering-structure aerodynamics and fluid-structure coupling problems at high Reynolds numbers in the case of geometries with significant rounded surfaces, where the cost of a well-resolved LES may be prohibitive.

PART II
Simplified approach to flutter

1.7   INTRODUCTION

Modern long-span bridges are more and more sensitive to wind loads and aeroelastic phenomena due to challenging designs involving also high-performance materials, which allow lighter structures and lower vibration frequencies. In particular, an adequate and reliable safety margin with respect to the onset of the aeroelastic instability known as flutter, which can induce the collapse of the structure, has to be warranted.

Classical flutter is a self-excited phenomenon due to the aeroelastic coupling of vertical bending and torsional modes, which introduces energy into the system leading to divergent or large-amplitude limit-cycle oscillations. Relevant for bridge structures is also torsional flutter, wherein negative damping in a torsional mode can be attained without any coupling with other modes. Both phenomena are usually approached with semi-empirical models [cc-ee,9], in which some aerodynamic coefficients, the so-called flutter derivatives, have to be experimentally determined in the wind tunnel. Given the strong dependence of the calculated flutter velocity on these coefficients, the experimental phase and the identification procedure are extremely important [10].

Although it is important to compute in the most accurate way as possible the flutter critical wind speed and the response to turbulent wind, a certain effort has been devoted by the authors in the attempt to simplify the flutter problem, searching for approximate formulas for flutter prediction to be employed at early-design stages and implemented for the improvement of codes and standards [11,12]. Approximate approaches also help to better understand the mechanism leading to flutter instability and consequently allow a better tailoring of the structural design in order to avoid flutter.

In the literature there are several attempts to obtain simplified models of flutter assessment [ff-jj,13-16], that demonstrate the relevance of this issue. The most common simplified method is the quasi-steady theory. The limits of this approach were discussed in [kk,14,15], while its absolute inadequacy to predict torsional flutter instability was highlighted by Nakamura [ll].

1.8   MECHANICAL MODEL

In a flutter analysis, normally only the onset instability wind speed is sought for the design of bridge structures. Therefore, under the assumption of small oscillations perturbating the flow, the structure can be modeled as a two-degree-of-freedom (DoF) linear oscillator, as follows:

$$m\left[\ddot{h}(t)+2\zeta_h\omega_h\dot{h}(t)+\omega_h^2 h(t)\right]=L_{se}(t,K) \tag{2}$$

$$I\left[\ddot{\alpha}(t)+2\zeta_\alpha\omega_\alpha\dot{\alpha}(t)+\omega_\alpha^2\alpha(t)\right]=M_{se}(t,K) \tag{3}$$

where h and α are the heaving displacement and the pitching rotation (Fig. 1.6), m and I the mass and the mass moment of inertia per unit length, ω_h and ω_α the circular eigenfrequencies, ζ_h and ζ_α the structural damping respectively in the heaving and pitching modes, L_{se} and M_{se} the self-excited lift and moment per unit length; $K = B\omega/U$ is the reduced frequency of oscillation, where B is the deck width, ω the circular frequency of oscillation at flutter, U the undisturbed mean flow speed. In the previous equations, the dot denotes derivatives with respect to time t. Classically the self-excited forces can be assumed as linear functions of structural displacements and velocities, parametrically dependent on the nondimensional reduced frequency of oscillation [cc,dd]:

$$L_{se}(t,K) = qB\left[KH_1^*(K)\frac{\dot{h}(t)}{U} + KH_2^*(K)\frac{B\dot{\alpha}(t)}{U} + K^2 H_3^*(K)\alpha(t) + K^2 H_4^*(K)\frac{h(t)}{B} \right] \tag{4}$$

$$M_{se}(t,K) = qB^2\left[KA_1^*(K)\frac{\dot{h}(t)}{U} + KA_2^*(K)\frac{B\dot{\alpha}(t)}{U} + K^2 A_3^*(K)\alpha(t) + K^2 A_4^*(K)\frac{h(t)}{B} \right] \tag{5}$$

where $q = 1/2\rho U^2$ is the mean dynamic pressure, ρ is the air density and the coefficients H_i^* and A_i^* are the flutter derivatives, which are functions of the reduced frequency of oscillation K as well as the mean angle of attack [14,17,mm]. This simple two-degree-of-freedom model can be extended to multimode analysis [dd,nn] of the bridge structure. Nevertheless, in most cases the flutter critical wind speed can be accurately calculated by considering two modes only [oo,18]. It is worth remarking that the classical linear model of Eqs. (4)-(5) has been found to be questionable in some instances, since a non-negligible dependence of flutter derivatives on the amplitude of oscillation has been observed [pp,19].

By assuming coupled harmonic oscillations at frequency ω and imposing the system complex determinant to vanish, one obtains a fourth-order and a third-order polynomial equations with respect to the nondimensional frequency of oscillation (flutter equations), whose common solution gives the critical flutter wind speed [ii].

Alternatively, it is possible to define the dissipative forces in the left-hand side of Eqs. (2)-(3) as imaginary stiffness terms [qq], by introducing the rate-independent damping coefficients g_h and g_α:

$$m\left[\ddot{h}(t) + (1+ig_h)\omega_h^2 h(t) \right] = L_{se}(t,K) \tag{6}$$

$$I\left[\ddot{\alpha}(t) + (1+ig_\alpha)\omega_\alpha^2 \alpha(t) \right] = M_{se}(t,K) \tag{7}$$
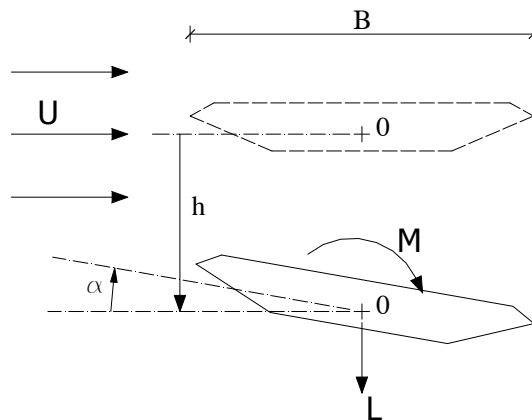
Figure 1.6   Reference scheme for displacements and self-excited forces

where i denotes the imaginary unit. The rate-independent damping coefficients can be related to the ratio-to-critical damping coefficients by the following relations:

$$g_h = 2\zeta_h \frac{\omega}{\omega_h} \qquad\qquad g_\alpha = 2\zeta_\alpha \frac{\omega}{\omega_\alpha} \tag{8-9}$$

The previously mentioned flutter equations can now be written as:

$$\left(1 - g_h g_\alpha\right)\frac{\mu^2}{\gamma_\omega^2}r_\alpha^2 X^2 - \left[r_\alpha^2 \mu^2 \left(1 + \frac{1}{\gamma_\omega^2}\right) + \frac{\mu}{\gamma_\omega^2}\left(A_3^* - g_h A_2^*\right) + r_\alpha^2 \mu \left(H_4^* - g_\alpha H_1^*\right) \right] X +$$

$$+ r_\alpha^2 \mu^2 + \mu A_3^* + r_\alpha^2 \mu H_4^* + H_4^* A_3^* - H_1^* A_2^* - H_3^* A_4^* + H_2^* A_1^* = 0 \tag{10}$$

$$\left(g_h + g_\alpha\right)\frac{\mu^2}{\gamma_\omega^2}r_\alpha^2 X^2 - \left[r_\alpha^2 \mu^2 \left(g_\alpha + \frac{g_h}{\gamma_\omega^2}\right) + \frac{\mu}{\gamma_\omega^2}\left(A_2^* + g_h A_3^*\right) + r_\alpha^2 \mu \left(H_1^* + g_\alpha H_4^*\right) \right] X +$$

$$+ \mu A_2^* + r_\alpha^2 \mu H_1^* + H_4^* A_2^* + H_1^* A_3^* - H_3^* A_1^* - H_2^* A_4^* = 0 \tag{11}$$

where $r_\alpha = 1/B \cdot (I/m)^{1/2}$ is the nondimensional radius of gyration, $\mu = 2m/(\rho B^2)$ is the mass ratio of the deck section, $\gamma_\omega = \omega_\alpha/\omega_h$ is the still-air frequency ratio and $X = \omega_\alpha^2/\omega^2$ is a nondimensional frequency parameter. The advantage of this approach is that the flutter equations simplify to second-order polynomial equations of the frequency parameter X and hence manipulations are easier.

1.9 APPROXIMATE FORMULAS

It is possible to remark that by assuming $1 - g_h g_\alpha \approx 1$, Eq. (10) can be written as follows:

$$\left[\mu A_3^* - r_\alpha^2 \mu^2 \left(X - 1\right) \right] \cdot \left(1 - \frac{X}{\gamma_\omega^2}\right) - r_\alpha^2 \mu H_4^* \left(X - 1\right) + \left(g_h \mu A_2^* + g_\alpha \gamma_\omega^2 r_\alpha^2 \mu H_1^*\right)\frac{X}{\gamma_\omega^2} +$$

$$+ H_4^* A_3^* - H_1^* A_2^* - H_3^* A_4^* + H_2^* A_1^* \cong \left[\mu A_3^* - r_\alpha^2 \mu^2 \left(X - 1\right) \right] \cdot \left(1 - \frac{X}{\gamma_\omega^2}\right) = 0 \tag{12}$$

The approximation in Eq. (12) holds for all the dynamic and aerodynamic data of real bridge structures which have been collected in a database [14,15], unless $X \approx \gamma_\omega$, i.e., $\omega \approx \omega_h$. This condition is unrealistic, provided that the frequency ratio is not very close to one. A simplified equation is therefore obtained for the frequency parameter:

$$X = 1 + \frac{A_3^*}{r_\alpha^2 \mu} \tag{13}$$

Furthermore, Eqs. (10) and (11) can be linearly combined in order to eliminate the term in X^2 and all the terms which contain a second power of the damping coefficients can be neglected. Several

terms in the resulting equation are clearly negligible with respect to the others, once the range of variability of the dynamic and aerodynamic parameters has been identified with reference to the previously mentioned bridge database [14,15]. Therefore the following simplified equation can be obtained:

$$X = \gamma_\omega^2 \frac{r_\alpha^2 \mu \cdot (g_h + g_\alpha) + A_3^* (g_h + g_\alpha) - A_2^* - r_\alpha^2 H_1^*}{r_\alpha^2 \mu \cdot (\gamma_\omega^2 g_h + g_\alpha) + g_\alpha A_3^* - A_2^* - \gamma_\omega^2 r_\alpha^2 H_1^*}$$

(14)

By comparison with Eq. (13), eliminating a couple of negligible terms, one obtains:

$$A_2^* A_3^* + \gamma_\omega^2 r_\alpha^2 H_1^* A_3^* - r_\alpha^2 \mu A_2^* \left(\gamma_\omega^2 - 1\right) + r_\alpha^4 \mu^2 g_\alpha \left(\gamma_\omega^2 - 1\right) = 0$$

(15)

Eq. (15) allows to determine the flutter critical reduced frequency of oscillation, which appears as argument of the flutter derivatives. Then, through Eq. (13) the nondimensional frequency parameter X can be calculated and the critical wind speed is finally obtained. More details about the simplification procedure can be found in [14-16]. Besides the convenient analytical form of the proposed equations, it is important to stress the fact that only three out of eight flutter derivatives are retained. These functions are the so-called "direct" flutter derivatives, which can be measured in the wind tunnel also with single-degree-of-freedom experimental set-ups. Clearly Eqs. (13) and (15) represent a remarkable simplification of the flutter problem.

From the analysis of Eq. (13) it is possible to notice that the mechanism with which the torsional frequency decreases up to the flutter frequency is very simple, absolutely analogous to the case of 1-DoF systems, depending only on the flutter derivative A_3^*, and it is unaffected by the structural damping.

In contrast, the analysis of Eq. (15) is less immediate but it can be remarked that the structural damping can play a significant role in the equation for the critical reduced frequency of oscillation through one term depending only on the structural properties of the bridge. These observations are in agreement with the results of Chen and Kareem [rr], who found that the structural damping does not influence significantly frequency, aerodynamic damping and complex mode shape and the aeroelastic modal damping can be simply estimated as the sum of structural modal damping and the aerodynamic damping estimated with zero structural damping. Moreover, only the structural damping of the torsional mode has an influence on the flutter mechanism. This is reasonable as it is the evolution under wind of the torsional mode (torsional branch) to get unstable, i.e., at the critical wind speed it is the eigenvalue relative to torsion that exhibits positive real part.

As it is clear from the procedure of simplification of the flutter equations, the approximate Eqs. (13) and (15) do not hold for frequency ratios very close to unity, in the same way as Selberg's [ss] and Rocard's [hh] formulas for the flat plate. Nevertheless, it seems that a frequency ratio of about 1.3, or sometimes even less, is sufficient to obtain an acceptable degree of approximation. Frequency ratios very close to unity are fairly uncommon and usually characterize either super-long-span bridges or very unconventional structures, which are not expected to be analyzed with simplified methods, requiring instead careful experimental campaigns since the very beginning of the design procedure.

If damping is neglected the proposed model reduces to Nakamura's one [ff], although it was obtained in a completely different way [14,15]. The simplified solution of the flutter equations proposed by Chen [gg] accounts for the structural damping contribution and is also based on the assumption of well separated frequencies. In addition, this approach retains only four flutter de-

rivatives, namely H_3^*, A_1^*, A_2^* and A_3^*. The fact that the considered flutter derivatives are different from those emphasized in that work should not be seen as a contradiction, in view of existing flutter derivative inter-relations [tt,uu]. In particular, the fact that the proposed formulas depend only on the coefficients H_1^*, A_2^* and A_3^* does not mean that these are the most important derivatives for the instability mechanism and that the others can be neglected. On the contrary, the apparent redundancy of the classical model of self-excited forces [Eqs. (4)-(5)] just allows to express the critical condition with three aerodynamic parameters instead of eight.

The fact that the present equation for the critical reduced frequency of oscillation does account for the contribution of structural damping is an important feature of the model. In fact, as remarked in [rr], while the role of structural damping on the instability onset is negligible in the case of "hard-type flutter", it is significant in the case of "soft-type flutter". In the second instance the negative damping builds up slowly with increasing wind speed, so that a small translation of the curves of total damping due to an increase of the structural damping is able to induce a significant increment of the critical wind speed. In contrast, the change of sign of the total damping is abrupt for hard-type flutter and therefore the instability condition is little sensitive to small translations of its curve. Only in the case of soft-type flutter devices such as tuned mass dampers can be effective in controlling the flutter instability [rr] and the effect of large self-excited drag forces can be non-negligible [vv]. This issue will be further analyzed later on in this chapter.

It is still necessary to precise that, if the damping is known as ratio-to-critical instead of rate-independent coefficient, the procedure of calculation of the critical reduced frequency of oscillation through Eq. (15) becomes iterative. Eq. (9) with $\omega = \omega_\alpha$ is used to obtain a first estimate of g_α and then, once the critical flutter frequency has been calculated through Eq. (13), the rate-independent damping coefficient is updated and the flutter calculation is repeated. One iteration is normally enough to obtain convergence.

1.10   MODEL VALIDATION

In order to validate Eqs. (13) and (15) the following procedure has been followed. A large number of structural parameters for various typologies of existing bridges (suspension, cable-stayed and footbridges) have been collected and compared [14,15]. Since mass and moment of inertia enter in the flutter equations [Eqs. (10)-(11)] in the form of the nondimensional parameters μ, $r_\alpha^2\mu$ and $r_\alpha^2\mu^2$, two bridge structures were identified as representative of opposite extreme dynamics and used as references in the following analyses: the Tsurumi Fairway Bridge, Japan ($\mu = 35.7$ and $r_\alpha = 0.249$) and the Rio Guamà Bridge, Brazil ($\mu = 178.6$ and $r_\alpha = 0.353$). They are both cable-stayed bridges but Rio Guamà Bridge is characterized by a concrete deck and consequently by a remarkable mass with respect to the chord B. In contrast, Tsurumi Fairway Bridge presents a relatively light steel deck with a large chord length.

In order to draw as general as possible conclusions, it is important to consider a large number of dynamic and aerodynamic data. Assuming that flutter derivatives depend on reduced frequency of oscillation and cross-section geometry only, it is possible to combine the aerodynamics of a bridge with the dynamic properties of a completely different one, performing calculations on ideal structures. This observation is important because it allows to employ for the calculations all the reliable aerodynamic and dynamic data available to the authors. In particular, the first validation tests were performed considering the flutter derivatives of a theoretical flat plate [qq,ww], which is always an important benchmark for bridge aeroelasticity, and a rectangular cylinder with a chord-to-thickness ratio $B/D = 12.5$, the bluffer one among those studied by Matsumoto [tt] not prone to torsional flutter.
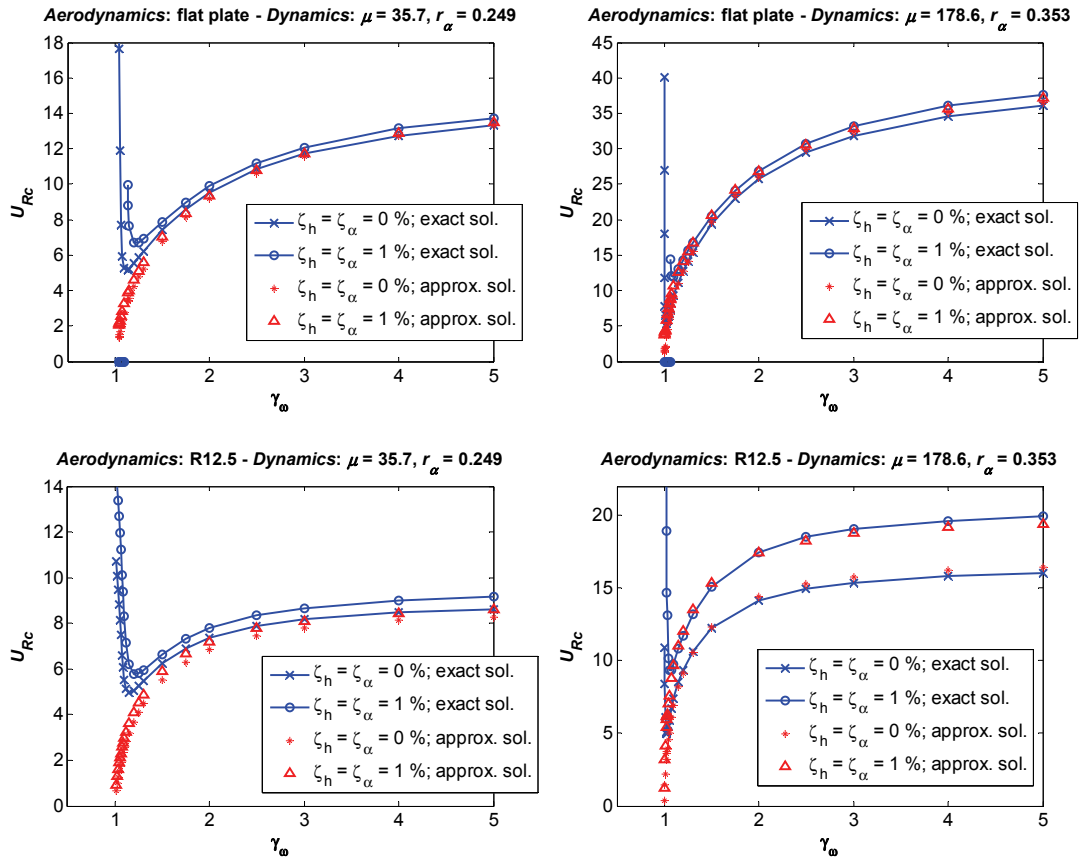
Figure 1.7 Comparison between approximate and exact solutions of the flutter equations ($U_{Rc} = 2\pi/K_c$ is the flutter critical reduced wind speed) for different values of the frequency ratio γ_ω and two values of the ratio-to-critical damping coefficients in the case of classical flutter instability
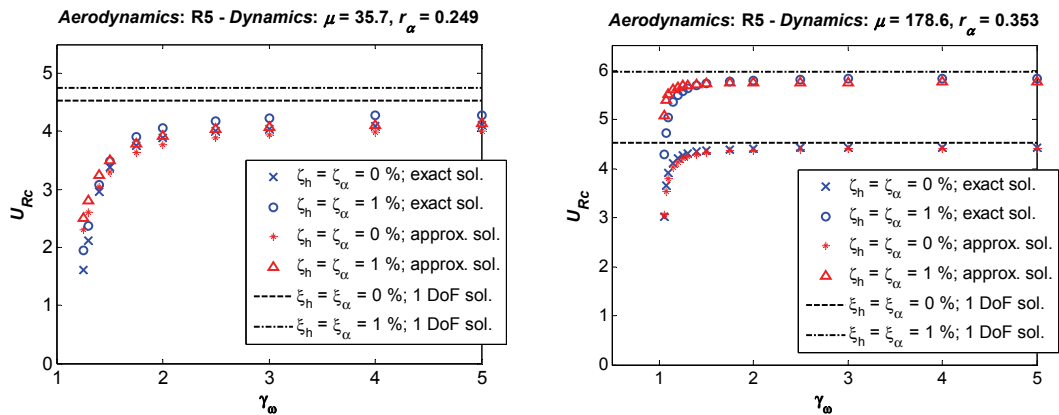
Figure 1.8 Comparison between approximate and exact 1-DoF and 2-DoF solutions of the flutter equations ($U_{Rc} = 2\pi/K_c$ is the flutter critical reduced wind speed) for different values of the frequency ratio γ_ω and two values of the ratio-to-critical damping coefficients in the case of torsional flutter instability

Case	Aerodynamics	μ (-)	r_α (-)	γ_ω (-)	ζ_h (%)	ζ_α (%)
1	Flat plate	35.7	0.249	2.38	0.5	0.5
2	Flat plate	24.1	0.374	1.32	0.6	0.7
3	R12.5	178.6	0.353	1.96	0.8	0.8
4	R12.5	27.7	0.357	2.29	0.5	0.5
5	Akashi Kaikyo	55.6	0.422	2.34	0.5	0.3
6	Tsurumi	35.7	0.249	2.38	0.5	0.5
7	Tsurumi	55.5	0.250	2.06	0.2	0.2
8	R14.3F	47.2	0.539	1.54	0.5	0.5
9	R14.3F	27.7	0.357	2.29	0.5	0.5
10	R20	38.7	0.286	2.27	0.2	0.5

Tab. 1.2   Case studies (classical flutter)

Case	Exact solution			Approx. solution					
	f_c (Hz)	U_{Rc} (-)	U_c (m/s)	f_c (Hz)	Δf_c (%)	U_{Rc} (-)	ΔU_{Rc} (%)	U_c (m/s)	ΔU_c (%)
1	0.315	10.75	128.7	0.315	+0.1	10.43	-3.0	124.9	-2.9
2	0.071	6.72	28.9	0.071	+0.5	5.51	-18.0	23.8	-17.6
3	0.562	16.80	134.2	0.563	+0.1	16.83	+0.2	134.5	+0.2
4	0.308	7.64	66.0	0.314	+1.7	7.01	-8.2	61.6	-6.6
5	0.138	16.14	79.2	0.138	-0.3	15.91	-1.5	77.2	-1.7
6	0.377	8.34	119.5	0.352	-6.7	9.89	+18.5	132.2	+10.6
7	0.880	11.04	217.6	0.836	-5.0	12.72	+15.3	238.3	+9.5
8	0.180	11.41	24.6	0.179	-0.1	10.59	-7.2	22.8	-7.3
9	0.284	10.16	80.9	0.283	-0.6	9.35	-8.0	74.0	-8.5
10	0.338	11.21	90.2	0.340	+0.7	10.79	-3.7	87.4	-3.1

Tab. 1.3   Results for the case studies in Tab. 1.2 (f_c is the coupling frequency, U_{Rc} is the reduced flutter wind speed, U_c is the flutter wind speed)

Case	Aerodynamics	μ (-)	r_α (-)	γ_ω (-)	ζ_h (%)	ζ_α (%)
1	Tacoma	47.2	0.539	1.54	0.5	0.5
2	R5	47.2	0.539	1.54	0.5	0.5
3	R5	35.7	0.249	2.38	0.5	0.5
4	R5	178.6	0.353	1.96	0.8	0.8
5	R5	24.1	0.374	1.32	0.6	0.7
6	R10	47.2	0.539	1.54	0.5	0.5

Tab. 1.4   Case studies (torsional flutter)

Case	1-DoF solution			2-DoF exact solution			Approx. solution					
	f_c (Hz)	U_{Rc} (-)	U_c (m/s)	f_c (Hz)	U_{Rc} (-)	U_c (m/s)	f_c (Hz)	Δf_c (%)	U_{Rc} (-)	ΔU_{Rc} (%)	U_c (m/s)	ΔU_c (%)
1	0.200	4.81	11.5	0.200	4.81	11.5	0.200	0.0	4.81	0.0	11.5	0.0
2	0.189	5.05	11.5	0.190	4.41	10.0	0.190	+0.4	4.35	-1.4	9.94	-1.0
3	0.376	4.64	66.3	0.377	4.08	58.5	0.385	+2.0	3.94	-3.2	57.7	-1.3
4	0.626	5.73	50.9	0.626	5.56	49.4	0.626	+0.1	5.52	-0.7	49.1	-0.6
5	0.066	4.74	19.0	0.067	2.76	11.2	0.070	+3.3	2.90	+5.0	12.2	+8.5
6	0.182	9.89	21.6	0.188	7.65	17.3	0.189	+0.1	7.46	-2.5	16.9	-2.3

Tab. 1.5   Results for the case studies in Tab. 1.4 (the differences are calculated with respect to the 2-DoF exact solution)
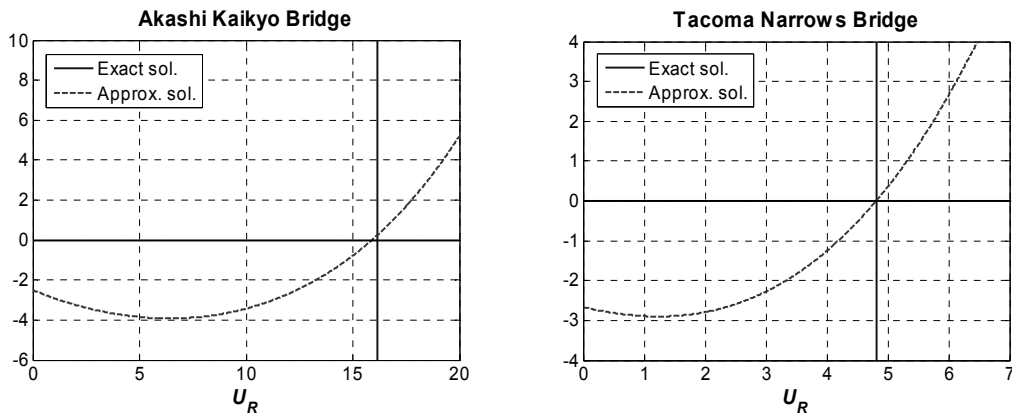
Figure 1.9   Graphic solution of the approximate Eq. (15) for two bridges. The exact solution of the flutter equations is also reported

In Fig. 1.7 the previously discussed reference dynamics and aerodynamics are combined and the rigorous solution of the flutter equations [Eqs. (10)-(11)] are compared to that given by the approximate formulas [Eqs. (13) and (15)] in terms of critical reduced wind speed $U_{Rc} = 2\pi/K_c$, where K_c is the critical reduced frequency of oscillation, for different values of the frequency ratio γ_ω and structural damping. It is clear that the approximation offered by the simplified method is good unless the frequency ratio is very close to one. It is also apparent in the bottom right frame of the figure that, when the effect of damping is significant, the simplified equations are able to correctly account for it.

A similar analysis was performed also in the case of a deck cross section prone to torsional flutter. In particular, the flutter derivatives measured in [tt] for a 5:1 rectangular cylinder were considered. Results are reported in Fig. 1.8, along with the solution of the 1-DoF problem. It is worth noting that the 2-DoF and 1-DoF approaches usually give close results, unless the frequency separation is small. Nevertheless, it was observed in [oo,vv] that the coupling of heaving and pitching motions generally reduces the critical wind speed in the case of torsional flutter. Also in this case the agreement between exact and approximate solutions is very good and the simplified equations are able to take into account the unfavorable effect of coupling between bending and torsion and the role played by damping (right frame of Fig. 1.8).

As further validation, various case studies were taken into account for classical and torsional flutter instabilities in Tabs. 1.2-1.5. In particular, cases 5-6 in Tabs. 1.2-1.3 and case 1 in Tabs. 1.4-1.5 refer respectively to the Akashi Kaikyo Bridge [xx], Japan, Tsurumi Fairway Bridge [yy], Japan, and Original Tacoma Narrows Bridge [cc], USA, for both dynamic and aerodynamic properties. All the other case studies are ideal. The flutter derivatives of a rectangular cylinder with a chord-to-thickness ratio of 20 [tt] (R20) and 10 [tt] (R10), as well as a rectangular cylinder with semicircular fairings and chord-to-thickness ratio of 14.3 [zz] (R14.3F) were used too. Concerning the structural properties, case study 2 of Tabs. 1.2-1.3 and 5 of Tabs. 1.4-1.5 refer to the 1992-proposed-design of Messina Strait Bridge, Italy; case studies 4 and 9 of Tabs. 1.2-1.3 to the Bosporus I Strait Bridge, Turkey; case study 7 of Tabs. 1.2-1.3 to the Indiano Bridge, Italy; case study 10 of Tabs. 1.2-1.3 to the Normandy Bridge, France. The interested reader can find more details about the dynamic properties of these bridges in some authors' previous publications [14,15]. It is apparent in the tables that the degree of approximation offered by the simplified formulas is good, often limited to few percents and in most cases below 10 %. Just for test cases 2, 6 and 7 (Tabs. 1.2-1.3) the errors are larger but well below 20 %. For test case 2 the discrepancy was expected as the frequency ratio is small, namely $\gamma_\omega = 1.32$ (the dynamic parameters of the 1992-proposed design of Messina Strait Bridge are considered in this case). In contrast, both test case 6 and 7 refer to the flutter derivatives of the Tsurumi Fairway Bridge. It is worth noting that for this fairly streamlined cross section the values assumed by the coefficient H_4^* are surprisingly high, thus rendering the proposed formulas slightly less accurate. In fact, the absolute value of the coefficient is in this case much larger not only than the one predicted by the Theodorsen's theory for a flat plate but also for most bridge deck sections, which usually show values close to zero. This is the reason why in several formulations, such as the original one in [cc], this coefficient was even neglected along with A_4^*.

It can also be observed in Tabs. 1.3 and 1.5 that the approximate formula for the critical frequency is very accurate, almost exact in most cases (except test cases 6 and 7 in Tab. 1.3). Also, the agreement with the rigorous 2-DoF results is extremely good in case of structures prone to torsional flutter (Tab. 1.5) and always significantly better than the results of the 1-DoF approach.

Fig. 1.9 shows the pattern of the function on the right hand side of Eq. (15) and its zero crossing as compared to the exact solution of the flutter equations in the case of the Akashi Kaikyo Bridge (test case 5 of Tabs. 1.2-1.3) and Tacoma Narrows Bridge (test case 1 of Tabs. 1.4-1.5).

1.11   ANALYSIS OF THE MECHANISM OF INSTABILITY

The simplified formulas of Eqs. (13) and (15) can also be used to better understand the mechanism of flutter instability. To this purpose all the terms in Eq. (15) depending on the aerodynamic stiffness coefficient A_3^* can be moved to the right hand side of the equation:

$$A_2^* - r_\alpha^2 \mu g_\alpha = \frac{1}{\gamma_\omega^2 - 1} \frac{A_3^*}{r_\alpha^2 \mu} \left(A_2^* + \gamma_\omega^2 r_\alpha^2 H_1^* \right) \tag{16}$$

If Eq. (13) is now substituted into Eq. (16), one obtains:

$$A_2^* - r_\alpha^2 \mu g_\alpha = \frac{X-1}{\gamma_\omega^2 - 1} \left(A_2^* + \gamma_\omega^2 r_\alpha^2 H_1^* \right) \tag{17}$$

In the case of sections not prone to torsional flutter ($A_2^* < 0$), this equation can be interpreted as follows: the progressive reduction of the torsional frequency X-1 due to the aerodynamic coefficient A_3^* is transformed into negative aerodynamic damping through a weighting factor depending on the flutter derivatives H_1^* and A_2^*, the frequency ratio and the nondimensional radius of gyration. Instability is reached when this negative damping equals the positive structural damping and the direct aerodynamic damping in torsion (A_2^*).

Eq. (16) can also be rearranged in the following manner:

$$\overline{A}_2^* - \frac{2I g_\alpha}{\rho B^4} = 0 \tag{18}$$

where

$$\overline{A}_2^* = A_2^* - \frac{1}{\gamma_\omega^2 - 1} \frac{\rho B^4}{2I} A_2^* A_3^* - \frac{\gamma_\omega^2}{\gamma_\omega^2 - 1} \frac{\rho B^2}{2m} H_1^* A_3^* \tag{19}$$

Then the 2-DoF flutter critical condition was written as for the 1-DoF torsional flutter instability, by substituting the flutter derivative A_2^* with the modified function $\overline{A}_2^*$. In the case of a cross section prone to torsional flutter the difference between A_2^* and $\overline{A}_2^*$ tends to be small [16]. As said before, the term proportional to $H_1^* A_3^*$, which is equivalent to $A_1^* H_3^*$, gives the main destabilizing contribution, in agreement with the conclusions of other authors [tt,gg,jj]. Nevertheless, if the nondimensional mass moment of inertia $I/(\rho B^4)$ and the frequency ratio are not too large, also the term proportional to $A_2^* A_3^*$ can play a non-negligible destabilizing role.

This simple flutter formulation can give some indications to tailor the structure at early-design stages and increase the flutter critical wind speed by modifying the structural dynamic properties of the bridge. In particular, it can help to understand to which extent the classical strategies are really efficient. Obviously an increase of the torsional frequency (especially by increasing the torsional stiffness of the structure) has a positive effect, because the dimensional critical wind speed increases, once the reduced critical wind speed has been fixed. The deck width plays an analogous role. However, more interesting is to understand how the reduced critical wind speed can be increased. From Eq. (19) it is apparent that in the case of classical flutter instability an increase of the deck mass per unit length m has always a favorable effect with respect to flutter. Conversely,

if A_2^* takes small values and the frequency ratio is already fairly large, a further increment of the frequency separation does not produce any appreciable increase of the reduced critical wind speed. In the same conditions an increase of the mass moment of inertia I tends to be not effective. However, the reduced critical wind speed tends to be more sensitive to variations of the mass moment of inertia in case of large values of the structural damping in torsion, due to the second term of Eq. (18). Nevertheless, it must be remarked that the discussed parameters are generally related (for instance, the frequency ratio depends on the ratio of the mass moment of inertia to the mass of the deck) and it is not possible to change them in a completely independent way. A detailed discussion of the effects on the flutter instability mechanism of the different structural dynamic parameters can be found in [16].

The simplified formulas can also help to explain the reasons for the different types of flutter instability highlighted in [rr]. It is worth noting that, once the bridge structural properties are fixed, one can observe hard- or soft-type flutter depending on the aerodynamic properties, as clearly shown in Fig. 1.10. In the same way, given the flutter derivatives, the type of instability can change depending on the structural properties of the bridge (see the lower frames of Fig. 1.7 and Fig. 1.8). It is evident from Eq. (16) that, if $r_\alpha^2 \mu$ is large and in particular if μ is large, the negative aerodynamic damping builds up slowly with increasing wind speed [rr]. In addition to that, in case A_2^* takes small negative values, the role of structural damping on the mechanism of instability is non-negligible and soft-type flutter occurs. In fact, with reference to Fig. 1.10, the rectangular cylinder R12.5 with respect to the flat plate presents similar values of H_1^* and A_3^* but much smaller absolute values of A_2^* and that is why one observes soft-type flutter for the former and hard-type flutter for the latter.

Finally, it should be remarked that when a 2-DoF flutter calculation is performed, either rigorous or simplified, the choice of the critical modes susceptible to couple is crucial. This selection must be based on the mode coupling coefficient [ii,18], which accounts for imperfect mode shape similarity, on the frequency ratio and on the absolute value of the torsional frequency. In many cases the choice is obvious in practice but sometimes more than one calculation are necessary to find the smallest flutter critical wind speed. Just in few cases, especially at erection stages of a bridge, the mode shapes are fairly complicated and this choice is not trivial. Sometimes even a multimode approach is necessary to properly account for the actual mechanism of instability [jj].

1.12   CONCLUDING REMARKS

In the second part of this chapter it was shown that the problem of flutter stability can be analytically simplified by manipulating the flutter equations on the basis of experimental evidences. The procedure leads to two approximate equations, through which the critical reduced wind speed and the flutter frequency can be calculated with just three flutter derivatives instead of the usual eight coefficients. These formulas give accurate results provided that the frequency separation of the critical modes is not too small. This result represents a considerable simplification and it allows a deeper understanding of the flutter mechanism and the consequent better tailoring of the bridge structure at early-design stages. In particular, the proposed formulas help to explain the role played by the damping and other structural parameters in the instability onset.
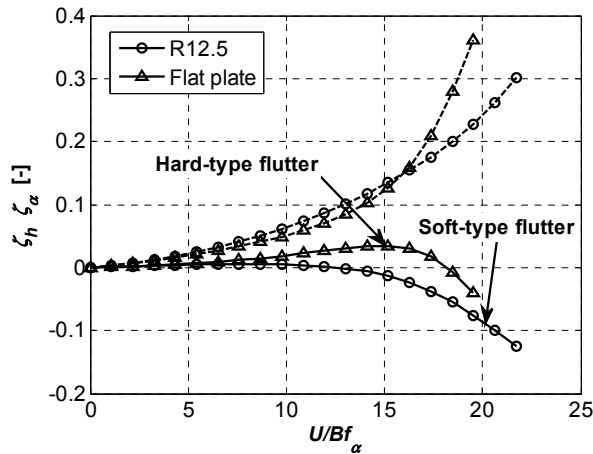
Figure 1.10 Example of soft-type and hard-type flutter for the same structure ($\mu = 178.6$, $r_\alpha = 0.353$, $\gamma_\omega = 1.96$, $\zeta_h = \zeta_\alpha = 0$) with different aerodynamic properties. The total modal damping (structural + aerodynamic) is plotted against the normalized wind speed (f_α is the still air torsional frequency). Solid and dashed lines refer respectively to torsional- and heaving-branch modal damping

1.13   BASIC REFERENCES

PART I

[a]   Bartoli G., Bruno L., Buresti G., Ricciardelli F., Salvetti M.V., Zasso A. 2008. *BARC overview document*. <http://www.aniv-iawe.org/barc>.

[b]   Schewe G., 2009. Reynolds-number-effects in flow around a rectangular cylinder with aspect ratio 1:5. . *Proc. 5th European and African Conference on Wind Engineering* (C. Borri, G. Augusti, G. Bartoli & L. Facchini eds.), Florence, Italy. Firenze University Press, Florence.

[c]   Shimada K., Ishihara T. 2002. Application of a modified *k-ε* model to the prediction of aerodynamic characteristics of rectangular cross-section cylinders. *J. Fluids Struc.* 16(4), 465-485.

[d]   Bruno L., Fransos D., Coste N., Bosco A. 2010. 3D flow around a rectangular cylinder: a computational study. *J. Wind Eng. Ind. Aerodyn.* 98(6-7), 263-276.

[e]   Okajima A. 1982. Strouhal numbers of rectangular cylinders. *J. Fluid Mech.* 123, 379-98.

[f]   Nakamura Y., Ohya Y., Tsuruta H. 1991. Experiments on vortex shedding from flat plates with square leading and trailing edges. *J. Fluid Mech.* 222, 437-447.

[g]   Mills R., Sheridan J., Hourigan K. 2002. Response of base suction and vortex shedding from rectangular prisms to transverse forcing. *J. Fluid Mech.* 461, 25-49.

[h]   Nakamura Y., Mizota T. 1975. Torsional flutter of rectangular prisms. *J. Eng. Mech. Div.* 101(EM2), 125-142.

[i]   Matsumoto M. 2005. Personal communication.

[j]   Nakamura Y., Yoshimura T. 1982. Flutter and vortex excitation of rectangular prisms in pure torsion in smooth and turbulent flows. *J. Sound Vib.* 84(3), 305-317.

[k]   Nakamura Y., Nakashima M. 1986. Vortex excitation of prisms with elongated rectangular, H and ⊦ cross-sections. *J. Fluid Mech.* 163, 149–69.

[l]   Parker R., Welsh M.C. 1983. Effects of sound on flow separation from blunt flat plates. *Int. J. Heat Fluid Flow* 4(2), 113-127.

[m]   Matsumoto M., Shirato H., Araki K., Haramura T., Hashimoto T. 2003. Spanwise coherence characteristics of surface pressure field on 2-D bluff bodies. *J. Wind Eng. Ind. Aerodyn.* 91, 155-163.

[n]   Stokes A.N., Welsh M.C. 1986. Flow-resonant sound interaction in a duct containing a plate, II: square leading edge. *J. Sound Vib.* 104(1), 55-73.

[o]   Galli F. 2005. *Comportamento aerodinamico di strutture snelle non profilate: approccio sperimentale e computazionale*. Master's thesis, Politecnico di Torino, Turin, Italy.

[p]   Ricciardelli F., Marra A.M. 2008. Sectional aerodynamic forces and their longitudinal correlation on a vibrating 5:1 rectangular cylinder. *Proc. 6th International Colloquium on Bluff Body Aerodynamics and Applications* (M. Belloli, F. Cheli, G. Diana, S. Muggiasca, D. Rocchi & A. Zasso eds.), Milan, Italy.

[q]   Gerhold T., Galle M., Friedrich O., Evans J. 1997. Calculation of complex three-dimensional configurations employing the DLR-Tau code. *Proc. 35th AIAA Aerospace Sciences Meeting and Exhibit*, AIAA Paper 97-0167, Reno, Nevada, USA.

[r]   Shur M.L., Spalart P.R., Strelets M.Kh., Travin A.K. 1999. Detached-eddy simulation of an airfoil at high angle of attack. *Proc. 4th International Symposium on Engineering Turbulence Modelling and Experiments* (W. Rodi & D. Laurence eds.), Ajaccio, France (Elsevier, Amsterdam), 669-678.

[s]   Travin A.K., Shur M.L., Strelets M.Kh., Spalart P.R. 1999. Detached-eddy simulations past a circular cylinder. *Flow Turbul. Combust.* 63, 293-313.

[t]   Spalart P.R., Jou W.-H., Strelets M.Kh., Allmaras S.R. 1997. Comments on the feasibility of LES for wings, and on a hybrid RANS/LES approach. *Advances in DNS/LES, Proc. 1st AFOSR International Conference on DNS/LES* (C. Liu & Z. Liu eds.), Ruston, Louisiana, USA (Greyden Press, Columbus, Ohio), 137-147.

[u]   Spalart P.R., Allmaras S.R. 1992. A one-equation turbulence model for aerodynamic flows. *Proc. 30th AIAA Aerospace Sciences Meeting and Exhibit*, AIAA Paper 1992-0439, Reno, Nevada, USA.

[v]   Spalart P.R. 2001. *Young-person's guide to Detached-Eddy Simulation grids*. NASA CR-2001-211032.

[w]   Šoda A. 2006. *Numerical investigation of unsteady transonic shock/boundary-layer interaction for aeronautical applications*. Ph.D. Thesis, RWTH Aachen, Germany.

[x]   Weinman K., van der Ven H., Mockett C., Knopp T., Kok J., Perrin R., Thiele F. 2006. A study of grid convergence issues for the simulation of the massively separated flow around a stalled airfoil using DES and related methods. *Proc. European Conference on Computational Fluid Dynamics* (P. Wesseling, E. Oñate & J. Périaux eds.), Egmond aan Zee, The Netherlands.

[y]   Whitfield D.L., Janus J.M. 1984. Three-dimensional unsteady Euler equations solution using flux vector splitting. *Proc. 17th AIAA Fluid Dynamics, Plasma Dynamics and Lasers Conference*, AIAA Paper 84-1552, Snowmass, Colorado, USA.

[z]   Rung T., Lübcke H., Xue L., Thiele F., Fu S. 1999. Assessment of Explicit Algebraic Stress Models in transonic flows. *Proc. 4th International Symposium on Engineering Turbulence Modelling and Experiments* (W. Rodi & D. Laurence eds.), Ajaccio, France (Elsevier, Amsterdam), 659-668.

[aa]   Wilcox D.C. 1988. Reassessment of the scale-determining equation for advanced turbulence models. *Am. Inst. Aeronaut. Astronaut. J.* 26(11), 1299-1310.

[bb]   Shur M.L., Spalart P.R., Squires K.D., Strelets M.Kh., Travin A.K. 2005. Three dimensionality in Reynolds-Averaged Navier-Stokes solutions around two-dimensional geometries. *Am. Inst. Aeronaut. Astronaut. J.* 43(6), 1230-1242.

PART II

[cc] Scanlan R.H., Tomko J.J. 1971. Airfoil and bridge deck flutter derivatives. *J. Eng. Mech. Div. Proc. ASCE* 97(EM6), 1717-1737.

[dd] Simiu E., Scanlan R.H. 1996. *Wind Effects on Structures: Fundamentals and Applications to Design*. 3rd Edition, Wiley, New York.

[ee] Caracoglia L., Jones N.P. 2003. Time domain vs. frequency domain characterisation of aeroelastic forces for bridge deck sections. *J. Wind Eng. Ind. Aerodyn.* 91(3), 371-402.

[ff] Nakamura Y. 1978. An analysis of binary flutter of bridge deck sections. *J. Sound Vib.* 57(4), 471-482.

[gg] Chen X. 2007. Improved understanding of bimodal coupled bridge flutter based on closed-form solutions. *J. Struct. Eng.* 133(1), 22-31.

[hh] Frandsen A.G. 1966. Wind stability of suspension bridges. Application of the theory of "thin airfoils". *Proc. International Symposium on Suspension Bridges*, Lisbon, Portugal, 609-627.

[ii] Dyrbye C., Hansen S.O. 1997. *Wind Loads on Structures*. 1st Edition, Wiley, New York.

[jj] Øiseth O., Rönnquist A., Sigbjörnsson R. 2010. Simplified prediction of wind-induced response and stability limit of slender long-span suspension bridges, based on modified quasi-steady theory: a case study. *J. Wind Eng. Ind. Aerodyn.* 98(12), 730-741.

[kk] Bisplinghoff R.L., Ashley H., Halfman R L. 1996. *Aeroelasticity*. 1st Edition, Dover Publications, New York.

[ll] Nakamura Y. 1979. On the aerodynamic mechanism of torsional flutter of bluff structures. *J. Sound Vib.* 67(2), 163-177.

[mm] Diana G., Resta F., Zasso A., Belloli M., Rocchi D. 2004. Forced motion and free motion aeroelastic tests on a new concept dynamometric section model of the Messina suspension bridge. *J. Wind Eng. Ind. Aerodyn.* 92(6), 441-462.

[nn] Jain A., Jones N.P., Scanlan R.H. 1996. Coupled flutter and buffeting analysis of long-span bridges. *J. Struct. Eng.* 122(7), 716-725.

[oo] Chen X., Matsumoto M., Kareem A. 2000. Aerodynamic coupling effects on flutter and buffeting of bridges. *J. Eng. Mech.* 126(1), 17-26.

[pp] Diana G., Resta F., Rocchi D. 2008. A new numerical approach to reproduce bridge aerodynamic non-linearities in time domain. *J. Wind Eng. Ind. Aerodyn.* 96, 1871-1884.

[qq] Fung Y.C. 1993. *An Introduction to the Theory of Aeroelasticity*. Dover Publications, New York.

[rr] Chen X., Kareem A. 2003. Efficacy of tuned mass dampers for bridge flutter control. *J. Struct. Eng.* 129(10), 1291-1300.

[ss] Selberg A. 1961. *Oscillation and aerodynamic stability of suspension bridges*. Acta Polytechnica Scandinavica, Civil Engineering and Building Construction Series 13, Oslo, Norway.

[tt] Matsumoto M., 1996. Aerodynamic damping of prisms. *J. Wind Eng. Ind. Aerodyn.* 59, 159-175.

[uu] Scanlan R.H., Jones N.P., Singh L. 1997. Inter-relations among flutter derivatives. *J. Wind Eng. Ind. Aerodyn.* 69-71, 829-837.

[vv] Chen X., Kareem A. 2006. Revisiting multimode coupled bridge flutter: some new insights. *J. Eng. Mech.* 132(10), 1115-1123.

[ww] Theodorsen T. 1934. *General theory of aerodynamic instability and the mechanism of flutter*. NACA, Langley Research Center, Hampton, NACA Technical Report 496, Annual Report 20.

[xx]   Katsuchi H., Jones N.P., Scanlan R.H. 1999. Multimode coupled flutter and buffeting analysis of the Akashi Kaikyo Bridge. *J. Struct. Eng.* 125(1), 60-70.

[yy]   Singh L., Jones N.P., Scanlan R.H., Lorendeaux O. 1995. Simultaneous identification of 3-dof aero-elastic parameters. *Proc. 9th International Conference on Wind Engineering*, Wiley Eastern Ltd., New Delhi, 972-981.

[zz]   Chowdhuri A.G., Sarkar P.P. 2004. Identification of eighteen flutter derivatives of an airfoil and a bridge deck. *Wind Struct.* 7(3), 187-202.

1.14   LIST OF PUBLICATIONS

PART I

[1]   Mannini C., Šoda A., Schewe G. 2010. Unsteady RANS modelling of flow past a rectangular cylinder: Investigation of Reynolds number effects. *Computers and Fluids* 39(9), 1609-1624.

[2]   Mannini C., Šoda A., Voß R., Schewe G. 2010. Unsteady RANS simulations of flow around a bridge section. *J. Wind Eng. Ind. Aerodyn.* 98(12), 742-753.

[3]   Mannini C., Šoda A., Voß R., Schewe G. 2007. URANS and DES simulation of flow around a rectangular cylinder. In: *Notes on Numerical Fluid Mechanics and Multidisciplinary Design, vol. 96, Proc. 15th DGLR-Fach-Symposium der STAB* (C. Tropea, S. Jakirlic, H.-J. Heinemann, R. Henke & H. Hönlinger eds.), Darmstadt, Germany (Springer, Berlin, Heidelberg, New York), 36-43.

[4]   Mannini C., Šoda A., Voß R., Schewe G. 2007. CFD simulation of flow around bridge sections. *Proc. 12th International Conference on Wind Engineering*, Cairns, Australia, 831-838.

[5]   Mannini C., Šoda A., Schewe G., Weinman K. 2008. Detached-Eddy Simulation of flow around a 1:5 rectangular cylinder. *Proc. 6th International Colloquium on Bluff Body Aerodynamics and Applications* (M. Belloli, F. Cheli, G. Diana, S. Muggiasca, D. Rocchi & A. Zasso eds.), Milan, Italy.

[6]   Mannini C., Weinman K., Šoda A., Schewe G. 2009. Three-dimensional numerical simulation of flow around a 1:5 rectangular cylinder. *Proc. 5th European and African Conference on Wind Engineering* (C. Borri, G. Augusti, G. Bartoli & L. Facchini eds.), Florence, Italy. Firenze University Press, Florence.

[7]   Mannini C., Šoda A., Weinman K., Schewe G. 2009. 3-D numerical investigation of flow past a rectangular cylinder. *Proc. 6th International Congress of Croatian Society of Mechanics*, Dubrovnik, Croatia.

[8]   Mannini C., Šoda A., Schewe G. 2010. Unsteady flow past a 5:1 rectangular cylinder: computational investigation on three-dimensional spanwise effects. *Proc. 5th International Symposium on Computational Wind Engineering*, Chapel Hill, North Carolina, USA.

PART II

[9]   Costa C., Borri C. 2006. Application of indicial functions in bridge deck aeroelasticity. *J. Wind Eng. Ind. Aerodyn.* 94(11), 859–881.

[10] Bartoli G., Contri S., Mannini C., Righi M. 2009. Towards an improvement in the identification of bridge deck flutter derivatives. *J. Eng. Mech.* 135(8), 771-785.

[11] Mannini C., Bartoli G., Flamand O., Grillaud G. 2007. A simplified method of flutter assessment: first steps towards flutter derivative generalization. *Proc. 12th International Conference on Wind Engineering*, Cairns, Australia, 2343-2350.

[12] Bartoli G., Mannini C., Ricciardelli F. 2009. Una nuova definizione normativa del carico aerodinamico e del limite di stabilità al flutter per gli impalcati da ponte. *Proc. 10ᵗʰ Italian National Conference on Wind Engineering IN-VENTO*, Cefalù, Italy.

[13] Bartoli G., Righi M. 2006. Flutter mechanism for rectangular prisms in smooth and turbulent flow. *J. Wind Eng. Ind. Aerodyn.* 94, 275-291.

[14] Mannini C. 2008. *Flutter Vulnerability Assessment of Flexible Bridges – Wind-Tunnel Tests, Probabilistic Model, Analytical Investigation*. Verlag Dr. Müller, Saarbrücken.

[15] Bartoli G., Mannini C. 2008. A simplified approach to bridge deck flutter. *J. Wind Eng. Ind. Aerodyn.* 96(2), 229-256.

[16] Mannini C., Bartoli G. 2009. Analisi del meccanismo del flutter per impalcati da ponte: sensibilità rispetto ai parametri dinamici della struttura. *Proc. 10ᵗʰ Italian National Conference on Wind Engineering IN-VENTO*, Cefalù, Italy.

[17] Mannini C., Bartoli G. 2008. Investigation on the dependence of bridge deck flutter derivatives on steady angle of attack. *Proc. 6ᵗʰ International Colloquium on Bluff Body Aerodynamics and Applications* (M. Belloli, F. Cheli, G. Diana, S. Muggiasca, D. Rocchi & A. Zasso eds.), Milan, Italy.

[18] Bartoli G., Mannini C. 2005. From multimodal to bimodal approach to flutter. *Proc. 6ᵗʰ European Conference on Structural Dynamics* (C. Soize & G.I. Schuëller eds.), Paris, France (Millpress, Rotterdam), 349-354.

[19] Mannini C., Ferrucci M., Bartoli G. 2010. Effetti non lineari nelle derivate di flutter di un impalcato da ponte. *Proc. 11ᵗʰ Italian National Conference on Wind Engineering IN-VENTO*, Spoleto, Italy.

WITH CONTRIBUTION FROM:

Günter Schewe, Institute of Aeroelasticity, German Aerospace Center (DLR) of Göttingen, Germany
Ante Šoda, Faculty of Mechanical and Naval Engineering, University of Zagreb, Croatia

2 Innovative deck configurations and suspension systems for long-span bridges

Piero D'Asdia, Sofia Febo
Università "G. D'Annunzio" di Chieti-Pescara

2.1 INTRODUCTION

The University of Chieti-Pescara Research Unit of AER_BRIDGE project have been dealing with the structural response bridges to wind actions. The studies developed during the past co-financed projects (1997-1998 "RESACIV" - Researches and experimental campaigns for building aerodynamics and wind engineering; 1999-2000 "ACME-CUE" - Analysis, control and mitigation of aeolian risk in buildings and urban environment; 2001-2002 "WINDERFUL" - Control the aeolian risk and ensure the serviceability of structures and infrastructures; 2003-2005 "PERBACCO" - Performance during the whole life, innovation and design criteria of structures and infrastructures withstanding eolic action and other natural events) represent the starting point to achieve the goals of the present research project.

In particular, during these two years, the activities have been focused on wind-structure interaction of long-span suspension bridges with multiple-box steel deck. Although classical multiple-box girder decks are characterized by a high aeroelastic stability, the increase of the span length of recent bridges causes a dangerous sensitivity to aeroelastic phenomena, within both serviceability and ultimate limit states: it is extremely important to guarantee a reliable safety margin with respect to the collapse due to flutter. This aim has been pursued by improving the system stability from a structural and an aerodynamic point of view: on the one hand, the influence of the box spacing on the aeroelastic behaviour of the deck has been investigated, and, on the other, the possibility to enhance the flutter stability with innovative structural solutions (by increasing the frequency separation or by obtaining torsional-to-bending frequency ratios smaller than one) has been tested. The results, summarized in the following sections of this chapter, and reported in details in the cited papers, has been obtained interpreting numerical and experimental analysis, in collaboration with the University of Florence and the University of Trieste.

2.2 DEVELOPMENTS IN DESIGNING WIND-RESISTANT LONG-SPAN BRIDGES

The span length of modern suspension bridges has always been increasing and consequently the control of the structural response to steady and unsteady wind loads is nowadays a design priority: it is important to postpone flutter to high wind speed, in spite of low natural frequencies and low frequency ratios usually characterizing long-span bridges, while drag and moment forces

have to be kept as low as possible. The deck, therefore, has a key role in designing long-span bridges, despite being a secondary element in the static behaviour of the whole system.

In view of this assumption, traditionally, the design solutions to control aeroelastic stability of suspension bridges aim to follow two possible approaches: if, on the one hand, to increase deck stiffness may be one of the choices (*e.g.* adopting stiffening truss, which is basically stable from an aeroelastic point of view, with static aerodynamic coefficients slightly dependent from rotations, but with rather high values of drag forces; the deck of the Akashi Kaikyo suspension bridge in Japan is a recent example); on the other, to improve its aerodynamic characteristics is a feasible alternative (*e.g.* adopting a streamlined section, which generally presents very low drag coefficient, if the deck height is less than 3 m). Although both approaches appear to be an effective design criteria for small or medium-span bridges, they involve significant technical and economic consequences for long-span bridges: it is necessary to increase the deck height, and consequently the structural supports dimensions (main cables and towers with their anchorages), to obtain sufficient resistance to wind actions, enhancing the construction costs.

Only recently, the design approach of decks has undergone a further development. Multiple-box stiffening girder decks seem to meet lightness and aerodynamic requirements fairly well. For these reasons, in the last years a special attention has been devoted to this cross-section layout: *e.g.* Matsumoto *et al.* [a,b], Sato *et al.* [c], Ogawa *et al.* [d] and Larose and D'Auteuil [e].

One of the most outstanding applications of this deck configuration is the design of Messina Strait Bridge (Italy) proposed in 1992: a 3300 m main-span suspension bridge [f,g,h] (Fig. 2.1-2.2), whose cross section is characterized by three curved boxes, connected every 30 m by transversal beams. This structural solution, presenting very low drag static coefficients and low structural weight, seems to be, now, the best structural solution to ensure both aeroelastic stability (in the range of wind speeds of practical interest) and a good balance between technical and economic requirement for long-span bridges.
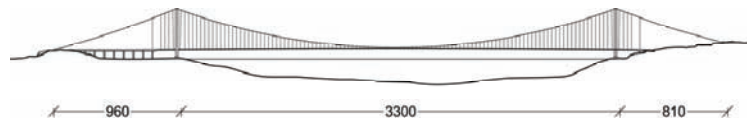
Figure 2.1   Messina Strait bridge lateral view
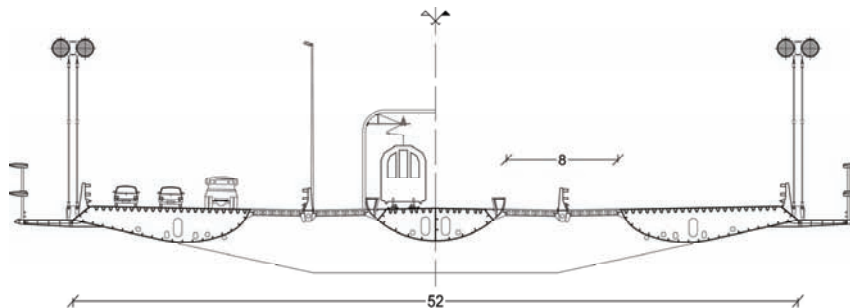
Figure 2.2   Messina Strait bridge deck section (1992)

Experience made during the design studies for the Messina Strait bridge was, certainly, valuable and the original project is only marginally improvable. Moreover, these studies were oriented to achieve the best result for that specific situation: a bridge with a long span (3300 m), with an exceptional deck width (60 m) to place ten roadway lanes (two reduced lanes in addition to inspection and maintenance) and two railway lanes. In that situation, it was immediately clear

that changes to the pure suspension system (main cables in the configuration due to their weights and deck loads through vertical hangers) were not necessary, and only the aerodynamic study of the deck was sufficient to ensure good performances for both aeroelastic stability and vibrations due to vortex-shedding. Nevertheless, today, it is required to extend the studies conducted for the specific case of Messina bridge to different configurations, in order to obtain reductions of construction costs (*e.g.* adopting simplified multiple-box decks with some lower aerodynamic characteristics, but with adequate performance in terms of aeroelastic stability against flutter, vortex-shedding, etc.). During this research project, starting from the original Messina Strait bridge design (1992), sets of different multiple-box deck configurations have been investigated to achieve this goal. In particular, to obtain realistic proposals of suspension bridges in terms of design criteria, two are the main design approaches that have been pursued:

(a)   *in primis*, the analysis of the influence of different spacing between longitudinal boxes in the aeroelastic response of the whole structural system;

(b)   *in secundis*, the evaluation of the possibility to increase the aeroelastic stability of long-span bridges by means of innovative solutions affecting the structural side of the design, testing:

(b.1)   the benefits on the of natural frequencies separation after introducing some simple structural elements (*e.g.* crossed hangers);

(b.2)   the possibility to obtain the total inhibition of the flutter instability mechanism by inverting the torsional and the bending natural frequencies of the lower modes with similar shapes.

The original grids between the boxes have not been considered within these studies, according to the recent deck configuration proposed during the General Contractor selection in 2005 (Fig. 2.3). As a consequence, the two lanes for railway maintenance have been eliminated and the total number of road lanes has been reduced, from the original three to two for each roadway.
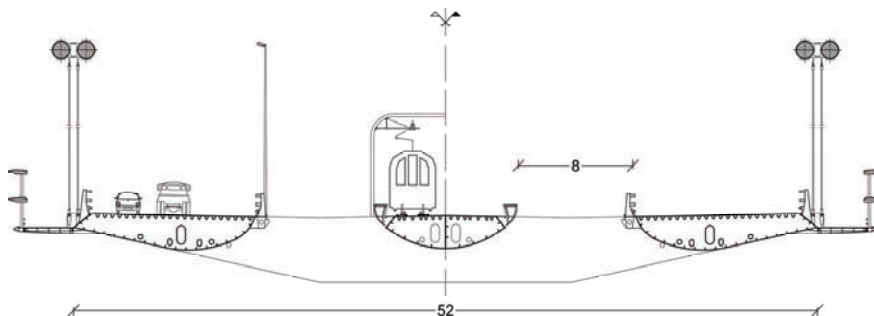
Figure 2.3   Messina Strait bridge deck section (2005)

The central span (3300 m), the side spans (960 m and 810 m), the maximum sag of the suspension cables (300 m) and the tower height (around 380 m) have been unchanged, while the deck geometry, the distance between the main cables and the shape of the towers have been varied in order to obtain the examined configurations.

In the case of the approach (a), four bridges reproducing the basic geometry of Messina Strait bridge, each one characterized by a progressive reduction of the gap between longitudinal boxes, have been analyzed. The results, shown in Section 2.3, have been used to determine the bridge system with the best balance between construction costs and adequate performance in terms of aeroelastic stability against classical flutter.

In Section 2.3, the first results about an ongoing research about nine new multiple-box deck layouts, with simplified boxes supporting railway, are also presented. In this context, different boxes spacing in relation to different vertical hangers distances have been taken into account.

In the second part of the chapter, the point of view drastically changes, as the possibility to increase the aeroelastic stability of long-span bridges by means of innovative solutions affecting the structural side of the design has been investigated.

In particular, as regards the approach (b1), higher frequency separation between lower modes with similar shapes has been tested after introducing four pairs of "crossed hangers" on the bridge models reproducing the original Messina bridge and the first four bridges presented in (a). The results shown in Section 2.4 have been useful to evaluate the benefits of this structural solution on classical flutter wind velocity.

As regards the approach (b2), different bridge configurations have been analysed to find a structural solution with torsional-to-bending frequency ratios smaller than one. As a matter of fact, a suspension bridge with this characteristic could be in a position to avert dynamic instability phenomena due to classical flutter. Referring to this approach, whose results are shown in Section 2.5, the basic idea is to avoid classical flutter by inverting the torsional and the vertical bending natural frequencies of the lower modes with similar shapes (that is to obtain torsional-to-vertical bending frequency ratios lower than one), by modifications of the mass distribution over the deck with respect to the position of the suspension cables. As a matter of fact, if this was possible and compatible with all the design constraints, the effect of fluid-structure interaction would be the reduction with the wind speed of the torsional frequency and, at the same time, the increase of the vertical bending frequency: the modes would tend to further separate instead of coupling and consequently they could not give rise to classical flutter. This happens even if such frequencies tend to coincide in still air. This result is theoretically well known but completely unexplored in practice [i].

It is worth noting that the natural modes that tend to couple are those that present similar shapes, so in these studies only those modes with torsional and vertical modal forms characterized by the same number of nodes, are considered. Accordingly, as only the inversion of critical frequencies does not eliminate the problem entirely, since higher modes can still couple, however, the coupling of the fundamental modes happens, in general, at the lowest wind velocity, so that, considering higher modes means to delay significantly the onset of flutter.

Finally, being released from the need to introduce structural solutions designed to increase the deck torsional stiffness (beyond the stiffness strictly necessary for the static stability) or to optimize its aerodynamic characteristics (beyond the limit to ensure a good behaviour against vortex-shedding, turbulence and torsional flutter), the design efforts can be focused primarily on the research of that particular distribution of masses on the deck that is able to ensure the pursued result. This approach also greatly reduces laborious numerical simulations and experimental campaigns in wind tunnel.

In order to obtain further reductions in construction costs with respect to aerodynamically more sophisticated solutions, the results about some simple structural typologies to support traffic lanes, such as truss girders or steel boxes as transversal beams and orthotropic slabs on steel beams or steel boxes for the roadway, are shown in Section 2.5.

For each examined configuration, after evaluating the new scheme of dead and live loads acting on the decks and after redesigning each structural element, experimental and numerical analysis have been carried out. The whole process, starting from the original design criteria of Messina '92, ensure that the reliable safety margins within both serviceability and ultimate limit states are not inferior to those of the initial project. Thus, the structural weight reductions that have been obtained (steel for deck elements, cables and towers), can be considered fully representative of the variations in costs among different bridge layouts.

To obtain a geometrical optimization of multi-box decks, it has been considered suitable to realize an experimental campaign in the "CRIACIV" (Inter-university Research Center on Building Aerodynamics and Wind Engineering) boundary layer wind tunnel, using 1:100 scale models and the design solution 1992 for the Messina bridge as reference.

To evaluate the static and dynamic structural response to dead, anthropogenic and eolic actions, several numerical simulations have been build up. To this purpose, different numerical models have been realized, using section and full three-dimensional finite element (FE) models. Most of the numerical analysis have been performed using "Tenso", a software to solve nonlinear problems of two and three-dimensional FE models consisting of "cable" and "beam" elements, implemented by the Research Unit. In particular, to weigh the influence of the main static deformed configurations on the stability range, many modal analysis have been performed for each examined bridge under dead loads. The results have been used for subsequent evaluations of the frequency modes directly involved in the classical flutter (about the first twenty modes).

The structural response to wind actions has been assessed with both frequency-domain and time-domain analysis.

In the case of time-domain analysis, an incremental-iterative process to find the solution of the equilibrium equations has been used. This kind of numerical procedure allows to define a scalar relationship between forces and displacements, that is characteristic of each structure studied and that allows to reduce to a one-Degree-of-Freedom (1-DoF) equivalent system the search of the maximum displacement of a structural system subject to some external actions. The dynamic integration is made up in terms of Lagrangian coordinates and mechanical damping is estimated through the mass and stiffness matrices (Rayleigh). As for the wind speed, its main component is considered variable with the height of each structural element, following the "Logarithmic Law" introduced by Monin Oberoff. Finally, a quasi-steady load model (QS) [1] has been used, getting the aerodynamic data from the aerodynamic coefficients measured in the CRIACIV wind tunnel, whereas the aeroelastic derivatives are seldom measured with dependence on the flow angle of attack. The sign convention adopted to implement this numerical process is shown in Figure 2.4 and the aeroelastic forces (Lift, Drag and Moment, respectively) have been derived from the following formulations:

$$F_L(\theta) = \frac{1}{2}\rho U_r^2 B C_L(\theta) \tag{2.1}$$

$$F_D(\theta) = \frac{1}{2}\rho U_r^2 B C_D(\theta) \tag{2.2}$$

$$F_M(\theta) = \frac{1}{2}\rho U_r^2 B C_M(\theta) \tag{2.3}$$

where ρ is the air density, U_r is the relative velocity, B is the deck width, $C_L(\theta), C_D(\theta)$ and $C_M(\theta)$ are the aerodynamic coefficients for lift (L), drag (D) and Torsion (M), functions of the actual angle of incidence θ.
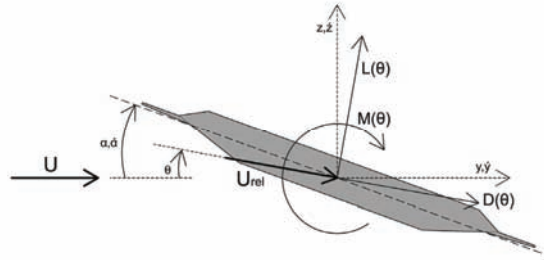
Figure 2.4   Sign convention for forces, displacements and velocities

All time-domain analysis, whose duration is 1000 s, have been preformed for a range of wind speed of practical interest.

The results of experimental and numerical analysis, synthesized in the next Sections and reported in detail in [11-17], highlight the actual possibility of achieving reductions in construction costs, while retaining acceptable performance in terms of stability against flutter, in the case of a long-span bridge with multiple-box deck.

2.3   SENSITIVITY ANALYSIS OF AEROELASTIC BEHAVIOUR OF LONG-SPAN BRIDGES WITH MULTIPLE-BOX DECKS

In this section, the results about static and aeroelastic numerical tests performed on four bridge models, reproducing the basic geometry of Messina Strait bridge, are shown. These deck profiles are characterized by a different distance between longitudinal boxes (8 m, 6 m, 4 m e 2 m).
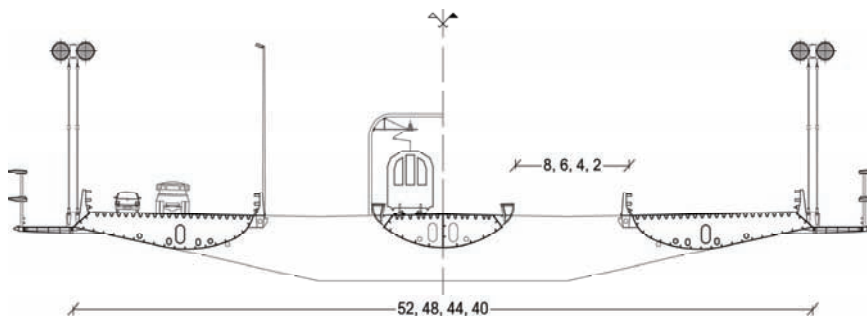
Figure 2.5   Deck cross-section scheme of the four solutions investigated (a1), (a2), (a3) and (a4)

The geometry and the size of the three longitudinal boxes supporting roadways and railways (including their weight and stiffness) is the same adopted in the reference project, while the size of the transversal beams changes from the original width of 52 m (a1) to 48 m (a2), 44 m (a3) and 40 m (a4). As a consequence, due to the elimination of the original grids between the boxes (and the related four road lanes, while the maximum rail loads remain unchanged) and due to the variation of deck widths, the loads acting on the examined cross beams are lower than the original one. In Figure 2.5, the layouts of the four decks are summarized.

2.3.1 Feasibility study

To better analyze the effects of the new load conditions on the examined bridges and, in particular, to evaluate the weight reductions on the transversal beams, four numerical models, made up of "shell" FE, have been realized (Fig. 2.6). After varying the plate thickness and after redesigning the shape of the transversal beams (adapting deck width and height, systematically), new stress-deformation conditions have been evaluated in order to select the better geometrical shapes, according to the original design criteria.
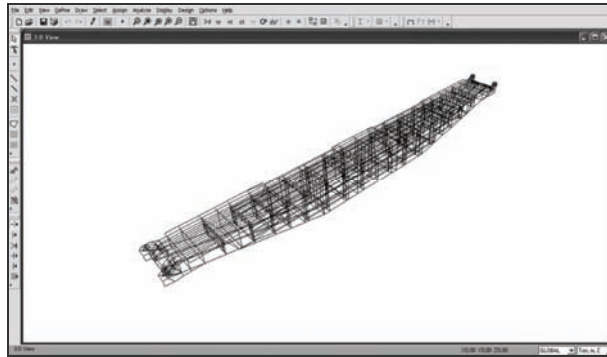
Figure 2.6   "Shell" FE model of the (a1) transversal beam

Having obtained the size of the new transversal beams, both the suspension cables and the towers have been redesigned too, respecting the original design criteria.

In Table 2.1, and in details in [1], the weight reductions of the examined bridges (a1-4), in comparison with the original Messina bridge weight, are summarized.

Deck Configurations	Steel weight reduction
bridge (a1)	-17 %
bridge (a2)	-20 %
bridge (a3)	-22 %
bridge (a4)	-23 %

Tab. 2.1   Weight reductions of the examined bridges (a1-4) in comparison with the original Messina bridge

To optimize the parametric analysis and to reproduce the principal dynamic characteristics (and, *in primis*, the modal characteristics) of the detailed model, the "shell" FE deck models have been replaced with the "beam" FE deck models. Each two-dimensional model has been realized with the same initial masses distributions of the corresponding three-dimensional ones.

For all the numerical models of each deck configuration (a1-4), modal analysis has been carried out to minimize, for subsequent iterations, the differences due to two schematizations of the structure. In particular, after considering the first four modes with similar shape, the geometric characteristics of the two-dimensional models have been varied in order to obtain the same natural period of vibration as the corresponding three-dimensional ones (the results of the particular case that refers to the model (a1) is shown in Fig 2.7-2.8). This aim was achieved by changing the value of the vertical moment of inertia of both the transversal and longitudinal beams, reaching a very good approximation with a difference between corresponding modal frequencies below 1%. The full results of this analysis are reported in [1,2].

It is important to specify that the identification process (the outputs of which have been used to define the geometric characteristics of the decks in the global numerical models) has been realized without considering all the local modes of vibration produced by the many degrees of freedom of the three-dimensional models and by the multiple modes due to deck symmetry.
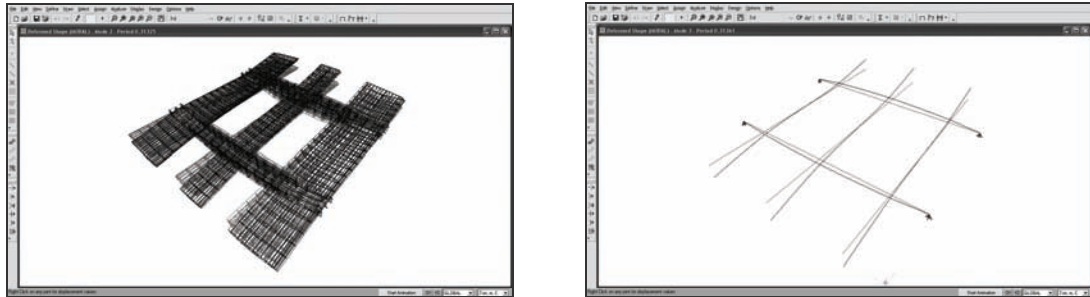
Figure 2.7   1st vertical mode of the deck (a1), constituted by shell FE model - T=0.31 s (left), compared with the corresponding beam FE model - T=0.31 s (right)
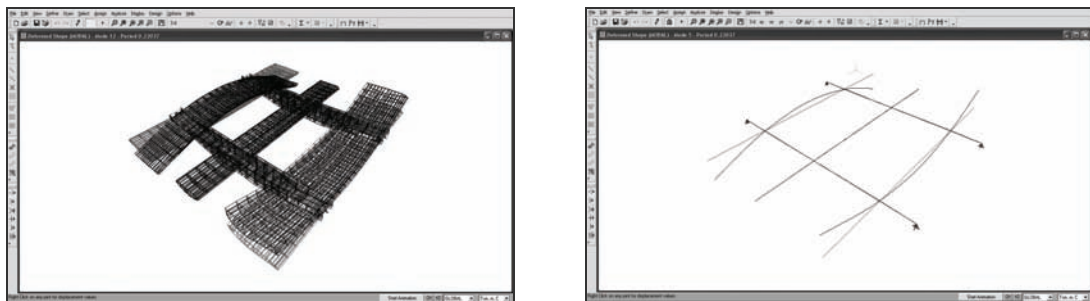
Figure 2.8   1st torsional mode of the deck (a1), constituted by shell FE model - T=0.22 s (left), compared with the corresponding beam FE model - T=0.22 s (right)

2.3.2   Modal analysis results in still air

After implementing a full three-dimensional FE model for the four bridges, different modal analysis have been performed with Tenso to obtain the first twenty modes and to evaluate the relationship between the 1st torsional and the 1st vertical modal frequencies in relation to the decks width reductions (Fig. 2.9). All numerical models consist of 1006 joints, 592 "cable" FE and 925 "beam" FE.
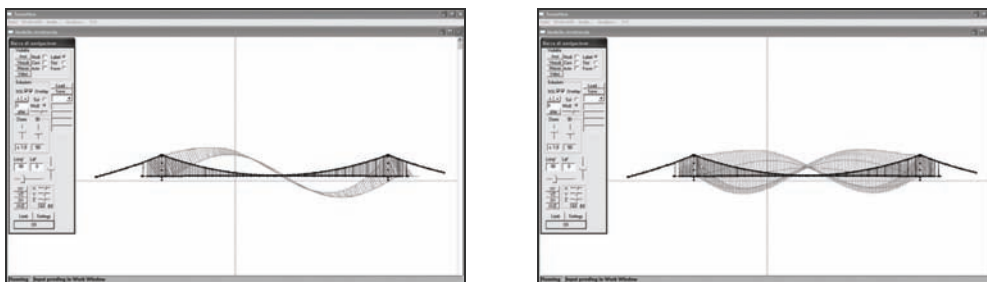
Figure 2.9   1st vertical (left) and 1st torsional (right) modal shapes referring to FE models of the bridges (a1-4) and Messina bridge

In Table 2.2, and in [1,2], the frequencies values related to the first two torsional (1st f_α) and vertical (1st f_h) modes and the 1st torsional-to-1st bending frequency ratio (1st $\gamma_\omega = 1^{st}$ $f_\alpha / 1^{st}$ f_h) in still air are indicated, for each examined bridge including the original Messina bridge.

The analysis results show how, while decreasing the deck width, the frequency of the 1st bending mode remains almost unchanged and the frequency of the 1st torsional mode increases from 0.08094 Hz (obtained for the original Messina bridge) to 0.0866 Hz (obtained for the bridge (a4)), enhancing the separation between the modes which are directly involved in the flutter phenomenon (from the original ratio of 1.33, obtained for the original Messina bridge, to 1.43 obtained for the bridge (a4)).

This phenomenon indicates, theoretically, a growing of flutter wind speed in proportion with the reduction of the deck width.

Deck Configurations	Modal Frequencies		
	1st f_α [Hz]	1st f_h [Hz]	1st γ_ω
Messina '92 bridge	0.0804	0.0604	1.33
bridge (a1)	0.0821	0.0604	1.36
bridge (a2)	0.0823	0.0604	1.38
bridge (a3)	0.0847	0.0605	1.40
bridge (a4)	0.0866	0.0605	1.43

Tab. 2.2   Modal frequencies of the examined configurations (a1-a4) in comparison with Messina bridge

2.3.3   Frequency-domain analysis results

Starting from the results obtained during static tests performed in wind tunnel for models with fairings [2] and using a software developed by the Research Unit, critical wind velocities of flutter have been deduced using a frequency domain analysis on the section models of decks (a1-4). This procedure, developed under the assumption of the QS theory (*i.e.* for sufficiently high reduced wind speed), while introducing an error (whereas for the high wind speed of flutter that have been obtained is not so relevant), leads to significant results at least as regards the comparison between the different bridge configurations that have been examined [k,l,m].

The critical wind speed for aeroelastic instability is that of a classical two-Degree-of-Freedom (2-DoF) flutter [k], in which only two natural modes (with similar shapes, one vertical and one torsional) are involved.

In Table 2.3, critical wind speeds (U_C), calculated as shown in [k,l,m], and the natural periods of vibration (T_C) are indicated.

Deck Configurations	T_C [s]	U_C [m/s]
Messina '92 bridge	15.03	94.0
bridge (a1)	12.89	86.7
bridge (a2)	12.96	79.4
bridge (a3)	12.86	88.6
bridge (a4)	13.16	65.1

Tab. 2.3   Wind velocity of flutter of the configurations (a1-4) and Messina bridge

The analysis results show that the deck width reduction lowers the critical wind speed of flutter, from 90 m/s (obtained for Messina bridge) to 65 m/s (obtained for the bridge (a4)).

2.3.4   Time-domain analysis results

Using the experimental data referring to the original Messina deck [n], time-domain analysis have been performed with Tenso, for each examined bridge (a1-4) and for the original one. Following the sign convention shown in Figure 2.4, in Figures 2.10-2.12 the time-domain analysis results are shown, being *Fy* and *Fz* the drag and lift aeroelastic forces and *Mx* the aeroelastic moment.

In particular, Figure 2.10 shows the values of the aeroelastic forces referred to the original Messina bridge under a wind speed of 95 m/s; Figure 2.11 shows the values of the aeroelastic forces referred to the bridge (a1) under a wind speed of 90 m/s and Figure 2.12 shows the values of the aeroelastic forces referred to the bridge (a2) under a wind speed of 85 m/s.
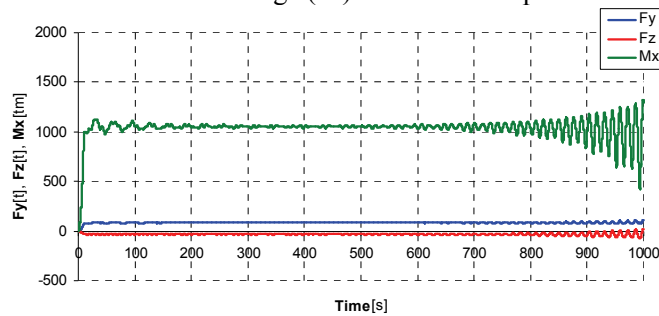
Figure 2.10   Aeroelastic forces for the original Messina bridge obtained from the static coefficients reported in [n] under a wind speed of 95 m/s
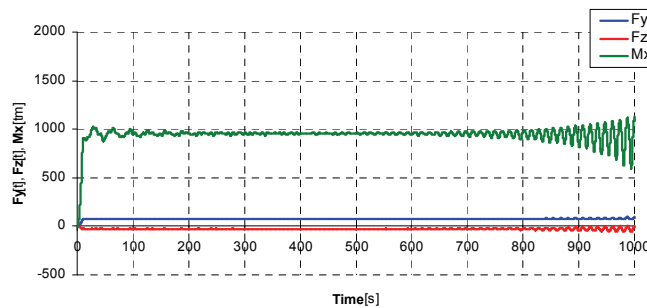
Figure 2.11   Aeroelastic forces for the bridge (a1) obtained from the static coefficients reported in [n] under a wind speed of 90 m/s
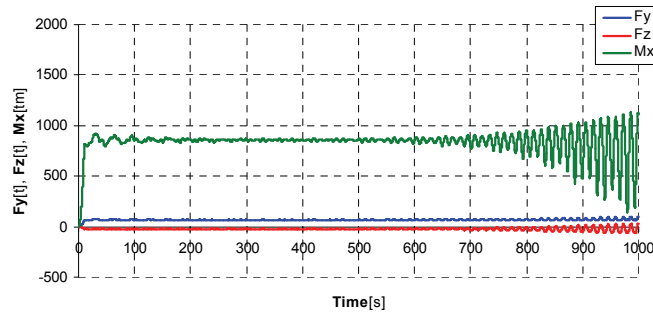
Figure 2.12   Aeroelastic forces for the bridge (a2) obtained from the static coefficients reported in [n] under a wind speed of 85 m/s

The time-domain analysis results underline that, there is a minimal change in the flutter critical wind velocity with respect to deck width reduction (the same trend was disclosed also by frequency-domain analysis results shown in the previous Section). The masses reduction involves a lowering of critical wind velocity of flutter just over 5%, passing form the original Messina bridge to the bridge (a1). The same happens reducing the deck width, *i.e.*, passing from the configuration (a1) to the configuration (a2). That fact is largely confirmed by the results of aeroelastic tests performed in CRIACIV wind tunnel for the section models of the examined decks and reported in [2]: a critical wind velocity of flutter equal to 25.3 m/s for the bridge (a1) and a critical wind velocity of flutter equal to 24.8 m/s for the bridge (a1).

2.3.5   Work in progress

To extend the studies on the aeroelastic sensitivity of multiple-box decks for long-span bridges, retaining the intent to investigate possible savings in construction costs and, simultaneously, an acceptable aerodynamic behaviour, a new parametric study about multiple-box decks has been developed, considering:

- a simplification of the structures supporting the railways, including the introduction of a new way for rail maintenance;
- a systematic decrease of the distance between vertical hangers;
- a reduction of the gap between the longitudinal beams.
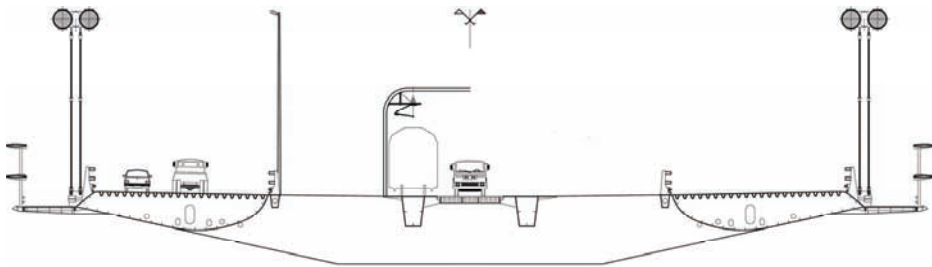
Figure 2.13   Deck cross-section scheme of the three investigated solutions (a5-7)

	Deck Configurations	Deck width [m]	Hanger distance [m]	Trasversal beam height [m]	Railway box height [m]
(a5)	bridge (a5.1)	52	30	4.50	2.0
	bridge (a5.2)	52	25	4.50	1.8
	bridge (a5.3)	52	20	4.50	1.6
(a6)	bridge (a6.1)	49	30	4.15	2.0
	bridge (a6.2)	49	25	4.15	1.8
	bridge (a6.3)	49	20	4.15	1.6
(a7)	bridge (a7.1)	46	30	3.80	2.0
	bridge (a7.2)	46	25	3.80	1.8
	bridge (a7.3)	46	20	3.80	1.6

Tab. 2.4   Geometric characteristics of the nine new bridges (a5-7)

In particular, after replacing the original railway box with two simplified boxes with different height (from 2 m, 1.8 m to 1.6 m) in relation to a systematic decrease of the distance between vertical hangers (from 30 m, 25 m to 20 m) and after reducing the gap between the longitudinal beams (from 52 m, 49 m to 46 m), nine new bridges have been obtained as synthesized in Figure 2.13 and in Table 2.4.

Also in these cases, numerical models of the new transversal beams, made up of "shell" FE, have been realized in order to contain stress-deformation values within the range defined in the original design criteria.

Having obtained the size of the new transversal beams, both the suspension cables and the towers have been also redesigned, with respect to original design criteria.

In Table 2.5, the weight reduction estimate about the global structures examined (a5-a7), in comparison with the original Messina bridge weight, are summarized.

Deck Configurations	Steel weight reduction
deck (a5.1)	-15 %
deck (a5.2)	-16 %
deck (a5.3)	-20 %
deck (a6.1)	-16 %
deck (a6.2)	-17 %
deck (a6.3)	-22 %
deck (a7.1)	-17 %
deck (a7.2)	-19 %
deck (a7.3)	-23 %

Tab. 2.5   Weight reductions of the entire examined structures (a5-a7) in comparison with the original Messina bridge

After obtaining the geometric characteristics of each deck (implementing an identification process the "beam" FE similar to that described in Section 2.3.1), a full three-dimensional FE model for each of the four bridges has been implemented and, with Tenso, different modal analysis have been carried out. The numerical models referring to the bridges with vertical hangers spaced 30 m apart consist of 1115 joints, 592 "cable" FE and 925 "beam" FE, while the numerical models referring to the bridges with vertical hangers spaced 20 m apart consist of 1673 joints, 890 "cable" FE and 1728 "beam" FE.

Deck Configurations	Modal Frequencies		
	$1^{st} f_\alpha$ [Hz]	$1^{st} f_h$ [Hz]	$1^{st} \gamma_\omega$
Messina '92 bridge	0.0804	0.0604	1,33
bridge (a5.1)	0.0848	0.0605	1.40
bridge (a5.3)	0.0838	0.0599	1.40
bridge (a6.1)	0.0859	0.0605	1.42
bridge (a6.3)	0.0875	0.0596	1.46
bridge (a7.1)	0.0872	0.0605	1.44
bridge (a7.3)	0.0880	0.0600	1.46

Tab. 2.6   Modal frequencies of the examined configurations (a5-a7) and Messina bridge

In Table 2.6, the frequency values related to the first two torsional ($1^{st} f_\alpha$) and vertical ($1^{st} f_h$) modes and the 1st torsional-to-1st bending frequency ratio in still air ($1^{st} \gamma_\omega = 1^{st} f_\alpha / 1^{st} f_h$) are indicated, for the bridges examined with vertical hangers spaced 30 and 20 m apart, including the original Messina bridge.

Even for these cases, the progressive reduction of the deck width tends to increase the frequencies of the 1st torsional mode, while the frequencies of 1st bending mode tends to remain constant, with positive effects on the separation between the modes directly involved in the flutter instability.

As this new group of bridges appear to be functional and with no serious aeroelastic problems (at least, around zero angle of attack), further investigations, both experimental and numerical, are currently underway to complete the feasibility study and response to flutter.

2.4   STRUCTURAL SOLUTIONS TO INCREASE FLUTTER WIND VELOCITY

To increase torsional stiffness of the classic suspension system and, consequently, to improve the aerodynamic performance of long-span suspension bridges, it is possible to adopt different structural solutions [o].

Probably the oldest technique to increase torsional stiffness is the introduction of auxiliary cables inserted in radial direction from the top of the tower ("additional cable stays"), as proposed by Roebling for the Brooklyn bridge. This method, although not strictly necessary for this structure, was used to suppress the oscillations caused by vortex-shedding at low wind speed [p]. The system of radial cables is effective to increase the torsional stiffness when applied to bridges with stiff towers or, alternatively, if the cables are anchored near the centre line in the case of bridges with flexible towers.

The "mono-dual cable" solution, for which the two main cables are unified into a single cable over the towers, allows combinations of low torsional inertia with desirable deformation characteristics. The aerodynamic stability of a long-span bridge with "mono-dual cable" system is similar to a classic smaller suspension bridge.

Another structural device used to increase the aerodynamic performance is the introduction of "crossed hangers" as done in the Deer-Isle bridge [q]. The "crossed hangers" increase torsional stiffness of suspension bridges because they neutralize "in phase" movements of the main cables. The "crossed hangers" require main cables to be reciprocally fixed in the lateral direction and the introduction of compressed elements, for bridge-spans below a certain limit. This system contributes significantly to the rotational inertia of the system.
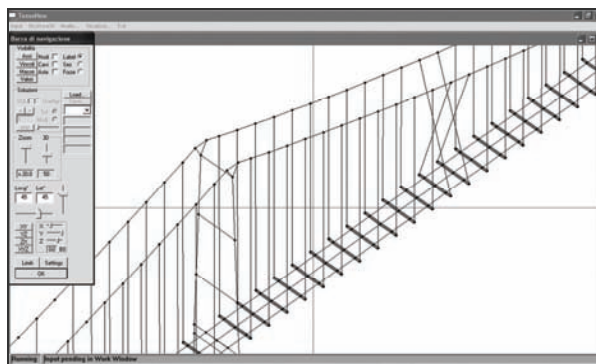
Figure 2.14   Bridge (a1) FE model with crossed hangers located at 360 and 390 m from each tower

To investigate the possibility to increase security against aeroelastic instability of multiple-box decks, the effect of the introduction of four pairs of "crossed hangers" (located at 360, 390, 1050 and 1080 m from each tower) (Fig. 2.14) on the aeroelastic response of bridges with configurations (a1-a4) and of the original Messina bridge has been analyzed. "Crossed hangers" are, in fact, a structural solution that, apart from being a feasible device to use on a long-span bridge with the geometric characteristics such as the ones studied herein, simultaneously, satisfies the requirements of cost reductions and benefits for the aeroelastic stability [r].

2.4.1 Modal analysis results in still air

To evaluate the relationship between the 1st vertical and 1st torsional modal frequencies (Fig. 2.9) for the bridges (a1-4) after introducing four pairs of "crossed hangers" in each numerical model, different modal analysis have been performed with Tenso.

In Table 2.7, the frequency values related to the first two vertical (1st f_h) and torsional (1st f_α) modes and the 1st torsional-to-1st bending frequency ratio in still air (1st $\gamma_\omega = 1^{st}$ $f_\alpha / 1^{st}$ f_h) are indicated, for each bridge examined including the original Messina bridge.

Deck Configurations	Modal Frequencies		
	1st f_α [Hz]	1st f_h [Hz]	1st γ_ω
Messina '92 Bridge	0.0925	0.0603	1.53
Bridge (a1)	0.0926	0.0603	1.53
Bridge (a2)	0.0917	0.0603	1.52
Bridge (a3)	0.0898	0.0604	1.49
Bridge (a4)	0.0870	0.0605	1.44

Tab. 2.7 Modal frequencies of the configurations examined (a1-a4) in comparison with Messina bridge

The results of modal analysis show that the introduction of "crossed hangers" is an efficient technique to increase the separation between the frequencies (from the original ratio equal to $\gamma_\omega = 1.33$, without "cross hangers", to $\gamma_\omega = 1.53$, with "crossed hangers", for the original Messina bridge). This benefit, however, is lost as the distance between longitudinal boxes reduces. In the case of the bridge (a4), the 1st torsional-to-1st bending frequency ratio obtained with or without "cross hangers" is virtually the same (from the original ratio $\gamma_\omega = 1.43$, without "crossed hangers", to $\gamma_\omega = 1.44$, with "crossed hangers").

2.4.2 Time-domain analysis results

Even in this case, using the experimental data referring to the original Messina deck [n], time-domain analysis have been performed with Tenso, for each bridge examined (a1-4) and for the original one, after the introduction of "crossed hangers".

Following the sign convention shown in Figure 2.4, the time-domain analysis results are shown in Figures 2.19-2.20, being *Fy* and *Fz* the drag and lift aeroelastic forces and *Mx* the aeroelastic moment. In particular, Figures 2.19-2.20 show the values of the aeroelastic forces for the original Messina bridge obtained with the static coefficients reported in [n] and wind speed equal to 110 m/s and 130 m/s, respectively.

Time-domain analysis results show that the introduction of four pairs of "crossed hangers" in the original Messina bridge has a positive effect on the critical wind speed of flutter: from the original velocity of 90 m/s, without "cross hangers", to about 120 m/s, with "cross hangers",

confirming the conclusions derived from modal analysis discussed in previous Section 2.4.1. In fact, the aeroelastic forces stabilize at 110 m/s, while they grow indefinitely at 130 m/s.

2.5 INNOVATIVE STRUCTURAL SOLUTIONS AGAINST CLASSICAL FLUTTER INSTABILITY

Besides the possibility to separate the critical frequencies, the possibility of having torsional-to-bending frequency ratios smaller than one ($\gamma_\omega = f_\alpha/f_h < 1$) has been also investigated. As a matter of fact, a suspension bridge with this characteristic could be in a position to avert dynamic instability phenomena due to classical flutter.

It is noteworthy that, among all the components of a suspension bridge, the deck and the main cables are designed to support anthropogenic loads. Their structural roles change with increasing the span. For suspension bridges with span up to 1000 m, the deck stiffness constitutes a significant portion of the whole structural stiffness. As the span increases, the deck contribution to overall stiffness decreases, while increasing the main cables stiffness. From a static point of view, this means that, while rising the span, the stiffness of the global structure increases. From a dynamic point of view, this peculiarity implies a reduction of the ratio between the frequencies associated with the vertical and torsional modes of the deck.

In order to evaluate the contribution of the deck stiffness in the case of Messina bridge, modal analysis has been performed with Tenso, after concentrating the deck masses on the main cable joints. The results, reported in Table 2.8, show that the deck stiffness, is not entirely negligible, as the two frequencies differ by about 10%. With that mass distribution, the torsional-to-bending frequency ratios would be equal to one, if the torsional deck stiffness was negligible.

Starting from these results new configurations have been investigated, with the aim of obtaining the inversion of critical frequencies. In particular, the following cases have been analyzed:

(b2.1) three-box decks with three suspension cables, whose results are given in Section 2.5.1;

(b2.2) twin-box decks with two suspension cables, whose results are given in Section 2.5.2.

Deck Configurations		Modal Frequencies		
		1st f_h [Hz]	1st f_α [Hz]	1st γ_ω
Messina '92 bridge		0.0604	0.0804	1.33
Messina '92 bridge with deck masses concentrated on main cables		0.0624	0.0690	1.11
Messina '92 bridge with deck masses concentrated on main cables and deck stiffness = 0		0.0620	0.0648	1.04

Tab. 2.8   Frequencies of the 1st vertical and 1st torsional modes of the Messina bridge with different mass configurations

2.5.1   Three-box decks with three suspension cables

A first attempt to obtain torsional-to-bending frequency ratios smaller than one ($\gamma_\omega = f_\alpha/f_h < 1$) has been carried out after introducing a third suspension cable in the centre of the original
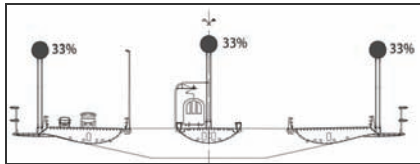
Messina bridge deck (Fig. 2.15) [1,2,3,4,5]. The original grids between the boxes have not been considered within this study.

The shape, the dimension, and the position of the road and railway boxes are the same as in the original design of 1992 (apart from the small widening of the railway box due to the introduction of a third hanger), whereas the cross beam can be conceived with reduced thicknesses. The overall cable mass has been kept unchanged for the configuration (b2.1.1)
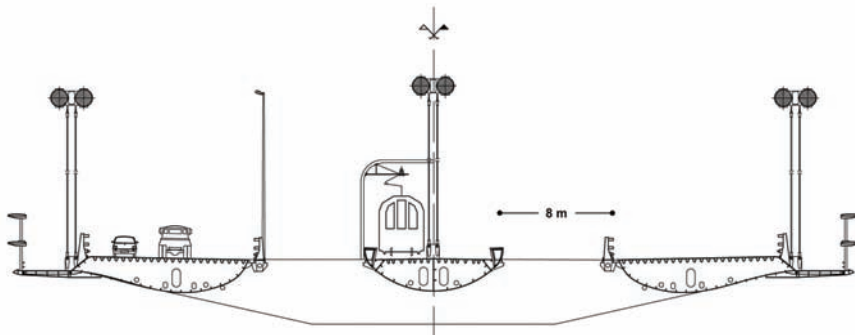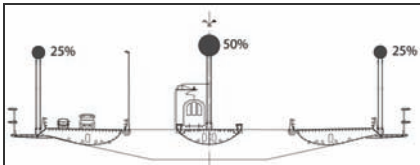
Figure 2.15   Three-box deck cross-section scheme with three suspension cables (b2.1)

As the presence of the central cable does not allow to invert the natural frequencies (the ratio between critical frequencies goes from the original γ_ω=1.33 to γ_ω=1.30 after introducing the third cable) (Tab. 2.9), another configuration with three suspension cables have been analyzed. In this last case, the mass of the central cable is twice of each cable on the sides (b2.1.1).

Deck Configuration		Modal Frequencies		
		1st f_h [Hz]	1st f_α [Hz]	1st γ_ω
bridge (b2.1.1)		0.0605	0.0789	1.30

Tab. 2.9   Frequencies of the 1st vertical and 1st torsional modes of the bridge (b2.1.1)

Deck Configuration		Modal Frequencies		
		1st f_h [Hz]	1st f_α [Hz]	1st γ_ω
bridge (b2.1.2)		0.0605	0.0773	1.28

Tab. 2.10   Frequencies of the 1st vertical and 1st torsional modes of the bridge (b2.1.2)

The results of modal analysis for configuration (b2.1.2) (Tab. 2.10) show that, even for this case, a minimum reduction of the ratio between critical frequencies has been obtained (the ratio between critical frequencies goes from the original γ_ω=1.33 to γ_ω=1.28). It is possible to obtain a frequency ratio γ_ω=1.10 only by assigning almost the total mass to the central cable, 90 %, which is obviously just a mathematical abstraction.

As a matter of fact, the configuration with three suspension cables produces no appreciable effects on the inversion of critical frequencies.

2.5.2 Twin-box decks with two suspension cables

An another configuration analyzed provides a twin-box deck with two suspension cables closer to each other and masses mainly placed on the outer sides.

2.5.2.1 Feasibility study

Leaving unchanged the philosophy of the original Messina bridge, and considering, for simplicity, only longitudinal boxes supporting road traffic, three different configurations of the suspension bridge have been analyzed. In particular, the deck models (summarized in Fig. 2.16), obtained by changing the positions of cables and boxes, are:

(b2.2.1)   the deck configuration with 26 m gap between suspension cables;

(b2.2.2)   the deck configuration with 39 m gap between suspension cables;

(b2.2.3)   the deck configuration with 52 m gap between suspension cables.

Specifically, the so-called configuration (b2.2.1), has been obtained from the original deck moving the suspension cables inside the road boxes, while maintaining the original width, B=54.5 m. The so-called configuration (b2.2.3), has been obtained from the original deck moving the suspension cables outside the road boxes. The deck width, in this case is equal to 80.5 m.

The increase of the distance between the main cables, while increasing the maximum bending moment value (due to the transversal beam mass only), reduces the deck rotation when subjected to the same concentrated unit force (for instance, keeping unchanged the diameter of the suspension cables, the second deck presents torsional rotations equal to one half of those of the deck (b2.2.1)), with considerable benefits in terms of transverse deck deflection under unfavourable traffic load configurations.
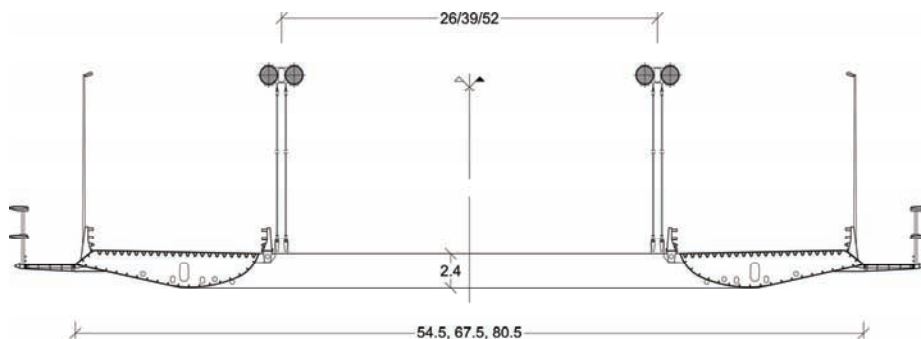
Figure 2.16   Twin-box deck cross-section scheme with 26, 38 and 52 m gap between the two suspension cables (b2.2.1)

The configuration (b2.2.2) represents an intermediate case between the configurations (b2.2.1) and (b2.2.3), with space between the main cables equal to 39 m and deck width equal to 67.5 m.

The bending moment and the shear stress in the transversal beams are practically the same in the three cases and, therefore, their weights (and costs) increase only linearly with the spacing between the suspension cables, so that the difference in the total weight of the three decks is negligible. Obviously, the new deck configurations implied a modified design of the towers and suspension cables as well, according to the performance requirements of the original design of Messina bridge.

The study of the twin-box layouts follows the aim of achieving long-span suspension bridges for which it is possible to envisage an inversion of critical frequencies, only modifying the mass distribution on the decks. The choice to retain the original shape of the road boxes, however, ensures the persistence of a good aerodynamic behaviour (static response under wind, vortex-shedding, response to turbulence).

After defining the geometry, taking into account the actual traffic load conditions, new dead weights of the bridges have been calculated, as shown in Table 2.11.

Deck Configurations	Steel weight reduction
deck (b2.2.1)	-37 %
deck (b2.2.2)	-35 %
deck (b2.2.3)	-34 %

Tab. 2.11   Weight reductions of the entire examined structures (b2.2) in comparison with the original Messina bridge

As shown in Table 2.11, despite all the precautions related to the simplifications made, the aim to obtain an optimization of the construction costs seem to be possible. To obtain a cost optimization, in terms of structural weights, is an actual possibility, even assuming to re-introduce the Messina bridge railway box (which represents approximately 20% of the weight of the entire dead load of the deck).

2.5.2.2   Modal analysis results in still air
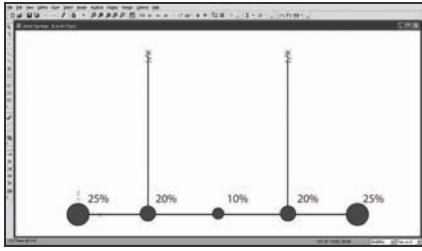
To investigate the structural behaviour of the preliminary twin-box decks, modal analysis has been performed on the simplified section models referring to configurations (b2.2.1) and (b2.2.2) with different mass distributions. Each model consists of infinitely stiff beam FE connected to two spring-supported cables.

The results for deck configurations with mass distribution similar to those presented in this Section are shown in Table 2.12 and, more extensively [1,4].

It is important to note that the value of the critical frequencies of the modes involved in the flutter instability (which are directly dependent on the characteristics of the springs) is not as important as their ratio (which is independent of the springs themselves).

Since the analysis results shown above suggest the achievement of the critical frequencies inversion ($\gamma_\omega = f_\alpha/f_h < 1$), it has been decided to further their studies with additional modal analysis.

For each bridge with the twin-box deck configurations (b2.2), a full three-dimensional FE numerical model has been set up (Fig. 2.17). On each model a modal analysis with Tenso has been performed, under dead loads, in order to derive the frequencies and shapes (Fig. 2.18) of the most significant natural modes. The results are reported in the Table 2.13.

Deck Configuration		1st γ_ω
	deck (b2.2.1)	0.81
	deck (b2.2.2)	0.88

Tab. 2.12 Ratio between critical frequencies (1st vertical to 1st torsional modes) of the bridges (b2.2.1) and (b2.2.2)
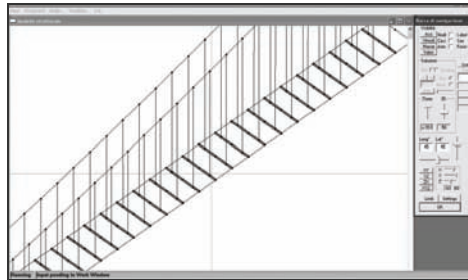
Figure 2.17 Bridge (b.2.2.3) full three-dimensional FE model
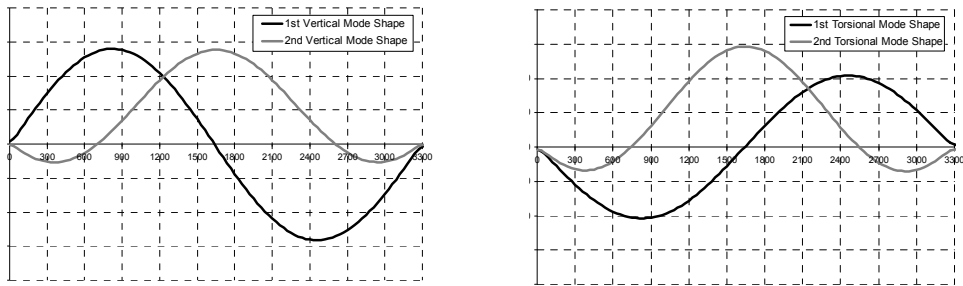
Figure 2.18 Shape of the first two vertical (on the left) and torsional (on the right) modes of the bridge (b2.2.3)

Deck Configurations	Modal Frequencies					
	1st f_α [Hz]	1st f_h [Hz]	1st γ_ω	2nd f_α [Hz]	2nd f_h [Hz]	2nd γ_ω
bridge (b2.2.1)	0.06052	0.06074	0.99	0.07731	0.08211	0.94
bridge (b2.2.2)	0.06077	0.06099	0.99	0.07720	0.08201	0.94
bridge (b2.2.3)	0.06192	0.06181	1.00	0.07814	0.08197	0.95

Tab. 2.13 Modal frequencies of the configurations (b2.2)

In view of the results summarized herein, configurations denoted as (b.2.2.1), (b.2.2.2) and (b.2.2.3) are retained as effective solutions to design long-span suspension bridges with frequency ratios lower than one. Even if the 1st torsional-to-1st bending frequency ratio is about one in still

air, the attainment of the aim against flutter instability is substantially obtained. In fact, it is known that the frequency separation is expected to increase under wind as a consequence of the reduction of the torsional frequency and of the slight increase of the vertical bending frequency. Consequently, the modes should tend to further separate instead of coupling, thus not giving rise to classical flutter. Moreover, the achievement of the aim of flutter-instability suppression is confirmed by the 2nd torsional-to-2nd bending frequency ratio, that is smaller than one for all the configurations examined.

Modal analysis on twin-box decks of bridges with railways are underway. First numerical results on section models show that it is possible to obtain torsional-to-bending frequency ratios smaller than one if the centres of gravity of the boxes are external with respect to the suspension cable planes.

2.5.2.3 Time-domain analysis results

In order to complete the analytical studies, time-history analysis have been performed on the global numerical model referring to the configuration described in Section 2.5.2.1. The self-excited forces acting on the deck have been obtained from the static aerodynamic coefficients, measured in the CRIACIV wind tunnel for the decks shown in [5] (for the deck model with or without spoilers), following the QS analytical method.

The analysis results underline that flutter instability does not occur up to high wind speeds for both configurations (b.2.2). In Figures 2.21-2.22, time-domain analysis results are shown for the configuration (b.2.2.3) under a wind speed of 90 m/s, being Fy and Fz respectively the drag and lift aeroelastic forces on the bridge deck, Mx the aeroelastic moment with respect to the longitudinal x-axis of the deck, all referring to the sign convention of Figure 2.4. In particular, the aeroelastic forces in Figure 2.21 refer to the experimental model without spoilers, whereas the aeroelastic forces in Figure 2.22 are obtained from the static coefficients measured for the model with spoilers. Although large static deflections are evident over 100 m/s wind velocity for both bridge configurations, no flutter instability occurs in the wind speed range of interest.

Numerical and experimental studies show that such a bridge can be reasonably designed and the selected solution is a twin-box girder deck with masses mainly placed externally with respect to the suspension system. It is worth noting that this typology of multiple-box deck sections can be also very performing from the aerodynamic point of view, if correctly designed.

The aeroelastic behaviour of structures with frequency ratios lower than one has been both numerically and experimentally studied. No unexpected aeroelastic phenomena have been observed, while 1-DoF torsional flutter has been observed in the wind-tunnel only under particular conditions that are not significant from a design point of view.

2.5.2.4 Work in progress

The use of boxes similar to those of the design of the Messina bridge deck (which require sophisticated metallic carpentries) leads to design of more expensive structures than those obtainable in a "traditional" way, at least for spans up to 3300 m.

In order to understand whether this type of deck with inverted frequencies can be economically advantageous for bridges with more or less 3000 m span lengths, it is necessary to verify if the relaxation of the aerodynamic constraints on the longitudinal beams can allow cost reductions by means of the use of simpler solutions from the constructional point of view. As a matter of fact, for these structures the aerodynamic optimization of the deck is supposed to be much less enhanced, since only a reduction of the static (in particular the drag and moment coefficients) and dynamic wind loads due to buffeting and vortex-shedding is required and not a substantial increment of the flutter critical wind speed.
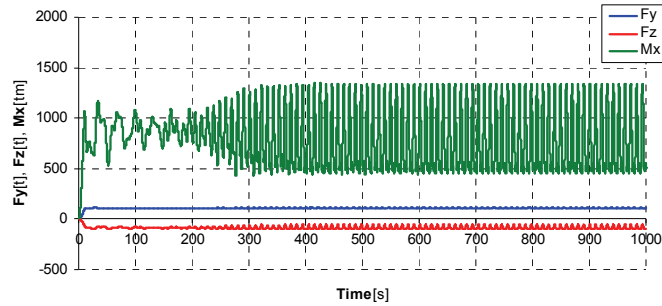
Figure 2.19   Aeroelastic forces for the original Messina bridge with "crossed hangers" obtained with the static coefficients reported in [n] and wind speed of 110 m/s
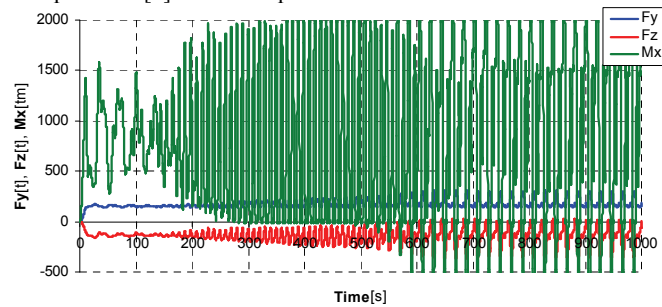
Figure 2.20   Aeroelastic forces for the original Messina bridge with "crossed hangers" obtained with the static coefficients reported in [n] and wind speed of 130 m/s
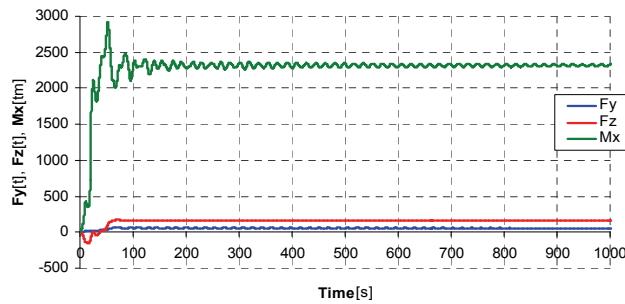
Figure 2.21   Aeroelastic forces for the bridge (b2.2.3) obtained with the static coefficients reported in [5] (model without spoilers) and wind speed of 90 m/s
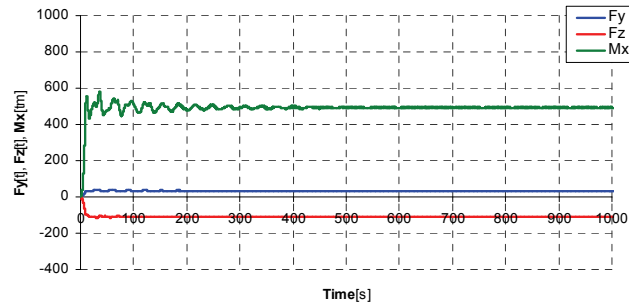
Figure 2.22   Aeroelastic forces for the bridge (b2.2.3) obtained with the static coefficients reported in [5] (model with spoilers) and wind speed of 90 m/s

To evaluate cost reductions with respect to aerodynamically more sophisticated solutions (such as the one of Messina bridge), some simple structural typologies have been taken into account, such as truss girders or steel boxes as transversal beams and orthotropic slabs supported by steel beams or steel boxes for the roadway. Each deck configuration has been pre-designed for various values of the longitudinal spacing between the hangers (in a range between 20 and 30 m). In these cases the minimal required aerodynamic performance can be guaranteed through more or less simple non-structural aerodynamic appendices and in particular fairings [j].

During this research campaign an analytical-experimental approach has been followed. Assuming reasonable values of the aerodynamic coefficients for the different deck solutions, pre-designs of the bridge have been obtained with a suspension scheme able to guarantee the inversion of the first pairs of modal frequencies (*i.e.*, the torsional frequencies are lower than the corresponding vertical bending frequencies). Then the designs have been refined in order to limit the torsional rotations due to traffic loads.

Starting from the encouraging preliminary results obtained for the modified configurations of Messina bridge (Figs. 2.16), some simple deck configurations have been taken into account, in order to obtain the inversion of the first couples of modal frequencies, with respect to the original design criteria. The deck configuration with the roadways supported by an orthotropic steel slab and four steel beams with double T section and with steel boxes as transversal beams is one of the solutions investigated (Fig. 2.23). For this structural solution the distance between the main cables is 40 m and the steel mechanical characteristics of different structural elements of the deck are the same as for the original Messina bridge, in order to obtain realistic proposals of suspension bridges, in terms of design criteria.

The geometric characteristics of the structural elements have been defined considering both the local and the global static response of the bridge under dead loads and different operating load conditions. In particular, once defined the number of lanes, the total amount of traffic loads and their position and referring to asymmetric traffic actions at the serviceability limit state, the dimension of the transversal boxes has been defined locally, accepting simultaneously a transversal slope just over 1% and operating stresses well below the yield strength.

The longitudinal structures which support the roadways, have been stiffened with L-section steel elements, introduced to connect the main double T-section beams (Fig. 2.24), according to the plan scheme showed in Figure 2.25.

The geometric and mechanical characteristics of the towers, cables and hangers have been evaluated after finding the actual new permanent loads and mass distributions.

In order to evaluate the frequency ratio between vertical and torsional modes of the suspension bridge with the geometrical characteristics described above, full three-dimensional FE numerical models of deck sections and global structures have been set up. In particular, the global model consists of 1670 joints, 884 cable elements and 1360 frame elements.

Referring to numerical global model results (Tab. 2.14), even if the 1[st]torsional-to-1[st]bending frequency ratio is about one in still air, the attainment of the aim against flutter instability is substantially obtained. The achievement of the aim against flutter instability is confirmed by the 2nd torsional-to-2nd bending frequency ratio, that is smaller than one too.

To complete analytical studies, time-domain analysis have been performed on the global numerical model referring to the configuration examined. The self-excited forces acting on the deck have been obtained from the static aerodynamic coefficients measured in the CRIACIV wind tunnel for the deck shown in [7], following the QS analytical method.
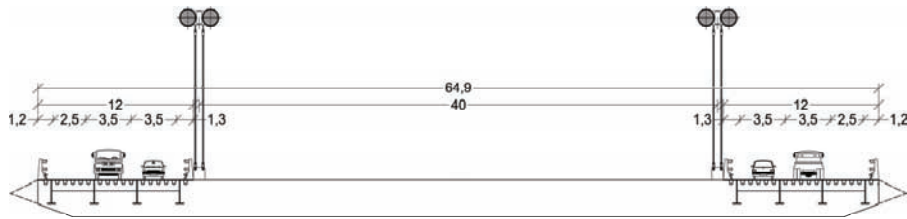
Figure 2.23 Cross-section (AA) of the simplified deck with main suspension cables spaced 40 m apart
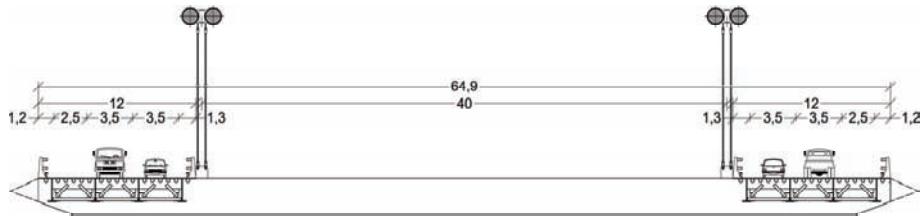
Figure 2.24 Cross-section (BB) of the simplified deck with main suspension cables spaced 40 m apart
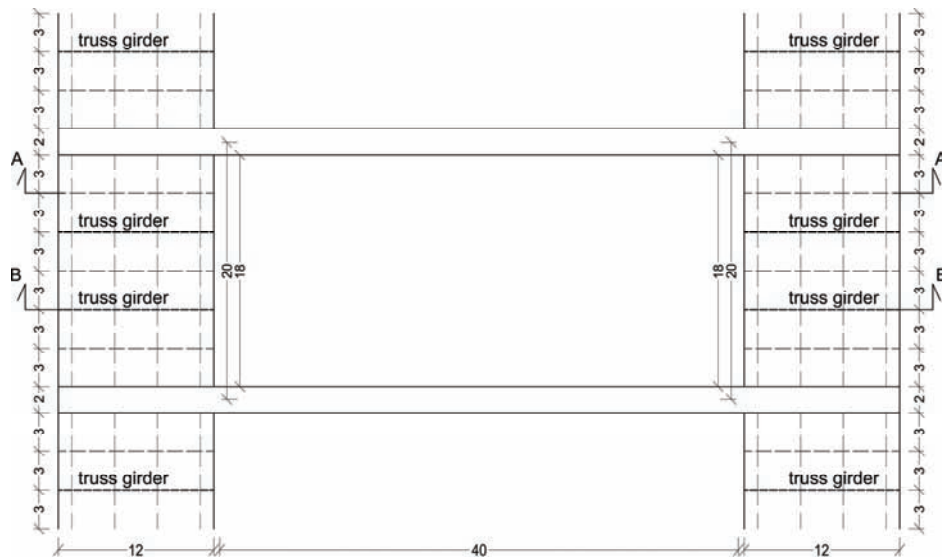
Figure 2.25 Plan of the simplified deck with main suspension cables spaced 40 m apart

Deck Configurations	Modal Frequencies					
	1st f$_\alpha$ [Hz]	1st f$_h$ [Hz]	1st γ_ω	2nd f$_\alpha$ [Hz]	2nd f$_h$ [Hz]	2nd γ_ω
Simplified twin-box deck	0.0602	0.0608	0.99	0.0725	0.0804	0.90

Tab. 2.14   Modal frequencies of the bridge with simplified twin-box deck

The analysis results show that flutter instability does not occur up to high wind. Although non-negligible static deflections and rotations have been found, no classical flutter instability occurs up to 60 m/s wind speed. Further numerical analyses with higher wind velocities show an increase of rotations due to the low torsional stiffness of longitudinal beams. This phenomenon can be

reduced after introducing few pairs of X-shaped structural elements to connect the truss girders in the longitudinal beams.

The preliminary results obtained for the long-span suspension bridge with a simplified twin-box deck configuration seem to lead to the conclusion that the proposed solution is feasible and can imply a significant reduction of costs of deck construction, with respect to the much more sophisticated metallic carpentries designed for Messina bridge.

To complete the feasibility study and response to flutter, further investigations, both experimental and numerical, are currently underway.

2.6   BASIC REFERENCES

[a]   Matsumoto M., Yoshizumi F., Yabutani T., Abe K., Nakajima N. 1999. Flutter stabilization and heaving-branch flutter. *J. Wind Eng. Ind. Aerodyn.* 83, 289-299.

[b]   Matsumoto M., Taniwaki Y., Shijo R. 2002. Frequency characteristics in various flutter instabilities of bridge girders. *J. Wind Eng. Ind. Aerodyn.* 90, 1973-1980.

[c]   Sato H., Kusuhara S., Ogi K., Matsufuji H. 2000. Aerodynamic characteristics of super long-span bridges with slotted box girder. *J. Wind Eng. Ind. Aerodyn.* 88, 297-306.

[d]   Ogawa K., Shimodoi H., Oryu T. 2002. Aerodynamic characteristics of a 2-box girder section adaptable for a super long span suspension bridge. *J. Wind Eng. Ind. Aerodyn.* 90, 2033-2043.

[e]   Larose G.L., D'Auteuil A. 2004. On the Reynolds number sensitivity of the aerodynamics of bluff bodies with sharp edges. *Proc. 8th Italian National Conference on Wind Engineering IN-VENTO* (F. Ricciardelli et al. eds.), Reggio Calabria, Italy (Aracne, Roma), 21-29.

[f]   Brancaleoni F., Diana G. 1993. The aerodynamic design of the Messina Straits Bridge. *J. Wind Eng. Ind. Aerodyn.* 48, 395-409.

[g]   Diana G., Falco M., Bruni S., Cigada A., Larose G.L., Damsgaard A., Collina A. 1995. Comparisons between wind tunnel tests on a full aeroelastic model of the proposed bridge over Stretto di Messina and numerical results. *J. Wind Eng. Ind. Aerodyn.* 54-55, 101-113.

[h]   D'Asdia P., Sepe V. 1998. Aeroelastic instability of long span suspended bridges: a multi-mode approach. *J. Wind Eng. Ind. Aerodyn.* 74-76, 849-857.

[i]   Dyrbye C., Hansen S. 1997. *Wind loads on Structures*. Wiley, New York.

[j]   De Miranda M., Bartoli G. 2001. Aerodynamic optimization of decks of cable-stayed bridges. *Proc. IABSE Symposium*, Seoul, South Korea.

[k]   Simiu E., Scanlan R.H. 1996. *Wind Effects on Structures*. 3rd edition, Wiley, New York.

[l]   Jain A., Jones N.P., Scanlan R.H. 1996. Coupled aeroelastic and aerodynamic response analysis of long-span bridges. *J. Wind Eng. Ind. Aerodyn.* 60, 69-80.

[m]   Sepe V., Caracoglia L., D'Asdia P. 2000. Aeroelastic instability of long-span bridges: contributions to the analysis in frequency and time domains. *Wind and Structures* 1, 41-58.

[n]   Larose G.L., Livesey F.M. 1997. Performance of streamlined bridge decks in relation to the aerodynamics of a flat plate. *J. Wind Eng. Ind. Aerodyn.* 69-71, 851-860.

[o]   Astiz M.A., Andersen E.Y. 1990. On wind stability of very long spans in connection with a bridge across the Strait of Gibraltar. In: *Strait Crossing* (J. Krokeborg ed.), Balkema, Rotterdam.

[p]   Plowden D. 1974. *The spans of North America*. W.W. Norton & Co., New York.

[q]   Bosch H. 1987. A wind tunnel investigation of the Deer Isle-Sedgewick Bridge (Phase 1). In: *Federal Highway Administration Report*, n. FHWA/RD-87/027, McLean, Virginia.

[r]   Ostenfeld K.H., Larsen A. 1992. Bridge engineering and aerodynamics. *Proc. 1ˢᵗ International Symposium on Aerodynamics of Large Bridges*, Copenhagen, Denmark.

2.7   LIST OF PUBBLICATIONS

[1]   Febo S. 2007. *Decks and structural systems for very long span bridges*. PhD Thesis, Università degli Studi "G. D'Annunzio" di Chieti-Pescara, Italy.

[2]   Bartoli G., D'Asdia P., Febo S., Mannini C., Pastò S., Procino L. 2006. Analisi di sensibilità aeroelastica nella progettazione di ponti sospesi di grande luce - Parte I: prove in galleria del vento; Parte II: aspetti progettuali. *Proc. 9ᵗʰ Italian National Conference on Wind Engineering IN-VENTO*, Pescara, Italy.

[3]   Bartoli G., D'Asdia P., Febo S., Mannini C., Pastò S., Procino L. 2007. Innovative solutions for the design of long-span bridges: investigation on the aeroelastic behaviour of multiple-box girder deck sections. *Proc. 12ᵗʰ International Conference on Wind Engineering ICWE*, Cairns, Australia.

[4]   D'Asdia P., Febo S. 2007. Proposta di ponte sospeso con frequenze torsionali più basse delle flessionali. *Proc. 21ˢᵗ CTA Conference*, Catania, Italy.

[5]   Bartoli G., D'Asdia P., Febo S., Mannini C., Pastò S., Procino L. 2008. Innovative solutions for long-span suspension bridges. *Proc. 6ᵗʰ International Colloquium on Bluff Bodies Aerodynamics and Applications BBAA*, Milan, Italy.

[6]   Bartoli G., D'Asdia P., Febo S., Mannini C., Pastò S., Procino L. 2008. Proposta di impalcati innovativi per ponti sospesi di grande luce. *Proc. 10ᵗʰ Italian National Conference on Wind Engineering IN-VENTO*, Cefalù, Italy.

[7]   Bartoli G., D'Asdia P., Febo S., Mannini C., Noè S., Procino L. 2009. Innovative configurations for long-span suspension bridges. *Proc. 5ᵗʰ European and African Conference on Wind Engineering EACWE*, Florence, Italy.

[8]   D'Asdia P., Febo S., Bartoli G., Mannini C., Procino L., Noè S. 2009. Innovative steel multi-box deck configurations for very long span suspension bridges. *Proc. 22ⁿᵈ CTA Conference*, Padua, Italy.

WITH CONTRIBUTION FROM:

Gianni Bartoli, University of Florence
Claudio Mannini, University of Florence
Salvatore Noè, University of Trieste
Stefano Pastò, University of Florence
Lorenzo Procino, CRIACIV BLWT
Vincenzo Sepe, University "G. D'Annunzio" of Chieti-Pescara

2A   Appendix to Chapter 2: Geometrically nonlinear finite element analysis

Fabio Rizzo, Piero D'Asdia
Università "G. D'Annunzio" di Chieti-Pescara

2A.1   INTRODUCTION

The non linear finite element analyses used to acquire data for this research were calculated with a software called TENSO, now in its eight edition. This non-commercial software was first written in the '70s but evolved into its fullest configuration in the '90s when professor and engineer Piero D'Asdia and his group used it to design the Messina Strait bridge. In recent years many subroutines have also been completed and updated, creating an instrument that is ideal for analyzing structures with non-linear geometric characteristics such as cable structures, suspension bridges or tensostructures. All the algorithms in subroutines that compose the program were reconstructed and re-tested during this research project in order to record all the flow charts and mathematical procedures executed by the program. The object of this appendix is to illustrate the main characteristics of the software and demonstrate its potential.

2A.2   FINITE ELEMENT MODEL

TENSO can evaluate parabolic cable structures in various ways: dividing the cable into a suitable number of rectilinear cable elements makes it possible to configure an elastic catenary configuration or a parabolic cable. The rectilinear cable finite element requires only nodal loads. Possible applications include suspension bridges with a center distance between hangers that is sufficiently small compared to the cable span so that loads can be considered as concentrated on the nodes. Another application is cable net roofs where the distance between cables compared to the maximum span of the roof is sufficiently small. When the finite element model contains this kind of element the global stiffness matrix is updated for each loading step by assembling stiffness matrices of the elements varied according to the strains found in the previous step. This takes into account the geometric nonlinearity of the structure. The parabolic cable finite element is used to calculate cable structures with uniformly distributed loads. Use of this method depends on the distribution of the load on the cable: if the load is distributed along the cable span direction then the cable has a parabolic configuration; if the load is distributed along the axis of the cable then the finite element used is an elastic catenary element.

The uniform section beam finite element makes it possible to calculate the stiffness matrix of the beam and to account for axial forces coming from eventual pre-stressing or concomitant thermal loads. This aspect is important, for example, when studying suspension bridges where axial force values are very high in the elements that form the towers and the deck. Beam finite elements with variable sections, used, for example, to optimize structural members, calls for identifying ten coefficients for a polynomial description of changes in areas and moments of inertia along axis of the beam. The stiffness matrix was evaluated using a numerical procedure based on the point validity of the elastic bond and on description of the range of displacement using six independent functions.

The procedure initially calculates the flexibility matrix of the element, applying a system of forces and evaluating a natural displacement system. These terms are obtained as displacement values from actions of unitary forces to which an iterative algorithm converges. This algorithm recalculates them at each step using, along the axis of the beam, the balance conditions between stress characteristics and the natural forces on the configurations. These correspond to the displacement field obtained in polynomial form, requiring resolution of the twelve conditions of kinematic compatibility and balance furnished by the previous step. The Gauss method is used for the numerical integrations that are required. Four stiffness balance sub-matrices are then numerically obtained from the flexibility matrix by inversion and multiplication with the balance matrices in the current configuration. The program also has the possibility of introducing nodal dampers.

2A.3   NONLINEAR STATIC AND DYNAMIC ANALYSIS

Tenso software simultaneously uses two methods to better approximate the global configuration of a strongly strained structure: both by non linear incremental step by step numerical analysis and by variable stiffness matrix progressive iteration methods as well as by the secant method.

Using the incremental step by step method makes it possible to transform the non linear problem into a series of linear problems, each phase of which takes into account the load and strain history evaluated during of the previous step. A portion of load (ΔP) small enough to make sure the classic elasticity method can be used is applied for each step of analysis. This simple and classical approach, however, contrasts with the impossibility of a priori establishing the exact dimensions of a sufficiently small load step, with the serious risk of not being able to check the quality of the solution. Various methods of transient stiffness matrix or instantaneous stiffness matrix have been developed to solve this problem. These are basically vector versions of the Newton-Raphson (N.R.) method for solving non-linear equation systems.

If displacements are large, the new stiffness matrix, K_{k+1}, evaluated based on the updated geometric solution and based on the internal stress state, multiplied by the displacement vector, δ_{k+1}, gives an internal forces vector, P_{k+1} that is not in balance with the external forces vector; the difference between these two force vectors is the out-of-balance force vector, R_{k+1}. This vector is then applied as an external load to correct the displacements $\Delta\delta_{k+1}$. This increment in the displacements vector is then used to update the geometric shape of the structure.

The method used in Tenso to solve non linear dynamic analyses is the Newmark-beta method. The reasons behind this choice are to be found in its excellent performance especially regarding unconditioned stability and regarding the relative simplicity of calculations compared to other algorithms.

The implementation procedure takes place in these consecutive phases: reading of initial boundary conditions; solution of the stiffness matrix with Newmark method β and γ, parameters that determine the stability and the precision of the integration procedure, set equal to ¼ and ½; defini-

tion of the force vector; step by step calculation with an iterative process and check of numerical system convergence. A check of solution precision is performed at each integration step in order to evaluate the possibility of using a smaller integration step. The node reactions furnished by the stiffness of the generically strained structure, by the very nature of the integration algorithm, will generally be different from the applied external loads. These differences represent the unbalanced loads. The Newmark algorithm that is used contains a correction by which precision is calculated as the ratio between the unbalanced load norms and those of the loads applied on the unrestrained degrees of freedom. For each integration step there are non-null unbalanced loads that are added to the next loading step, bringing the load – deviation path near to the real path.

2A.4   WIND-STRUCTURE INTERACTION

It is possible to evaluate wind loads, during a non linear static or dynamic analysis done using Tenso, both based on analytical calculations and directly from wind tunnel data. Special simplifications are possible when analyzing suspension or stayed bridges. Drag, lift and moment forces on the deck can be calculated starting from the static polars obtained on section models in wind tunnels, as was done to study aerodynamic and aero-elastic behavior for the Messina Strait Bridge. It is then possible to simulate the effect of vortex shedding on the decks of suspension or cable-stayed bridges, on cables, hangers or stays and antennas just as along all slender structures such as towers or chimneys.

The vibrations generated by vortex shedding are often cause of structural collapse (by exceeding ultimate yield strength) or, more frequently, of fatigue collapse or of performance malfunctions (the amplitude of vibrations can make the structure difficult or even dangerous to use). This is a particularly non linear phenomenon, influenced by many factors tied both to the characteristics of the incident flow (such as, for example, the distribution of mean speed along the structure and, above all, the intensity of turbulence) and to the interactions between flows and structural motion. Tenso includes a subroutine of this wind load model that simulates the particular form of interaction between motion and force that is characteristic of the synchronization between the vortex shedding and natural vibration. This concept is based on three empirical relations that make the size of the synchronization interval, the lift coefficient value and the motion-force phase depend on the amplitude of the oscillation. In this way it correctly reproduces the hysteresis characteristics of the phenomena [d].

2A.5   BASIC REFERENCES

[a]   Smith I. M., Griffiths D.V. 1982. *Programming the Finite Element Method*. Wiley, New York.

[b]   Crisfield M.A. 1991. *Non-Linear Finite Element Analysis of Solids and Structures*, Vol.1. Wiley, New York.

[c]   Simiu E., Scanlan, R.H. 1986. *Wind Effects on Structures*. Wiley, New York.

[d]   D'Asdia P., Sepe V., Caracoglia L., Noè S. 2003. A model for vortex-shedding induced oscillations of long-span bridges. *Proc. 2nd International Structural Engineering and Construction Conference ISEC-02*, Rome, Italy (Balkema, Rotterdam), 2331-2336.

3   Structural design assisted by wind tunnel testing

Massimo Majowiecki, Nicola Cosentino
Università IUAV di Venezia

3.1   INTRODUCTION

This Chapter presents some of the recent experiences in wind tunnel testing, made by the Authors within the design stage of steel structures. According to principle of the «design assisted by testing», contemplated by the Eurocode, the combination of tests and calculations is increasingly used. Multiples are the motivation of this increasing interest/demand. The sophisticated architectural shapes (culminating in the «free form design»), the absence of corresponding reliable fluid-dynamics models and the increasing flexibility of structures are probably the main ones. Not less important is the opportunity/necessity to confirm by control checks the assumptions made in the design, specially with respect to complex aeroelastic phenomena, such as lock-in, flutter, rain-wind induced vibration, etc..

The main purpose of the paper is to outline the potentiality of the presented tests and the main problems encountered in their use. These aspects have to be accurately evaluated in defining the test specifications.
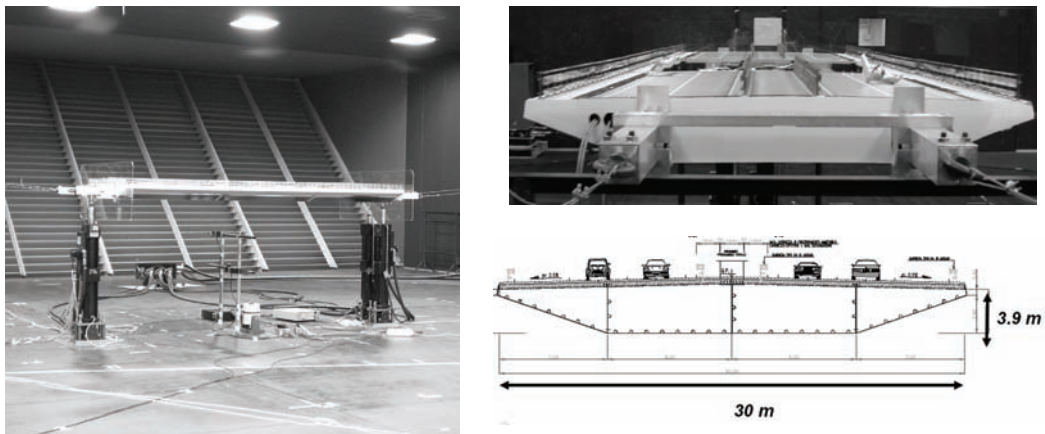
Figure 3.1   Experimental deck model and deck section (Adige River Bridge)

The use of some data analysis techniques (such as the proper orthogonal decomposition, the sensitivity analysis, etc.), in keeping the essential design parameters, is presented too.

The presented experiences refer to the tests performed during the design of: a cable stayed bridge on the Adige river (on the A31 motorway - Italy); the New Braga Stadium (Braga - Portugal); the new Unipol headquarter Tower (Bologna - Italy); the tall building and the roof on «Piazza delle Città Lombarde» (Milan - Italy); the new Bologna town-hall (Bologna - Italy).

3.2   THE ADIGE RIVER BRIDGE

The design of the Adige river cable stayed bridge [1] was assisted by wind tunnel tests aimed to check the aerodynamic and the aeroelastic behaviour of the deck and of the tower. The tests were carried out at the «Politecnico di Milano» boundary layer wind tunnel (Fig. 3.1).

Regarding the bridge deck, the aerodynamic static coefficients and the flutter derivatives (with a particular focus on the low reduced velocity values) were measured. The bridge deck was modeled by an elastic mockup made by an aluminum structure. Since the (expected) ratio between the flexural and the torsional frequencies was quite close to the unity (0.85), this ratio was reproduced at the model scale to correctly take it into account for flutter investigation.

The quasi-steady aerodynamic forces were measured in low turbulence conditions, at different angles of attack. The aerodynamic coefficients (Fig. 3.2) allow to determine the quasi-steady wind forces on the deck and to check the sensitivity to galloping.

The aeroelastic behaviour was investigated by both a direct and an inverse method. By the direct method the wind induced forces on the deck, under an imposed 1-DOF motion, are measured.
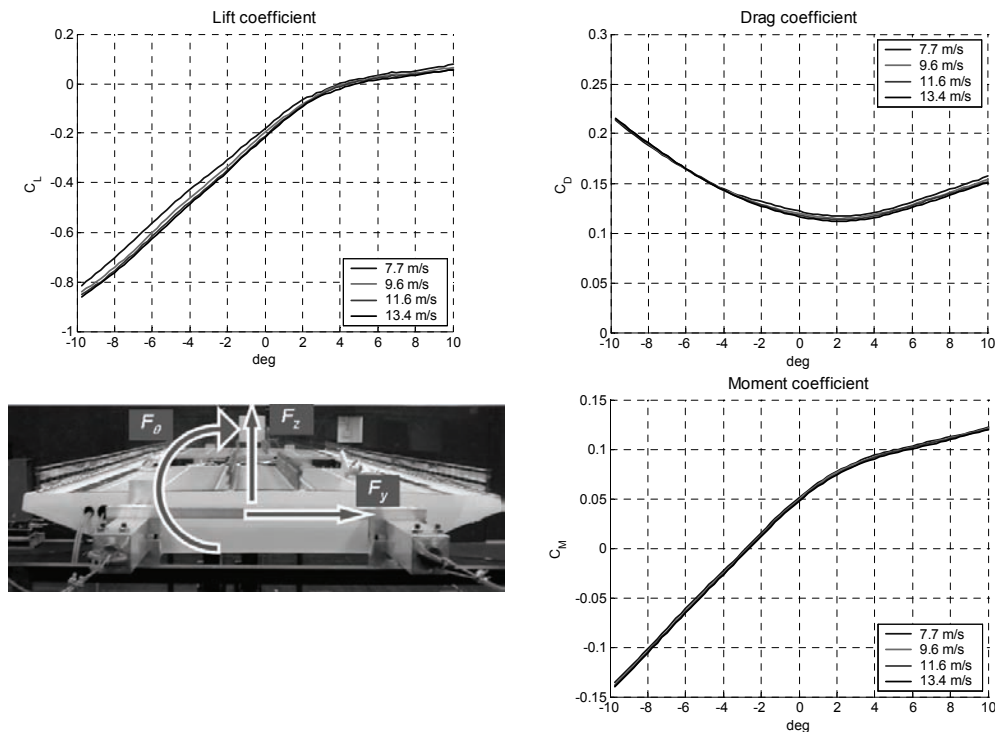
Figure 3.2   The aerodynamic static coefficients and their sign convention

This allows to define and change a-priori the (mean) angle of attack; it also allows a large reproducibility of the tests. On the other hand, the inverse method consist in measuring the forces on the duck during a free motion. This procedure allows to investigate the vortex shedding mechanism.

Based on the wind tunnel measured aeroelastic derivatives (Fig. 3.3), the flutter critical conditions (velocity and frequency) have been investigated by mean of the classical Scanlan-Tomko procedure (Fig. 3.4). The order of magnitudes have been checked by comparing the results with those obtained by the simplified Theodorsen theory. The influence of the angle of attack and of the inherent structural damping on the critical parameters has been checked too.

In order to keep the aeroelastic behaviour at very low wind speeds, an alternative approach to the flutter problem has been adopted. The aerodynamic forces are written as:

$$F_z = \frac{1}{2}\rho V^2 BL\left(-h_1^*\frac{\dot{z}}{V} - h_2^*\frac{B\dot{\vartheta}}{V} + h_3^*\vartheta + h_4^*\frac{\pi}{2V_\omega^{*2}}\frac{z}{B}\right)$$

$$F_\vartheta = \frac{1}{2}\rho V^2 B^2 L\left(-a_1^*\frac{\dot{z}}{V} - a_2^*\frac{B\dot{\vartheta}}{V} + a_3^*\vartheta + a_4^*\frac{\pi}{2V_\omega^{*2}}\frac{z}{B}\right)$$

(3.1)
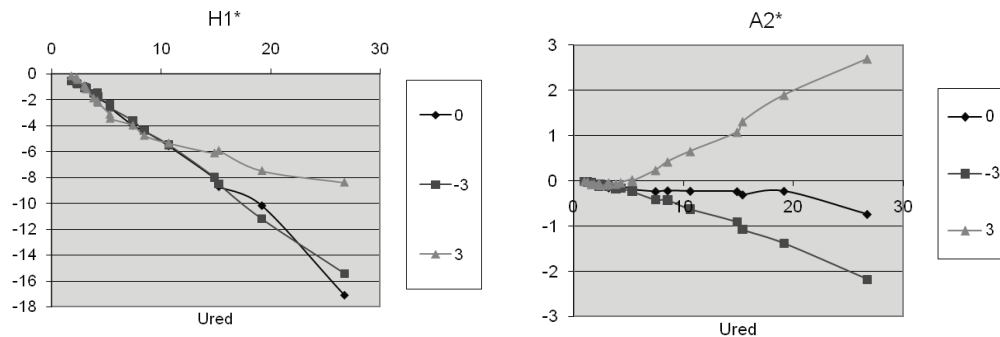
Figure 3.3   Flutter derivatives H1* and A2*, for the attack angles 0°, 3°, -3°
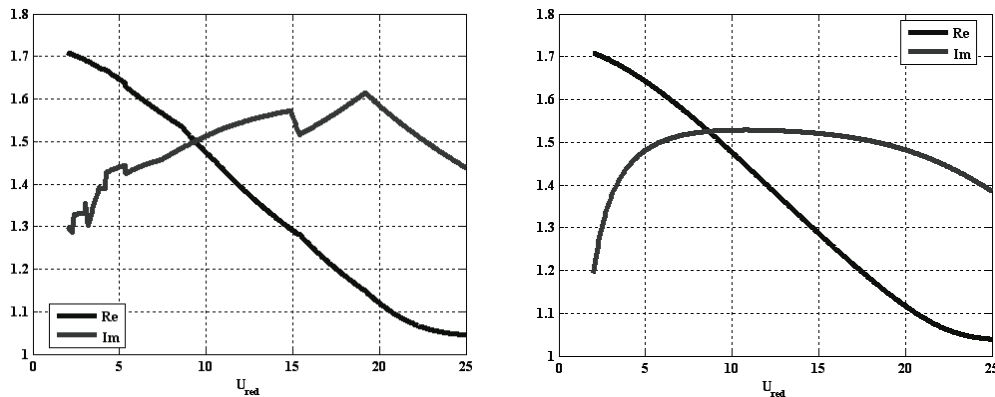
Figure 3.4   Real and imaginary parts of the flutter equation solution. Coupling of modes 1 and 3 – angle of attack 0° - linear interpolation (left) vs polynomial fitting of experimental coefficients (right)

where B and L are the deck dimensions (L = unit length), ρ is the air density, V is the wind speed, $V^*_\omega = V/\omega B$ is the reduced velocity, ω is the angular frequency, θ and z are the deck DOFs. It is possible to calculate the minimum damping necessary to avoid the excitation due to vortex shedding. By considering only the equation of motion for the vertical displacement (which, in the present case, corresponds to the first vibration mode), the total damping is obtained by the superposition of aeroelastic and structural damping components.

In order to obtain stability against vortex-shedding, the total damping must be positive (Fig. 3.5):

$$\xi \geq -\frac{\rho V^* B^2 h_1^*}{8m\pi} \tag{3.2}$$
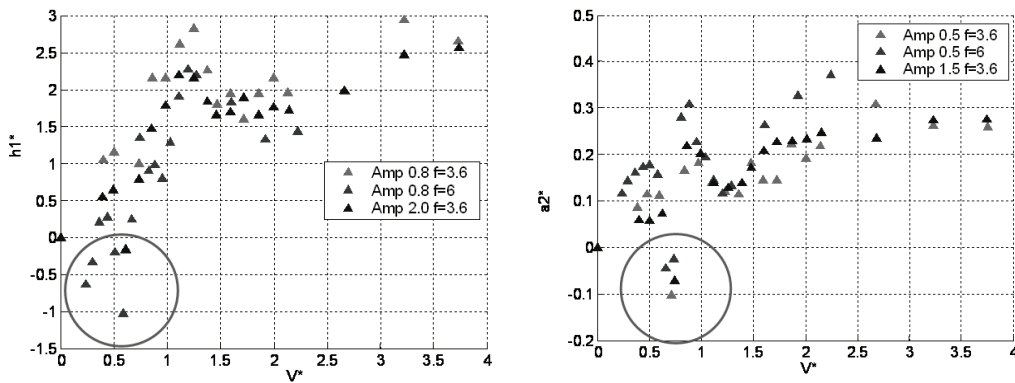
Figure 3.5 Flutter derivatives h1* and a2*, at low reduced velocity
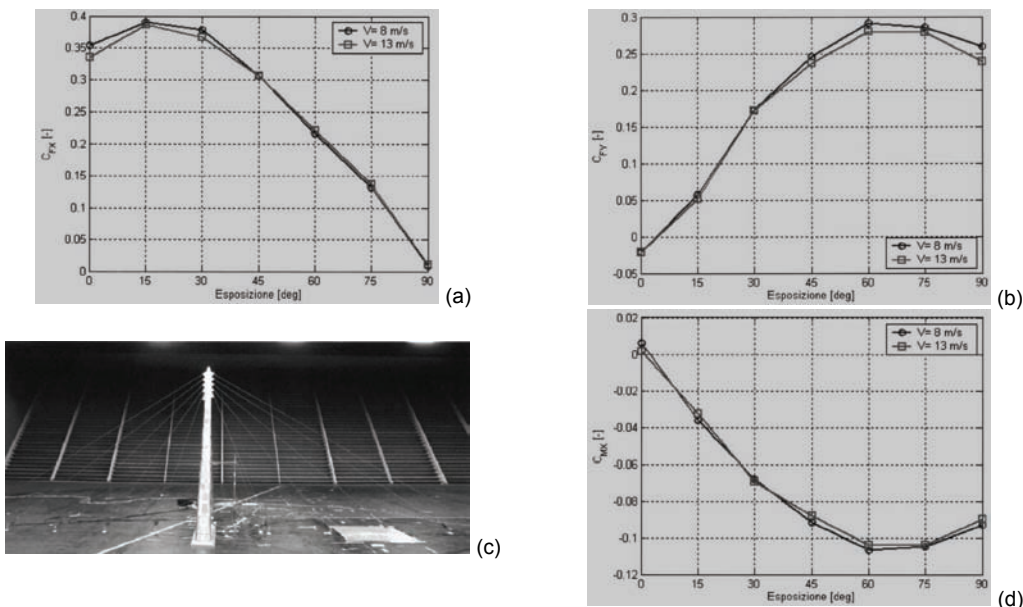
Figure 3.6 Aerodynamic coefficients at the pylon base: (a) C_{FX}, (b) C_{FY}, (d) C_{MX}
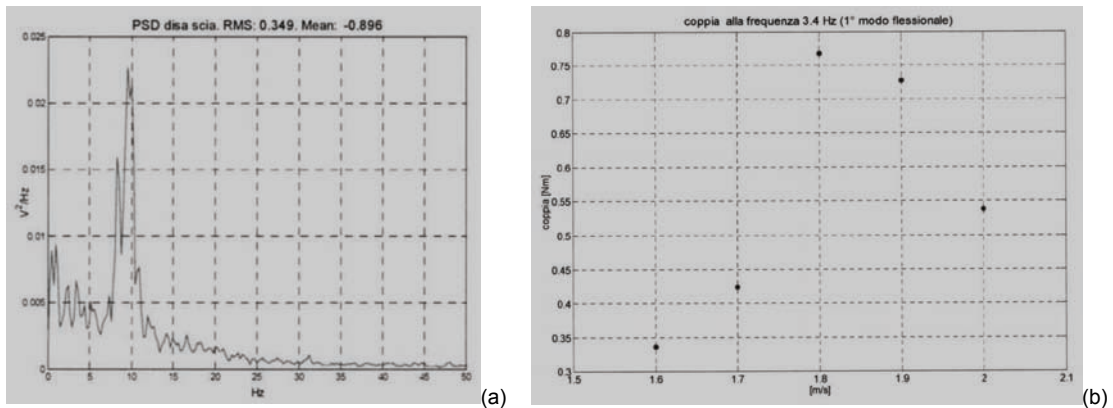
Figure 3.7   Spectral properties of the wake (a) and base bending moment vs wind speed (b)

V^* being the reduced velocity $V^* = V / Bf$. Of course, this is an approximate procedure, because vortex shedding is a strongly non-linear phenomenon; it is here treated by a linear approach, but this allows to estimate the order of magnitude for the minimum structural damping which is necessary to protect the structure from vortex-shedding.

The bridge tower model (flexible aeroelastic model) was firstly placed on a dynamometric balance to determine the aerodynamic forces and moments (Fig. 3.6) due to smooth wind. The same model was then linked to the ground and equipped by accelerometers and extensometers to measure the vibration induced by the vortex shedding. An independent anemometer measured the wake wind speed.

The aerodynamic forces are used in the design of the tower sections. The "in-wake" wind velocity spectra (Fig. 3.7a) allow to determine the Strouhal number; the relatively low dynamic magnification factor (DMF) of the bending moment (in the pylon) at the lock-in velocity (Fig. 3.7b) shows a moderate sensitivity to vortex shedding.

3.3   THE NEW BRAGA STADIUM

The tests for the design of the new Braga Stadium suspended roof [2-7] were carried out, independently, at the "RWDI" and at the "Politecnico di Milano" wind tunnels. "RWDI" tests were performed on rigid models, to measure the pressure field on the roof, while a flexible (aeroelastic) model was tested at the "Politecnico di Milano", in order to check the aerodynamic stabilities and the effectiveness of a possible external damping system.

The wind pressures were derived from the tests on a rigid model (Fig. 3.8). Since the pressure time histories were simultaneously measured at different points, within the upper and the lower sides of the roof panels, the instantaneous pressure fields were available.

Due to the different spatial distribution of upper and lower pressure taps, preliminary interpolation was required to obtain the differential pressures, which represent the actual load on the structure. Despite the apparent simplicity of this operation, the instantaneous interpolation gave rise to uncertainties and numerical difficulties.

The design wind speeds at the stadium site were derived from 1:1500 scaled wind tunnel tests (including a wide stadium surroundings), while the pressure coefficients were measured in 1:400 model.
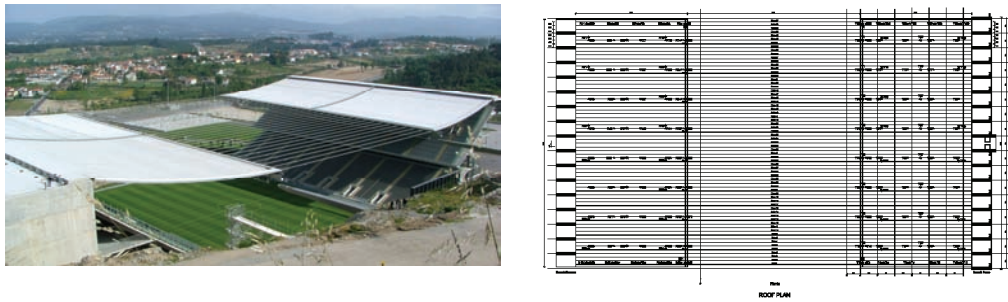
Figure 3.8   The New Braga Stadium and the RWDI pressure taps arrangement

Both the wind speed profiles and turbulence presented different features in 1:400 tests with respect to 1:1500 ones. In order to match the peak gust velocities between the two scale models at 25 and 50 m heights (roof position), an equivalent design wind speed was calculated by RWDI. The "double model" was a source of further uncertainties and data treatment problems. It also outlined a more general problem which often occurs in defining the model reference height: due to the imperfect reproduction of the wind profile, significant errors can befall when wind tunnel dimensionless coefficients are used with reference to standard codes design wind speed.

Mode = 1 - Variance = 0.1449   Mode = 2 - Variance = 0.0748
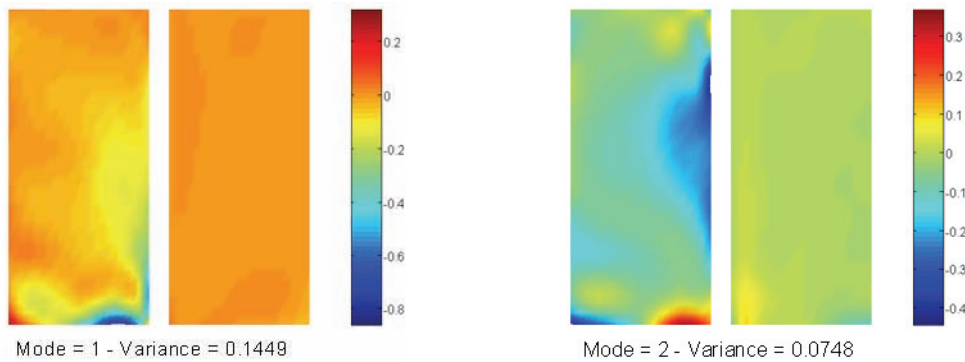
Figure 3.9   Proper orthogonal decomposition of the measured wind pressure fields

(a)   (b)   (c)
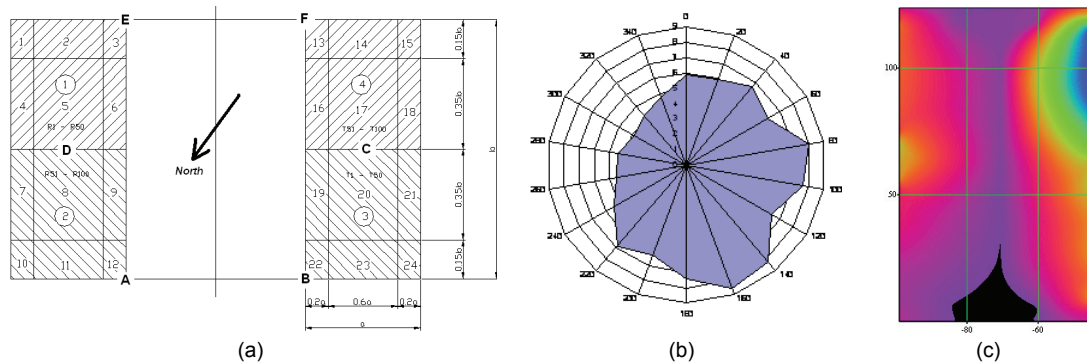
Figure 3.10   References points/regions for the response evaluation and the sensitivity analysis (a), minimum reliability index β for each direction (b) and distribution of β values along the slab (c)

The orthogonal decomposition techniques have been adopted to simplify the pressure representation, and to reduce the computational effort. The structural response was determined by separately evaluating the mean, the quasi-steady and the resonant response. The first term simply takes into account the mean pressure distributions. The second one is obtained by performing a classical covariance proper orthogonal decomposition (POD). The third one takes into account the dynamic amplification of a suitable number of structural vibration modes, each one being excited by the unsteady wind pressures.

The analytical procedure is synthesized in the following equations, while a typical result is summarized in Table 3.1 (with the reference to Fig. 3.10a). The Eqs. (3.3) resume the procedure to decompose (POD) a pressure field (Fig. 3.9), the Eqs. (3.4) determine the mean and the quasi-static response and the Eqs. (3.5) refer to the resonant contribution.

Let $\boldsymbol{p}(t) = \{p_1(t) \ ... \ p_m(t)\}^T$ be a Gaussian stationary nil mean m-variate random process. Let $\mathbf{C}_p$ be the covariance (for $\tau = 0$) matrix of $\boldsymbol{p}(t)$. This matrix is symmetric and positive definite, thus it admits the modal decomposition:

$$\mathbf{C}_p = \sum_{k=1}^{m} \phi_k \phi_k^T \lambda_k \ ; \qquad \phi_i \phi_j^T = \delta_{ij} \ ; \qquad \phi_i^T \mathbf{C}_p \phi_j = \delta_{ij} \lambda_j \ ; \qquad \boldsymbol{p}(t) = \sum_{k=1}^{m} \phi_k x_k(t) \tag{3.3}$$

where λ_k and ϕ_k are k^{th} eigenvalue and eigenvector of $\mathbf{C}_p$ and $\boldsymbol{x}(t) = \{x_1(t) \ ... \ x_m(t)\}^T$ is the m-variate random process, image of $\boldsymbol{p}(t)$ in the transformed space.

The generic response $R(t)$ of a linear system to the load $\boldsymbol{p}(t)$ can be expressed as:

$$R(t) = \sum_{k=1}^{s} x_k(t) \cdot R_k \ ; \qquad \sigma_{R,qs}^2 = \sum_{k=1}^{s} \sigma_{x_k}^2 R_k^2 \ ; \qquad R_{qs} = \overline{R} \pm g_{qs} \sigma_{R,qs} \tag{3.4}$$

where R_k is the generic response (load, deflection, etc.) due to the static distribution ϕ_k; $\sigma_{x_k}^2$ is the variance of the process $x_k(t)$; g_{qs} is the quasi-steady gust factor; $\sigma_{R,qs}$ is the standard deviation of R; R_{qs} is the quasi-steady peak (minimum and maximum) response.

The inclusion of resonant effects can be accomplished using the equations:

$$R_{qs+res} = \overline{R} \pm \sqrt{g_{qs}^2 \sigma_{R,qs}^2 + g_{res}^2 \sigma_{R,res}^2} \ ; \qquad g_{res}^2 \sigma_{R,res}^2 = \sum_{h=1}^{n} g_h^2 \sigma_{R_h}^2$$

$$g_h = \sqrt{2 \ln(f_h T)} + \frac{0.577}{\sqrt{2 \ln(f_h T)}} \ ; \qquad M_h = \int_A m(x,y) \cdot \psi_h^2(x,y) \cdot dA \tag{3.5}$$

$$Q_h(t) = \int_A p(x,y,t) \cdot \psi_h(x,y) \cdot dA \ ; \qquad \sigma_{R_h}^2 = R_h^2 \frac{\pi}{4 \cdot \xi_h} \frac{f_h \cdot S_{Q_h}(f_h)}{(2 \cdot \pi \cdot f_h)^4 M_h^2}$$

where g_h is the hth modal gust factor; f_h is the natural frequency of the hth mode; T is the sample length (typically one hour); $\sigma_{R_h}^2$ is the variance of response R associated to the mode h; $\psi_h(x,y)$ is the hth mode shape, in terms of deflection normal to the surface at the position (x,y); R_h is the response corresponding to this deflection; $m(x,y)$ is the mass per unit area; ξ_h is the hth modal damping; $S_{Q_h}(f)$ is the modal force spectrum.

The resonant contribution is proportional to the square of the inherent structural damping ratio. Since this contribute was the most important in the case of the Braga Stadium (see Table 3.1), a

more appropriate evaluation of the structural damping was necessary (full scale dynamic characterization) and an experimental check of the resonant and aeroelastic effects was made (aeroelastic model).

The aeroelastic model (1:70) was tested at the "Politecnico di Milano" boundary layer wind tunnel (BLWT) in both smooth flow (without external environmental reconstruction) and turbulent flow (with external environmental reconstruction). The aeroelastic stability was checked up to 58 m/s (full scale). In turbulent wind conditions, oscillation up to 40-50 cm full scale, as order of magnitude, were recorded. The aeroelastic model was also tested by placing (at the roof corners) linear viscous dissipative devices (C = 100-150 kN s/m at full scale). Damping ratios up to 7-8% were reached. The response was subsequently reduced of about 50%, so confirming the analytical estimations.

In January 2004 the structure was equipped with a permanent monitoring system, to measure different parameters (such as pressures, accelerations, wind velocity, cable stresses, etc.) at different significant points of the structure (Fig. 3.11).

As it was found numerically and confirmed by the aeroelastic model, the resonant response is dominant and the structural inherent damping was a very important parameter in determining the response.

Node	$\overline{R}$	$g_{qs}^2 \boldsymbol{\sigma}_{R,qs}^2$	$\overline{R} \pm \sqrt{g_{qs}^2 \boldsymbol{\sigma}_{R,qs}^2}$	$g_{res}^2 \boldsymbol{\sigma}_{R,res}^2$	$\overline{R} \pm \sqrt{g_{qs}^2 \boldsymbol{\sigma}_{R,qs}^2 + g_{res}^2 \boldsymbol{\sigma}_{R,res}^2}$
A	0,1550	0,0250	0,3131	0,3027	0,7275
B	-0,0837	0,0115	-0,1910	0,3076	-0,6486
C	-0,0441	0,0014	-0,0812	0,0433	-0,2555
D	0,0930	0,0052	0,1652	0,0419	0,3101
E	0,0621	0,0092	0,1582	0,2040	0,5238
F	-0,0198	0,0016	-0,0599	0,2018	-0,4709

Table 3.1 Typical response contributions, in terms of vertical displacement at some roof locations: mean (col. 2), quasi-static (col. 4) and total response (col. 6)

Figure 3.11 Monitoring system on the whole structure
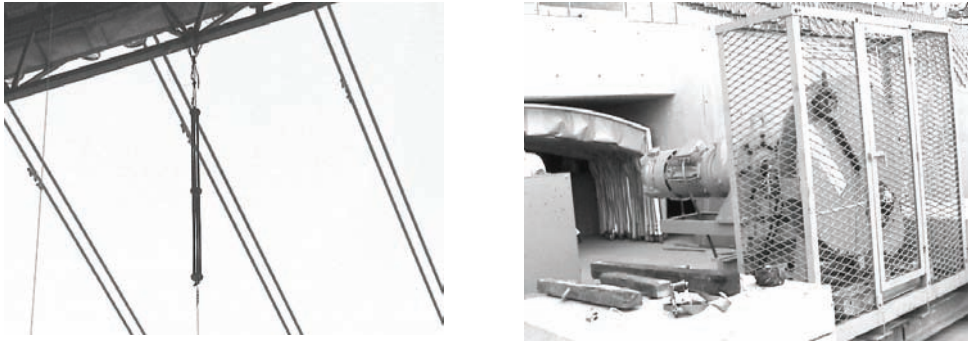
Figure 3.12 Images of the exciting system
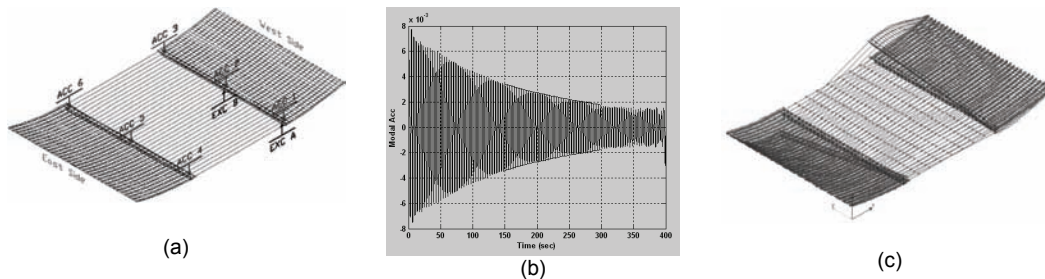
Figure 3.13 Exciting-measuring positions (a), typical free motion record (b) and 1st natural mode (c)

The dynamic characterization was performed to determine the actual value of the damping ratio for the first modes. To excite the system, a cable was attacked to the border steel girder through a pre-tensioned spring (Fig. 3.12a) and it was harmonically moved (sinus wave) at the other end by an electrical engine (Fig. 3.12b). To measure the structural dynamic response under the applied dynamic loads and the free vibration decay after the loading excitation stop, 6 accelerometers were placed on the roof slab (Fig. 3.13a).

In order to evaluate the natural modal shapes and the corresponding modal damping, the free vibration decay time series, recorded after the resonant harmonic excitation stops, have been used (Fig. 3.13b). The modal shapes were determined by orthogonal decomposing (POD) the recorded signals (Fig. 3.13c).

3.4   THE UNIPOL TOWER

The design of the "Unipol" tall (123 m) building [8] was assisted by wind tunnel tests carried out at the CRIACIV[1] (Florence/Prato, Italy) boundary layer wind tunnel on a rigid model 1:350 scaled and equipped with 125 pressure taps (Fig. 3.14).

---

[1] Cento di Ricerca Interuniversitario di Aerodinamica delle Costruzioni e Ingegneria del Vento (Univ. di Firenze, Roma La Sapienza, Perugia, Trieste, Venezia IUAV, Chieti D'Annunzio); www.criaciv.unifi.it.
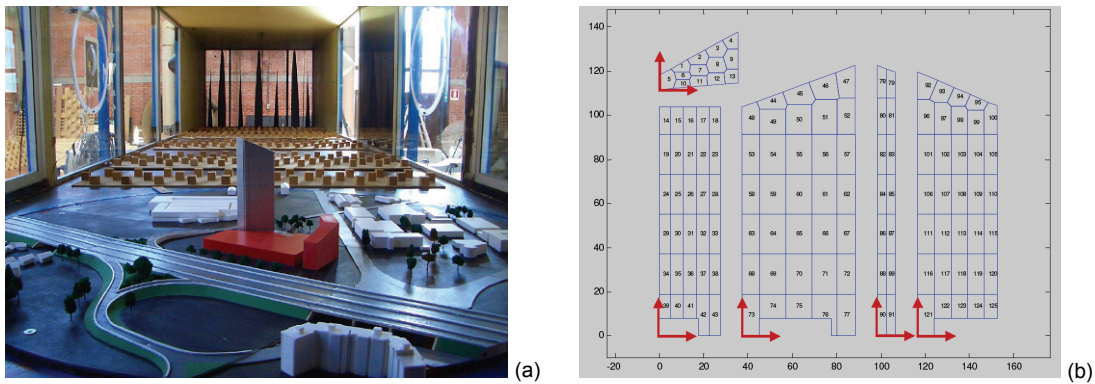
Figure 3.14   The Unipol Tower wind tunnel model (a) and the pressure taps locations (b)
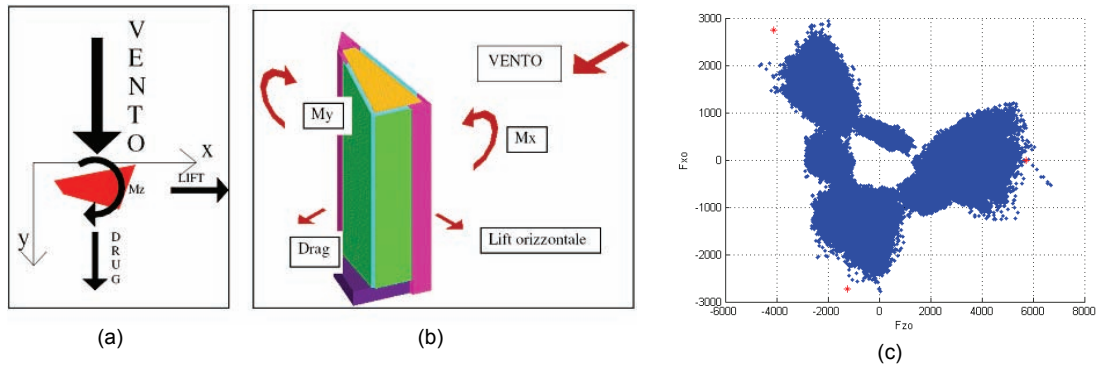
Figure 3.15   Wind tunnel reference system (a,b) and correlation locus of longitudinal-transversal force

The aim of the tests was to determine the aerodynamic forces by both the simultaneous measurement of pressures at 125 points on the facades and the direct measurement of the base global forces by means of a dynamometric balance. In addition, pressures and flow within a double skin facade, which covers part of the building, were required to be checked.

Once the preliminary treatment and reliability problems were overcome, the simultaneous pressure fields were retained. The design forces on the building were evaluated at different levels, by taking into account the correlation between the components. Due to the asymmetry of the structure, the significant load combinations were determined by means of the longitudinal-transversal force locus (Fig. 3.15c), by including all the tested wind directions. In addition, information on local pressures were also available. The measurement of simultaneous pressure fields is quite "rich" of information, even if the comparison with directly measured global forces is suggested.

3.5   THE MILAN «ASRL»

The new Milan regional government centre ("Altra Sede Regione Lombardia" - ASRL) includes different steel structures: from the roof on the central place to parts of the tall main building.
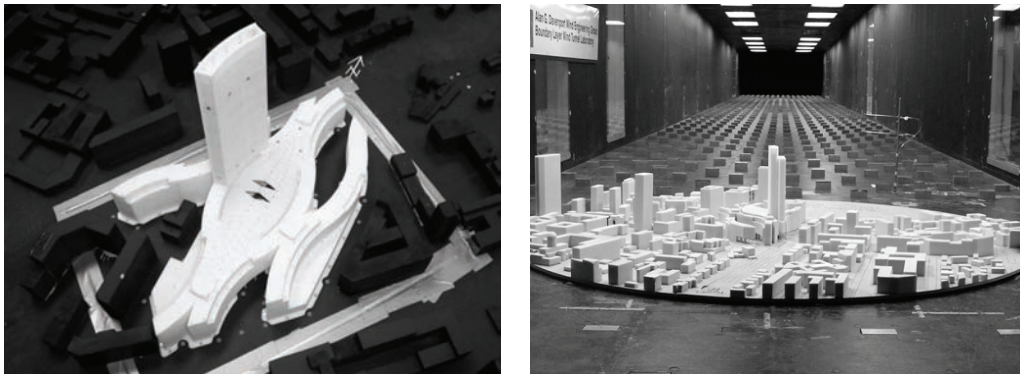
Figure 3.16 Wind tunnel model of the ASRL buildings and surrounding

The tests [9] were carried out at the "Alan G. Davenport Wind Engineering Group" BLWT (Fig. 3.16). Since the analysis included both the wind climate and the global design forces, this was a comphrehensive wind tunnel study. In particular, the following informations were provided: (a) overall wind loads suitable for use in the design of the structural system of the tower; (b) local peak pressures acting on the external surfaces of the project; (c) local net peak pressures (external pressure minus internal pressure) suitable for use in the design of the windows and cladding; (d) load distributions for structural analysis of the Piazza roof; (e) prediction of the wind environment in pedestrian areas around the site; (f) smoke flow through the Piazza roof opening.

The resulting net pressure coefficients from the wind tunnel tests were combined with the design probability distribution of wind speed and direction to form predictions of net suctions and pressures for various return periods (Fig. 3.17).

Regarding the Piazza Roof, five different structural load cases were considered and arranged by means of the measured pressure time histories at 107 locations. The load cases arrangement was oriented to maximize the overturning moments about edge lines of the roof as well as the center line of the roof, the shear in the x direction and uplift in the z direction (Fig. 3.18). Predictions of the load cases were made by combining the angle-by-angle aerodynamic data with the Milan wind climate model.

(a)

(b)
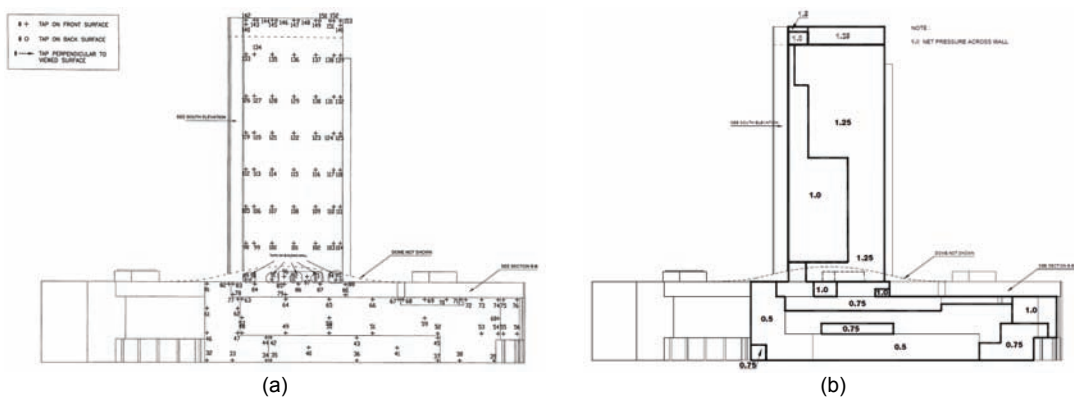
Figure 3.17 Example of pressure taps location on the Tower (a) and pressure distribution (b)

(a)

(b)

Pressure Distribution

(c)
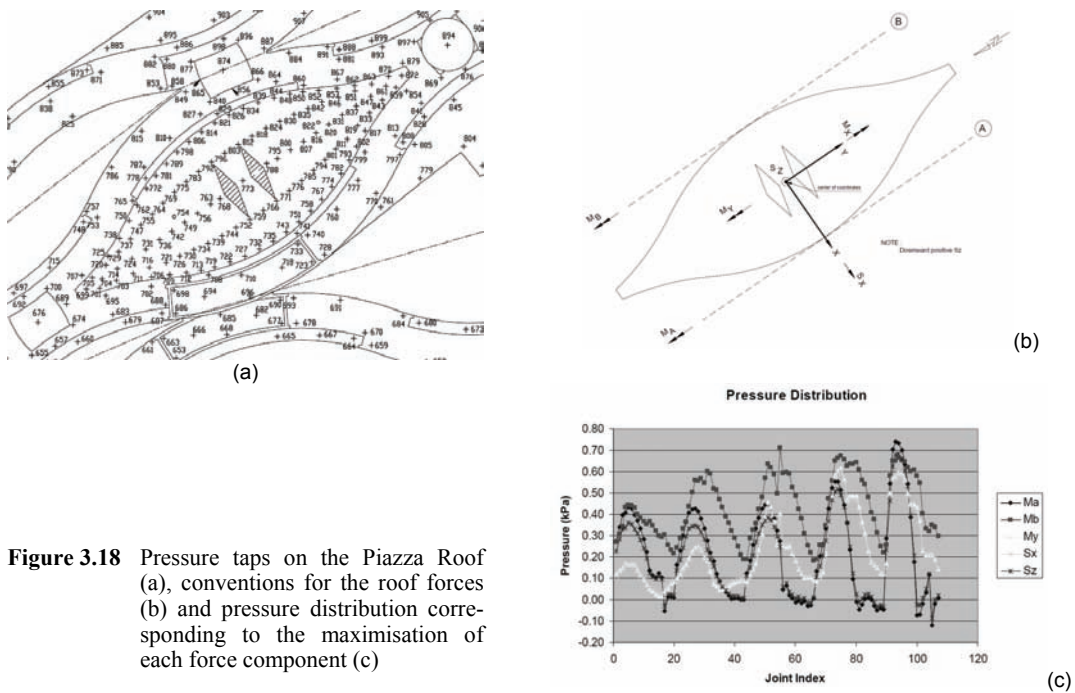
Figure 3.18 Pressure taps on the Piazza Roof (a), conventions for the roof forces (b) and pressure distribution corresponding to the maximisation of each force component (c)

Equivalent static loads were determined by using the load-response-correlation (LRC) method, based on the influence function for the load action and the correlation of the measured pressure data.

Fig. 3.19a shows the locations where pedestrian level wind speeds were measured. Experimental results were combined with the extratropical wind climates to provide predictions of the wind speeds expected to be exceeded for 5% of the time and those expected to be exceeded once per year. These predictions were compared directly with acceptance criteria for pedestrian comfort and safety, respectively (Fig 19b,c).

(a)

(b)

(c)
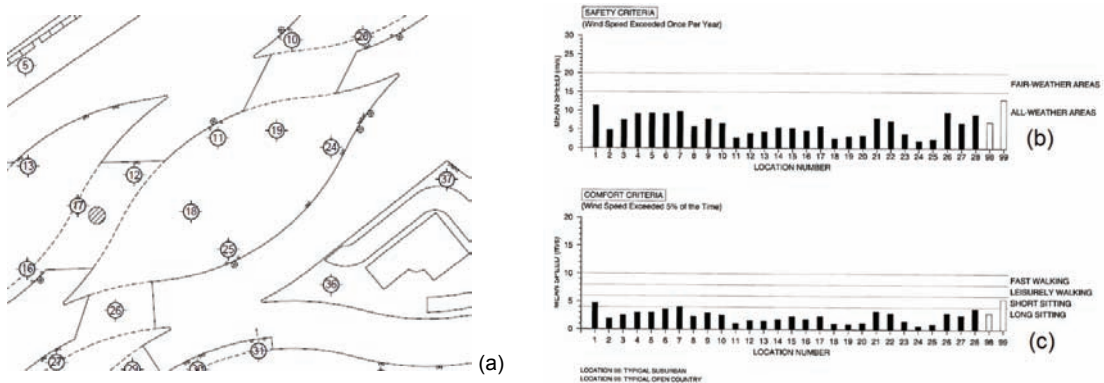
Figure 3.19 Location of measurements (a) and predicted mean wind speeds compared with criteria for pedestrian safety (b) and comfort (c)
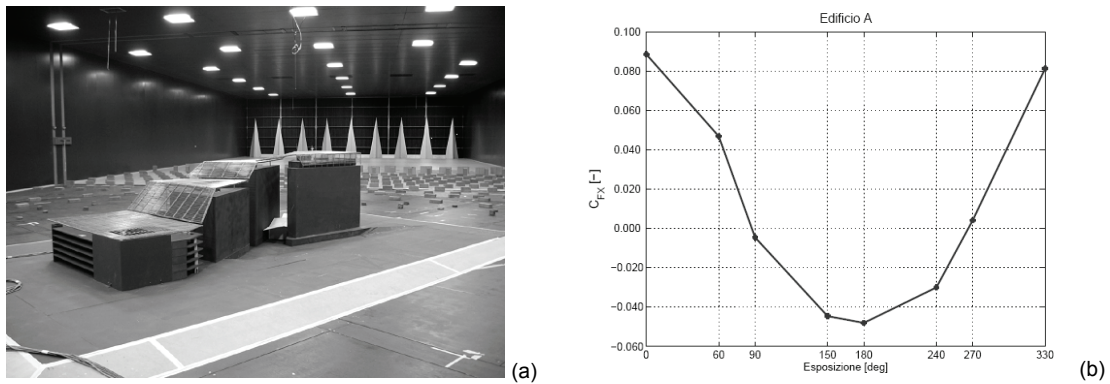
Figure 3.20 Bologna Town Hall model (a) and a typical force coefficients diagram on the roof (b)

Finally, the effectiveness of the Piazza roof opening to allow smoke to escape was determined by the plume rise height of the smoke generated in the open space underneath the roof. Analytical calculations of the plume rise were carried out for low wind conditions as well as nominal one week return and one month return wind speeds. The results suggest that the plume rise heights are much larger than the height of the Piazza roof from the ground and the smoke generated in a fire can likely escape the enclosure.

3.6   BOLOGNA TOWN HALL

The Bologna town hall structural design was assisted by wind tunnel tests performed at the "Politecnico di Milano" BLWT [10,11]. Two different models were arranged: a 1:50 model of the whole structure (Fig. 3.20a), for the measurement of loads on roofs and facades; a 1:1 model of a roof tube array (Fig. 3.22), to check the sensitivity to vortex shedding.

The 1:50 model of the whole structure was used to measure the forces on the roof (by means of dynamometric balances) and the pressures on facades (by means of appropriate distribution of pressure taps).

Loads on the roofs were given in terms of force coefficients (Fig. 3.20b), while pressures on facades were given in terms of pressure coefficient diagrams (Fig. 3.21a,b) and global maps (Fig. 3.21c).

The building roof is covered by a series of tube arrays, regularly spaced. The length of tubes varies between 7 and 14 m. The length-diameter ratio (up to 39), the light weight (aluminum) and the end connection type (which produces a very low damping ratio, approximately $\xi = 0.2\%$) make the tubes susceptible of dynamic excitation. Since the Scruton number is approximately 2.3, it is expected that the tubes are sensitive to vortex shedding excitation.

In the case of isolated cylinder, this Scruton number value gives rise to oscillations of about 0.3 diameters. The array effect is also tested in the wind tunnel (Fig. 3.22). The results substantially confirm the previsions made for the single tube, the recorded displacement being 0.25 diameters as order of magnitude.

Wind tunnel tests showed that the tube oscillation can reach amplitudes which can induce damage on the tubes themselves and on the connection, as well as appreciable oscillation of the whole roof. In addition, the "look-in" velocity (Fig. 3.23) corresponds to mean wind speed characterized by a low return period.
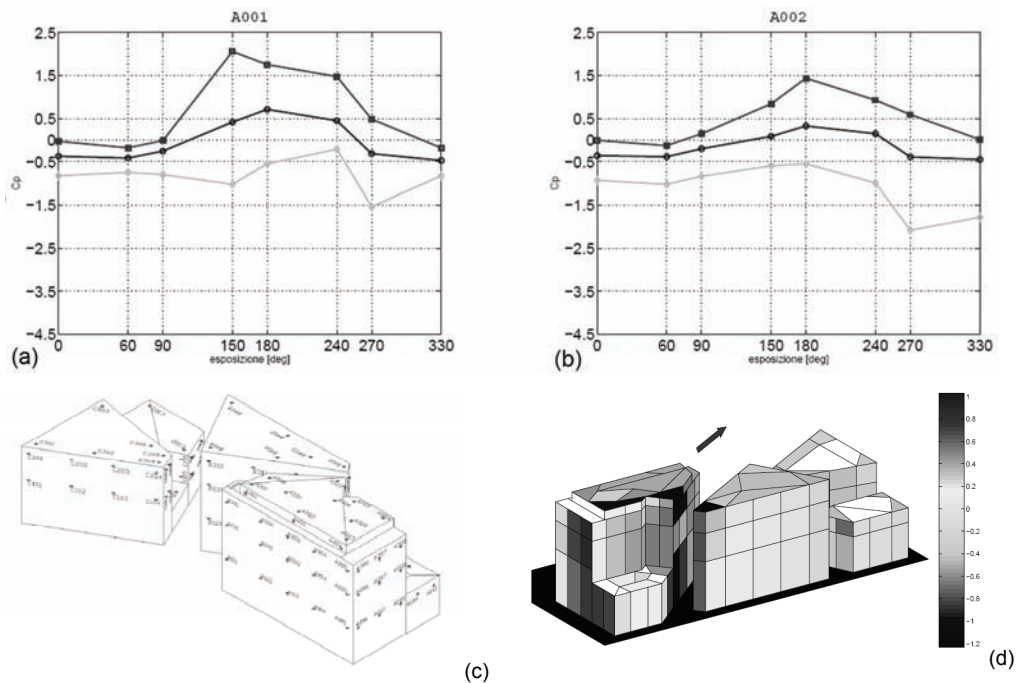
Figure 3.21 Typical pressure coefficients on facades (a,b), pressure taps location (c) and typical pressure
                map (c) for the Bologna Town Hall

Wind tunnel tests suggested to implement design solution to avoid or reduce the sensitivity to vortex shedding. Possible ways to do so are aerodynamic solutions (such as placing spires on the tubes) and/or adding mechanical damping to the tubes. The final designer-owner decision was to realize the roof without any countermeasure, to monitor it and to evaluate 'on site' the opportunity of acting on the tubes (a case of design assisted by testing and monitoring).

3.7   CONCLUSION

According to principle of the "design assisted by testing", contemplated by the Eurocode, the combination of tests and calculations is increasingly used. The motivations of this increasing interest-demand are various: from the sophisticated architectural shapes to the absence of corresponding reliable fluid-dynamics models, from the increasing flexibility of structures to the necessity of checking complex aeroelastic phenomena.

The paper outlined the potentiality of wind tunnel testing and the main problems encountered in their use. These aspects have to be accurately evaluated in defining the tests specifications. The use of some data analysis techniques (such as the proper orthogonal decomposition, the sensitivity analysis etc.), in keeping the essential design parameters, was presented too.

The cited tasks were presented by referring to some of the recent experiences, made by the Authors within the design stage of steel structures: a cable stayed bridge on the Adige river (on the A31 motorway - Italy); the New Braga Stadium (Braga - Portugal); the new Unipol headquarter Tower (Bologna - Italy); the tall building and the roof on «Piazza delle Città Lombarde» (Milan - Italy); the new Bologna town-hall (Bologna - Italy).
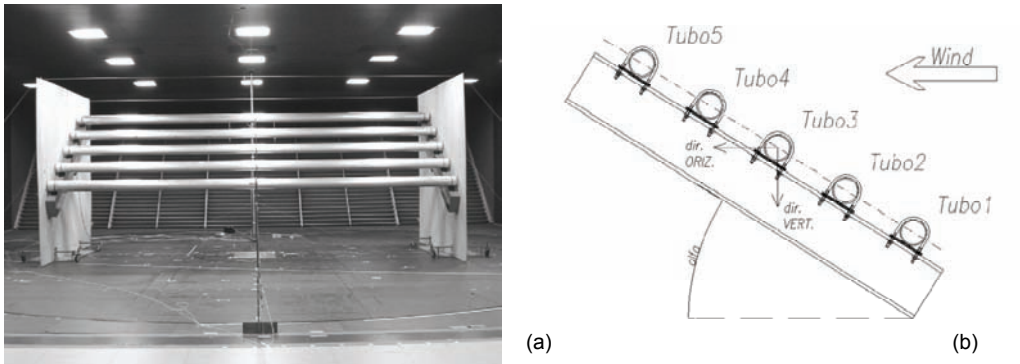
Figure 3.22   Wind tunnel model (a) and scheme (b) of one of the tube array
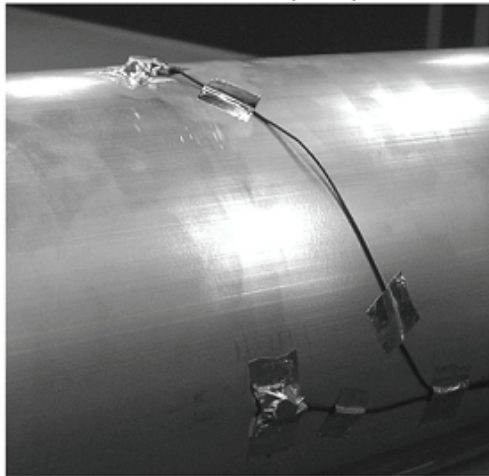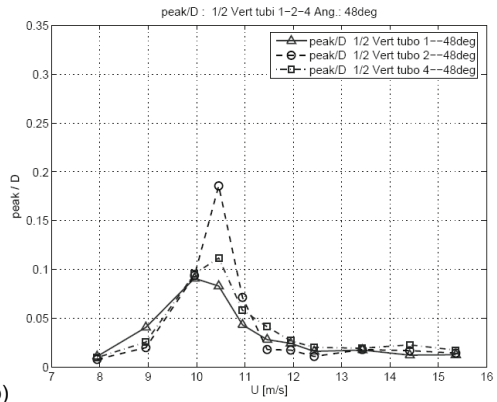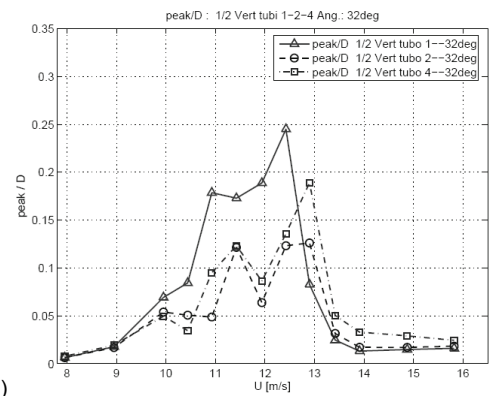
Figure 3.23   Accelerometers on a tube of the array (a) and vibration amplitudes (b,c) for different angles of the array setup

3.8   BASIC REFERENCES

[1]   Majowiecki M., Cosentino N., Costa C. 2007. Wind Effects and Cables Damping at the Adige Cable Stay Bridge. *Proc. IASS Symposium 2007*, Venice, Italy.

[2]   Majowiecki M., Cosentino N. 2007. Dynamic Aspects of the New Braga Stadium Large Span Roof. *Proc. IASS Symposium 2007*, Venice, Italy.

[3]   Marini M., Cosentino N., Majowiecki M. 2005. Dynamic characterization of the New Braga Sta-
        dium large span suspension roof. *Proc. International Conference on Experimental Vibration Analy-
        sis for Civil Engineering Structure EVACES*, Bordeaux, France.

[4]   Cosentino N., Majowiecki M. 2004. Analysis and mitigation of the wind induced response of large
        span suspended roofs: the case of the new Braga Stadium. *Proc. 8th Italian National Conference on
        Wind Engineering IN-VENTO*, Reggio Calabria, Italy.

[5]   Bertero R.D., Carnicer R., Puppo A.H. 2003. *Sensibility wind analysis of the roof structural system -
        Stadium of Braga – Portugal*. Final Report.

[6]   Puppo A.H., Bertero R.D. 1992. Evaluation of Probabilities using Orientated Simulation. *J. Struct.
        Eng.* 118(6), 1683-1704.

[7]   Diana G., Bocciolone M., Collina A., Tosi A., Rocchi D. 2003. *Wind tunnel investigation on Braga
        Stadium.* Journal Final Report.

[8]   Borri C., Bartoli G., Procino L. 2007. *Edificio a torre di via Larga (Unipol): prove in galleria del
        vento per la determinazione delle pressioni sulle facciate e delle forze globali al suolo.* Rapporto fi-
        nale.

[9]   Quiroga P. 2005. *A study of wind effects for Milan Lombardi Government Center.* Report BLWT-
        SS21-2005.

[10]   Diana G. 2005. *Comune di Bologna - Sede dei Servizi Unificati - Prove in galleria del vento su mo-
        dello in scala 1:50 dell'intero complesso*. Report 0202.PM.RC-F.001.001.

[11]   Diana G. 2005. *Comune di Bologna - Sede dei Servizi Unificati - Prove in galleria del vento su un
        modello in scala 1:1*. Report 0202.PM.RC-F.002.001.

4   Computational simulation of crowd and wind flow over bridge structures

Luca Bruno, Nicolas Coste, Davide Fransos, Fiammetta Venuti,
Politecnico di Torino

The activity of the research Unit at Politecnico di Torino has dealt with the dynamic response of bridges and footbridges subjected to the wind flow around their deck and to the crowd flow along it. In either application, both the one-way action of the flow on the structure and the two-way interaction between the flow and the structure have been investigated. The knowledge of the wind or crowd flow dynamics is needed to determine the load applied on the structure, while the modelling and solution of the multi-physics overall system is required to evaluate interaction phenomena.

Despite the different nature of the phenomena, both problems have been described in a unified modelling framework and solved through a common computational approach. The wind and crowd multi-scale flow dynamics, due to classical and active particles respectively, are modelled in the frame of continuum mechanics by means of conservation equations in their differential form. The complex interacting systems resulting from the coupling of the structure with the wind or the crowd are handled in the frame of the so-called partitioned approach.

In the following, a synthesis of the obtained scientific results is proposed for the crowd structure interaction (part I of the chapter, references [1-3,6,8,11]) and the wind action (part II, references [12,17,19]). The interested reader can refer to the cited publications of the research Unit for the topics not covered in the chapter. In particular:

- modelling and simulation of the crowd dynamics: references [4,5,7,9,10];
- modelling and simulation of the wind loads on deck and wind-structure interaction under uncertain conditions: references [13-16,18,20-22].

The research program has been coordinated with the research Unit at University of Reggio Calabria for the study of the crowd-structure interaction (part I), and with the research Unit at University of Florence for the study of the wind flow around a bridge deck, with particular emphasis on the conception, development and study of an aerodynamic benchmark (part II).

The Part I is co-authored by L. Bruno and F. Venuti, while the Part II is co-authored by L. Bruno, N. Coste and D. Fransos.

PART I
Crowd-structure interaction in lively footbridges:
modelling and computational simulation

4.1 INTRODUCTION

Over the last few decades, several footbridges have shown a great sensitivity to human induced vibration in the lateral direction (e.g. [a,b]). The phenomenon, known as synchronous lateral excitation, can take place every time a great number of pedestrians walk upon a surface that laterally oscillates with a frequency near to the lateral walking frequency. The deck lateral motion can be triggered by an external action (e.g. wind) or by the pedestrians themselves, who synchronise among each other in the presence of high crowd density. Hence, a second kind of synchronisation can take place: when a pedestrian walks on a laterally moving surface, because of the attempt to maintain the body balance, he/she walks his/her legs more widespread and adapts his/her frequency to the one of the moving surface, that is, he/she synchronises with the structure. Therefore, the lateral motion of the upper part of the torso increases and the resulting lateral force grows in turn. This phenomenon is amplified if the pedestrian walks within a crowd, since the synchronisation among pedestrians increases the effects of the pedestrian-structure synchronisation. The synchronous lateral excitation phenomenon has never caused structural failures, since it is self-limited, that is, when the vibrations exceed a limit value, pedestrians stop walking or touch the handrails, causing the vibration to decay. In order to provide a deep knowledge of this kind of phenomena, an intense research activity, reviewed in [c], has been done in the recent years, providing the scientific background of some recently published design guidelines [d,e,f].

The most relevant data concerning pedestrian behaviour have been obtained with an empirical approach. Laboratory tests involving a pedestrian walking on both a motionless platform [g] and a laterally moving treadmill [b,h], permitted the lateral force exerted by one pedestrian to be measured and interesting information about the synchronisation between the pedestrian and the structure to be obtained. Moreover, the behaviour of a pedestrian within a crowd has been investigated by means of in situ experiments [b,i] and through the observation of the videos recorded during crowd events [a].

To the authors' knowledge, so far the structural effects of walking people have been evaluated through the proposal of different load models (e.g. those in [d,j]), i.e. the crowd is simply viewed as a load. The first attempt to model the crowd and the structure as parts of a complex dynamical system has been proposed by the writers in [k,l], where the overall modelling framework has been drawn. The same approach has been adopted without meaningful variations and improvements in [l]. It is based on the decomposition of the coupled multiphysical crowd-structure dynamical system into two subsystems, the Crowd and the Structure, interacting between each other by means of forcing terms. Subsequent works has been devoted by the authors to the a-part development of each single model component [4,5].

In the present work the updated components are collected in the initial modelling framework and the latter is implemented in an ad-hoc developed multi-physics numerical code. The whole improved model is applied to an actual crowd event on a real footbridge, the T-bridge (Japan). The available and detailed in-situ measurements of both crowd conditions and structural response allow the complete comparison between them and the computational results. The same case study has been used to perform sensitivity analysis to evaluate some properties of the model.

4.2 MATHEMATICAL MODEL

The main features of the developed model lie in the mathematical and numerical partitioning of the coupled system into two physical subsystems and in the two-way interaction between them,

according to the so-called partitioned approach first proposed by Park and Felippa [m] and gener-
ally applied to Fluid-Structure Interaction problems. In the following, each part of the model is
described referring to the framework schematized in Fig. 4.1.
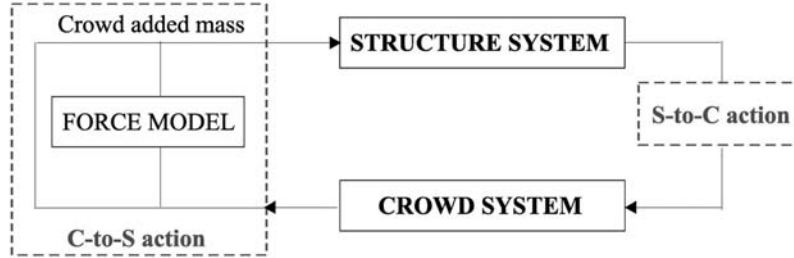
Figure 4.1   Scheme of the time-domain coupled model

4.2.1   The Structure subsystem

The Structure subsystem is modelled as a nonlinear three dimensional (3D) damped dynamical
system, whose equation of motion can be written as:

$$[m_S + m_C(\rho)]\frac{\partial^2 q}{\partial t^2} + \mathscr{C}\frac{\partial q}{\partial t} + \mathscr{L}q = F(\rho, \tilde{\tilde{z}}) \tag{4.1}$$

where $q(x,y,z,t)$ is the structural displacement, x, y, z and t being the space and time independent
variables; m_S and m_C are the structural and crowd mass, respectively; $\mathscr{C}$ and $\mathscr{L}$ are the damping
and stiffness operators, respectively; $\rho(x,t)$ is the crowd density; F is the applied lateral force;
$\tilde{\tilde{z}} = \tilde{\tilde{z}}(x,t)$ is the envelope of the lateral acceleration of the deck. Non linearity arises from two
terms: first, the forcing term F is a function of both the crowd density and the lateral acceleration
of the deck; second, the overall mass m is given by the sum of the structure and the crowd mass.
The latter derives from the solution of the equation governing the Crowd subsystem, that is in turn
dependent on the solution of Eq. (4.1).

4.2.2   The Crowd subsystem

The Crowd subsystem is described by a 1D first-order macroscopic model, that is, the crowd
flow is assumed to be a continuous fluid and its dynamics is described through the derivation of
an evolution equation for the mass density, which is closed by a phenomenological relation that
links the crowd velocity v to the crowd density in the form:

$$\begin{cases} \dfrac{\partial \rho}{\partial t} + \dfrac{\partial}{\partial x}(\rho v) = 0 \\[2mm] v = v_M \left\{ 1 - \exp\left[-\gamma\left(\dfrac{1}{\rho} - \dfrac{1}{\rho_M} \right) \right] \right\} \end{cases} \tag{4.2}$$

where x and t are the space and time independent variables, v_M is the mean maximum velocity,
ρ_M is the maximum admissible density and γ is a coefficient that makes the relation sensitive to
different travel purposes (leisure/shopping, commuters/events, rush hour/business). Both v_M and
ρ_M are made sensitive to the geographic area and the travel purpose by means of coefficients,
which are determined from the observation data reported in [n]. In such a way the model is sensi-
tised to both biometrical and psychological factors that are known to strongly affect crowd behav-
iour. The complete description of the closure equation model is given in [5].

A further improvement of the crowd model is proposed by introducing a space dislocation into the crowd density–velocity relation:

$$v = v[\rho(x + \delta, t)] \tag{4.3}$$

where $\delta \geq 0$ is the anisotropic dislocation length. The crowd density ρ in the crowd density–velocity relation is therefore not a local density, but is forward dislocated in space. From the phenomenological point of view, the dislocation takes into account the pedestrians' attitude to react to what they see in a stretch of road in front of them. It is worth pointing out that the dislocation length is expected to depend on the walking speed, i.e. the faster the walking speed, the larger δ. In this sense, the dislocation length is analogous to the sensory distance d_s, which was defined by Fruin as the length required by a pedestrian to perceive, evaluate and react [o], except that the former is related to a cluster of pedestrians at the macroscopic scale, while the latter refers to one pedestrian at a microscopic scale. Bearing this analogy in mind, the dislocation length is defined as:

$$\delta(\rho) = d_s(\rho)\frac{d_c}{d_0} \tag{4.4}$$

where the $d_s(\rho)$ law was proposed by the authors in [5] by fitting experimental data [p], $d_0 = 0.36$ m is the averaged body depth and d_c is the characteristic dimension of a cluster of pedestrians.

4.2.3 Structure-to-Crowd action

In order to account for the Structure-to-Crowd action, the closure equation has to be adapted to make the walking speed sensitive to the deck lateral motion. The following assumptions are retained from phenomenological observation:

- the motion of the platform, described by its acceleration $\ddot{z}$, reduces the walking velocity;
- the pedestrians adjust their step to the platform motion with a synchronisation time delay $\Delta\tau$, which is expected to be greater than the time interval between two succeeding footfalls;
- after the pedestrians have stopped because of excessive lateral vibrations at time t_s, a stop-and-go time interval Δt_r should elapse before they start walking again.

According to these hypotheses, the term v_M in the closure equation (4.2) is multiplied by a corrective function $g(\widetilde{\ddot{z}})$, which takes into account the sensitivity of v to the platform acceleration. $g(\widetilde{\ddot{z}})$ is equal to unity for acceleration under the threshold of motion perception $\ddot{z}_c = 0.2$ m/s^2 and linearly decreases to zero, value reached for acceleration above $\ddot{z}_M = 2.1$ m/s^2.

4.2.4 Crowd-to-Structure action

The Crowd-to-Structure action takes place in two ways. On the one hand, the mass m is constantly updated by adding the pedestrian mass m_C to the structural mass m_S. On the other hand, the lateral force $F(t)$ exerted by the pedestrians is expressed as a function of both the crowd density ρ and the lateral acceleration of the deck $\widetilde{\ddot{z}}$.

A complete description of the macroscopic force model is provided in [9]: herein, only a few basic points are given. The lateral force F exerted by a cluster of n pedestrians walking along a portion of the bridge span is given by the sum of three terms:

$$F(x,t) = F_{ps}(x,t) + F_{pp}(x,t) + F_s(x,t) \tag{4.5}$$

where F_{ps} is the component due to n_{ps} pedestrians synchronised to the structure, F_{pp} is due to n_{pp} pedestrians synchronised to each other and F_s is due to n_s uncorrelated pedestrians. The above-mentioned numbers of pedestrians are defined as:

$$
\begin{aligned}
n_{ps} &= nS_{ps} \\
n_{pp} &= nS_{pp}(1 - S_{ps}) \\
n_s &= n - n_{ps} - n_{pp}
\end{aligned}
\tag{4.6}
$$

by introducing two synchronisation coefficients. The pedestrian-structure synchronisation coefficient S_{ps} is a function of the deck lateral acceleration $\tilde{\ddot{z}}$ and of the frequency ratio $f_r = f_{pl} / f_s$, where f_{pl} is the lateral step frequency, which depends on the walking velocity, and f_s is the structural frequency:

$$
S_{ps}(\tilde{\ddot{z}}, f_r) = [1 - e^{-b(\tilde{\ddot{z}} - \ddot{z}_c)}][e^{-\eta(f_r - 1)^2}]
\tag{4.7}
$$

where $\eta = 50e^{-20\tilde{\ddot{z}}/\pi}$ and $b = 2.68$. The pedestrian-pedestrian synchronisation coefficient S_{pp} is a function of the crowd density:

$$
S_{pp}(\rho) = \frac{1}{2}\left\{1 + erf\left[a\left(\rho - \frac{\rho_{sync} + \rho_c}{2}\right)\right]\right\}
\tag{4.8}
$$

where $a = 3.14$, $\rho_c = 0.3$ ped/m^2 is the upper limit for unconstrained free walking and $\rho_{sync} = 1.8$ ped/m^2 is the density value that corresponds to the total synchronisation of the pedestrians.

Hence, the components of the total force are expressed as follows:

$$
\begin{aligned}
F_{ps} &= n_{ps}G[\alpha(\tilde{\ddot{z}})\sin(2\pi f_s t + \pi) + \alpha(\tilde{\dot{z}})\cos(2\pi f_s t)] \\
F_{pp} &= n_{pp}\alpha G\sin(2\pi f_{pl}t) \\
F_s &= \sqrt{n_s}\,\alpha G\sin(2\pi f_{pl}t)
\end{aligned}
\tag{4.9}
$$

where G is the weight of one pedestrian and α is the Dynamic Load Factor (DLF), equal to 0.04 in F_{pp} and F_s. The DLFs of the two terms of F_{ps} are expressed as piecewise functions of the envelopes of the deck lateral acceleration and velocity time history $\tilde{\ddot{z}} = \tilde{\ddot{z}}(x,t)$ and $\tilde{\dot{z}} = \tilde{\dot{z}}(x,t)$, respectively [9] (Fig. 4.2). Their trend comes from fitting to experimental data for velocity/acceleration values under the serviceability thresholds ($\dot{z}_s, \ddot{z}_s$). For higher values of the deck motion they follow a qualitative trend which guarantees the self-limitation of the F_{ps} component.

The F_s component is based on the Matsumoto et al.'s [q] model for uncorrelated pedestrians. The lateral step frequency f_{pl}, which is half the vertical step frequency f_p, is determined through a fitting of the data in [r]:

$$
f_p = 0.35v^3 - 1.59v^2 + 2.93v
\tag{4.10}
$$
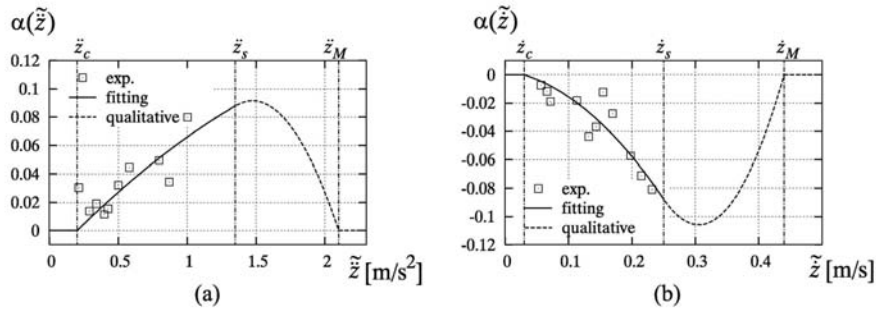
Figure 4.2   DLFs of the components in phase with $\tilde{\ddot{z}}$ (a) and $\tilde{\dot{z}}$ (b)

4.3   COMPUTATIONAL APPROACH

The solution of the mathematical model is obtained by means of computational simulation performed in the space and time domains. The coupled system is decomposed by means of differential partitioning, that is, the system is first decomposed into subsystems (or fields) and then each field is spatially discretised separately [m]. The differential partitioning allows each field to be treated with discretisation techniques and solution algorithms that are known to perform well for the isolated system and allows the use of non-matching grids.

The 1D crowd field is discretised in space by means of Finite Difference Method. The solution of the mass conservation Partial Differential Equation (PDE) is approximated by means of the Lax-Friederichs scheme in its conservation form [s]. The Finite Element (FE) Method is employed for the space discretisation of the 3D structural multi-degree-of-freedom (MDOF) model. A Beta-Newmark step-by-step integration method is employed to solve the set of Ordinary Differential Equations (ODE) that describes the structural subsystem [t].

The two subsystems are characterized by non-matching grids in space while they share the same discretisation in time. The structure space grid is coarser than the crowd one, since the structure deformed shape requires less nodes to be described than the pedestrian traffic phenomena, because only the first global lateral modes of the deck are expected to be mainly excited. As far as the time step Δt is concerned, it has to be chosen in order to guarantee both the Courant-Friederichs-Lewy (CFL) stability condition for the PDE [s] and the desired accuracy solution of the ODE. It follows that the time step is $\Delta t \leq 1/(20 f_{s,max})$, where $f_{s,max}$ is the frequency of the highest mode of interest.

4.4   DESCRIPTION OF THE CASE STUDY: THE T-BRIDGE (JAPAN)

The proposed model has been tested by simulating a crowd event on the T-bridge (Toda Park Bridge, Toda City, Japan), which has been widely described by Fujino and coworkers [a,i,u].

In the following, only some characteristics are recalled. The T-bridge is a cable-stayed footbridge with a two-span continuous steel box girder, a two-plane multi-stay cable system with 11 stays per plane and a 61.4 m-high tower made of reinforced concrete. The total bridge length L is about 180 m and the road deck width B is 5.25 m. The girder is fixed longitudinally and transversely at the tower position. Concrete was poured inside the box girder on the side span to reduce the uplift force at the end support. The bridge mass is 800 kg/m^2 and the damping ratio around 0.7%. The footbridge connects a boat race stadium to a bus terminal. Therefore, at the end of boat races the bridge is crossed by a great number of pedestrians, sometimes more than 20000, who leave the stadium to reach the bus terminal. In these situations, lateral vibrations of the girder of up to 1 cm were recorded.

4.4.1 Description of the structural model

In order to reduce the degrees of freedom of the T-bridge FE model and to simplify the structural analysis, a single-girder (spine) model is used, that is, the bridge deck is modelled using a single central spine with offset rigid links to provide cable anchor nodes. The deck stiffness is assigned to the spine elements and the deck translational mass (lumped mass approach) is assigned to the spine nodes. The towers and the deck are modelled with elastic beam elements and the cables with truss elements. The FE model geometry is represented in Fig. 4.3, while Fig. 4.4 compares the first structural modes reported in [a] with the ones obtained with the present model.
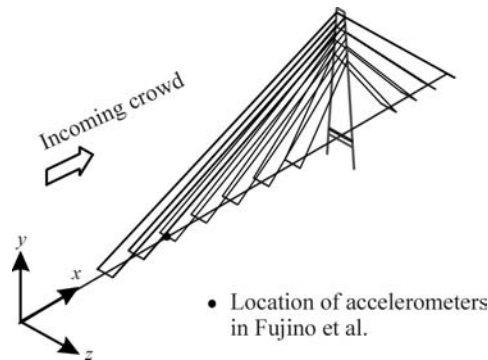
Figure 4.3   FE model with direction of the incoming crowd
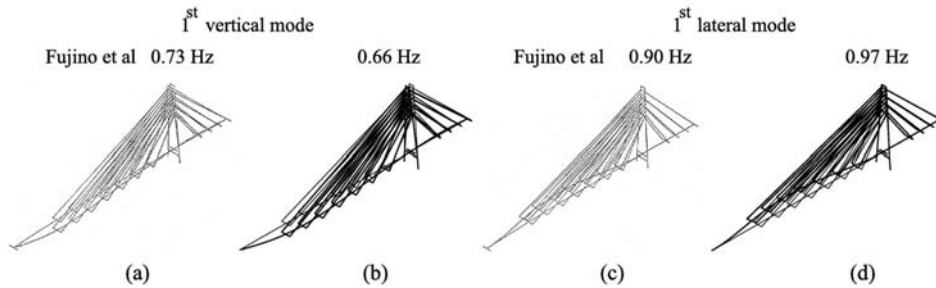
Figure 4.4   T-bridge first vertical and lateral modes

4.4.2 Description of the crowd condition along the deck

The different crowd conditions recorded on the T-bridge have been described in a qualitative way in several papers. The most crowded event is reported in [a], when more than 20000 people left the stadium and crossed the bridge in about 20 minutes. In the most congested situation, about 2000 people walked simultaneously on the bridge. Less crowded situations are described in [i,u]: a maximum number of around 12000 people crossed the bridge in 12 to 20 minutes, with a crowd density varying between 0.8 and 1.5 ped/m^2.

The simulated condition represents an average of the events reported in the literature. The initial condition on the density is $\rho(x,0) = 0.01$ ped/m^2, while the boundary condition (BC) at the inlet $\rho(0, t)$ (Fig. 4.5a) has been built in order to allow about 14000 pedestrians to pass over the bridge in 23 minutes, with a maximum density $\rho_h = 1.33$ ped/m^2. The incoming density shows a steady-state regime bounded between two transient ones, which correspond to the start and the end of the stadium evacuation. The velocity-density relation has been adapted for the case of Asia and rush-hour traffic (Fig. 5b), that is, $\rho_M = 7.7$ ped/m^2, $v_M = 1.48$ m/s and $\gamma = 0.273\rho_M$ [5].
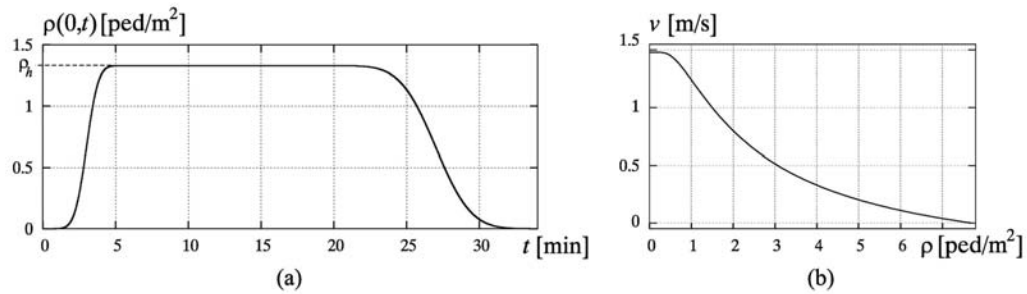
Figure 4.5   Crowd boundary condition at the inlet (a) and closure equation (b)

4.5   SIMULATION OF AN ACTUAL EVENT

The proposed approach allows the evolution of both subsystems to be described in space and time. Five crowd regimes can be identified from the time–space distribution of the crowd density (Fig. 4.6):

- Regime I 'advancing front': the leading pedestrians advance on the bridge, which is still partially empty.
- Regime II 'filling gradient': the crowd is in the transient condition of gradually filling the deck span.
- Regime III 'uniform crowd': the pedestrian density reaches its maximum value and is almost uniformly distributed along the footbridge.
- Regime IV 'vacating gradient': the crowd density gradually decreases at the footbridge entrance, but the whole span remains crowded.
- Regime V 'leaving front': the end of the crowd is leaving the footbridge, which is already partially empty.
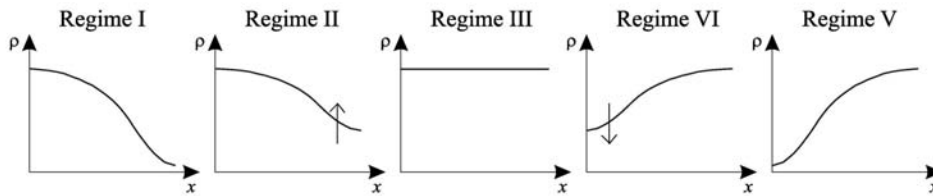
Figure 4.6   Scheme of the space distribution of ρ for the five regimes

The upper limit of regime I and the lower bound of regime V correspond respectively to the maximum and minimum difference $\Delta\rho = \rho(L,t) - \rho(0,t)$. The boundaries of regime III have been determined as the time window with a mean value of ρ along the span equal to 99% of the maximum density ρ_h and a standard deviation less than 0.01 ρ_h.

The results of the computational simulation are compared to the measurements reported in [a] for five time windows (Fig. 4.7), which roughly correspond to the windowing proposed by Fujino et al.. As for the structure results, the figure reports the time history of the deck lateral displacement in the node corresponding to the position of the accelerometers, the structure first lateral frequency f_s averaged over the period and the dominant frequency f, obtained through the PSD of the displacement in the considered period. As far as the crowd results are concerned, the instantaneous spatial distributions of the crowd density are reported, as well as the mean walking frequency f_{pl}.

Looking at the results, a very good agreement between the simulation and the measured data is evident. The maximum amplitude of the lateral deck displacement, of about 9 mm, matches the measurements very well. The maximum percentage of pedestrians synchronised with the structure is about 21%, which is in very good agreement with the observation data in [a], where a percentage of 20% is estimated. Similar considerations can be made for all the considered variables. It is worth pointing out that the dominant frequency of the deck vibration is always closer to the walking frequency than to the structure frequency. This means that the force components due to synchronised-among-each-other or uncorrelated pedestrians are dominant with respect to the one due to pedestrians synchronised with the structure, as also shown in Table 4.1.
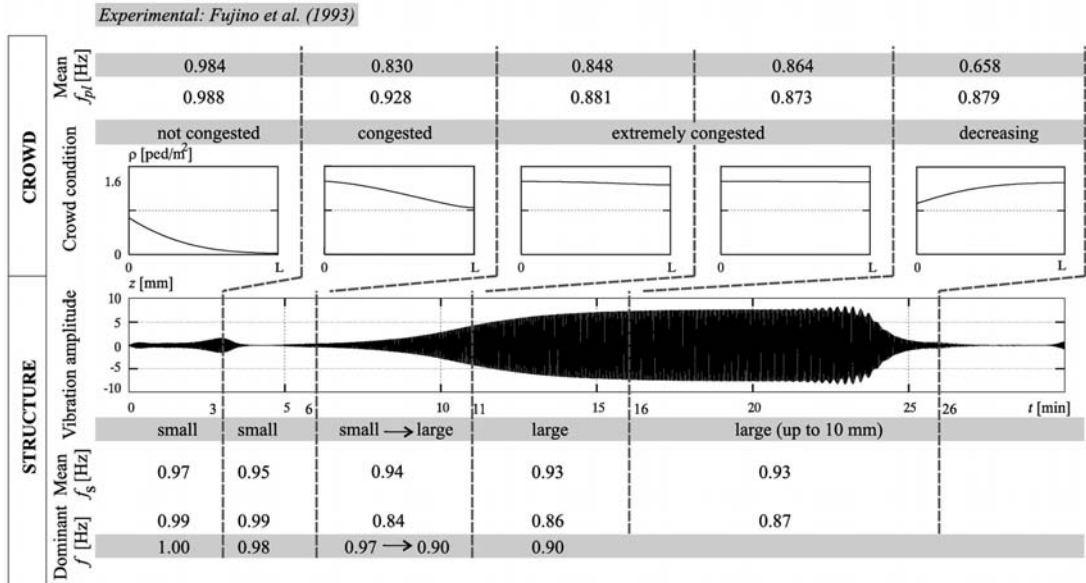
Figure 4.7   Comparison between the simulation results and the experimental data reported in [a], in gray

F	F_{ps}	F_{pp}	F_s	n_{ps}/n	n_{pp}/n	n_s/n
28.8	1.1	26.9	2.1	0.21	0.9	0.13

Tab. 4.1   Maximum amplitudes of each force parameter in the time interval 16-23 min

4.6   SENSITIVITY STUDIES ON THE DESIGN PARAMETERS

Several sensitivity studies have been performed on the same real structure in order to highlight how different design conditions can dramatically affect the response of a real structure. The studies are described in details in [2,8,10]: in the following, only two of them are reported.

4.6.1   Sensitivity study on travel purposes and geographic areas

Four computational simulations are performed by varying the coefficient γ and the value of ρ_M and v_M for the following combinations: Asia-rush hour (AR), Asia-commuters (AC), Asia-leisure (AL) and USA-leisure (UL), which correspond to a progressive decrease of v for $\rho > 0.8$ ped/m^2 (Fig. 4.8a). The substitution of the four fundamental laws in Eq. (4.10) leads to the f_p-ρ relations

represented in Fig. 4.8b. The first case (AR) refers to the conditions actually occurred on the T-bridge and described in the previous section.

The five regimes are highlighted in Fig. 4.9, which plots the deck acceleration time histories in $x = 0.3L$, corresponding to the node monitored by Fujino et al. [a]. First, it can be noticed that the gradual decrease of the pedestrian velocity from AR to UL causes longer regimes I and II and a consequent progressive shortening of regime III. The main consequence can be seen in the deck response, which is gradually shifted in time and decreasing: the case with rush-hour traffic causes a deck vibration amplitude which is almost three times the amplitude obtained in a leisure traffic condition in the same geographic area. The lock-in threshold $\ddot{z}_c$ is exceeded only in the first case AR. In every traffic condition, the regimes I and V are characterized by two local maxima of the structural response that can be related to the travelling load effects. In particular, the highest response in these regimes for the case AC is due to a value of f_r closer to the unity, which means that the pedestrian lateral force is almost resonant with the excited first lateral mode of the deck.
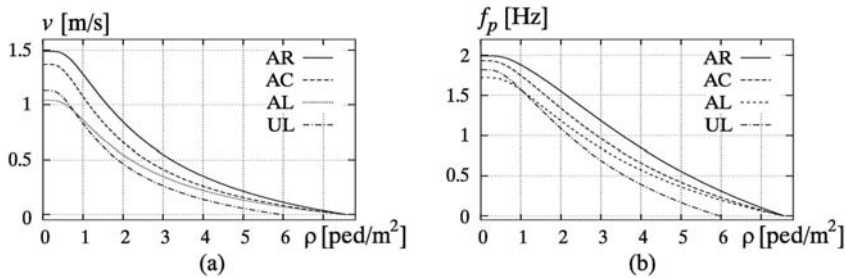
Figure 4.8 v-ρ (a) and f_p-ρ (b) relations
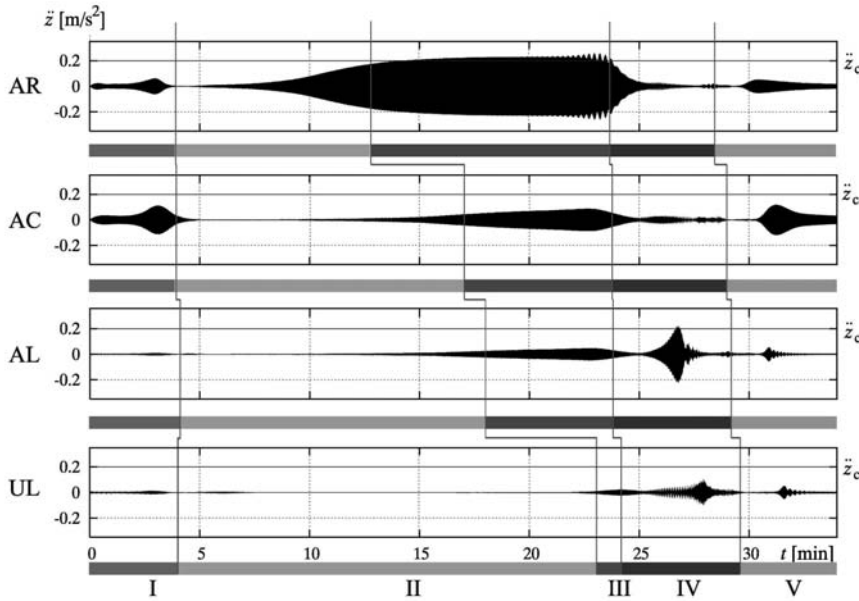
Figure 4.9   Deck lateral acceleration at $x = L/3$

4.6.2 Sensitivity study on the crowd density

The second sensitivity study presented herein is performed on the crowd BCs at the inlet, by varying the maximum value reached by the density ρ_h [0.8; 1.33; 2.0] ped/m^2 (see Fig. 4.5a).

Fig. 4.10 shows that the maximum amplitude of the deck lateral acceleration during Regime III does not correspond to the case with the highest density $\rho_h = 2$ ped/m^2. Increasing values of ρ_h correspond to increasing amplitude of the total force but also to a decrease of f_r due to the effect of the crowd added mass. As a consequence, when $\rho_h = 0.8$ ped/m^2, the total force is an order of magnitude less that in the case $\rho_h = 2$ ped/m^2, but the force is almost resonant with the deck first mode and, therefore, it induces the highest structural response. The almost steady-state response for $\rho_h = 2$ ped/m^2 is due to the fact that, in the same time window, the crowd density exceeds the value above which $S_{pp} = 1$. Therefore, all pedestrians are synchronised to each other and walk with the same frequency, which is sufficiently far from the structural frequency f_s to prevent resonance.
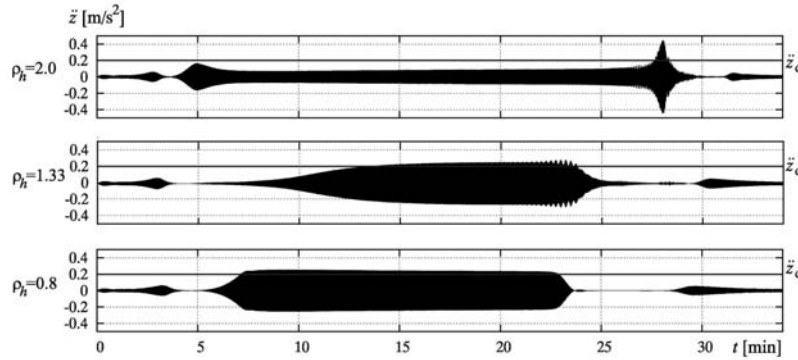
Figure 4.10 Deck lateral acceleration at $x = L/3$

4.7 CONCLUDING REMARKS

In this work a crowd-structure interaction model to describe the synchronous lateral excitation phenomenon has been presented. The model has been implemented in an ad hoc computational code, which has been used to perform simulations of actual or ideal events, using the T-bridge in Japan as a case study.

The results obtained from the simulation of a real event show an excellent agreement with the recorded data, both for the evolution in time of the crowd condition along the span and for the maximum value of the lateral displacement of the deck.

The sensitivity studies highlight the capabilities of the proposed approach to evaluate the effects of various physical parameters on the crowd dynamics and structural response. The structural response is particularly sensitive to the crowd travel purpose and geographic area. Hence, in the conceptual design phase, it is important to plan the kind of pedestrian traffic that the footbridge is most likely to incur during its lifetime.

The sensitivity study on the crowd density has shown that a more crowded condition does not always correspond to higher deck vibrations, due to the effects of the crowd added mass, which changes the dynamical properties of the footbridge and modifies the f_r ratio. Simplified comfort criteria, based on the limitation of the number of pedestrians crossing the bridge, might not always be effective in preventing the synchronous lateral excitation phenomenon. However, the complexity of the phenomenon makes it difficult to conceive compact comfort criteria which can take into account all features involved.

PART II
Analysis of the separated flow around a benchmark deck section profile
through computational simulation

4.8 INTRODUCTION

The aerodynamic behaviour of rectangular cylinders has attracted the attention of the scientific community since the experimental reference works of [v] and [w]. On one hand, both the two dimensional (2D) and three dimensional (3D) features of the low-Reynolds number flow around rectangular cylinders has been clarified in several studies, e.g. in [x]. On the other hand, the high-Reynolds number flow (i.e. Re $\geq$ 1. 10^4) has been studied by means of both experimental and computational approaches, with emphasis on its dependence on the chord-to-depth ratio, e.g. in [y, z, aa].

Recently, a Benchmark on the Aerodynamics of a Rectangular Cylinder (BARC) has been proposed in order to provide a contribution to the analysis of the high-Reynolds number, turbulent, separated flow around a fixed sharp-edged rectangular cylinder with chord-to-depth ratio $B/D = 5$ [v]. For this benchmark, the depth-based Reynolds number has to be in the range 2. $10^4 \leq Re_D \leq 6$. 10^4, the oncoming flow has to be set parallel to the base of the rectangle ($\alpha = 0$) and the maximum intensity of the longitudinal component of turbulence has to be $I_u = 0.0$. In spite of the simple geometry, it is believed that the problem could be of interest not only for fundamental research purposes, but also to provide useful information on the bridge deck aerodynamics. In the perspective of the BARC benchmark, an exploratory computational study has been performed within the research project to preliminary check the benchmark requests for computational, to provide a phenomenological interpretation of the simulated flow and to point out some remaining difficulties and unclear aspects in the problem. In particular, the present work focuses on three main aspects:

1. the comparison among the large amount of results provided in literature is a difficult task because the experimental and computational set-ups are heterogeneous and not fully described and because only integral aerodynamics parameters are often provided. In this study, the obtained aerodynamic coefficients are compared with some results in literature [aa, z] in order to roughly assess the reliability of the adopted approach;

2. the evaluation of the 3D features of the flow around nominally 2D bluff cylinders remains an inescapable task also even for elongated rectangular sections. Apart from the span-wise correlation coefficient and the coherence spectral function, which are generally employed for long cylinders, the Proper Orthogonal Decomposition (POD) methodology is being adopted more and more for the analysis and synthesis of random flow fields in bluff body aerodynamics applications. An application to rectangular cylinders has been proposed by Liaw [dd] using the pressure database obtained from 2D computational simulations. The POD application proposed in the present study extends the Liaw's post processing to the fluctuating pressure on the 2D lateral surface of the cylinder in order to discuss the field spanwise features;

3. finally, according to the authors, some difficulties remain in describing the expected complex flow phenomena around the cylinder and in relating such phenomena to the fluctuating aerodynamic forces acting on the cylinder itself. The present result analysis is addressed to point out the main 2D flow structures, to propose a mapping of the cylinder side surface based on the flow structures above, to establish relationships between the instantaneous vortical structures, the pressure field and the aerodynamic forces.

4.9   FLOW MODELLING AND COMPUTATIONAL APPROACH

The 3D, turbulent, unsteady flow around the cylinder is modelled in the frame of the Large Eddy Simulation approach to turbulence using the classical time-dependent filtered Navier-Stokes equations

$$\frac{\partial \overline{u_i}}{\partial x_i} = 0, \tag{4.10}$$

$$\frac{\partial \overline{u_i}}{\partial t} + \frac{\partial \overline{u_i u_j}}{\partial x_j} = -\frac{1}{\rho}\frac{\partial \overline{p}}{\partial x_i} + \frac{\partial}{\partial x_j}\left[\nu\left(\frac{\partial \overline{u_i}}{\partial x_j} + \frac{\partial \overline{u_j}}{\partial x_i}\right) + \tau_{ij}^s\right], \tag{4.11}$$

where x and t are the space and time coordinates, $\overline{u}$ and $\overline{p}$ are the filtered velocity and pressure, ν is the kinematic viscosity and ρ the fluid density. The sub-grid stress tensor is expressed according to Boussinesq's assumption as

$$\tau_{ij}^s = \nu_t\left(\frac{\partial \overline{u_i}}{\partial x_j} + \frac{\partial \overline{u_j}}{\partial x_i}\right) = \nu_t 2\overline{S_{ij}}, \tag{4.12}$$

so that the equation system can be closed by a transport equation for the kinetic energy k_t of the unresolved stresses [ee]

$$\frac{\partial k_t}{\partial t} + \frac{\partial}{\partial x_j}\left(\overline{u_j}k_t\right) = \frac{\partial}{\partial x_j}\left[(\nu + \nu_t)\frac{\partial \overline{k_t}}{\partial x_j}\right] + P_k - C_\varepsilon\frac{k_t^{3/2}}{l_\varepsilon}, \tag{4.13}$$

where $P_k = 2\nu_t\overline{S_{ij}}\,\overline{S_{ij}}$, $\nu_t = C_k l_k k_t^{1/2}$, the constants are set equal to $C_\varepsilon = 1.05$, $C_k = 0.07$ and $l_\varepsilon = l_k = \Delta$, where Δ is the characteristic spatial length of the filter, related to the mesh size and defined as the cubic root of the mesh cell volume. The modelling of the flow in the turbulent boundary layer is accomplished by introducing a filter width δ damped according to the Van Driest approach:

$$\delta = \min\left\{\Delta, \frac{k}{C_\Delta}y\left(1 - \exp\left(-\frac{y^+}{A^+}\right)\right)\right\} \tag{4.14}$$

where $k = 0.4187$ is the Von Karman constant, $C_\Delta = 0.158$, $A^+ = 26$ is the Van Driest constant, y the distance to the wall, $y^+ = u_\tau y/\nu$ the non dimensional wall unit and u_τ the shear velocity [ee]. In other terms, the characteristic spatial length of the filter in the turbulent boundary layer is not necessarily related to the mesh size, but the minimum value between Δ and the one obtained from the damping function in Eq. 4.14 is locally adopted in space and time.

The computational domain and the boundary conditions (b.c.) are shown in Figure 4.11(a). The spanwise length of the domain is set equal to $L/B = 1$ on the basis of a short review of past LES simulations applied to elongated, reattached-type rectangular cross-sections: the adopted spanwise length in [z] ($B/D = 4$) is equal to $L/B = 0.5$ and equal to $L/B = 1$ in [gg] ($B/D = 5$). Dirichlet b.c. on the velocity field and on the sub-grid kinetic energy k_t are imposed at the inlet boundaries. Neumann b.c. on the normal component of the stress tensor **T** and on k_t are imposed at the outlet boundaries. Periodic b.c. are imposed on both the side surfaces and on the upper-lower surfaces. No-slip b.c. are imposed at the section surface. The initial conditions are obtained from a previous

LES simulation carried on one non-dimensional time unit, where the standard Smagorinsky sub-grid model [hh] has been employed.
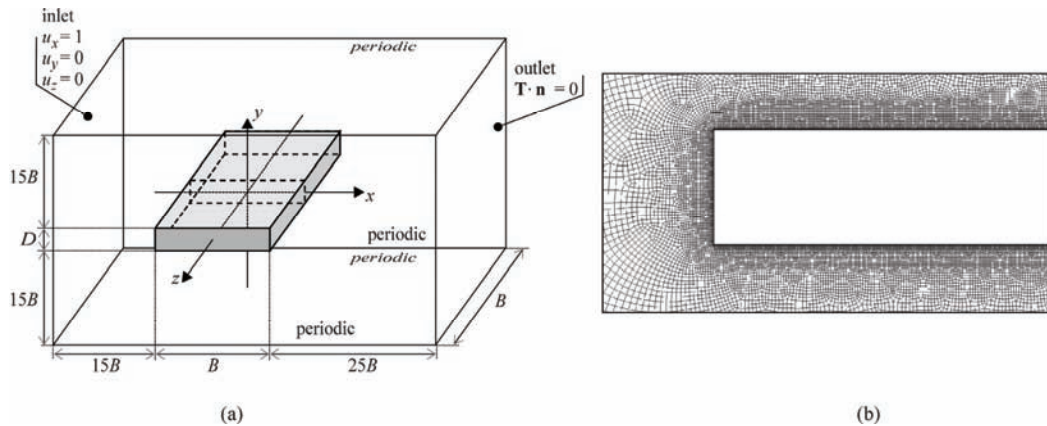
Figure 4.11 Computational domain and b.c. (a), computational grid in the x-y plane around the leading edge (b)

The OpenFoam® Finite Volume open source code is used in the following to numerically evaluate the flow-field. The cell-centre values of the variables are interpolated at face locations using the second-order Central Difference Scheme for the diffusive terms. The convection terms are discretised by means of the so-called Limited Linear scheme, a 2nd order accurate bounded Total Variational Diminishing (TVD) scheme resulting from the application of the Sweby limiter [ii] to the central differencing. The advancement in time is accomplished by the implicit two-step second order Backward Differentiation Formulae (BDF) method. The pressure-velocity coupling is achieved by means of the pressure-implicit PISO algorithm.

A hexahedral grid is adopted to discretise the spatial computational domain. The grid is hybrid in the x-y plane and structured along the spanwise direction z. The grid in the x-y plane around the leading edge is shown in Figure 4.11(b). A body-fitted, structured grid layer is generated at the wall, (near wall cell thickness $\Delta y/B = 5.0\ 10^{-4}$, 6 cells in the grid layer, expansion ratio equal to 1.05). The constant discretization step along the cylinder wall is $\Delta x/B = 2.0\ 10^{-3}$. An unstructured quadrilateral grid is used in the remaining part of the x-y plane. The 3D grid is obtained by the structured projection of the 2D hybrid grid along the spanwise direction z, where 24 cells are employed to uniformly discretise the domain length. Sensitivity studies on the grid density in the spanwise dimension could be of interest during the BARC benchmark activity, as recently undertaken by [jj]. The resulting overall number of cells is about $1.75\ 10^6$. The time is nondimensionalised by U and D, where U is the free stream velocity. The non-dimensional time-step is set equal to $\Delta t = 5\ 10^{-3}$. The simulation is extended over $T = 800$ non dimensional time units in order to have a long enough statistical sample to obtain converged statistics, disregarding the initial transient solution. Computations are carried out on 8 Intel Quadcore X5355 2.66GHz CPUs and require about 2.5GB of RAM memory and 15 days of CPU time for the whole simulation.

4.10   APPLICATION AND RESULTS

The incoming flow is characterised by a Reynolds number Re = UD/v = 4.e+4, an incidence $\alpha = 0$ and a turbulence intensity $I_u = 0\%$ (ideal smooth flow). The cylinder cross section is characterised by sharp edges and smooth surfaces.

4.10.1 Integral parameters

The main aerodynamic integral parameters are analysed in order to roughly place the present results in the large number of data available in literature about pressure forces and wake frequencies for this aspect ratio. More accurate and point-wise comparisons are hard to propose at present because of the incomplete information about the experimental or computational set-up in each study. The mean value and the standard deviation of the drag $C_D = F_D/(1/2 \; \rho U D)$ and lift coefficient $C_L = F_L/(1/2 \; \rho U D)$ are retained. The Strouhal number $St = f_1 D/U$ is evaluated from the heuristic analysis of the lift spectrum, where f_1 is the dominant frequency.

The extent of the sampling window is a key and critical element for the extraction of meaningful statistical parameters in the CFD approach, due to the computational costs involved in long physical time simulations. Herein, the transient solution, due to the initial conditions, approximately covers the first 150 non dimensional time units, which are discarded. In order to optimise the sampling extent during the stationary regime, the convergence of the mean values and standard deviations of the drag and lift coefficients have been checked, as for the Strouhal number, for increasing extents of the sampling window. A non dimensional sampling extent $T_s \geq 400$ has been found to be required to avoid a residual larger than 5% in the statistical first moments. In the following, $T_s = 500$ is retained, which corresponds to around 60 vortex-shedding periods.

Figure 4.12 compares the present results with experimental and computational data collected in [aa] and with the results obtained in [z].
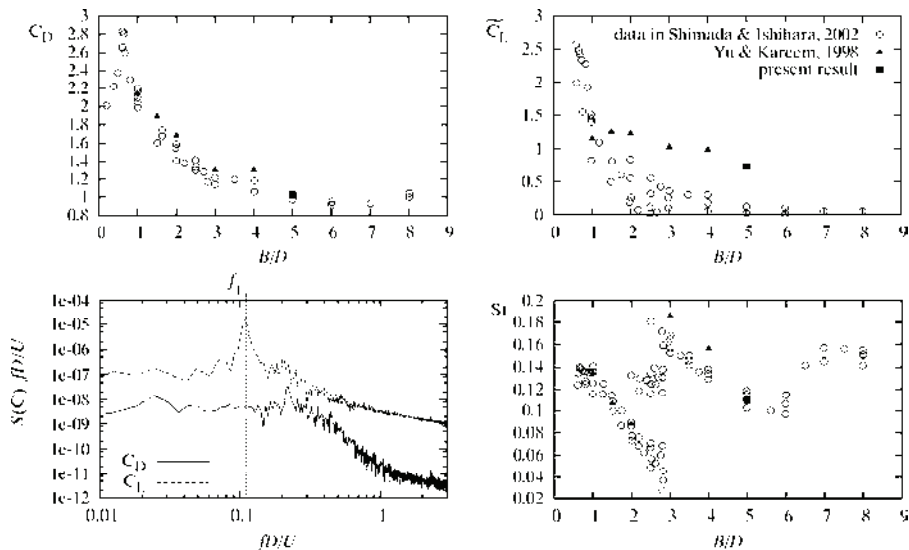
Figure 4.12 Mean drag and rms lift coefficients, Strouhal number: comparison with results from literature

The obtained mean drag coefficient $\overline{C}_D$ and St number are in good agreement with the other data obtained at the same chord-to-depth ratio and they are in accordance with the general parameter trend versus the B/D ratio. Some results from literature concerning the standard deviation of the lift coefficient show a significant scatter: in particular, the higher the B/D ratio, the higher the differences among the results. The reasons for the above mentioned scatter are not completely clear: the expected parameter sensitivity to physical incoming flow conditions (e.g. Re number, turbulence intensity and integral length scale), experimental set-up conditions and/or computational model components (e.g. turbulence modelling, numerical approaches) could be systemati-

cally addressed in future research. For now, it can be noticed that the present 3D LES result is in agreement with the trend obtained by [z], using the same approach, while [aa] pointed out a significant underestimation of the fluctuating force components in most of the RANS models.

4.10.2 3D flow features

The main aim of this section is to evaluate whether 3D flow features exist around a nominally 2D rectangular cylinder and in which way they contribute to the overall flow dynamics. Figure 4.13 shows the instantaneous vorticity field around the obstacle.
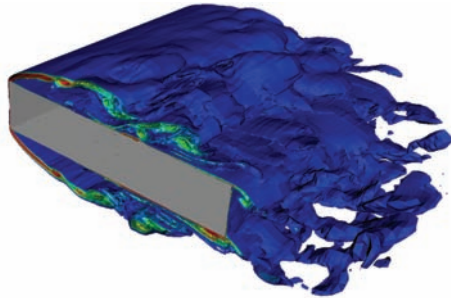
Figure 4.13   3D instantaneous vorticity magnitude iso-surface ($\omega \geq 20$)

From a qualitative point of view, 3D flow structures clearly appear even though the flow field 2D main features hold. Generally speaking, the further the location from the separation point at the leading edge, the more significant the 3D features of the flow structures. In particular, the flow seems almost 2D just downstream the separation point, while the wake structure is clearly 3D.

The fluctuating pressure on the upper side surface of the cylinder is analysed through the POD methodology in order to quantitatively evaluate the field spanwise features.
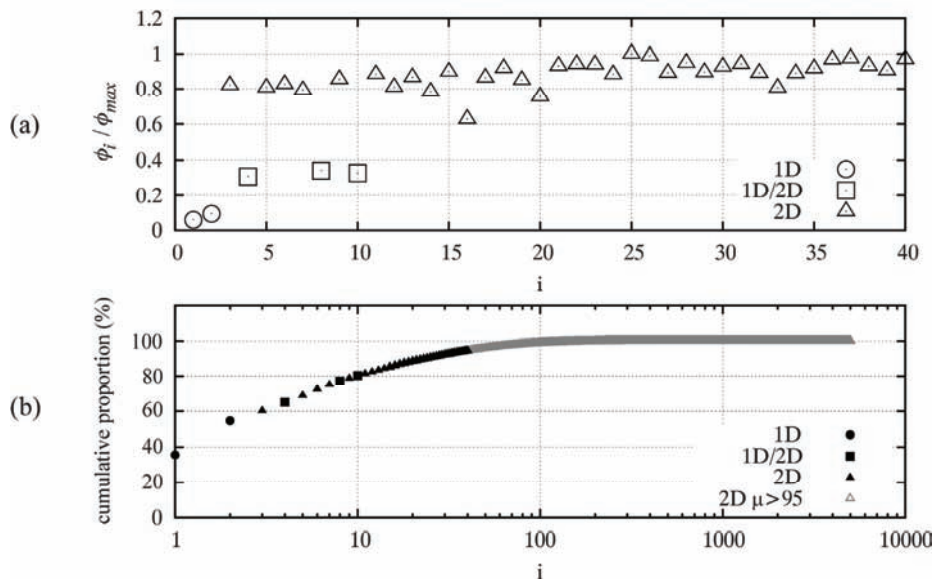
Figure 4.14   POD analysis: (a) eigenvector 2D indicator and (b) eigenvalue cumulative proportion

The analysis employs the pressure results stored in every grid points on the upper side surface of the obstacle. The non dimensional sampling time is equal to $\Delta t_{POD} = 2.5 \ 10^{-2}$, the non dimensional sampling window is equal to $T_{POD} = 500$. In what follow, pressure modes which are nearly constant along the z direction are labelled as "1D", while the modes which show variability along both the x and z directions are labelled as "2D": they reflect the 2D and 3D features on the flow field around the surface, respectively. A 2D indicator is proposed for the i-th eigenvector $\Phi_i(x,z)$, in order to assess the 1D/2D nature of each mode in a compact form, as the along-x average of the along-z standard deviation $\phi_i = mean_x (std_z (\Phi_i))$. Figure 4.14(a) graphs the ratio ϕ_i / ϕ_{max} for $1 \leq i \leq 40$. Very low values of the ratio $\phi_i / \phi_{max} \leq 0.1$ result from the first two modes which can therefore be considered as mainly 1D. The 4th, 8th and 10th eigenvectors show intermediate ϕ values ($0.3 \leq \phi_i / \phi_{max} \leq 0.4$), and cannot therefore be ascribed to either the 1D or to the 2D ones. Finally, the other eigenvectors show high values of the ratio $\phi_i / \phi_{max} \geq 0.6$, having significant 2D trends.

The cumulative eigenvalue proportion is plotted in Figure 4.14(b), where each mode is once more classified according to its prevailing 1D or 2D feature. The overall 1D mode contribution is equal to 54.7%, where the 1st mode contributes 35.63% and the 2nd mode 19%. The 1D/2D modes contribute 8.2%, while the 2D ones contribute 37.1%. It is worth pointing out that the cumulative proportion up to the 40th mode is 95%, while there is a total of 5000 modes. This means that about 0.8% of the modes can reproduce a relatively detailed structure of the wind pressure fluctuations acting on each point of the side surface within an error of around 5%.

4.10.3 2D flow features

In order to focus on the 2D flow phenomena that mainly affect the aerodynamic behaviour of the cylinder, the main mean flow structures are pointed out and discussed first. Some unclear aspects of the mean flow downstream the separation point are clarified by analysing the flow dynamics in the same zone. Second, some 2D instantaneous flow fields around the whole cylinder section are sampled to point out some of the main mechanisms that are responsible for the fluctuating pressure and the aerodynamic force variation. The topology of the mean flow around the obstacle is shown in Figure 4.15: the streamlines obtained from the velocity field averaged in time and along the spanwise dimension are plotted in the upper part of the figure, while a synthetic scheme of the recognised mean flow structures is proposed in the lower part.
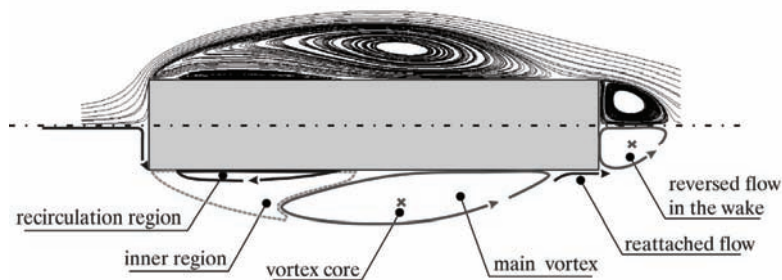
Figure 4.15 Streamlines averaged in time and along the spanwise dimension (above) and scheme of the recognised mean flow structures (below)

The mean flow separates at the leading edge and reattaches just upstream the trailing edge, while the reversed flow in the wake approximatively extends along 0.76D. The main vortex shows an inclined major axis, while a thin recirculation region is clearly visible close to the lateral wall, between the main vortex and the separation point, without reaching the latter. In a large flow

region between the main vortex and the recirculation region, called herein "inner region", no mean structures can be easily recognised.

The mean wall shear stress coefficient $\overline{Cf}$ distribution on the lower half perimeter is plotted in Figure 4.16 and ascribed to the mean flow structures discussed above.
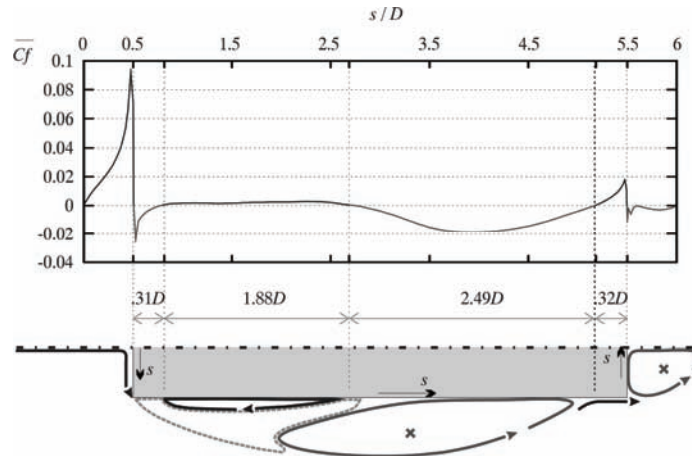
**Figure 4.16**   Recognised mean flow structures and mean friction coefficient distribution

On one hand, the changes in sign of $\overline{Cf}$ permit the *x*-length of these structures to be measured. In particular, the distance of the reattachment point from the separation one is equal to $x_R/B = 0.933$, which is larger than the one estimated by [cc] based on the distributions of the time-averaged pressure coefficient and rms value ($x_R/B = 7/8$). This slight discrepancy can be ascribed to the adopted different identification methods, but another possible explanation can be found looking at the difference between the present incoming flow conditions (ideal smooth flow) and the experimental ones affected by wind tunnel residual incoming turbulence [kk]. Deeper sensitivity studies would be required to verify this hypothesis. On the other hand, the Cf distribution allows to shed some light into the "inner region" flow. In fact, the clockwise recirculation region involves positive $\overline{Cf}$ values, while negative ones are located just downstream the separation point up to the recirculation region. According to the authors, this second interval cannot be directly ascribed to an upwind extension of the main vortex, but could correspond to other counterclockwise flow structures. Bearing in mind that the flow is mainly 2D along the inner region (Figure 4.13), time-averaging is supposed to partially hide the instantaneous structures which take place in this region during the vortex growth and shedding. In order to verify this hypothesis, the dynamics of the local flow downstream the separation point is analysed in the following. Figure 4.17 shows the instantaneous pathlines in this region. Some recognised clockwise and counterclockwise vortices are sketched. Dashed lines joint the vortex centre in successive times. The sequence mainly takes into exam the shedding process of three vortices (v_1, v_2, v_3) and the related flow structures. Grey dash-dot lines refers to vortices successively shed. The qualitative exam of the sequence does not aim to provide the rigorous measure of the flow structures, but to contribute to understanding the essential physics of the local flow. The vortices are not shed from the separation point, but from the apex of a pseudo-triangular region just downstream it (outlined for instance by dash lines at times since 787.25 to 788.50) which includes a sort of elongated clockwise "bubble" in the shear layer just downstream separation together with a secondary counterclockwise vortex close to the surface, caused by the velocity field induced by the growing vortex.
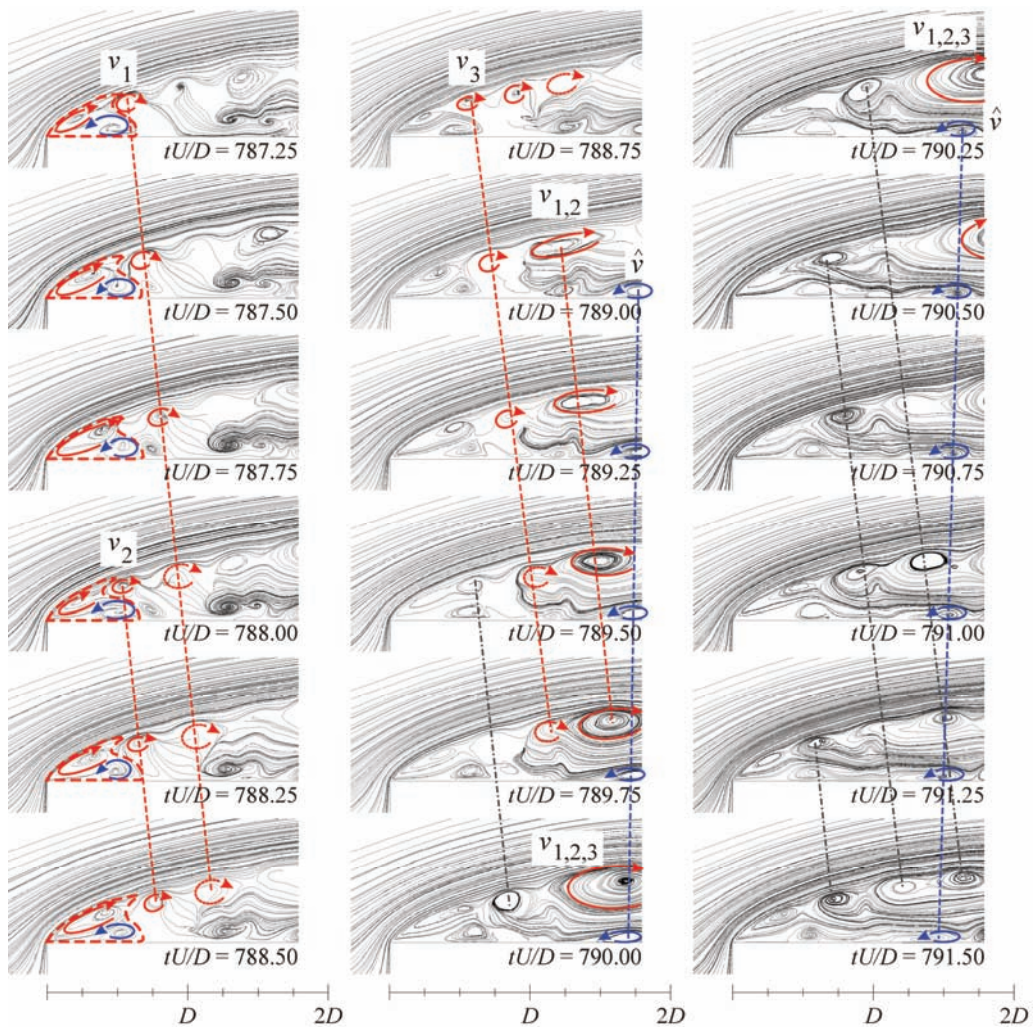
Figure 4.17 Vortex shedding from the pseudo-triangular region and coalescence

The pseudo-triangular region remains substantially attached to the body during the shedding cycle, even if it oscillates and its geometry changes: the secondary vortex is nearly constant in time and space, while the "bubble" slightly pulsates attaining its maximum and minimum elongation just before and after the vortex shedding, respectively. These structures, which characterise the simulated fully-developed flow downstream the separation point, recall the ones first recognised by Pullin and Perry [ll] in the transient flow involved by a starting vortex past a 90° edge. The simulated instantaneous flow pattern at the first sampling time (tU/D = 787.25) is compared with one of the flow visualisations proposed by Pullin and Perry in Figure 4.18. Despite the differences between the overall flow conditions, the clear analogy seems to confirm the research perspectives expressed by Buresti [mm]: "[...] it is reasonable to infer that many of the features observed in the transient flow field around the wedge, induced by increasing the upstream velocity, may be qualitatively similar to those occurring near a bluff body separation point during the roll up of a forming vortex". In other terms, the pseudo-triangular region seems to be a case-insensitive, basic flow structure in bluff-body aerodynamics, even if its "extent is a function of the

body shape, and in particular of the afterbody" [mm]. In the present case-study, the pseudo-triangular region spans over about $5/8D$ from the separation point.
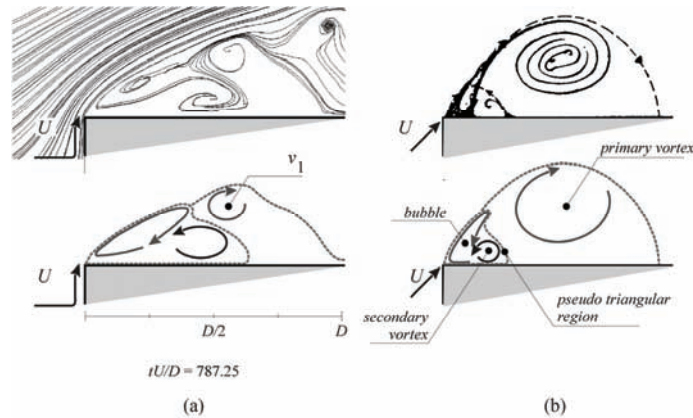
Figure 4.18 Present study instantaneous pathlines (a) and instantaneous streaklines after [ll] (b)

The primary vortex shedding period is equal to about 0.75 non dimensional time unit and it is convected along the wall with a velocity estimated around $0.48U$. At $tU/D = 788.75$, three primary vortices (v_1, v_2, v_3) successively shed from the apex are travelling along the side surface. During the following non-dimensional time unit (second column in Figure 4.17), they successively coalesce in a single vortex ($v_{1,2,3}$, $tU/D = 790.00$). The resulting vortex induces a secondary counter-clockwise vortex $\hat{v}$ close to the side surface. Unlike the nearly-constant secondary vortex included in the pseudo-triangular region, the vortex $\hat{v}$ is convected upstream by the velocity field induced by the main vortex with a velocity estimated around $0.14U$.

Once the mean field along the side surface and the instantaneous field downstream the separation point have been discussed, Figure 4.19(a) makes an attempt to relate them: the instantaneous pathlines refer to the sampled time at which the maximum number of primary vortices (v_1, v_2, v_3) are present at the same time past the pseudo-triangular region ($tU/D = 788.75$); the recognised instantaneous structures in the mean inner region are plotted with continuous lines, while the mean structures are drawn with dashed lines. It follows that the mean inner region can be viewed as the one which contains the pseudo-triangular region, the primary vortices shed from it and the secondary counter-clockwise vortices $\hat{v}$ induced by the large vortex resulting from the coalescence of the primary vortices. In particular, the mean recirculation region results from the contribution of several instantaneous vortices, namely the steady one included in the pseudo-triangular region and the ones convected upstream. Figures 4.19(b)-(d) graph the distributions of the pressure mean value, standard deviation and skewness, respectively. Both the recognised flow structures and the pressure distributions allow to propose a physical-based guess mapping of the lateral surface. The mapping results from four recognised zones, whose extent is roughly evaluated at the external boundary of the separating shear flow: they are named, quoted and graphically represented with grey patterns in Figure 4.19. It is worth stressing that the rigorous identification of the x-length of these zones, even though possible, is not the scope of this work, while approximate but phenomenon-based lengths have been preferred to make a guess at the relationship between the fluid flow phenomena and the aerodynamic forces. The "vortex shedding" (vs) region is defined as the x-distance from the separation point to the apex of the mean inner region: it contains the instantaneous primary vortices shed by the pseudo-triangular region and it is characterised by a $\overline{Cp}$ plateau and low $\widetilde{Cp}$ values. The main vortex x-length is split into two zones in order to distinguish

the part of the side surface where the coalescence of the primary vortices takes place and the one where the instantaneous reattachment occurs: the watershed point between these regions is obtained not only by looking at the point where the vortex-induced reversed flow close to the wall has a non null vertical component, but also remembering the critical aspect ratio $B/D \approx 3$ that distinguishes separated-type and reattached-type rectangular sections.
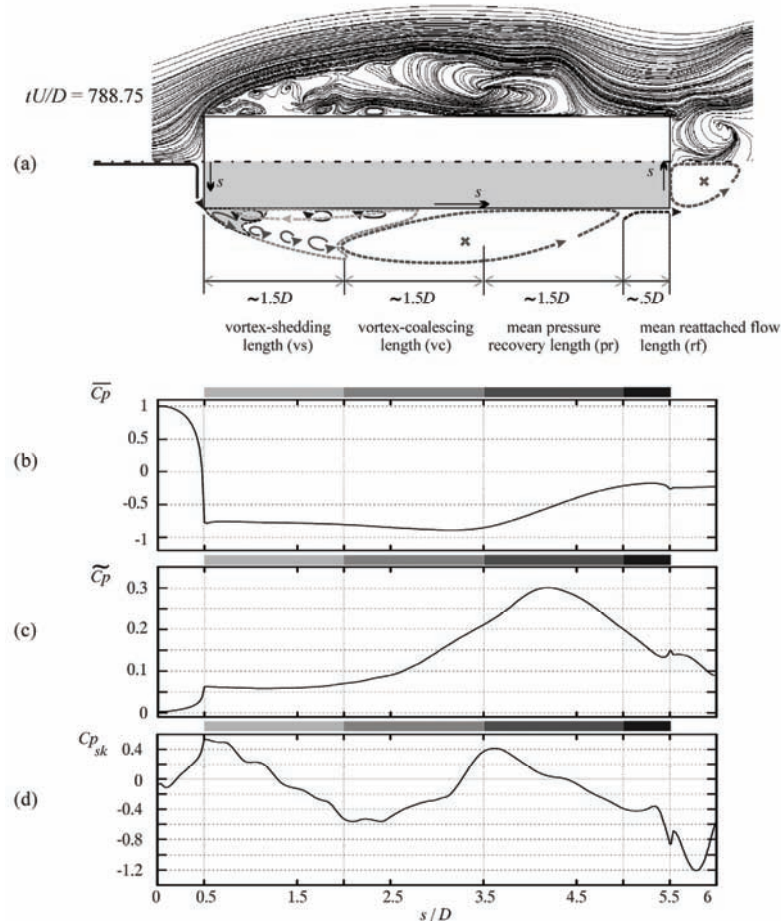
Figure 4.19 Instantaneous pathlines, flow structures and lateral surface mapping (a), pressure coefficient distributions along the central section (b-d)

The "vortex-coalescing" (*vc*) zone shows the maximum value of the mean suction and a steep increase of the fluctuating component, while the mean "pressure recovery" gives the name to the second region (*pr*), where the maximum rms value also occurs. The "mean reattachment flow" (*rf*) region is regained from above and it is characterised by another $\overline{Cp}$ plateau. Finally, it is worth pointing out that the longest lengths show a change in sign of the pressure skewness and that the bound of each length corresponds to its relative maximum or minimum values. Although deeper studies are needed to interpret this evidence, the features of the Cp_{sk} distribution seems to confirm the significance of the selected zones. The same partition of the side-surface applies to the spectral content of the pressure signals: a window of the *Cp* time histories at the mid point of each length and the normalised PSDs along the side surface are plotted in Figure 4.20. The pres-

sure fluctuations in the *vs* and *pr* lengths are mainly characterised by one frequency component, which corresponds to the prevailing frequency in the lift coefficient (*St* number).
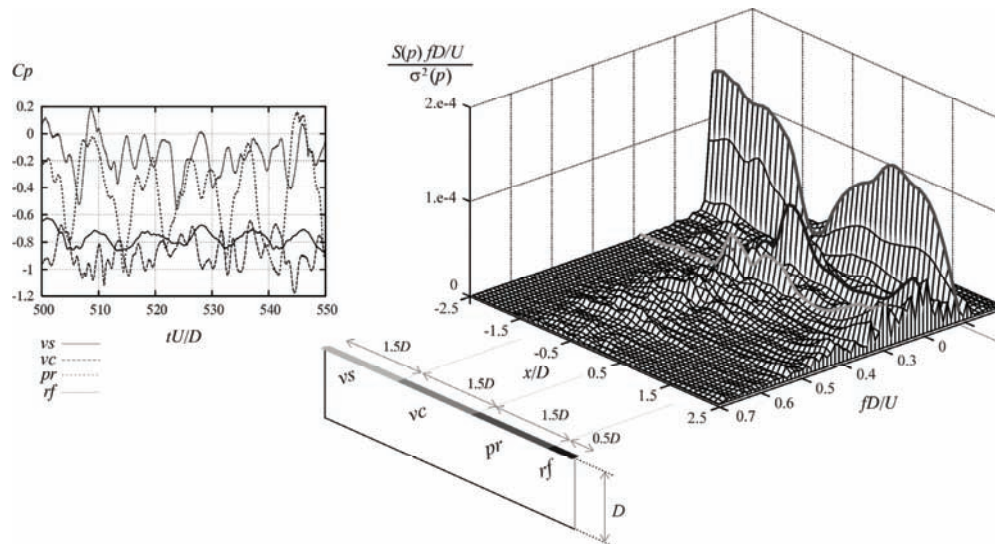
Figure 4.20   Pressure time histories and Power Spectral Density along the upper side surface

On the contrary, the points in the *vc* and *rf* lengths show a broad band spectrum, where the most significant frequencies are higher than *St*. The largest pressure fluctuations along the *pr* length (Figure 4.19(c)) and its narrow spectral content close to *St* (Figure 4.20) seem to suggest that this region contributes to the lift fluctuation component to the greatest extent. This is in agreement with the conclusions drawn by [cc]. In order to verify this hypothesis, Figure 4.21 gives an example of the attempt made to relate the instantaneous lift coefficient $C_L(t)$ to the in-stantaneous flow field, described by the vorticity magnitude contours around the central section and by the pressure distribution along the four regions in which the side surfaces have been parti-tioned. Four instants, corresponding to null, maximum, null and minimum values of the lift coef-ficient, have been retained for sampling. The (+) sign in the instantaneous vorticity magnitude fields corresponds to counter-clockwise eddies, while the (-) sign refers to clockwise ones. The suction peaks in the *Cp* distributions clearly correspond to the travelling vortices alternatively shed from the leading-edge and convected along the side surfaces. In spite of their magnitude, the suctions at the upper and lower side surfaces approximately cancel each other, and no significant effects on the net lift force arise. Positive pressure is recovered along part of the *pr* lengths at the lower and upper side surfaces and it involves the maximum and minimum lift values, respec-tively. This positive pressure recovery takes place at the time in which a new vortex is shed from the *vs* length and the previous one is already convected in the wake. In other words, the instanta-neous pressure recovery grows in the time and space domains in between two consecutive vor-tices shed from the leading edge. At the same time, the *pr* length along the opposite side surface is submitted to a deep suction due to the vortex travelling along it. Hence, the pressure resultant forces at the upper and lower *pr* lengths do not cancel each other as they have the same direction. The pressure-induced net lift force acting on the *pr* length predominates over the contribution of the other regions to the overall lift acting on the whole section, as Figure 4.22 demonstrates. Nev-ertheless, it is important to point out that the described mechanism is not the sole responsible for the aerodynamic behaviour of the cylinder: according to the authors, further analysis would be re-

quired to identify complementary flow phenomena and to order them according to their contribution to the overall aerodynamic behaviour.
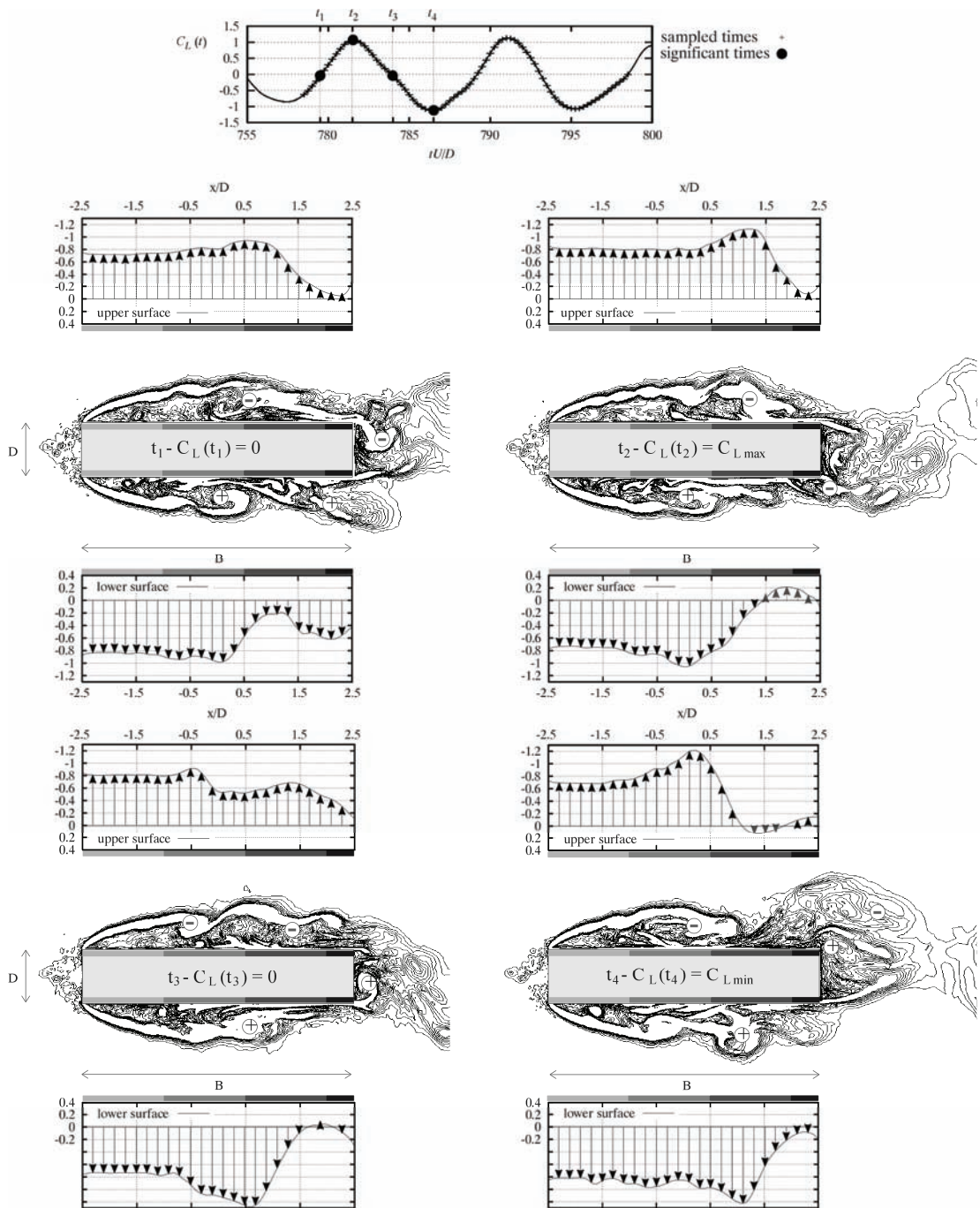
Figure 4.21 Instantaneous vorticity fields and pressure distributions along a vortex-shedding period
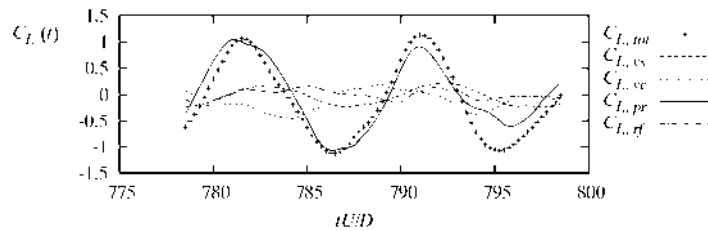
Figure 4.22 Net lift components expressed by the identified lengths

4.11 CONCLUDING REMARKS

A computational study has been proposed in this work to analyse some flow features of the high Reynolds number, turbulent, separated and reattached flow around a fixed rectangular cylinder with chord-to-depth ratio equal to 5.

Some partial conclusions can be made: the overall simulated aerodynamic behaviour seems to agree well with the results in literature, even though the latter are sometimes scattered; the POD analysis shows that, even though the 3D flow features are not negligible, the main phenomena which drive the aerodynamic forces remain 2D; the computational approach postprocessing facilities have been employed to shed some light on the relationships between the vortex shedding and convection mechanisms, the instantaneous pressure field and the aerodynamic forces.

Further studies are required to check the present proposal, to complete the knowledge of the main fluid flow phenomena which drive the section aerodynamics and to provide a complete database for validation and comparison purposes. In this perspective, the newborn BARC benchmark could offer an useful research framework to the scientific community adopting both computational and experimental approaches.

4.12 BASIC REFERENCES

PART I

[a]   Fujino Y., Pacheco B.M. , Nakamura S., Warnitchai P. 1993. Synchronisation of Human Walking Observed during Lateral Vibration of a Congested Pedestrian Bridge. *Earthquake Eng. Struct. Dyn*. 22, 741-758.

[b]   Dallard P., Fitzpatrick T., Flint A., Le Bourva S., Low A., Ridsdill R. M., Willford M. 2001. The London Millennium Footbridge. *The Structural Engineer* 79, 22, 17-33

[c]   Živanovic S., Pavic A., Reynolds P. 2005. Vibration serviceability of footbridges under human-induced excitation: a literature review. *J. Sound Vib*. 279, 1-74.

[d]   FIB Federation International du Beton. 2006. *Guidelines for the design of footbridges*, FIB Bulletin No. 32, Lausanne.

[e]   SETRA/AFGC. 2006. *Passerelles piétonnes – Evaluation du comportement vibratoire sous l'action de piétons. Guide méthodologique.* Paris.

[f]   Butz C., Feldmann M., Heinemeyer C., Sedlacek G., Chabrolin B., Lemaire A., et al. 2008. *Advanced load models for synchronous pedestrian excitation and optimised design guidelines for steel footbridges (SYNPEX)*, RFS-CR 03019, Research Fund for Coal and Steel.

[g]   Andriacchi T.P., Ogle J.A., Galante J.O. 1997. Walking speed as a basis for normal and abnormal gait measurements. *J. Biomech*., 10, 261-268.

[h]   Pizzimenti A.D. 2005. Experimental evaluation of the dynamic lateral loading of footbridges by walking pedestrians. *Proc. 6th International Conference on Structural Dynamics*, Paris.

[i]   Nakamura S. 2003. Field measurement of lateral vibration on a pedestrian suspension bridge. *The Structural Engineer* 81(22), 22-26.

[j]   Nakamura S., Kawasaki T. 2006. Lateral vibration of footbridges by synchronous walking. *J. Constr. Steel Res.* 62, 1148-1160.

[k]   Venuti F., Bruno L., Bellomo N. 2005. Crowd structure interaction: dynamics modelling and computational simulations. *Proc. 2nd International Conference Footbridge 2005*, Venice.

[l]   Bodgi J., Erlicher S., Argoul P. 2007. Lateral vibration of footbridges under crowd-loading: Continuous crowd modeling approach. *Key Engineering Materials* 347, 685-690.

[m]   Park K.C., Felippa C.A., Farhat C. 1999. *Partitioned analysis of coupled mechanical systems*. Report no. CU-CAS-99-06, University of Colorado.

[n]   Buchmueller S., Weidmann U. 2006. *Parameters of pedestrians, pedestrian traffic and walking facilities*. Ivt Report no. 132, ETH Zurich.

[o]   Fruin J.J. 1997. *Pedestrian planning and design*, Elevator World Inc.

[p]   Seyfried A., Steffen B., Klingsch W., Boltes M. 2005. The fundamental diagram of pedestrian movement revisited. *J. Stat. Mech.* 10.

[q]   Matsumoto Y., Nishioka T., Shiojiri H., Matsuzaki K. 1978. Dynamic design of footbridges. *IABSE Proceedings*. P17/78, 1-15.

[r]   Bertram J.E., Ruina A. 2001. Multiple walking speed-frequency relations are predicted by constrained optimisation. *J. Theor. Biol.* 209, 445-453.

[s]   Leveque R.J. 1992. *Numerical methods for conservation laws*. Birkhauser, Zurich.

[t]   Clough R., Penzien J. 1987. *Dynamics of structures*. McGraw-Hill, New York.

[u]   Nakamura S., Fujino Y. 2002. Lateral vibration on a pedestrian cable-stayed bridge. *Structural Engineering International* 12(4), 295-300.

PART II

[v]   Okajima A. 1982. Strouhal numbers of rectangular cylinders. *J. Fluid Mech.* 123, 379-398.

[w]   Norberg C. 1993. Flow around rectangular cylinders: pressure forces and wake frequencies. *J. Wind Eng. Ind. Aerodyn.* 49, 187-196.

[x]   Tan B.T., Thompson M.C., Hourigan F. 2004. Flow past rectangular cylinders: receptivity to transverse forcing. *J. Fluid Mech.* 515, 33-62.

[y]   Yu D., Kareem A. 1996. Two-dimensional simulation of flow around rectangular prism. *J. Wind Eng. Ind. Aerodyn.* 62, 131-161.

[z]   Yu D., Kareem A., 1998. Parametric study of flow around rectangular prisms using LES. *J. Wind Eng. Ind. Aerodyn.* 77-78, 653-662.

[aa]   Shimada K., Ishihara T., 2002. Application of a modified k-ε model to the prediction of aerodynamic characteristics of rectangular cross-section cylinders. *J. Fluids Struct.* 16, 465-485.

[bb]   Bartoli G., Bruno L., Buresti G., Ricciarelli F., Salvetti M.V., Zasso A. 2008. *BARC Overview Document*. http://www.aniv-iawe.org/barc.

[cc]   Matsumoto M., Shirato H., Aaraki K., Haramura T., Hashimoto T. 2003. Spanwise coherence characreristic of surface pressure field on 2D bluf bodies. *J. Wind Eng. Ind. Aerodyn.* 91, 155-163.

[dd]   Liaw K.F. 2005. *Simulation of Flow around Bluff Bodies and Bridge Deck Sections using CFD*. Ph.D. Thesis, University of Nottingham.

[ee] Yoshizawa A. 1986. Statistical theory for compressible shear flows with the application of subgrid modelling. *Phys. Fluids* 29, 2152-2164.

[ff] De Villiers E. 2006. *The potential of large eddy simulation for the modelling of wall bounded flows.* Ph.D. thesis, Imperial College, London.

[gg] Mannini C., Soda A., Voss R., Schewe G. 2008. Detached-eddy simulation of flow around a 1:5 rectangular cylinder. *Proc. 6th International Colloquium on Bluff Bodies Aerodynamics and Applications,* Milano, Italy.

[hh] Smagorinsky J. 1963. General circulation experiments with the primitive equations. I. The basic experiment. *Monthly Weather Review* 91, 99-164.

[ii] Sweby P. K. 1984. High resolution schemes using flux limiters for hyperbolic conservation laws. *SIAM J. Num. Anal.* 21, 995-1011.

[jj] Mannini C., Weinman K., Soda A., Schewe G. 2009. Three-dimensional numerical simulation of flow around a 1:5 rectangular cylinder. *Proc. 5th European and African Conference on Wind Engineering*, Firenze, Italy.

[kk] Laneville A., Williams C. 1979. The effects of intensity and large scale turbulence on the mean pressure and drag coefficients of 2d rectangular cylinders. *Proc. 5th International Conference on Wind Effects on Building and Structures,* Fort Collins, Colorado.

[ll] Pullin D., Perry A. 1980. Some flow visualization experiments on the starting vortex. *J. Fluid Mech.* 97(2), 239-255.

[mm] Buresti G. 1998. Vortex-shedding from bluff bodies. Chapter 4 in: *Wind Effects on Buildings and Structures*, Balkema, Rotterdam.

4.13   LIST OF PUBLICATIONS

PART I

[1] Venuti F., Bruno L. 2009. Crowd-structure interaction in lively footbridges under synchronous lateral excitation: A literature review. *Physics of Life Reviews* 6, 176-206.

[2] Bruno L., Venuti F. 2009. Crowd-Structure Interaction in footbridges: modelling, application to a real case-study and sensitivity analyses. *J. Sound and Vib*. 323, 475-493.

[3] Venuti F., Bruno L., Bellomo N. 2007. Crowd dynamics on a moving platform: mathematical modelling and application to lively footbridges. *Math. Comput. Modell*. 45, 252-267.

[4] Venuti F., Bruno L. 2007. Pedestrian lateral action on lively footbridges: a new load model. SEI *Struct. Eng. Int.* 17(3), 236-241.

[5] Venuti F., Bruno L. 2007. An interpretative model of the pedestrian fundamental relation. *C.R. Mécanique* 335, 194-200.

[6] Venuti F., Bruno L. 2007. The synchronous lateral excitation phenomenon: modelling framework and application. *C.R. Mécanique* 335, 739-745.

[7] Venuti F., Bruno L. 2008. Pedestrian loads and dynamic performances of lively footbridges: an overview. Keynote Lecture*, Proc. CSHM2 Workshop*, Taormina.

[8] Venuti F., Bruno L. 2008. Synchronous lateral excitation on lively footbridges: modelling and application to the T-bridge in Japan. *Proc. 3rd International Conference Footbridge 2008*, Porto.

[9] Venuti F., Bruno L. 2008. A new load model of the pedestrians lateral action. *Proc. 3rd International Conference Footbridge 2008*, Porto.

[10] Bruno L., Venuti F. 2008. The pedestrian speed-density relation: modelling and application. *Proc. 3rd International Conference Footbridge 2008*, Porto.

[11] Venuti F. 2008. Crowd-Structure Interaction in laterally vibrating footbridges. *Proc. Fib PhD Symposium 2008*, Stuttgart.

PART II

[12] Bruno L., Fransos D., Coste N., Bosco A. 2009. 3D flow around a rectangular cylinder: a computational study. *J. Wind Eng. Ind. Aerodyn.* 98(6-7), 263-276.

[13] Bruno L., Canuto C., Fransos D. 2009. Stochastic aerodynamics and aeroelasticity of a flat plate via generalized Polynomial Chaos. *J. Fluid Struct*. 25, 1158-1176.

[14] Canuto C., Fransos D. 2009. Numerical Solution of Partial Differential Equations in Random Domains: An Application to Wind Engineering. *Commun. Comput. Phys*. 5, 515-531.

[15] Bruno L., Fransos D. 2008. Evaluation of the Reynolds number effects on the flutter derivatives of a flat plate by means of a new computational approach. *J. Fluid Struct*. 24, 1058-1076.

[16] Fransos D., Bruno L. 2006. Determination of the aeroelastic transfer functions for streamlined bodies by means of a Navier-Stokes solver. *Math. Comput. Modell*. 43, 506-529.

[17] Bruno L., Coste N., Fransos D. 2009. Analysis of the separated flow around a 5:1 rectangular cylinder through computational simulation. *Proc. 5th European and African Conf. on Wind Eng.*, Firenze.

[18] Bruno L., Fransos D. 2008. Edge degree-of-sharpness and integral length scale effects on the aerodynamics of a bridge deck. *Proc. BBAA VI International Colloquium*, Milano.

[19] Bruno L., Fransos D., Coste N., Bosco A. 2008. 3D flow around a rectangular cylinder: a computational study. *Proc. BBAA VI International Colloquium*, Milano.

[20] Bruno L., Fransos D. 2008. Aerodynamic regimes of a trapezoidal bridge deck. *Proc. 10th Nat. Conf. on Wind Eng.*, Palermo.

[21] Fransos D., Bruno L. 2008. Stochastic flutter derivatives of a flat plate. *Proc. 10th Nat. Conf. on Wind Eng.*, Palermo.

[22] Fransos D., Bruno L. 2006. Determination of flutter derivatives for streamlined bodies throughout a modified indicial approach by means of CWE: part I – Mathematical and computational modelling, part II – Sensitivity to physical parameters, *Proc. 9th Nat. Conf. on Wind Eng.*, Pescara.

4.14   INTERNATIONAL AWARDS

- 2008: the PhD Thesis "Stochastic Numerical Models for Wind Engineering" – author: D. Fransos, has been selected by AIMETA as the Italian finalist in the ECCOMAS yearly Ph.D. Theses Award.
- 2008: the paper [4] has been recipient of the yearly Outstanding Paper Award, promoted by the International Association for Bridge Structural Engineering.
- September 2008: the communication [11] has been recipient of the second prize at the 7th Ph.D. Symposium in Civil Engineering (Stuttgart, Germany), organized by Fédération Internationale du Béton.
- May 2007: the presentation of Venuti, F. "Crowd – Structure Interaction in Lively Footbridges: Modelling and Simulation" has been recipient of the first prize at the 2nd Young Engineers Symposium (Fribourg, Switzerland), organized by the Swiss national group of the International Association for Bridge Structural Engineering.

5 Synchronisation phenomena and their implications in the design of footbridges

Francesco Ricciardelli
Università Mediterranea di Reggio Calabria

5.1 THE DESIGN OF FOOTBRIDGES AGAINST PEDESTRIAN LOADING

Footbridge response to pedestrian loading is known to be strongly related to the possibility of occurrence of interaction phenomena among the pedestrians and of the pedestrians with the structure. These two types of interaction can be investigated based on the theory of synchronisation of non-linear dynamic systems. The first occurs when a number of pedestrians walk very close to each other, to the point of synchronising their walking frequency and phase, and it is therefore related to some crowd density parameter. The second occurs when the structure vibrates with a sufficiently large amplitude, and at a frequency sufficiently close to the pedestrians natural frequency, such to trigger their gait, and make them all walk at the structural vibration frequency and all with the same phase. This second type of synchronisation is therefore related to the dynamic characteristics of the footbridge. The possibility of occurrence of these two types of synchronisation was illustrated in more detail in [1]. However due to the complicated mathematics and to the difficulty in calibrating the parameters appearing in the models, an approach to the design of footbridges incorporating these two possible synchronised types of behaviour is yet unavailable.

In fact, present design practice in most of the cases neglects the possible occurrence of interaction phenomena, and considers the pedestrians as an external load. Only in a few cases more sophisticated loading patterns have been proposed and applied. Besides the possibility of establishing refined models incorporating possible synchronisation mechanisms, it is clear that the use of simple loading models based on the tools of linear structural dynamics is appealing for the designer, therefore it is of interest to assess their accuracy and to set the limits of their applicability.

In this section results of experiments aimed at defining the charatceristics of walker-footbridge synchronisation and of crowd synchronisation will be presented. In addition, loading models of footbridges will be presented together with their numerical validation.

5.2 EXPERIMENTAL EVALUATION OF GAIT PARAMETERS

An experimental campaign was carried out at the University of Reggio Calabria with the aim of defining the gait characteristics (frequency, stride and speed) and to identify their possible dependency on the physical characteristics of the individuals (age, height, weight). The tests consisted in the measurement of the time and number of steps required to walk a stretch of flat path of 72 m. The sample was made of 124 individuals with an average age of 27 years (STD = 12.6 years), an average height of 169 cm (STD = 11.7 cm), and an average weight of 663 N (STD = 163 N).

From the experiments the walking speed, frequency and amplitude were indirectly derived, and their relationship to the characteristics of the individuals are shown in Figs. 5.1 and 5.2. It was found that there is a minor decrease of the walking frequency with weight (0.0002 Hz/N) and age (0.0012 Hz/year), and a minor decrease of stride length with age (0.03 cm/year), whereas all the other parameters are sensibly independent of each other.
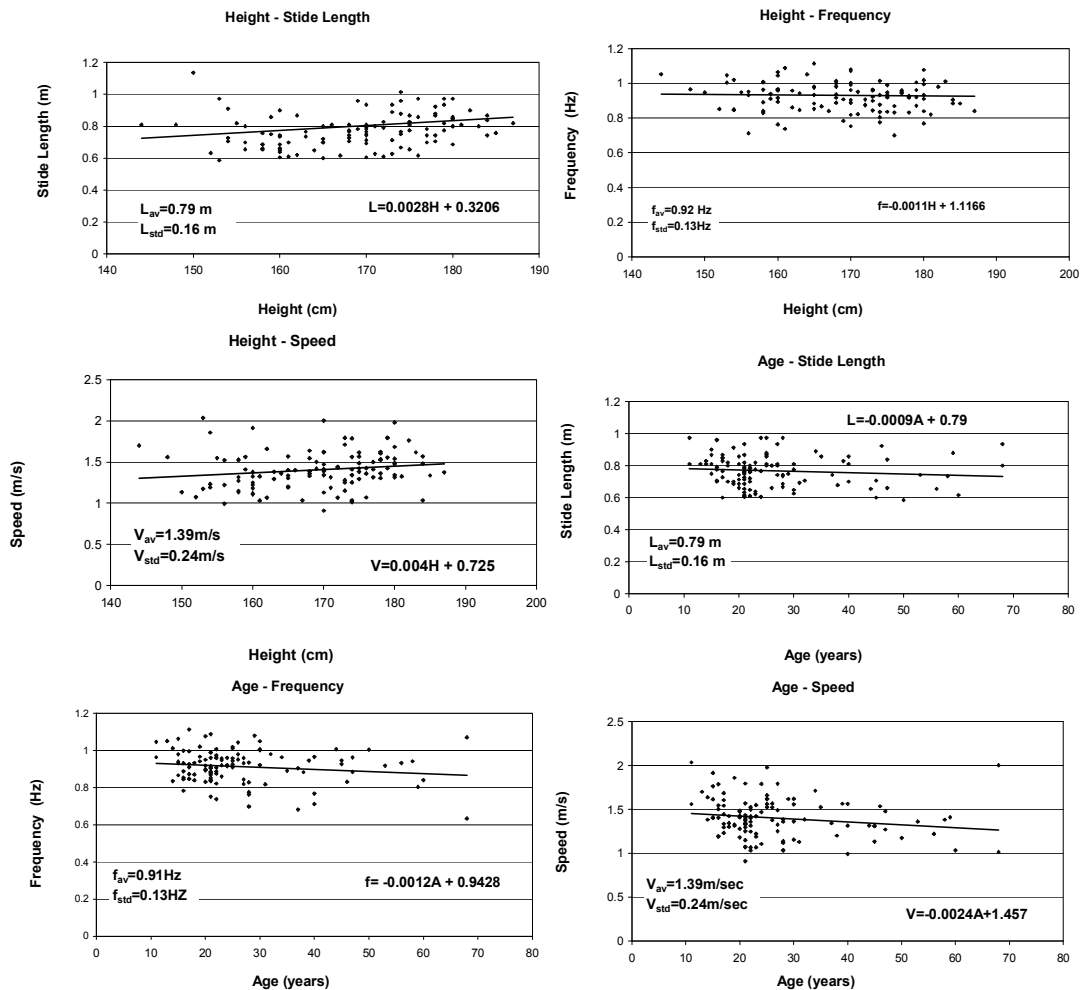
Figure 5.1   Dependency of gait parameters on height and age

Weight - Step size

Weight - Frequency

$L_{av}=0.79$ m
$L_{std}=0.16$ m

$L=0.0002W + 0,6257$

$f_{av}=0.92$ HZ
$f_{std}=0.13$ Hz

$f=-0.0002W + 1.0333$

Weight - Speed

$V_{av}=1.39$ m/s
$V_{std}=0.24$ m/s

• weight-velocity men   ▲ weight-velocity women
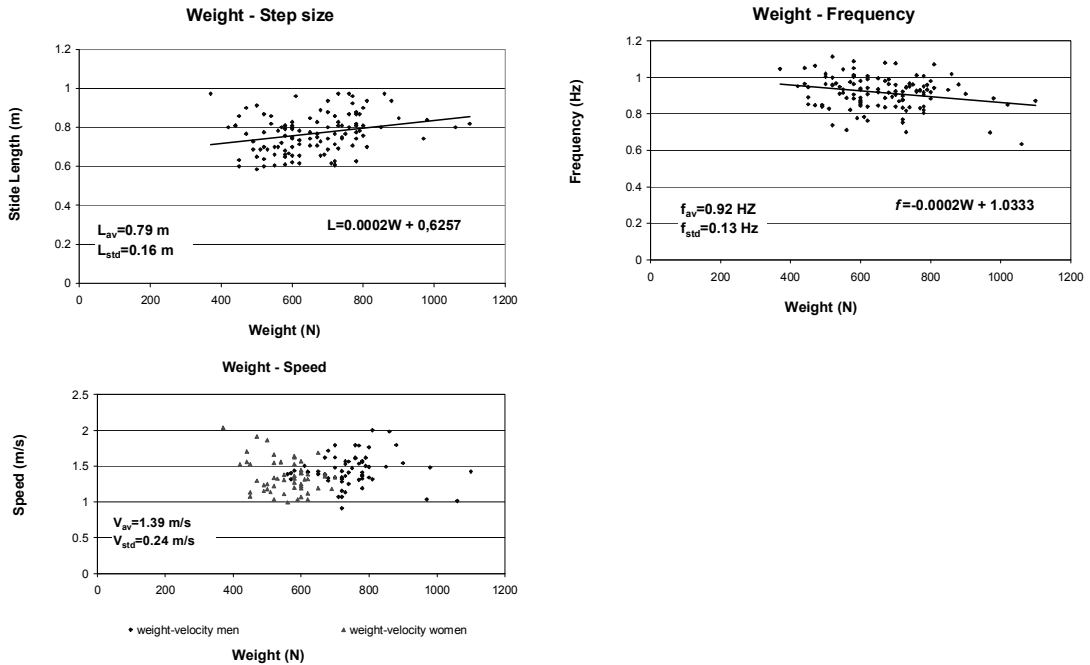
Figure 5.2   Dependency of gait parameters on weight

$L_{av}=0.79$ m
$L_{std}=0.19$ m

$f_{av}=0.92$ Hz
$f_{std}=0.11$ Hz

$V_{av}=1.39$ m/s
$V_{std}=0.23$ m/s
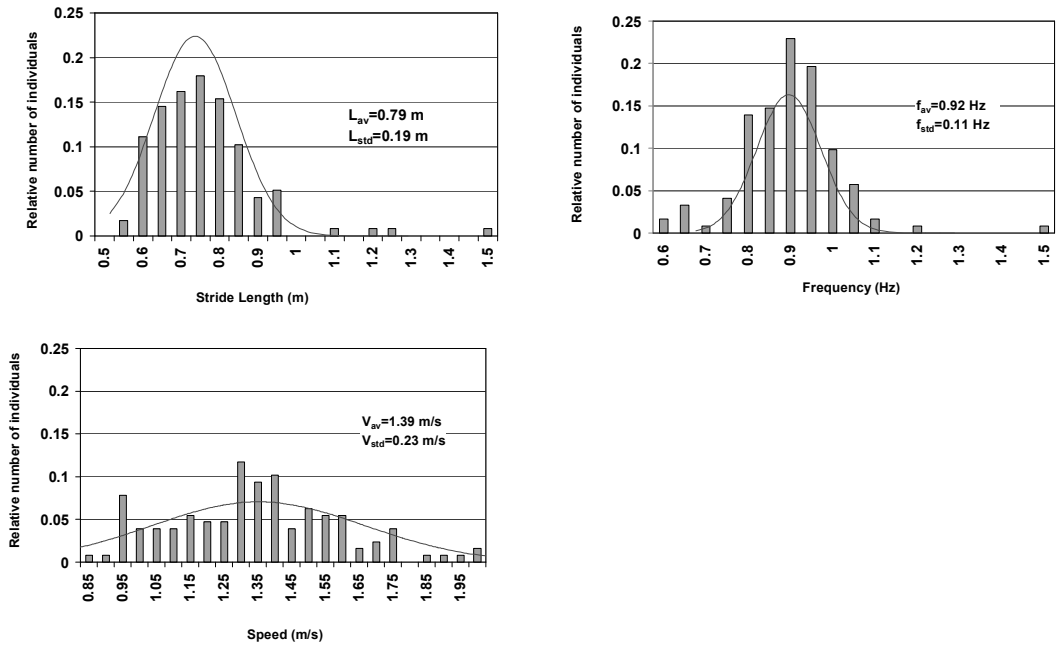
Figure 5.3   PDFs of stride length, frequency and speed
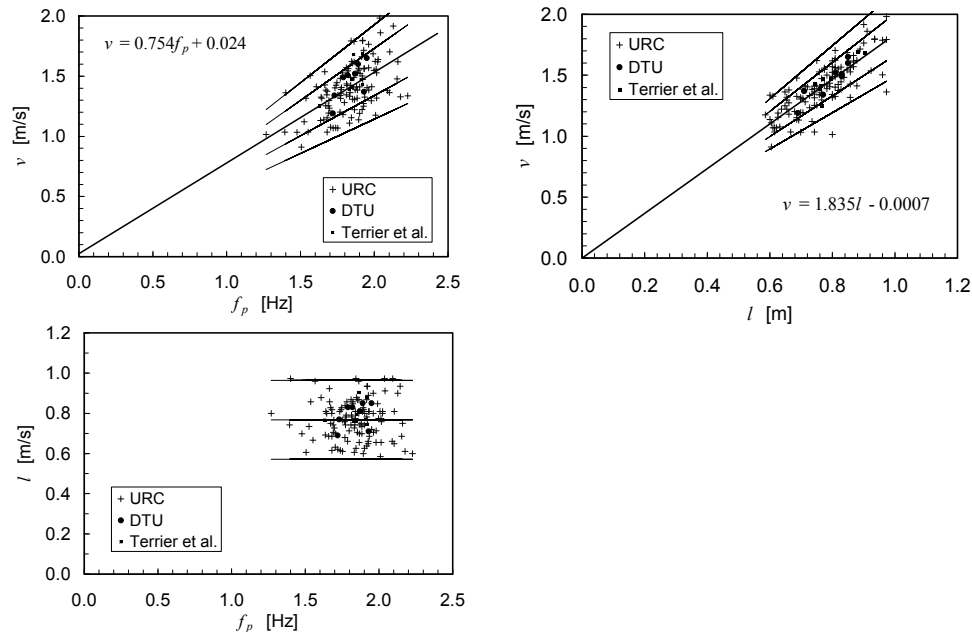
Figure 5.4   Relationship between stride length, walking frequency and walking speed

In Fig. 5.3 the frequency distributions of walking frequency, stride and speed are shown, together with their Gaussian approximation. The average walking frequency was found to be 0.92 Hz, lower than that of 1.00 found by Matsumoto [m], which confirms that gait characteristics depend on the lifestyle of the individuals.

For some applications it is of interest the relationship between the walking frequency f_p, the stride length l and the walking speed v. The tests revealed that walking speed can be reasonably assumed a linear function of both walking frequency and stride length, while the latter parameters are quite uncorrelated with each other. Such result is shown through Fig. 5.4. Together with the results of the tests carried out at the University of Reggio Calabria (indicated as URC), eight points are shown, coming from similar tests carried out at the Danish Technical University (indicated as DTU), and other eight points coming from the tests presented in [a].

Together with the experimental points, also the linear fits are shown, based only on the URC measurements. The fits show that the walking velocity is almost proportional to the walking frequency, therefore it seems reasonable to neglect the constant value of 0.024 m/s and assume a relationship of the type $v=0.754 \cdot f_p$, where the slope of the line is in good agreement with the measured mean stride length of 0.768 m. In Fig. 5.4 the lines of equation $v=[\text{mean}(l)\pm\text{RMS}(l)]\cdot f_p$ and $v=[\text{mean}(l)\pm2\cdot\text{RMS}(l)]\cdot f_p$ are also shown, which define the confidence ranges associated with the relationship between walking speed and stride length.

A similar approach can be applied to analyse the relationship between stride length and walking velocity. Also in this case, when the constant value of -0.0007 m/s is neglected the linear relationship $v=1.835 \cdot l$ is obtained from the URC measurements, whose slope is in perfect agreement with the measured mean walking frequency. Also in Fig. 5.4 the confidence ranges of the relationship between stride length and walking velocity are shown, through the lines of equation $v=[\text{mean}(f_p)\pm\text{RMS}(f_p)]\cdot l$ and $v=[\text{mean}(f_p)\pm2\cdot\text{RMS}(f_p)]\cdot l$. Finally, in Fig. 5.4 the relationship between the walking frequency and the stride length is shown. In this case the points are quite scat-

tered, without a clear trend. In the figure a line corresponding to the mean stride length from the URC measurements, together with the constant values [mean(l)±2·RMS(l)] are also shown.

5.3   CLOSED FORM RESPONSE OF FOOTBRIDGES TO THE CROSSING OF ONE PEDESTRIAN

The full details of this section are given in [6].

The equation of motion of an elastic beam featuring viscous damping and with a span-wise constant cross section is:

$$m\ddot{w}(x,t) + c\dot{w}(x,t) + EIw^{IV}(x,t) = q(x,t) \tag{5.1}$$

where $w(x,t)$ is the beam displacement, m and c are the beam mass and viscous damping per unit length, E is the Young's modulus of the material and I the moment of inertia of the cross section, and where $q(x,t)$ is the load per unit length at time t. It is convenient to express the beam response as a combination of the modal response in the relevant modes:

$$w(x,t) = \sum_i \phi_i(x)y_i(t) \tag{5.2}$$

where $\phi_i(x)$ is the i-th mode shape and $y_i(t)$ is the i-th generalised coordinate.

For a supported beam the i-th mode shape is:

$$\phi_i(x) = \sin\left(i\frac{\pi}{L}x\right) \tag{5.3}$$

where L is the beam span. In the case of a sinusoidal force moving at a constant speed v, the forcing function appearing in Eq. (5.1) is:

$$q(x,t) = \bar{F}\sin(\bar{\omega}t)\delta(x-vt) \tag{5.4}$$

where $\bar{F}$ and $\bar{\omega}$ are the amplitude and frequency of the force, and where $\delta(\cdot)$ indicates the Dirac delta function. The i-th modal force can be derived from Eqs. (5.3) and (5.4):

$$f_i(t) = \int_L q(x,t)\phi_i(x)dx = \bar{F}\sin\left(i\frac{\pi v}{L}t\right)\sin(\bar{\omega}t) \tag{5.5}$$

Finally, the equation of motion in the i-th mode is obtained as:

$$\ddot{y}_i + 2\xi_i\omega_i\dot{y}_i + \omega_i^2 y_i = \frac{\bar{F}}{mL}\left[\cos(\omega_{1i}t) - \cos(\omega_{2i}t)\right] \tag{5.6}$$

in which:

$$\omega_i = i^2\frac{\pi^2}{L^2}\sqrt{\frac{EI}{m}} \tag{5.7}$$

is the i-th natural frequency, and ξ_i is the i-th damping ratio.

From Eq. (5.6) it appears that the load is decomposed into the sum of two harmonic components, having the same amplitude, and circular frequencies:

$$\omega_{1i} = \bar{\omega}\left(1-\frac{i}{n}\right) \qquad\qquad \omega_{2i} = \bar{\omega}\left(1+\frac{i}{n}\right) \tag{5.8}$$

respectively. In Eqs. (5.8) the quantity:

$$n = \frac{2L}{l} \tag{5.9}$$

is equal to twice the ratio of the beam span to the wavelength $l = 2\pi v/\varpi$ of the load, i.e. is the total number of cycles the sinusoidal force applies to the beam.

The solution of Eq. (5.6) is:

$$y_i(t) = \frac{\overline{F}}{\omega_i^2 mL}\left[C_{1i}\sin(\omega_{1i}t + \varphi_{1i}) + C_{2i}\sin(\omega_{2i}t + \varphi_{2i}) + s_i C_{Di}e^{-\xi_i\omega_i t}\sin(\omega_{Di}t + \varphi_{Di}) \right] \tag{5.10}$$

where:

$$\omega_{Di} = \omega_i\sqrt{1 - \xi_i^2} \tag{5.11}$$

is the damped frequency of the beam in the i-th mode, and where:

$$C_{1i} = \frac{\omega_i^2}{\sqrt{\left(\omega_i^2 - \omega_{1i}^2\right)^2 + \left(2\xi_i\omega_i\omega_{1i}\right)^2}} \qquad\qquad C_{2i} = -\frac{\omega_i^2}{\sqrt{\left(\omega_i^2 - \omega_{2i}^2\right)^2 + \left(2\xi_i\omega_i\omega_{2i}\right)^2}}$$

$$\mathrm{tg}\varphi_{1i} = \frac{\omega_i^2 - \omega_{1i}^2}{2\xi_i\omega_i\omega_{1i}} \qquad\qquad \mathrm{tg}\varphi_{2i} = \frac{\omega_i^2 - \omega_{2i}^2}{2\xi_i\omega_i\omega_{2i}}$$

$$\tag{5.12}$$

$$C_{Di} = \sqrt{A_i^2 + B_i^2} \qquad\qquad \mathrm{tg}\varphi_{Di} = \frac{B_i}{A_i} \qquad\qquad s_i = -\mathrm{sgn}(A_i)$$

$$A_i = \frac{\xi_i}{\omega_i^2\sqrt{1 - \xi_i^2}}\left[\left(\omega_i^2 + \omega_{1i}^2\right)C_{1i}^2 - \left(\omega_i^2 + \omega_{2i}^2\right)C_{2i}^2 \right]$$

$$B_i = \frac{1}{\omega_i^2}\left[\left(\omega_i^2 - \omega_{1i}^2\right)C_{1i}^2 - \left(\omega_i^2 - \omega_{2i}^2\right)C_{2i}^2 \right]$$

The resonant response in the i-th mode is obtained by setting $\varpi = \omega_i$. Eqs. (5.8) become:

$$\omega_{1i} = \omega_i\left(1 - \frac{i}{n}\right) = \omega_i\left(1 - \frac{\xi_i}{\varepsilon_i}\right) \qquad\qquad \omega_{2i} = \omega_i\left(1 + \frac{i}{n}\right) = \omega_i\left(1 + \frac{\xi_i}{\varepsilon_i}\right) \tag{5.13}$$

It can be seen that the parameter $\varepsilon_i = n\xi_i/i$ is relevant to the system behaviour, as it is an index of the stationarity of the response. A large value of ε_i is associated with the response in a low mode of a beam of long span featuring high damping, and subjected to a high frequency load travelling at a low speed. The maximum transient response of such a system to a moving load is close to the response the system would experience if the same load were stationary at midspan. On the other hand, a small value of ε_i corresponds to the response in a high mode of a short span beam featuring low damping, subjected to a low frequency load moving at a high speed. In the latter case, the response is highly non-stationary.

Under the assumption that $i/n = \xi_i/\varepsilon_i \ll 1$, i.e. in the case in which the wavelength of the load is much smaller than the wavelength L/i of the deformed shape of the beam, a large number of cycles of the external load takes place between two nodes of the vibration mode. With the further assumption of low damping, Eqs. (5.12) can be approximated as:

$$C_{1i} \cong \frac{\varepsilon_i}{2\xi_i} \frac{1}{\sqrt{1+\varepsilon_i^2}} \cong -C_{2i} \qquad\qquad tg\varphi_{1i} \cong \frac{i}{n\xi_i} = \frac{1}{\varepsilon_i} \cong -tg\varphi_{2i}$$

$$A_i \cong -\frac{\varepsilon_i}{\left(1+\varepsilon_i^2\right)} \qquad\qquad B_i \cong -\frac{\varepsilon_i}{\xi_i\left(1+\varepsilon_i^2\right)} \qquad\qquad (5.14)$$

$$C_{Di} \cong \frac{\varepsilon_i}{\xi_i\left(1+\varepsilon_i^2\right)} \qquad\qquad tg\varphi_{Di} \cong \frac{1}{\xi_i} \gg 1 \qquad \left(\varphi_{Di} \to \pi/2\right)$$

$$s = -1$$

Being i/n small, then $\omega_{1i}^2 \cong \omega_{2i}^2 \cong \omega_i^2$. Eq. (5.10) becomes:

$$y(t) \cong -\frac{\overline{F}}{\omega_i^2 mL}\left\{\frac{\varepsilon_i}{\xi_i}\frac{1}{1+\varepsilon_i^2}\left[\sqrt{1+\varepsilon_i^2}\sin\left(\frac{\xi_i}{\varepsilon_i}\omega_i t - atan\frac{1}{\varepsilon_i}\right) + e^{-\xi_i\omega_i t}\right]\cos\left(\omega_i t\right)\right\} = -A(t)\cos\omega_i t \quad (5.15)$$

Eq. (5.15) describes a harmonic response with slowly varying amplitude. The maximum of the response can be approximated with the maximum of the envelope, and the time instant at which this occurs is found through solution of the equation:

$$\dot{A}(t) = \frac{\overline{F}}{\omega_i^2 mL}\left\{\frac{\omega_i}{1+\varepsilon_i^2}\left[\sqrt{1+\varepsilon_i^2}\cos\left(\frac{\xi_i}{\varepsilon_i}\omega_i t - atan\frac{1}{\varepsilon_i}\right) - \varepsilon_i e^{-\xi_i\omega_i t}\right]\right\} = 0 \qquad (5.16)$$

An approximate solution of Eq. (5.16) is:

$$\cos\left(\frac{\xi_i}{\varepsilon_i}\omega_i t - atan\frac{1}{\varepsilon_i}\right) = 0 \qquad\qquad (5.17)$$

The cosine in Eq. (5.17) vanishes at:

$$t^* = \frac{\varepsilon_i}{\xi_i\omega_i}\left(\frac{\pi}{2} + atan\frac{1}{\varepsilon_i}\right) \qquad\qquad (5.18)$$

This allows writing the approximate maximum of the normalised displacement transient response as:

$$\frac{y_{max}\omega_i^2 mL}{\overline{F}} \cong \frac{\omega_i^2 mL}{\overline{F}}A(t^*) = \frac{\varepsilon_i}{\xi_i}\frac{1}{1+\varepsilon_i^2}\left[\sqrt{1+\varepsilon_i^2} + e^{-\varepsilon_i\left(\frac{\pi}{2}+atan\frac{1}{\varepsilon_i}\right)}\right] = \left(\frac{y_{max}\omega_i^2 mL}{\overline{F}}\right)_{stat}\varphi(\varepsilon_i) \quad (5.19)$$

where:

$$\left(\frac{y_{max}\omega_i^2 mL}{\overline{F}}\right)_{stat} = \frac{1}{\xi_i} \qquad\qquad (5.20)$$

are the amplitudes of the normalised displacement and acceleration stationary response, and where:
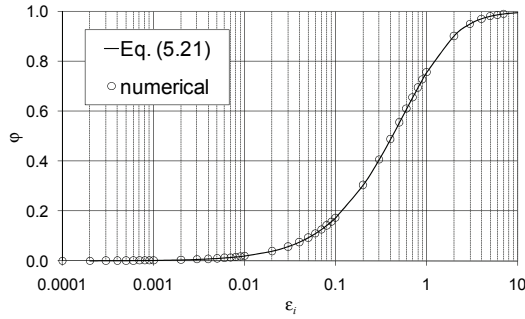
Figure 5.5 Transient resonant response coefficient

$$\varphi(\varepsilon_i) = \frac{\varepsilon_i}{1+\varepsilon_i^2}\left[\sqrt{1+\varepsilon_i^2} + e^{-\varepsilon_i\left(\frac{\pi}{2}+\mathrm{atan}\frac{1}{\varepsilon_i}\right)}\right] \tag{5.21}$$

is a transient resonant response coefficient (Fig. 5.5).

The maximum of the normalised transient response can then be calculated by evaluating the envelope $A(t)$ at time t^* .

When the moving load is not resonant with the beam, the dynamic behaviour is governed by the ratio of the excitation frequency to the natural frequency in the mode considered:

$$\alpha_i = \frac{\overline{\omega}}{\omega_i} \tag{5.22}$$

Eqs. (5.12) can be rewritten using the α_i parameter as:

$$C_{1i}, C_{2i} = \frac{1}{\sqrt{\left(1-\alpha_i^2\left(1\mp\frac{\xi_i}{\varepsilon_i}\right)^2\right)^2 + \left(2\xi_i\alpha_i\left(1\mp\frac{\xi_i}{\varepsilon_i}\right)\right)^2}} \qquad \mathrm{tg}\varphi_{1i}, \mathrm{tg}\varphi_{2i} = \frac{1-\alpha_i^2\left(1\mp\frac{\xi_i}{\varepsilon_i}\right)^2}{2\xi_i\alpha_i\left(1\mp\frac{\xi_i}{\varepsilon_i}\right)}$$

$$A_i = \frac{\xi_i}{\sqrt{1-\xi_i^2}}\left[\left(1+\alpha_i^2\left(1-\frac{\xi_i}{\varepsilon_i}\right)^2\right)C_{1i}^2 - \left(1+\alpha_i^2\left(1+\frac{\xi_i}{\varepsilon_i}\right)^2\right)C_{2i}^2\right] \tag{5.23}$$

$$B_i = \left[\left(1-\alpha_i^2\left(1-\frac{\xi_i}{\varepsilon_i}\right)^2\right)C_{1i}^2 - \left(1-\alpha_i^2\left(1+\frac{\xi_i}{\varepsilon_i}\right)^2\right)C_{2i}^2\right]$$

When the system is lightly damped, and rather away from resonance, Eqs. (5.23) can be approximated as:

$$C_{1i} \cong \frac{1}{\left|1-\alpha_i^2\right|} \cong -C_{2i} \qquad\qquad \varphi_{1i} \cong \varphi_{2i} \to \frac{\pi}{2}\operatorname{sgn}\left(1-\alpha_i^2\right)$$

$$A_i \cong -\frac{4\alpha_i^2}{\left(1-\alpha_i^2\right)^2}\frac{\xi_i^2}{\varepsilon_i}\operatorname{sgn}\left(1-\alpha_i^2\right) \qquad\qquad B_i \cong -\frac{4\alpha_i^2}{\left(1-\alpha_i^2\right)^2}\frac{\xi_i}{\varepsilon_i} \qquad (5.24)$$

and:

$$C_{Di} \cong \left|B_i\right| \cong \frac{4\alpha_i^2}{\left(1-\alpha_i^2\right)^2}\frac{\xi_i}{\varepsilon_i} \qquad \varphi_{Di} \to \frac{\pi}{2}\operatorname{sgn}\left(1-\alpha_i^2\right) \qquad s_i = \operatorname{sgn}\left(1-\alpha_i^2\right) \quad (5.25)$$

Based on Eqs. (5.24) and (5.25), Eq. (5.10) becomes:

$$y_i(t) \cong \frac{\overline{F}}{\omega_i^2 mL}\frac{2}{1-\alpha_i^2}\left[\sin(\alpha_i\omega_i t)\sin\left(\frac{\xi_i}{\varepsilon_i}\alpha_i\omega_i t\right)+\frac{\xi_i}{\varepsilon_i}\frac{2\alpha_i^2}{1-\alpha_i^2}e^{-\xi_i\omega_i t}\cos(\omega_{Di}t)\right] \qquad (5.26)$$

When the system is away from resonance, Eq. (5.26) provides a quite satisfactory approximation of Eq. (5.10), while it tends to loose accuracy as the system approaches resonance (i.e. as $\alpha_i \to 1$). An approximate envelope of Eq. (5.26) is obtained by setting:

$$\sin(\alpha_i\omega_i t)=\cos(\omega_{Di}t)=\pm 1 \qquad (5.27)$$

which gives:

$$B(t)=\pm\frac{\overline{F}}{\omega_i^2 mL}\frac{2}{\left|1-\alpha_i^2\right|}\left[\sin\left(\frac{\xi_i}{\varepsilon_i}\alpha_i\omega_i t\right)+\frac{\xi_i}{\varepsilon_i}\frac{2\alpha_i^2}{\left|1-\alpha_i^2\right|}e^{-\xi_i\omega_i t}\right] \qquad (5.28)$$

Opposite to Eq. (5.26), Eq. (5.28) is more accurate when the system is not too far from resonance, while it tends to loose accuracy as the system moves away from resonance (i.e. as $\alpha_i \to 0$ and as $\alpha_i \to \infty$). The procedure shown here is based on the approximation of the response through Eq. (5.26), and with the approximation of its envelope through Eq. (5.28). This means that the results are expected to loose accuracy both when the system gets very close to resonance, or when it moves very far from it. On the other hand, for intermediate values of α_i they are expected to be fairly accurate.

Following the same approach used for resonant oscillations, the maximum response can be found by setting:

$$\dot{B}(t)=\frac{\overline{F}}{\omega_i^2 mL}\frac{2\alpha_i}{\left|1-\alpha_i^2\right|}\frac{\omega_i\xi_i}{\varepsilon_i}\left[\cos\left(\frac{\xi_i}{\varepsilon_i}\alpha_i\omega_i t\right)-\xi_i\frac{2\alpha_i}{\left|1-\alpha_i^2\right|}e^{-\xi_i\omega_i t}\right]=0 \qquad (5.29)$$

A solution of Eq. (5.29) can be found by setting:

$$\cos\left(\frac{\xi_i}{\varepsilon_i}\alpha_i\omega_i t\right)=0 \qquad (5.30)$$

which gives the time instant at which the envelopes reach their maximum:
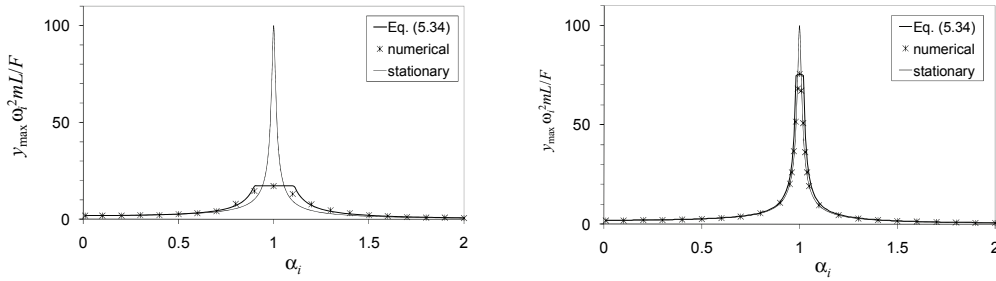
Figure 5.6   Transient Frequency Response Functions

$$t^* = \frac{\varepsilon_i}{\xi_i \omega_i} \frac{\pi}{2\alpha_i} \tag{5.31}$$

There results that the approximated maximum of the normalised response is:

$$\frac{y_{\max}\omega_i^2 mL}{\overline{F}} \cong \frac{\omega_i^2 mL}{\overline{F}} B(t^*) = \frac{2}{\left|1-\alpha_i^2\right|}\left[1+\frac{\xi_i}{\varepsilon_i}\frac{2\alpha_i^2}{\left|1-\alpha_i^2\right|}e^{-\frac{\pi\varepsilon_i}{2\alpha_i}}\right] \tag{5.32}$$

Eq. (5.32) proves quite accurate, except when α_i approaches unity, in which case the solution for a resonant load is more accurate.

Eq. (5.32) can be interpreted as a function of the frequency parameter α_i, depending on the damping parameter ξ_i and on the stationarity parameter ε_i. This allows its use, together with that of Eq. (5.19), to build Transient Frequency Response Functions (TFRF). In particular, Eq. (5.19) applies at and around resonance, while Eq. (5.32) applies away from resonance. On the other hand, as the system approaches resonance, Eq. (5.32) tends to infinity. This allows defining the TFRF as the minimum value calculated through Eq. (5.19) and Eq. (5.32), that is:

$$FRF_y(\xi_i,\varepsilon_i,\alpha_i) = \min\left\{\frac{2}{\left|1-\alpha_i^2\right|}\left[1+\frac{\xi_i}{\varepsilon_i}\frac{2\alpha_i^2}{\left|1-\alpha_i^2\right|}e^{-\frac{\pi\varepsilon_i}{2\alpha_i}}\right]; \frac{\varepsilon_i}{\xi_i}\frac{1}{1+\varepsilon_i^2}\left[\sqrt{1+\varepsilon_i^2}+e^{-\varepsilon_i\left(\frac{\pi}{2}+\operatorname{atan}\frac{1}{\varepsilon_i}\right)}\right]\right\} \tag{5.34}$$

In Fig. 5.6 the TFRF is plotted for a damping ratio $\xi_i = 0.01$, and two different values of the ε_i parameter of 0.1 (left) and 1.0 (right).

5.4   EXPERIMENTAL VALIDATION OF THE LOADING MODELS

The response model of Section 5.3 well applies to short span bridges. For a medium to long span footbridge the worst load condition proves to be that of the stationary action of a crowd. For the particular case in which the density of the crowd is low enough for the pedestrians not to interact with each other, therefore give rise to a synchronised behaviour, a loading model was presented by Ricciardelli [k]. Based on this, the RMS stationary acceleration response of a supported bridge can be written as:

$$\frac{a_{RMS}\cdot M}{W} = \sqrt{\delta BL\frac{8}{\pi\xi}\frac{f_o S_{Fe}(f_o)}{W}} \tag{5.35}$$

where $f_o S_{Fe}(f_o)$ is the non dimensional power spectrum of the equivalent load associated with one
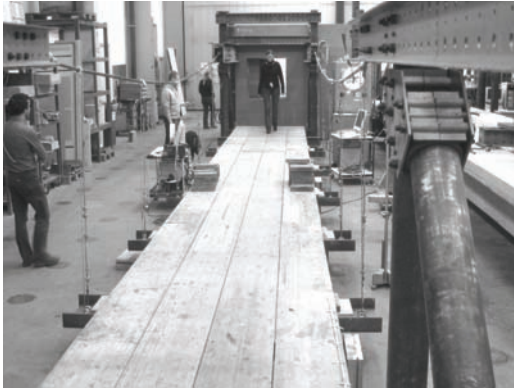
Figure 5.7   Model footbridge at DTU

pedestrian, δ is the density of pedestrians, and L and B are the span and width of the bridge.

The non dimensional power spectrum of the equivalent load associated with one pedestrian is obtained as the integral of the power spectrum $f_o S_F(f_o/f_p)$ of the load associated with one pedestrian centred at the frequency f_p weighted through the probability density $p(f_p)$ of the walking frequency:

$$f_o S_{Fe}(f_o) = \int_0^\infty f_o S_F(f_o/f_p) \cdot p(f_p) \cdot df_p \qquad (5.36)$$

For the loading models leading to Eqs. (5.19) and (5.32) and to Eq. (5.35) to be applicable, the amplitude of oscillation of the footbridge has also to be small enough for the pedestrians not to be affected in their gait. To investigate the modifications occurring to the walking parameters due to the footbridge oscillation tests were carried out at the Danish Technical University on a model footbridge, able to vibrate in the vertical direction. These also allowed verifying the limits of applicability of Eq. (5.19). The footbridge, shown in Fig. 5.7, is a suspended span of 12 m, whose design data and final dynamic characteristics are reported by Ingolfsson [l]. For the purpose of matching the average walking frequency, an additional mass of 1075 Kg was added at midspan. There resulted a first natural frequency of 1.95 Hz. The measured damping ratio proved to be dependent on the amplitude of oscillation. In particular a value of 0.5% was measured for low amplitudes up to 3.5 cm, a value of 0.6% for intermediate amplitudes up to 5.5 cm, and a value of 0.8% for larger amplitudes. In the following the value of 0.5% will be used, as in the tests the amplitude of oscillation never exceeded the value of 3.5 cm. The first modal mass in the configuration with the additional mass at midspan was estimated to be about 2020 Kg.

First, a set of tests was carried out to measure the undisturbed walking characteristics of the eight test persons which consisted in measuring the average walking frequency and speed and stride length on a fixed floor. The values obtained were considered as a reference for the measurements on the vibrating model footbridge. Then three sets of metronome tests were carried out on the model footbridge. In test #1 the metronome frequency was set equal to the bridge natural frequency, in test #2 it was set equal to 90% that (1.75 Hz), and in test #3 equal to 110% (2.15 Hz). In the metronome tests the persons were asked to try to keep the other walking parameters as natural as they could. Finally, free walking tests were carried out, in which the persons were asked to walk on the bridge according to his/her own pace rate. Each of the tests above was repeated three times, and the results were averaged.

In Tab. 5.1 the results of the free walking tests (on the stiff floor and on the vibrating foot-

n	W [N]	H [m]	gender	f_p [Hz]		l [m]		a [m/s^2]		ratio
				floor	bridge	floor	bridge	meas.	calculated	
1	559	1.60	F	1.72	1.70	0.69	0.69	0.31	0.25 (eq. 5.32)	0.81
2	647	1.77	F	1.93	1.94	0.71	0.76	1.68	2.98 (eq. 5.19)	1.77
3	736	1.76	M	1.79	1.82	0.83	0.89	1.24	0.86 (eq. 5.32)	0.69
4	785	1.80	M	1.88	1.83	0.85	0.90	1.98	2.81 (eq. 5.19)	1.42
5	697	1.74	F	1.87	1.90	0.81	0.87	1.95	2.76 (eq. 5.32)	1.42
6	687	1.80	M	1.82	1.82	0.83	0.85	1.48	2.52 (eq. 5.32)	1.70
7	736	1.78	M	1.95	1.90	0.85	0.89	2.26	2.86 (eq. 5.19)	1.27
8	1010	1.88	M	1.72	1.70	0.77	0.79	0.67	0.44 (eq. 5.32)	0.66

Tab. 5.1   Free walking results

bridge) are compared. It can be noticed that there is a minor difference between the walking frequencies measured on the footbridge and those measured on the floor, to be considered as a random fluctuation. On the other hand, a systematic increase of the stride length is noticed when the pedestrians walk on the footbridge. This ranges between 0 and 7%, and globally increases with the amplitude of oscillation of the footbridge. In Tab. 5.1 the measured response is also compared to that predicted through Eq. (5.19) or (5.32). Either the one or the other equation is used in each case, depending on how close to each other were the walking and vibration frequencies. The closed form solution of Eq. (5.32) predicts the measured response with an error in the range of −34% to +42%. This is mainly explained through the fact that this equation, even though quite accurate away from resonance, tends to become inaccurate as the system approaches resonance. Other causes of inaccuracy are associated with the experimental setup, with the assumption of a sinusoidal deformed shape, and with the short span of the footbridge. The closed form solution of Eq. (5.19), on the other hand, generally overestimates (between 42% and 77%) the measured response. This is mainly due to the fact that this equation applies in case of resonance, and in the free walking tests this condition is generally not achieved.

In Fig. 5.8 the measured non-dimensional load detuning (difference between walking and vibration frequencies) is plotted as a function of the theoretical non-dimensional load detuning (that calculated based on the walking frequency on the stiff floor). Measurement of a zero detuning would indicate that the pedestrian has synchronised its gait to the footbridge vibration. This situation, however, never occurred in the tests, suggesting that in none of the tests a walker-structure synchronisation mechanism took place. The maximum measured acceleration amplitude was 2.26 m/s^2, corresponding to a displacement amplitude of 1.51 cm. It is concluded that in this specific case of a short span, the synchronisation thresholds (both in terms of accelerations and displacements) are larger than the values above.

Finally in Tab. 5.2 the results of the metronome tests are presented. First it is noted that there is a discrepancy between the metronome frequency and the walking frequency, indicating that, especially in the resonance tests the walkers could not fully match the triggered frequency. For the resonance tests the measured acceleration is compared with that calculated through Eq. (5.19). The predicted acceleration always exceeds the measured one. For those walkers who could better match the metronome frequency (subjects # 2,4,5,7), the overestimation of the measured response through Eq. (5.19) is in the range of 26% to 64%. In this case the overestimation of the response by Eq. (5.19) is justified by the fact that when forced to follow the metronome frequency, the
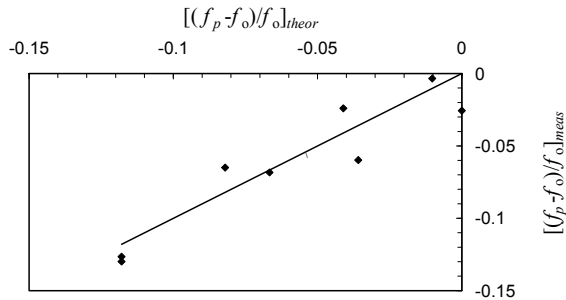
Figure 5.8   Measured vs. theoretical detuning

n	f_{metr}=1.95 Hz				f_{metr}=1.75 Hz				f_{metr}=2.15 Hz			
	f [Hz]	l [m]	a [m/s^2]	Eq. (3) [m/s^2]	f [Hz]	l [m]	a [m/s^2]	Eq. (4) [m/s^2]	f [Hz]	l [m]	a [m/s^2]	Eq. (4) [m/s^2]
1	1.85	0.73	1.23	2.41	1.75	0.72	0.455	0.364	2.08	0.73	0.666	1.07
2	1.94	0.76	1.82	2.98	1.77	0.72	0.656	0.459	2.08	0.77	0.697	1.11
3	1.88	0.94	2.01	2.67	1.75	0.89	1.00	0.438	2.11	0.89	1.38	1.20
4	1.96	0.90	2.36	3.21	1.75	0.87	1.32	0.491	2.15	0.88	1.38	1.01
5	1.96	0.88	1.93	2.88	1.77	082	0.622	0.486	2.14	0.89	1.11	0.919
6	1.98	0.87	1.97	2.95	1.77	0.90	1.08	0.504	2.11	0.89	0.982	1.02
7	1.96	0.94	2.30	2.89	1.77	0.85	1.09	0.394	2.13	0.85	1.26	1.02
8	1.89	0.85	2.23	4.04	1.73	0.84	0.781	0.451	2.10	0.84	1.16	1.56

Tab. 5.2   Metronome walking results

walkers tend to modify their walking parameters (see the increase in stride length), therefore modify the action to the footbridge. For the off-resonance tests the measured accelerations are compared with those calculated through Eq. (5.32). In this case the prediction error is larger when the walking frequency is lower than the vibration frequency (up to 63%), and smaller when the walking frequency is larger than the vibration frequency (as low as 4%).

5.5   EXPERIMENTAL INVESTIGATION OF WALKER-FOOTBRIDGE DYNAMIC INTERACTION PHENOMENA

In this section results from experimental investigations into lateral loads induced by pedestrians when walking on a laterally moving surface are presented. This is of particular interest when modelling the effect of crowd induced action on long-span and light-weight footbridges. It is shown that the movement of the structure has an adverse effect on the behaviour of the pedestrians and the loading they induced, which must be accounted for in design in order to reduce the susceptibility of the structure towards excessive pedestrian-induced vibrations.

During walking the ground reaction force, or simply GRF, occurs due to acceleration (and deceleration) of the centre of mass of the body. In general the GRF is a three dimensional vector which varies in both time and space. Early studies on lateral GRFs, revealed that the horizontal
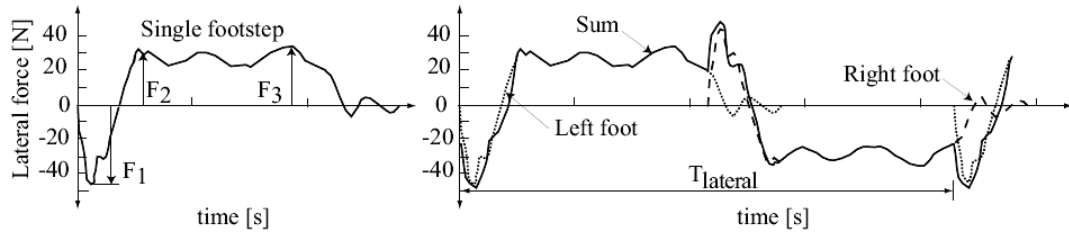
Figure 5.9 Typical shape of a lateral walking force time history, obtained from a single footstep (left) and from a superposition of two consecutive footsteps (right). From [b]

component of the force was generally very small and its lateral component is caused by balancing of the body during walking. A typical shape of the lateral GRF is shown in Fig. 5.9 for a single footstep (left) and continuous walking (right), under the assumption that all footsteps are identical, i.e. the same force pattern is replicated perfectly at each step during the entire walking. This perfect periodicity implies that the load can be written in terms of a Fourier series, with fundamental harmonic equal the duration of two consecutive steps:

$$F_L(t) = \sum_{j=1}^{\infty} G_j \sin\left(2\pi j f_w t - \phi_j\right) \tag{5.37}$$

in which f_w is the walking frequency, G_j and ϕ_j are load amplitude and phase angle of load harmonic j respectively. Typical values for G_1 are 4-10% of the body weight.

In [1] a frequency domain approach for modelling lateral pedestrian loads on a rigid surface (i.e. in the absence of lateral movement) is presented. The Power Spectral Density (PSD) for the first five harmonics of the lateral pedestrian load was given in a general (non-dimensional) form as:

$$\frac{S_{F_L}(f)f}{\tilde{F}_{L_j}^2} = \frac{2A_j}{\sqrt{2\pi}B_j}\exp\left\{-2\left[\frac{f/jf_w-1}{B_j}\right]^2\right\} \tag{5.38}$$

where A_j and B_j are parameters determined by the data fit and $\tilde{F}_{L_j}^2$ is the area under the PSD around the jth harmonic. The results are based on experimental work done by Pizzimenti [i], using the same Treadmill Ergometer Device as presented herewith.

Figure 5.10 TED setup (left) and pedestrian walking test in progress (right)
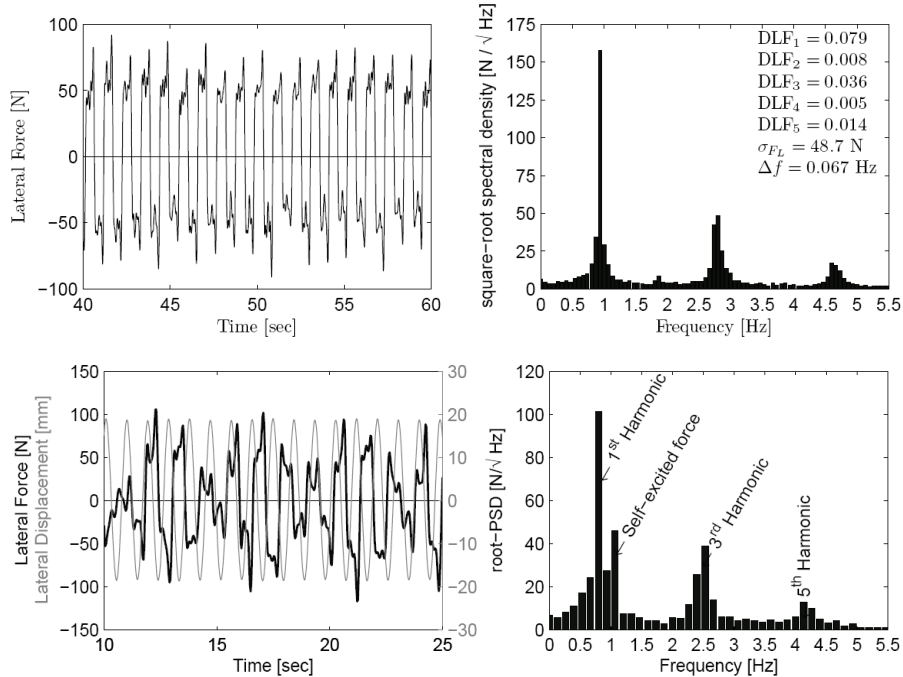
Figure 5.11 Typical examples of measured force and square-root PSD in absence of lateral treadmill motion (top) and with harmonic oscillation of around 20 mm at frequency around 1.1 Hz

When walking on a laterally oscillating surface, people tend to spread their feet apart and change their walking frequency and phase, to match that of the floor. The modification to gait due to floor oscillations is known within the civil engineering community as human-structure (dynamic) interaction or simply HSI. During the temporary closure of the Millennium Bridge, controlled pedestrian crowd tests were undertaken on the bridge which revealed that HSI affects the total pedestrian load such that a component in phase with and proportional to the velocity of the structure is observed. This finding suggested that the lateral pedestrian load can be treated as negative damping, which for a sufficient number of people cancels the inherent structural damping and in turn causes large vibration amplitudes.

During the summer 2009, seventy-one healthy volunteers (45 males and 26 females) aged 16 to 60 years, with average height 1.73 m (STD 0.01 m) and average weight 74.4 kg (STD 15.1 kg) participated in this study. A Treadmill Ergometer Device (TED), located in the CRIACIV laboratory in Prato was used to measure lateral GRFs during walking. In brief, the treadmill consists of three separate parts, Level 1 to 3. The base of the treadmill (level 1) is fixed on the laboratory floor. Level 2 consists of a steel frame connected to the base through rail guides, allowing horizontal motion. Level 3 consists of the walking surface (dimension 100x180 cm), which is made of a steel frame system covered with plywood panels and a rubber belt. The belt is driven by a motor. The lateral movement of the treadmill is obtained using a motor connected to Level 2 which controls the lateral vibration frequency and the amplitude. The connection between level 2 and 3, i.e. belt and the laterally driven frame, is made with 4 flexural load cells for measuring the lateral pedestrian load (Fig. 5.10).
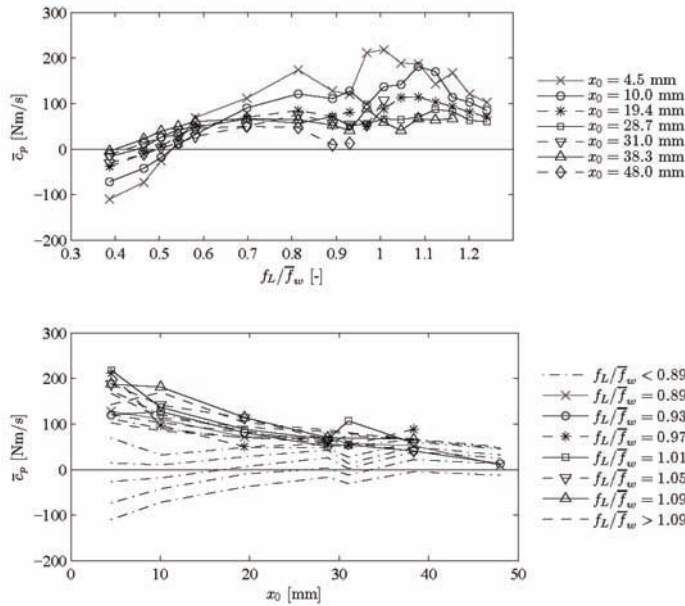
Figure 5.12 Average value of the pedestrian load coefficient as function of the normalised frequency (between lateral vibration frequency and mean walking frequency) for different lateral displacement amplitudes (top) and as function of lateral displacement amplitude (bottom) for various vibration frequencies.

Subjects were requested to walk on the treadmill, at a freely selected walking speed, during lateral sinusoidal movement at various vibration frequencies and amplitudes. Each subject performed several tests, each with duration 30 s, with vibration frequencies in the range 0.33 to 1.07 Hz and displacement amplitudes between 4.5 mm and 48 mm. Furthermore, each test subject performed a reference test, walking on the treadmill for 2 minutes in the absence of lateral vibration. Two typical results from the static and dynamic tests respectively are shown in Fig. 5.11. The main difference between the static and the dynamic tests is the existence of a load component at the frequency of the lateral treadmill vibration, denoted *the self-excited force*.

The magnitude of the self-excited force is quantified through the average work done by the pedestrian force per structural vibration cycle, through integration of the measured lateral force over the displacement of the structure. The average work is then normalized with the work done by a sinusoidal signal in phase with the velocity of the structure to obtain an equivalent sinusoidal load of the type:

$$F_{eq}(t) = c_p \dot{x}(t) = c_p \dot{x}_{b,0} \sin(\omega_L t - \phi) \tag{5.39}$$

which produces the same work per cycle as the measured force. This way, the pedestrian load is modelled as equivalent damping, with the load coefficient, c_p, determined as:

$$c_p = \frac{\dfrac{2}{T_{Tot}} \displaystyle\int_0^{T_{tot}} F_L(t) \dot{x}_b(t)\,\mathrm{d}t}{\dot{x}_{b,0}^2} \tag{5.40}$$
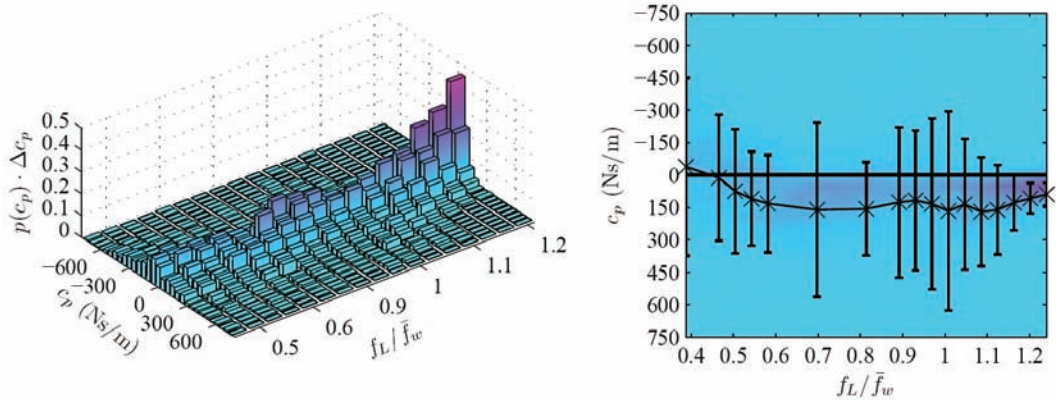
Figure 5.13 Probability distribution of pedestrian load coefficients at different frequencies shown in 3D (left) and shown in the ($c_p, f_L / \bar{f}_w$)-plan together with mean value $\bar{c}_p$ and $\pm\sigma_{cp}$ (right)

where $\dot{x}_{b,0}$ is the velocity amplitude of the treadmill, $F_L(t)$ measured pedestrian load and T_{Ttot} the total measurement time. Positive values of c_p imply that the pedestrian inputs energy into the structure and negative values imply an increase in the overall damping of the structure.

Pedestrian walking tests were performed at different lateral shaking frequencies, f_L, and amplitudes, $x_{b,0}$, with up to 70 test subjects at each particular combination of f_L and $x_{b,0}$. In Fig. 5.12, the mean value of c_p (taken for all the test subjects) for each frequency (normalized by the mean walking frequency of the population) and amplitude is presented, both as function of normalised frequency (top) and amplitude (bottom). In the top figure, the curves are made of an initial near–linear segment (up to $f_L/f_\omega \cong 0.8$ on the horizontal axis), followed by an almost horizontal segment. The slope of the linear segment and the value of the constant segment increases with decreasing amplitude. At the lowest frequencies c_p is negative (i.e. damping is added to the structure), but at higher frequencies ($f_L/f_\omega \geq 0.5$) the coefficient is positive. In addition, in the bottom figure there is a clear correlation between the average load coefficient and the displacement amplitude at most frequencies. In particular for $f_L/f_\omega > 0.89$, the negative damping decreases with increasing amplitude, which demonstrates the self-limiting nature of associated structural response. At lower frequencies, the added damping decreases for an increase in the displacement amplitude.

However, very large intersubject variability was observed in the tests, illuminated through a large scatter in the measured load coefficients. Therefore, the load coefficient is best described through its probability distribution and central moments (mean and standard deviation). In Fig. 5.13, the experimentally obtained probability distribution of c_p is shown for different frequencies, both in 3D (left) and in the (f_L, c_p) plane (right), where also the mean value $\pm\sigma_{cp}$ is shown.

Globally it was shown that pedestrian induced lateral load depends on the movement of the ground surface which needs to be accounted for when designing bridges for dynamic pedestrian loads. The relationship between the force and the movement of the structure possesses an unfortunate property, i.e. it increases in amplitude with the velocity of the structure, which causes a potential threat of divergent amplitude, when loaded with a sufficient number of pedestrians. Furthermore, large scatter in the data presented herewith, stresses the importance of treating the data through their probability distribution functions, rather than single characteristic numbers.

Future work should include definition of the probability distribution functions for the load coefficient for creation of a load model, further investigation into different types of synchronization and overall phase coherence.

Figure 5.14   Pedometer: recording device (left) and switch (right)

5.6   EXPERIMENTAL INVESTIGATION OF DYNAMIC INTERACTION PHENOMENA IN CROWDS

Experimental measurements on the dynamics of crowds and groups people were carried out between January and May 2009 at the University of Reggio Calabria, using simple, custom-built, electronic devices able to simultaneously record the foot contact time of a number of walkers. In addition to the walking frequencies, the possibility of aligning the signals on one single time scale allowed analysis of the phases among the walkers. Information about the phases is of interest when synchronisation phenomena are investigated, with particular application to the definition of pedestrian loading of footbridges.

The pedometer (Fig. 5.14) consists of two elements: a switch located at the heel and a re-cording device that is connected to the switch through a cable. The latter has an internal clock and a memory in which the contact times are recorded. The device is small and light, and can be worn at the leg, therefore not modifying the normal walk. In the tests rubber-sole, leisure shoes were used, to ensure comfort and stability to the walkers. Download of the data was carried out through a standard USB port. The internal clock of the pedometers can be reset with a radio signal, which allows having one common reference time scale for all the devices. So doing it is possible to investigate the lags between the contact time of pairs of walkers, therefore characterise their walking phase.

Tests were carried out on groups of walkers and on small crowds. By group a number of individuals is meant, who know each other and who walk together to a common destination therefore with the same speed. The surface area occupied by the group, therefore the density, is not imposed, but it is rather the result of the interaction between the members of the group. The control parameter for the group is the number of members. Groups of two, five and ten walkers were analysed. By crowd a large (larger than for a group) number of individuals is meant who are forced to walk close to each other because of space constraints, but that do not necessarily know each other nor walk to a common destination. The control parameter for the crowd is density. The walking speed of members of a crowd is not necessarily common to all members. However, when the density becomes large, the walking speed tends to become the same. In fluid dynamics this would correspond to a transition from turbulent to laminar flow. Crowds of densities δ of 0.5 walkers/m^2, 0.7 walkers/m^2 and of 1.5 walkers/m^2 were considered.

Before performing group and crowd tests, the undisturbed gait parameters of each walker were measured in a free-walking test. These were then used as reference values for comparison of those measured in the group and crowd tests.

Test	f_{mean} [Hz]	f_{std} [Hz]	I_f
G2-1	0.834 (0.939)	0.035 (0.027)	0.042 (0.029)
	0.829 (0.859)	0.028 (0.024)	0.033 (0.028)
G2-2	0.839 (0.901)	0.032 (0.040)	0.039 (0.045)
	0.839 (0.815)	0.037 (0.027)	0.044 (0.033)
G2-3	0.862 (0.889)	0.029 (0.032)	0.034 (0.036)
	0.864 (0.902)	0.039 (0.028)	0.045 (0.031)
G2-4	0.897 (0.981)	0.023 (0.020)	0.026 (0.020)
	0.929 (0.978)	0.027 (0.035)	0.029 (0.036)

Tab. 5.3   Frequencies from G2 tests

Group tests were performed over a length of about 130 m, which people walked four times. The four records were then assembled together by removing the pauses, so to obtain one single record of about five minutes. Five groups of two, three groups of fine and one group of ten were tested. In the group tests the way in which individuals occupy the space around them was also observed, to try to gather as much information as possible on the interaction occurring among the walkers.

Crowd tests required that the density be kept constant at a prescribed value. To achieve this, two different techniques were used, depending on the target density. For high-density crowds the density was kept constant by keeping constant the area of the surface occupied by the walkers. This area was 1.7 m wide and had a length depending on the number of walkers available and on the target density. As the rectangular area occupied by the walkers moved forward at a constant speed, all the walkers were forced to adjust to the same speed. Such type of behaviour is consistent with that observed in real life for high-density crowds. For low-density crowds the density was kept constant by keeping constant the rate of the random arrival of new walkers at the starting section of the testing path. Such arrivals followed a Poisson distribution. For all crowds tests a walking length of 80 m length was used, that was walked only once.

To understand the interaction occurring among the components of a group of walkers or of a crowd, knowledge is necessary of the undisturbed dynamic behaviour of each walker, i.e. walking speed and frequency and stride length. These parameters were measured during preliminary tests (P tests) on a sample of 34 individuals, from which the test subjects for the group and crowd tests were taken. The results of the P tests are not discussed here, but only used as reference in the discussion of the results of the group and crowd tests.

Group tests (G tests) were performed on five groups of two (G2 tests), three groups of five (G5 tests) and a group of ten (G10 tests) walkers. The results of only four of the five G2 tests are discussed, as one of the tests provided results that were found meaningless.

In Tab. 5.3 the statistics (mean, standard deviation and index of variation) of the walking frequency measured in the G2 tests are presented, and compared with those (in brackets) measured on the same walkers during the P test. The first observation is that when walking in pairs the mean walking frequency reduces (except for one case), with an average reduction of 4.6%. In particular both members of the pair tend to reduce their frequency, which suggests that such reduction is more the consequence of a two-way interaction between the walkers, rather that the one-way adjustment of one walker to the other. Such interaction can be ascribed to a more relaxed at-
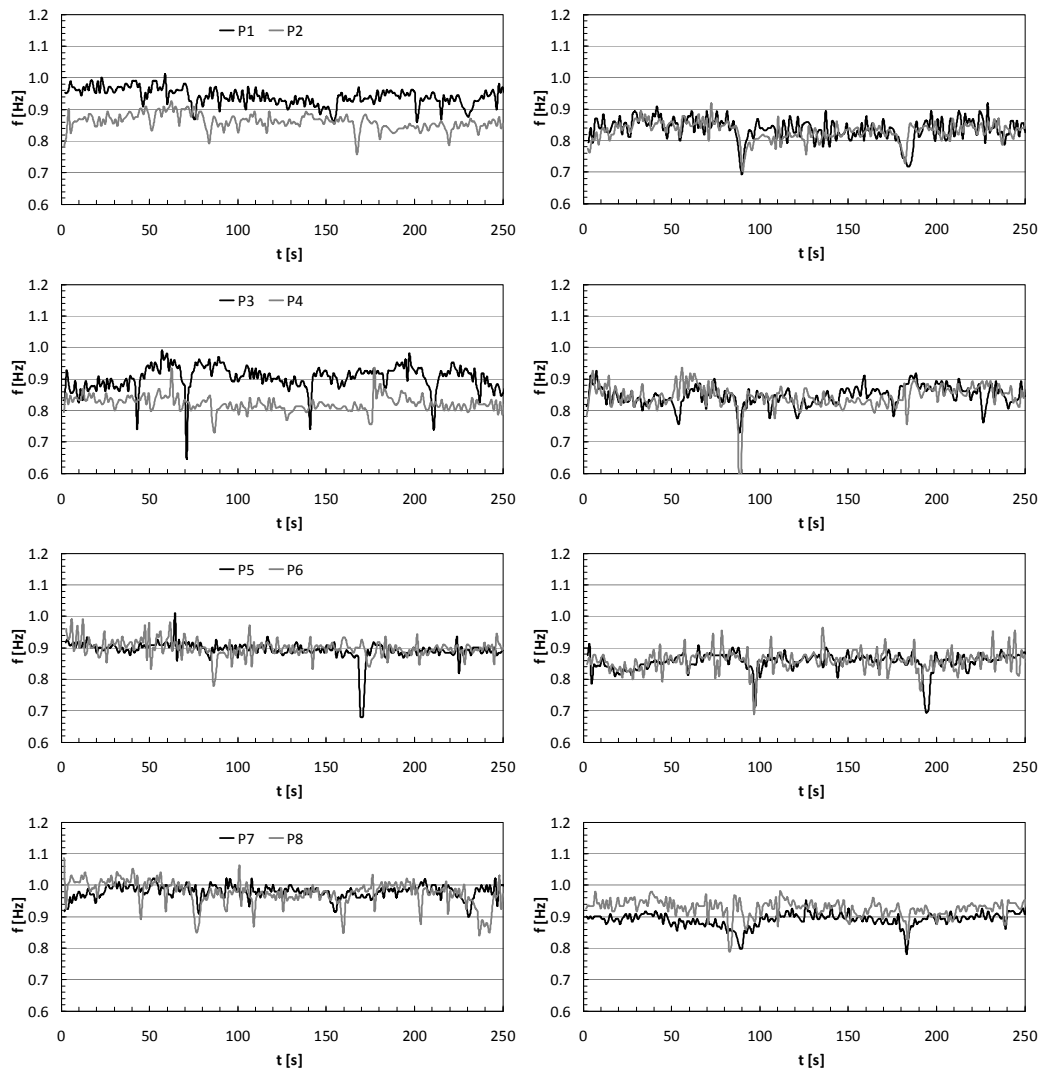
Figure 5.15 Instantaneous walking frequencies from G2 tests (right) and the corresponding P tests (left): G2-1 (first row), G2-2 (second row), G2-3 (third row), G2-4 (fourth row)

titude of the walkers when in company. In Fig. 5.15 time histories of the instantaneous walking frequencies are shown for the P and G2 tests, defined as:

$$f(t_i) = \frac{1}{t_{i+1} - t_i} \tag{5.41}$$

where t_i and t_{i+1} are the i-th and $(i+1)$-th contact times. Different types of behaviour can be pointed out. For the first pair a clear adjustment of the walking frequencies of the two walkers is visible. The mean frequency of the two walkers differs by 9% in the P tests and is almost coincident in the G2 test. This adjustment takes place at the expenses of an increase in the intra-subject variability (f_{std} and I_f) of the walking frequency of both walkers. This effect can better be seen from Fig. 5.16, where the phases:
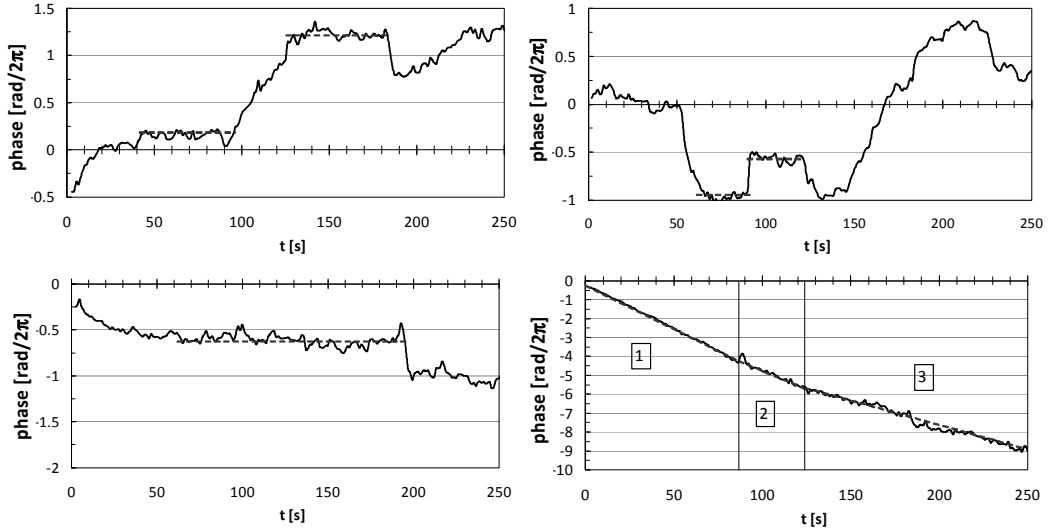
Figure 5.16   Phases of G2 tests: G2-1 (first row, left), G2-2 (first row, right), G2-3 (second row, left), G2-4 (second row, right)

$$\varphi_{jk}(t_i) = \left(t_i^j - t_i^k\right)\frac{f^j(t_i^j) + f^k(t_i^k)}{2} \tag{5.42}$$

between the walkers j and k at time t_i are plotted. In Eq. (5.42) t_i^j and t_i^k are the i-th contact times of walkers j and k, respectively, and $f^j(t_i)$ and $f^k(t_i)$ their instantaneous frequencies at times t_i^j and t_i^k. For about 50 s, from $t \cong 45$ s to $t \cong 95$ the two walkers have the same walking frequency, therefore they keep a constant phase of about $\pi/3$ ($\varphi/2\pi = 0.16$). At about time $t = 95$ s, the walker who showed a largest undisturbed walking frequency during the P tests increased his frequency to a slightly larger value of that of other walker. As a result the phase becomes (linearly) increasing.

This occurs for about 35 s, from $t = 95$ s to $t = 130$ s, until the phase difference gets back to a value of about $\pi/3$, to stay constant again for further 50 s, from $t = 130$ s to $t = 180$ s. In particular, the new value of the constant phase is $\varphi/2\pi = 1.22$, that is $\varphi = 2\pi + \pi/2.3$, indicating that the two walkers have locked-in again to the same frequency and phase, after one of the two has made one step more than the other. This is a discontinuous type of behaviour that is recognised in many of the tests performed.

Also for the second pair there is a strong frequency adjustment during the G2 test. The average frequencies of the two walkers differed by a 10% in the P test (0.901 Hz versus 0.815 Hz) and became exactly coincident in the G2 tests (0.839 Hz). This means that the two walkers walked exactly the same number of steps in the G2 test. This complete frequency synchronisation, however, is not accompanied by a phase synchronisation, as from Fig. 5.16 it can be seen how the phase fluctuates between -2π and 2π, being constant only for short durations, and never at the same value.

The same frequency adjustment of the first two pairs is found also in the third pair. In this case, however, this result was somehow expected, as the undisturbed walking frequency of the two walkers differed only by a 1.5% (0.889 Hz versus 0.902 Hz). In the G2 test both reduce their frequency (to 0862 Hz and 0.864 Hz, respectively), and a long frequency synchronisation of almost 140 s at a phase of about $\varphi = -4/3\pi$ ($\varphi/2\pi = -0.63$) can be observed from Fig. 5.16. Outside that

Test	f_{mean} [Hz]	f_{std} [Hz]	I_f
	0.877 (0.939)	0.083 (0.027)	0.094 (0.029)
	0.839 (0.859)	0.029 (0.024)	0.034 (0.028)
G5-1	0.857 (0.901)	0.037 (0.040)	0.043 (0.045)
	0.850 (0.815)	0.075 (0.027)	0.088 (0.033)
	0.875 (0.889)	0.020 (0.032)	0.023 (0.036)

Tab. 5.4   Frequencies from G5-1 test
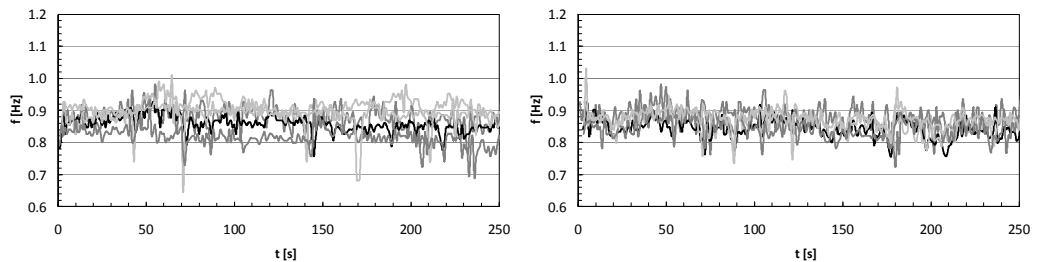
Figure 5.17   Instantaneous walking frequencies from P (left) and G5-1 (right) tests
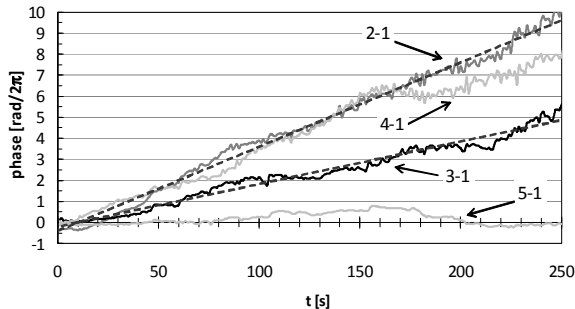
Figure 5.18   Phases of G5-1 test

range a slow decrease of the phase confirms the tendency of one of the walker to have a slightly higher frequency than the other, as observed in the P tests.

Finally, the fourth pair of walkers examined showed a completely different behaviour. In this case neither frequency nor phase synchronisation could be observed. The average walking frequencies of the two walkers differed by only 0.3% in the P tests (0.981 Hz versus 0.978 Hz), and diverged in the G2 tests (0.897 Hz versus 0.929 Hz) to a difference of 3%, indicating that the interaction in this case had more the characteristics of a disturbance. The phase has in this case a linear variation, at least for limited time durations. In particular constant values of the linear phase variation were observed from the beginning of the test to about $t = 100$ s (zone 1), from there to about $t = 130$ s (zone 2) and from there to the end of the test (zone 3).

In Tab. 5.4 the statistics (mean, standard deviation and index of variation) of the walking frequency measured in test G5-1 are presented, and compared with those (in brackets) measured on the same walkers during the P test. In Fig. 5.17 the time histories of the instantaneous walking frequencies are shown, as measured in the P and G5-1 tests. It can be observed that the interaction

occurring in the group walking brings a reduction of the averaged value of the mean walking frequency of the five walkers:

$$\bar{f} = \frac{1}{N}\sum_{i=1}^{N} f_{mean}^i \tag{5.43}$$

$N = 5$ being the number of walkers in the group, which goes from 0.880 Hz in the P tests to 0.860 Hz in the G5-1 test. This confirms the tendency of walkers in groups to walk in a more relaxed way. In addition a reduction is observed of the inter-subject variability of the mean walking frequency. This is measured through the index of variation of the mean walking frequency of the five walkers:

$$I_v = \frac{\sqrt{\sum_{i=1}^{N}\left(f_{mean}^i - \bar{f}\right)^2}}{N\bar{f}} \tag{5.44}$$

which is 0.053 in the P tests and reduces to 0.019 in the G5-1 test.

It is finally observed that the reduction of the inter-subject variability of the mean walking frequency is obtained at the expenses of an increase of the intra-subject variability of the walking frequency. This is measured through the averaged value of the index of variation of the walking frequency of the five walkers:

Test	f_{mean} [Hz]	f_{std} [Hz]	I_f
	0.886 (0.939)	0.033 (0.027)	0.037 (0.029)
	0.836 (0.859)	0.030 (0.024)	0.035 (0.028)
	0.855 (0.901)	0.038 (0.040)	0.044 (0.045)
	0.846 (0.815)	0.029 (0.027)	0.035 (0.033)
G10	0.869 (0.889)	0.024 (0.032)	0.028 (0.036)
	0.873 (0.902)	0.043 (0.028)	0.050 (0.031)
	0.926 (0.981)	0.023 (0.020)	0.025 (0.020)
	0.940 (0.978)	0.037 (0.035)	0.037 (0.036)
	0.930 (0.910)	0.026 (0.030)	0.028 (0.033)

Tab. 5.5   Frequencies from G10 test
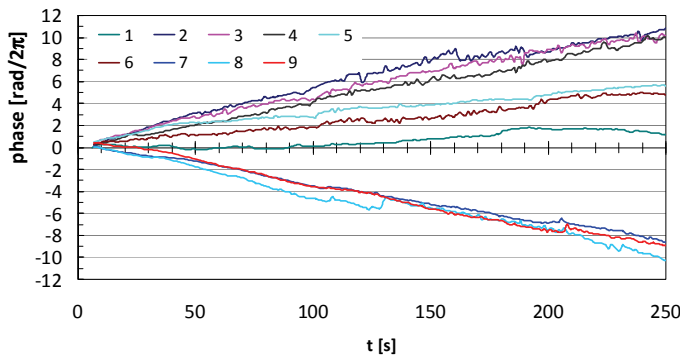
Figure 5.19   Phases of G10 test

$$\bar{I}_f = \frac{1}{N} \sum_{i=1}^{N} I_f^i \tag{5.45}$$

that increases from 0.034 of the P tests to 0.057 of the G5-1 test. This effect is considered as the result of the effort of the walkers put in keeping the same velocity and approximately the same frequency as the other members of the group. In doing so, they tend to walk in a less natural way, with the effect of decreasing the stationarity of their gait.

This effect can also be observed from Fig. 5.18, where the phases, as defined through Eq. (5.42) of four walkers with respect to the fifth are shown. Walkers 1 and 5 walk with the same mean frequency (0.877 Hz versus 0.875 Hz), therefore their phase stays almost constant. In particular it is zero from the beginning of the test to about $t = 80$ s; it then increases until it reaches the value of about π, which is kept from $t = 110$ s to $t = 180$ s, to drop down to zero again at $t = 200$ s. This indicates that these two walkers tend to walk either in phase of in opposite phase. Walkers 2 and 3, on the other hand, walk at a different frequency with respect to walker 1 (0.839 Hz and 0.857 Hz, respectively as opposed to 0.877 Hz), and such difference is kept constant in time so that there results a linear increase in phase. Finally a third type of behaviour is that of subject 4, who walks at a different mean frequency from walker 1 (0.850 Hz versus 0.877 Hz), but is unable to keep it constant (high intra-subject variability). There results a large increase in the index of variation of the walking frequency of walker 4 with respect to the undisturbed condition of the P test ($I_v = 0.088$ in the G5-1 test and $I_v = 0.033$ in the P test). In Fig. 5.18 this behaviour is identified with a phase that increases with varying slope.

Similar conclusions to those of G5-1 test could be drawn from the G10 test. In Tab 5.5 the statistics (mean, standard deviation and index of variation) of the walking frequency measured on 9 of the 10 walkers of test G10 are presented, and compared with those (in brackets) measured on the same subject during the P test. One time history could not be used due to a failure of the pedometer during the test, so one of the walkers was treated as a dummy when processing the data. Also in this case there is a reduction of the averaged value of the mean walking frequency $\bar{f}$,

Test	$\bar{f}$ [Hz]	$\tilde{f}$ [Hz]	$\bar{I}_f$
From [b]	0.923	0.112	0.121
C05	0.781	0.018	0.023
C07	0.816	0.046	0.056
C15	0.724	0.042	0.058

Tab. 5.6 Frequencies from C tests
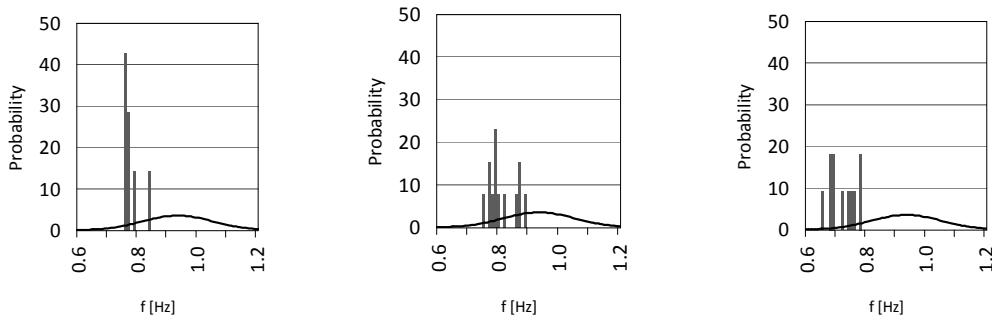
Figure 5.20 Frequency distribution from C tests

which goes from 0.908 Hz in the P tests to 0.885 Hz in the G10 test. Less dramatic is here the reduction of the index of variation of the mean walking frequency, which is 0.063 Hz in the P tests and reduced to 0.044 Hz in the G10 test. Consequently also the averaged value of the index of variation of the walking frequency has a negligible increase, from 0.032 of the P tests to 0.035 of the G10 test. Globally speaking it can be concluded that the interaction among walkers is lower in a group of ten than it is in a group of five. This is probably due to the fact that a group of five is small enough to behave as one single group, while a group of ten starts to become the assemblage of smaller subgroups behaving in a more or less independent way. This behaviour is somehow confirmed by Fig. 5.19, where the phases, as defined through Eq. (5.42), of nine walkers are shown, with respect to a theoretical walker having constant frequency $\bar{f} = 0.885$ Hz equal to the average value of the mean walking frequency of the nine walkers. It is clear how walkers 2, 3 and 4 on one side, and walkers 7, 8 and 9 on the other (but possibly also walkers 1, 5 and 6) tend to sub-group together (notice that parallel curves in the phase plots indicate constant phase shift between the walkers the curves refer to).

Crowd tests (C tests) were performed with densities of 0.5 walkers/m^2 (C05 tests), 0.7 walkers/m^2 (C07 tests) and 1.5 walkers/m^2 (C15 tests). For the C tests, the frequency characteristics are compared with those from a previous study of the undisturbed gait of a sample of 114 walkers of similar characteristics to those participating in the tests discussed here.

In Tab. 5.6 the inter-subject statistics of the mean walking frequency measured in the crowd tests are presented and compared with those of the undisturbed walk. These are the averaged value of the mean walking frequency defined in Eq. (5.43), the standard deviation of the mean walking frequency:

$$\tilde{f} = \frac{\sqrt{\sum_{i=1}^{N}\left(f_{mean}^{i} - \bar{f}\right)^2}}{N} \tag{5.46}$$

and the index of variation of the mean walking defined in Eq. (5.44).

It can be noticed that in all three tests there is a substantial reduction of the average and of the standard deviation of the mean walking frequency. However, such reduction does not appear to be related to the density parameter. In fact, the largest reduction of the average mean frequency occurs for a density of 1.5 walkers/m^2 (0.724 Hz versus 0.923 Hz, 22% reduction), and the largest reduction of the standard deviation of the mean frequency occurs for a density of 0.5 walkers/m^2 (0.018 Hz versus 0.112 Hz, 84% reduction) while for a density of 0.7 walkers/m^2 the reduction of both statistics is lower (12% and 59% reduction of $\bar{f}$ and $\tilde{f}$, respectively). The fact that the maximum reduction of $\bar{f}$ occurs for a large density of pedestrians is strictly related to the reduction of the walking speed occurring at large densities. The reduction of the standard deviation, however, is more related to the increase in the organisation of the walkers, and it is a surprising result that the maximum organisation is for a moderate density of 0.5 walkers/m^2.

Finally, in Fig. 5.20 the Gaussian PDF of the undisturbed walking frequency is compared with the histograms of the mean walking frequencies measured during the C tests. In the plots the areas of the Gaussian PDF and of the histograms are the same (and equal to 1), it is evident how the walkers in the crowd tend to walk in a very narrow range of frequencies.

5.7 BASIC REFERENCES

[a] Terrier P., Turner V., Schutz Y. 2005. GPS analysis of human locomotion: further evidence of long-range correlations in stride-to-stride fluctuations of gait parameters, *Human Movement Science* 24(1), 583-591.

[b] Zivanovic S., Pavic A., Reynolds P. 2005. Vibration serviceability of footbridges under human-induced excitation: a literature review. *Journal of Sound and Vibration* 279(1-2), 1-74.

[c] Dallard P., Fitzpatrick A.J., Flint A., Bourva S., Low A., Ridsdill-Smith R.M., Willlford M. 2001. The London Millennium Footbridge, *Structural Engineer* 79(22), 17-22.

[d] Brownjohn J., Zivanovic S., Pavic A. 2008. Crowd dynamic loading on footbridges. In *Proceedings of the Third International Conference Footbridge 2008*, Porto.

[e] Dziuba P., Grillaud G., Flamand O., Sanquier S., Tétard Y. 2001. La passerelle Solférino comportement dynamique. *Bulletin Ouvrages Métalliques* 1, 34-57 (In French).

[f] Ye Q., Fanjiang G.N., Yanev B. 2005. Investigation of the dynamic properties of the Brooklyn Bridge. In *Sensing Issues in Civil Structural Health Monitoring*. Springer Netherlands.

[g] Fujino Y., Pacheco B.M., Nakamura S.I., Warnitchai P. 1993. Synchronization of human walking observed during lateral vibration of a congested pedestrian bridge. *Earthquake Engineering & Structural Dynamics* 22(9), 741-758.

[h] Racic V., Pavic A., Brownjohn J. 2009. Experimental identification and analytical modeling of walking forces: Literature review. *Journal of Sound and Vibration* 326, 1-49.

[i] Pizzimenti A.D. 2005. Experimental analysis of the lateral pedestrian-induced mechanism of excitation of footbridges. PhD thesis, University of Reggio Calabria (In Italian).

[j] McRobie A., Morgenthal J., Lasenby J., Ringer M. 2003. Section model tests on human-structure lock-in. *Bridge Engineering* 156, 71-79.

[k] Ricciardelli F. 2005. Lateral loading of footbridges by walkers. *Proceedings of Footbridge 2005 – 2nd International Conference*, Venezia, Italy.

[l] Ingolfsson E.T. 2006. *Pedestrian-induced vibrations of line-like structures*. Masters Thesis, BYD.DTU, Technical University of Denmark.

[m] Matsumoto Y., Nishioka T., Shiojiri H., Matsuzaki K. 1978. Dynamic design of footbridges, *IABSE Proceedings*, 17/78, 1-15.

5.8 LIST OF PUBLICATIONS

[1] Ricciardelli F., Pizzimenti A.D. 2007. Lateral walking-induced forces on footbridges. *Journal of Bridge Engineering* 12(6), 677-688, ISSN: 1084-0702.

[2] Ricciardelli F., Briatico C., Ingolfsson E.T., Georgakis C.T. 2007. Experimental validation and calibration of pedestrian loading models for footbridges. *Proceedings of the International Conference on Experimental vibration analysis for civil engineering structures*, Porto, Portugal, 129-130, CD ROM and ISBN: 978 972 752 095 4.

[3] Ingolfsson E.T., Georgakis C.T., Jonsson J., Ricciardelli F. 2007. Vertical footbridge vibrations: towards an improved and confiable pedestrian loading model. *Proceedings of the 3rd International Conference on Structural Engineering, Mechanics and Computation*, Cape Town, South Africa.

[4]   Occhiuzzi A., Spizzuoco M., Ricciardelli F. 2008. Loading models and response control of foot-bridges excited by runners. *Journal of Structural Control and Health Monit*oring 15, 349-368, ISSN: 1554-2255.

[5]   Ricciardelli F. 2008. Risposta transitoria di travi appoggiate a carichi viaggianti. *3° Workshop Problemi di vibrazioni nelle strutture civili e nelle costruzioni meccaniche*, Perugia, Italy.

[6]   Ricciardelli F., Briatico C. 2009. Transient response of supported beams to moving sinusoidal forces. *Journal of Engineering Mechanics*, accepted for publication.

[7]   Ricciardelli F., Pansera A. 2010. An experimental investigation into the interaction among walkers in groups and crowds. *Proceedings of the 10th International Conference on Recent Advances in Structural Dynamics*, Southampton.

[8]   Ingolfsson E.T., Georgakis C.T., Jonson J., Ricciardelli F., Procino L. 2010. Experimental identification of lateral pedestrian loads on footbridges. *Proceedings of the 10th International Conference on Recent Advances in Structural Dynamics*, Southampton.

WITH CONTRIBUTION FROM:

Niccolò Bonanni, University of Florence
Carmelo Briatico, University of Reggio Calabria
Emanuela Calabrese, University of Reggio Calabria
Christos T. Georgakis, Technical University of Denmark
Einar T. Ingolfsson, Technical University of Denmark
Antonella Pansera, University of Reggio Calabria
Lorenzo Procino, CRIACIV

STRUMENTI
PER LA DIDATTICA E LA RICERCA

1. Brunetto Chiarelli, Renzo Bigazzi, Luca Sineo (a cura di), *Alia: Antropologia di una comunità dell'entroterra siciliano*
2. Vincenzo Cavaliere, Dario Rosini, *Da amministratore a manager. Il dirigente pubblico nella gestione del personale: esperienze a confronto*
3. Carlo Biagini, *Information technology ed automazione del progetto*
4. Cosimo Chiarelli, Walter Pasini (a cura di), *Paolo Mantegazza. Medico, antropologo, viaggiatore*
5. Luca Solari, *Topics in Fluvial and Lagoon Morphodynamics*
6. Salvatore Cesario, Chiara Fredianelli, Alessandro Remorini, *Un pacchetto evidence based di tecniche cognitivo-comportamentali sui generis*
7. Marco Masseti, *Uomini e (non solo) topi. Gli animali domestici e la fauna antropocora*
8. Simone Margherini (a cura di), *BIL Bibliografia Informatizzata Leopardiana 1815-1999: manuale d'uso ver. 1.0*
9. Paolo Puma, *Disegno dell'architettura. Appunti per la didattica*
10. Antonio Calvani (a cura di), *Innovazione tecnologica e cambiamento dell'università. Verso l'università virtuale*
11. Leonardo Casini, Enrico Marone, Silvio Menghini, *La riforma della Politica Agricola Comunitaria e la filiera olivicolo-olearia italiana*
12. Salvatore Cesario, *L'ultima a dover morire è la speranza. Tentativi di narrativa autobiografica e di "autobiografia assistita"*
13. Alessandro Bertirotti, *L'uomo, il suono e la musica*
14. Maria Antonietta Rovida, *Palazzi senesi tra '600 e '700. Modelli abitativi e architettura tra tradizione e innovazione*
15. Simone Guercini, Roberto Piovan, *Schemi di negoziato e tecniche di comunicazione per il tessile e abbigliamento*
16. Antonio Calvani, *Technological innovation and change in the university. Moving towards the Virtual University*
17. Paolo Emilio Pecorella, *Tell Barri/Kahat: la campagna del 2000. Relazione preliminare*
18. Marta Chevanne, *Appunti di Patologia Generale. Corso di laurea in Tecniche di Radiologia Medica per Immagini e Radioterapia*
19. Paolo Ventura, *Città e stazione ferroviaria*
20. Nicola Spinosi, *Critica sociale e individuazione*
21. Roberto Ventura (a cura di), *Dalla misurazione dei servizi alla customer satisfaction*
22. Dimitra Babalis (a cura di), *Ecological Design for an Effective Urban Regeneration*
23. Massimo Papini, Debora Tringali (a cura di), *Il pupazzo di garza. L'esperienza della malattia potenzialmente mortale nei bambini e negli adolescenti*
24. Manlio Marchetta, *La progettazione della città portuale. Sperimentazioni didattiche per una nuova Livorno*
25. Fabrizio F.V. Arrigoni, *Note su progetto e metropoli*
26. Leonardo Casini, Enrico Marone, Silvio Menghini, *OCM seminativi: tendenze evolutive e assetto territoriale*
27. Pecorella Paolo Emilio, Raffaella Pierobon Benoit, *Tell Barri/Kahat: la campagna del 2001. Relazione preliminare*
28. Nicola Spinosi, *Wir Kinder. La questione del potere nelle relazioni adulti/bambini*
29. Stefano Cordero di Montezemolo, *I profili finanziari delle società vinicole*
30. Luca Bagnoli, Maurizio Catalano, *Il bilancio sociale degli enti non profit: esperienze toscane*
31. Elena Rotelli, *Il capitolo della cattedrale di Firenze dalle origini al XV secolo*
32. Leonardo Trisciuzzi, *Barbara Sandrucci, Tamara Zappaterra, Il recupero del sé attraverso l'autobiografia*
33. Nicola Spinosi, *Invito alla psicologia sociale*
34. Raffaele Moschillo, *Laboratorio di disegno. Esercitazioni guidate al disegno di arredo*
35. Niccolò Bellanca, *Le emergenze umanitarie complesse. Un'introduzione*
36. Giovanni Allegretti, *Porto Alegre una biografia territoriale. Ricercando la qualità urbana a partire dal patrimonio sociale*
37. Riccardo Passeri, Leonardo Quagliotti, Christian Simoni, *Procedure concorsuali e governo dell'impresa artigiana in Toscana*
38. Nicola Spinosi, *Un soffitto viola. Psicoterapia, formazione, autobiografia*
39. Tommaso Urso, *Una biblioteca in divenire. La biblioteca della Facoltà di Lettere dalla penna all'elaboratore. Seconda edizione rivista e accresciuta*
40. Paolo Emilio Pecorella, Raffaella Pierobon Benoit, *Tell Barri/Kahat: la campagna del 2002. Relazione preliminare*
41. Antonio Pellicanò, *Da Galileo Galilei a Cosimo Noferi: verso una nuova scienza. Un inedito trattato galileiano di architettura nella Firenze del 1650*